High-Pressure Phase Behaviour of Saturated and Unsaturated Fatty Acid Esters in Supercritical CO$_2$
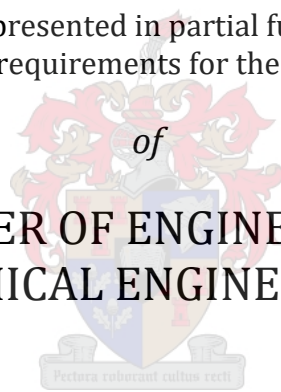
by

Jacobus Johannes Moorcroft

Thesis presented in partial fulfilment
of the requirements for the Degree

of

MASTER OF ENGINEERING (CHEMICAL ENGINEERING)

in the Faculty of Engineering
at Stellenbosch University

Supervisor

Prof. C.E. Schwarz

March 2020

Declaration

By submitting this thesis electronically, I declare that the entirety of the work contained therein is my own, original work, that I am the sole author thereof (save to the extent explicitly otherwise stated), that reproduction and publication thereof by Stellenbosch University will not infringe any third party rights, and that I have not previously in its entirety or in part submitted it for obtaining any qualification.

Date: *March 2020*

Plagiarism declaration

1. Plagiarism is the use of ideas, material and other intellectual property of another's work and presenting it as my own.

2. I agree that plagiarism is a punishable offence because it constitutes theft.

3. I also understand that direct translations are plagiarism.

4. Accordingly, all quotations and contributions from any source whatsoever (including the internet) have been cited fully. I understand that the reproduction of text without quotation marks (even when the source is cited) is plagiarism.

5. I declare that the work contained in this thesis, except where otherwise stated, is my original work and that I have not previously (in its entirety or in part) submitted it for grading.

Initials and surname: J. J. Moorcroft

Date: 14 November 2019

Abstract

A variety of high-value compounds can be found in the oils extracted from fish, plants, and algae. Chief among these are fatty acids. These compounds are frequently processed in the form of fatty acid ester oils, most notably methyl (FAMEs) or ethyl (FAEEs) esters. They are, however, often produced in mixtures of varying chain length and degree of unsaturation as a result of genetic and dietary variation between source organisms. In order to upgrade the quality of the oil, it is desired to alter the chain length distribution and degree of unsaturation distribution. Supercritical fluid fractionation (SCFF) is an attractive potential solution, as supercritical CO_2 is a safe and environmentally benign solvent. It has been shown that supercritical CO_2 is capable of fractionating fatty acid esters based on their hydrocarbon chain length. Little work has been done to investigate fractionation based on the degree of unsaturation independent of chain length, however, and phase behaviour data available in the literature is inconclusive.

This study aimed **to investigate the feasibility of the SCFF of FAMEs with CO_2 as solvent based purely on degree of unsaturation**. To achieve this aim, the study was divided into three objectives: (1) Measure phase behaviour data for binary FAME + CO_2 systems to investigate the influence of unsaturation on the phase behaviour; (2) Measure ternary phase behaviour and equilibrium data to investigate the influence of unsaturation on FAME mixture behaviour and the distribution of FAMEs between fluid phases; (3) Conduct thermodynamic modelling on the investigated systems to evaluate the ability of equations of state (EOSs) to describe the influence of unsaturation on FAME phase behaviour.

Binary high-pressure bubble and dew point data were measured using a synthetic-visual method for the methyl stearate + CO_2, methyl oleate + CO_2, and methyl linoleate + CO_2 systems. The family of C_{18} FAMEs was investigated as it includes a variety of industrially relevant compounds with varying degrees of unsaturation. The data showed that there is a difference in the phase transition pressures (and by extension solubility) between the saturated methyl stearate and the two unsaturated esters. However, there is no difference between the solubility of methyl oleate and methyl linoleate exceeding the experimental uncertainty of 1.8 bar. The solubility difference between saturated and unsaturated esters decreases as the temperature increases. The correlation of molecular order (CMO) was presented as an argument to explain the observed phase behaviour. These results indicate that supercritical CO_2 can distinguish between saturated and unsaturated FAMEs, supporting the possible application of SCFF.

For further investigation, high-pressure bubble and dew point data were measured with a synthetic-visual method for the ternary methyl stearate + methyl oleate + CO_2 system. The data showed that a higher methyl stearate content leads to higher phase transition pressures and decreased solubility, following a linear trend. This system thus exhibits no cosolvency or other nonideal interactions. Ternary vapour-liquid equilibrium (VLE) data were also measured for the methyl stearate + methyl oleate + CO_2 system. The distribution coefficients of methyl stearate were generally slightly higher than for methyl oleate. The relative solubility of methyl stearate relative to methyl oleate was found to be greater than one and to decrease with an increase in pressure. This data suggests that CO_2 is selective for methyl stearate, the less soluble species. A rigorous uncertainty analysis was performed, and revealed that there was considerable uncertainty present in the calculated relative solubilities. The uncertainty in the relative solubility data thus introduces doubt into any conclusions drawn from the data.

Thermodynamic modelling was conducted on the measured data with the predictive Peng-Robinson (PPR) and modified Sanchez-Lacombe (MSL) equations of state. While the PPR and MSL (with a regressed binary interaction parameter) could give reasonable descriptions of general C_{18} FAME phase behaviour, they were not able to describe, either qualitatively or quantitatively, the influence of unsaturation on the binary phase behaviour of C_{18} FAME + CO_2 systems. The models were also unable to predict both the measured data for the ternary system and the experimental relative solubility data. These results highlight the relevance of experimental phase equilibria measurements, particularly for systems that do not exhibit large differences in solubility, since the shortcomings of predictive modelling can potentially overshadow phase behaviour features that occur over small ranges of pressure or temperature.

Uittreksel

'n Verskeidenheid waardevolle komponente word in geëkstraheerde olies afkomstig van visse, plante en alge gevind. Vetsure vorm 'n groot deel van sulke olies, en word dikwels in die vorm van vetsuuresterolies, hoofsaaklik as vetsuurmetielesters (VSMEs) of vetsuuretielesters (VSEEs) geprosesseer. Die olies word vervaardig in mengsels met 'n verspreiding van koolstofkettinglengtes en graad van onversadigdheid as gevolg van genetiese variasie en dieetverskille tussen die organismes waaruit die olie geëkstraheer word. Die kwaliteit van die olie kan vir 'n spesifieke toepassing opgradeer word deur die verspreiding van kettinglengtes en oversadigdheid aan te pas. Superkritiese vloeierfraksionering (SKVF) is 'n aanloklike oplossing, aangesien superkritiese CO_2 'n veilige en omgewingsvriendelike oplosmiddel is. Dit is reeds bewys dat vetsuurester mengsels op grond van hul koolstofkettinglengtes geskei kan word deur superkritiese koolstofdioksied. Die fraksionering van vetsuur esters op grond van hul onversadigdheid ongeag koolstofkettinglengte is nog nie ondersoek nie, en die fasegedragsdata in die ope literatuur is onbeslis.

Die mikpunt van hierdie studie was dus **om die vatbaarhied van die SKVF van VSMEs met CO_2 as oplosmiddel alleenlik op grond van die graad van onversadigdheid te ondersoek**. Derhalwe is die studie in drie doelwitte verdeel: (1) Meet fasegedragsdata vir binêre VSME + CO_2 stelsels om die invloed van onversadigdheid op die fasegedrag te ondersoek; (2) Meet ternêre fasegedrags- en ewewigsdata om die invloed van onversadigdheid op VSME mengselgedrag en die verspreiding van VSMEs tussen vloeierfases te ondersoek; (3) Voer termodinamiese modellering op die gebestudeerde stelsels uit ter evaluering van die vermoë van toestandsvergelykings om die invloed van onversadigdheid op VSME-fasegedrag te beskryf.

Binêre hoëdruk borrel- en doupuntdata is vir die metiel stearaat + CO_2, metiel oleaat + CO_2, en linoleiensuur metiel ester + CO_2 stelsels gemeet. Die C_{18} familie VSMEs is ondersoek aangesien dit 'n verskeidenheid industrieel relevante komponente met verskillende grade van onversadigdheid bevat. Die data het getoon dat daar 'n verskil in die fase-oorgangsdrukke (en dus ook die oplosbaarheid) tussen die versadigde metiel stearaat en die twee onversadigde esters is. Daar is ook geen verskil tussen die oplosbaarheid van metiel oleaat en linoleiensuur metiel ester wat die eksperimentele onsekerheid van 1.8 bar oorskry nie. Die oplosbaarheidsverskil tussen versadigde en onversadigde esters neem af namate die temperatuur toeneem. Die korrelasie van molekulêre orde (KMO) is as 'n argument voorgestel om die waargenome fasegedrag te verduidelik. Hierdie resultate dui aan dat superkritiese CO_2 tussen versadigde en onversadigde VSMEs kan onderskei, wat die moontlike toepassing van SKVF ondersteun.

Verdere ondersoek is ingestel deur ternêre hoëdruk borrel- en doupuntdata vir die metiel stearaat + metiel oleaat + CO_2 stelsel te meet. Die data het getoon dat 'n hoër metiel stearaat inhoud tot hoër fase-oorgangsdrukke en verlaagde oplosbaarheid lei, wat 'n meestal lineêre tendens volg. Die sisteem toon dus geen verhoogde oplosbaarhied of ander nie-ideale interkasies nie. Ternêre damp-vloeistof ewewigsdata (DVE) is ook vir hierdie stelsel gemeet. Beide esters het lae verspreidingskoëffisiënte gehad, wat aandui dat daar 'n beperkte lading van die dampfase is. Die verspreidingskoëffisiënte vir metiel stearaat was in die algemeen effens hoër as vir metiel oleaat. Gevolglik is die relatiewe oplosbaarheid van metiel stearaat met betrekking tot metiel oleaat as groter as een bevind, en dat dit met toenemende druk afneem. Hierdie data stel voor dat CO_2 selektief vir metiel stearaat, die minder oplosbare spesie, is. 'n Omvattende onsekerheidsanalise is uitgevoer, en het aansienlike onsekerheid in die berekende relatiewe oplosbaarhede getoon. Daar bestaan dus redelike twyfel oor enige gevolgtrekkings wat oor die DVE data gemaak word.

Termodinamiese modellering is op die gemete data met die voorspellende Peng-Robinson (VPR) en die gewysigde Sanchez-Lacombe (GSL) toestandsvergelykings uitgevoer. VPR en GSL (met 'n geregresseerde binêre interaksie parameter) kon redelike beskrywings van die algemene C_{18} VSME-fasegedrag gee, maar kon nie kwalitatief of kwantitatief die invloed van onversadigdheid op die fasegedrag van binêre VSME + CO_2 stelsels beskryf nie. Die modelle kon ook nie die data vir die ternêre stelsel voorspel nie. Hierdie resultate beklemtoon die belang van eksperimentele fase-ewewig metings, spesifiek vir stelsels wat nie 'n groot oplosbaarheidsverskil toon nie, aangesien die tekortkominge van modellering moontlik die fasegedragseienskappe wat in klein druk- en temperatuurintervalle plaasvind, kan verbloem.

Acknowledgements

A research project is a daunting task to take on, and I would like to thank the following people for their help and support:

Nomenclature

	Symbols	
A	Chromatographic peak area	pAs (or µVs)
A'	Adjusted peak area	pAs (or µVs)
A_{kl}	Group-contribution parameter for predictive Peng-Robinson	J·cm^{-3}
a	HVDL parameters	
	Peng-Robinson energy parameter	J·mol^{-1}
	Modified Sanchez-Lacombe parameter	J·m^3·mol^{-2}
B_{kl}	Group-contribution parameter for predictive Peng-Robinson	J·cm^{-3}
b	Peng-Robinson volume parameter	m^3·mol^{-1}
	Modified Sanchez-Lacombe parameter	m^3·mol^{-1}
c	Detector response (Chromatography)	pA
	Volume shift parameter (modified Sanchez-Lacombe model)	cm^3·g^{-1}
c_{max}	Maximum detector response	pA
d	Discretisation (Chromatography)	dimensionless
	Number of lattice sites per molar mass unit (modified Sanchez-Lacombe model)	mol·g^{-1}
$\boldsymbol{F}$	Feature vector	
F_{OBJ}	Objective function	dimensionless
h	Sensor hysteresis	
K	Distribution coefficient	dimensionless
k_{ij}	Binary interaction parameter	dimensionless
M	Molar weight	g·mol^{-1}
m	Mass	g
N_C	Carbon number	
P	Pressure	bar
p	Sensor precision	
	Impurity mass fraction	g·g^{-1}
Q	Quadrupole moment	C·m^2
r	Sensor resolution (uncertainty analyses)	
	Intermolecular distance (intermolecular forces)	m

	Mass ratio (chromatography)	dimensionless
S	Standard deviation	
T	Temperature	K (or °C)
t	Time	s
t_b	Breakthrough time	s
u	Standard uncertainty	
V	Volume	mL
V_c	Critical volume	mL·mol⁻¹
v	Molar volume	m³·mol⁻¹
v^*	Volume per lattice site	cm³·mol⁻¹
w_1^{red}	Specific solvent-free mass fraction	g·g⁻¹
w	Signal length (chromatography)	s
	Individual component mass fraction (ternary HPBDP data)	g·g⁻¹
x	Liquid/solvent-poor mass fraction (VLE data)	g·g⁻¹
	Input quantity (uncertainty analyses)	
	Mole fraction (chromatography)	mol·mol⁻¹
y	Vapour/solvent-rich mass fraction (VLE data)	g·g⁻¹
	Output quantity (uncertainty analyses)	
z	Total solute fraction	g·g⁻¹

Greek symbols		
α	Relative solubility (VLE data)	dimensionless
	Straight line intercept (calibrations and uncertainty analyses)	
β	Slopes of calibrations or linear regression models	
Γ	Energy potential	J
δ	Random error	
ε	Correction factor (Calibrations)	
	Lattice energy (modified Sanchez-Lacombe model)	J·mol⁻¹
μ	Dipole moment	C·m
ρ	Density	g·mL⁻¹
Φ	Critical volume fraction	dimensionless
ϕ	Recovered solute composition	g·g⁻¹
ω	Acentric factor	dimensionless

Subscripts and superscripts

c	Critical property
$calc$	Calculated
$calib$	Calibration
exp	Experimental
$fluct$	Fluctuation
$hyst$	Hysteresis
i	Component i
ind	Indicated
j	Component j
m	Mixture property
$meas$	Measured
ref	Reference
res	Residue

Physical constants

ε_0	Dielectric permittivity of vacuum, 8.854e-12 $C^2J^{-1}m^{-1}$
k	Boltzmann's constant, 1.38e-23 $J \cdot K^{-1}$
R	Universal gas constant, 8.314 $J \cdot mol^{-1}K^{-1}$

Abbreviations

BIP	Binary interaction parameter
CMO	Correlation of molecular order
CSSRL	Constant solute-solute ratio lines
CV	Cross-validation
DHA	Docosahexaenoic acid
EOS	Equation of state
EPA	Eicosapentaenoic acid
FAE	Fatty acid ester
FAEE	Fatty acid ethyl ester
FAME	Fatty acid methyl ester
FID	Flame ionisation detector
FLE	Fluid-liquid equilibrium
GC	Gas chromatography
GRAS	Generally regarded as safe
GUM	Guide to the expression of uncertainty in measurement

HETP	Height equivalent to a theoretical plate
HPBDP	High-pressure bubble and dew point
HVDL	Haarhoff van der Linde model
LCEP	Lower critical end point
LLE	Liquid-liquid equilibrium
MAPE	Mean absolute percentage error
MSE	Mean squared error
MSL	Modified Sanchez-Lacombe
MSLR	Modified Sanchez-Lacombe with regressed interaction parameter
NIST	National Institute of Standards and Technology
PDSC	Pressure differential scanning calorimetry
PFSV	Purge flow split vent time
PPR	Predictive Peng-Robinson
ROLSI™	Rapid online sampler injector
SAFT	Statistical associating fluid theory
SCFE	Supercritical fluid extraction
SCFF	Supercritical fluid fractionation
SLE	Solid-liquid equilibrium
TCD	Thermal conductivity detector
TGA	Thermal gravimetric analysis
UCEP	Upper critical end point
VLE	Vapour-liquid equilibrium
VLLE	Vapour-liquid-liquid equilibrium

Contents

CHAPTER 1:
Introduction

The efficient utilisation and beneficiation of natural resources are central to the issue of sustainability and sustainable development.[1,2] The extracted oils from fish and other marine animals are rich in high-value lipid compounds that have been linked to improved heart health in humans.[3,4] Fishery waste and byproducts can contain significant amounts of these oils, and their extraction and beneficiation contributes to the sustainable use of natural resources.[5]

1.1. Project Motivation

Natural oil feedstocks contain a variety of triglycerides, which consist of three long-chain carboxylic acids (fatty acids) bonded to a glycerol backbone. The constituent fatty acids can differ in hydrocarbon chain lengths and degrees of unsaturation (the number of C=C bonds in the hydrocarbon chain), and the fatty acid structure directly influences the quality of the product nutraceutical supplement.

Triglyceride oils are difficult to process, as they require high processing pressures, and specific fatty acids cannot be targeted since they are sequestered in the triglyceride molecule. Triglycerides thus need to be hydrolysed into free fatty acids, or transesterified into fatty acid esters (FAEs) for further processing. FAEs have an advantage over free fatty acids, in that they require lower processing pressures. In this form, it is now possible to modify the fatty acid profile of the oil, improving its properties[3]

Due to the variation of chain length and degree of unsaturation in a transesterified oil sample, and the influence of these properties on the quality of the final product, separation technologies play an important role in upgrading the FAE oil. This is necessary to optimise the performance of the final product, to allow it to adhere to regulatory standards, or to concentrate it in the healthier constituents. There is thus both an economic as well as an environmental incentive for the extraction and processing of FAE oils derived from natural resources.

Several separation processes are available, but the prioritisation of environmental concerns and sustainability have placed special focus on the technique of supercritical fluid fractionation (SCFF). This processing strategy makes use of a gaseous solvent pressurised above its critical point. A supercritical fluid has superior solvent properties and avoids the use of potentially hazardous and expensive liquid solvents. It also reduces the complexity involved with the downstream separation of the product from the solvent.[3,6,7]

1. Introduction

Separation processes are governed by thermodynamics, which dictates the extent to which separation can take place at equilibrium.[8] Since thermodynamics relates to the phase behaviour, encompassing both phase equilibria (the distribution of components among different phases) and the influence of process conditions on the properties and features of these phases, it is important both in terms of determining whether a proposed separation process is feasible, as well as for performing design calculations.[9]

Several phase behaviour and fractionation studies have shown that FAEs can be fractionated on the basis of their chain length by supercritical CO_2.[3,7,10] The application of SCFF to the separation of FAEs purely on the basis of the degree of unsaturation is not as conclusive, however. No studies have focussed on assessing the phase behaviour of FAEs in a supercritical solvent where the hydrocarbon chain length was kept constant. The available data in the literature is not conclusive, as there are considerable discrepancies between published data sets, as well as compositional regions where data are absent.

Thermodynamic modelling is also a valuable tool for investigating the phase behaviour of systems of interest. Effective modelling diminishes the need for costly and time-consuming experiments, and facilitates the simulation of industrial processes.[11] It is thus beneficial to have a model that can describe the phase behaviour of a pertinent system, particularly if the model is predictive, and does not need to be correlated to experimental data.

1.2. Aims and Objectives

Given the deficiencies in the available literature data, **the aim of this investigation is to determine the ability of supercritical CO_2 to fractionate FAMEs based on degree of unsaturation** where the hydrocarbon backbone length is kept constant. In order to accomplish this aim, the study can be divided into three objectives:

1. *Investigate the influence of unsaturation on the phase behaviour of binary FAME + CO_2 systems* by measuring high-pressure bubble and dew point data for systems with a varying degree of unsaturation but constant hydrocarbon chain length to address the gap and discrepancy in literature data.

2. *Investigate the influence of unsaturation on the phase behaviour of ternary FAME + FAME + CO_2 systems* where one FAME is saturated, and the other is unsaturated, with both having the same hydrocarbon chain length.

    2.1. *Investigate the influence of unsaturation on the solubility of FAME mixtures in CO_2 and vice versa* by measuring high-pressure bubble and dew point data for ternary systems.

    2.2. *Investigate the influence of unsaturation on the compositions of coexisting fluid phases* by measuring high-pressure vapour-liquid equilibrium data for ternary systems.

3. *Investigate the ability of thermodynamic models to describe the influence of unsaturation on the phase behaviour of FAME + CO₂ systems* by conducting thermodynamic modelling for the systems considered in this work.

1.3. Project Scope

FAE + solvent systems can involve a wide range of components, with transesterified marine oils typically containing esters in the C_{10} to C_{24} range.[3] This study focuses on the C_{18} family of methyl esters. Many studies investigating the effect of unsaturation on a variety of properties or systems involving fatty acids or fatty acid esters use the C_{18} family of esters as model components.[12–17] This family of esters is also the shortest chain family with industrially relevant unsaturated members. Specifically, the components methyl stearate (saturated), methyl oleate (monounsaturated), and methyl linoleate (polyunsaturated) are investigated. Only the *cis*-isomers are considered in this investigation, as the *trans*-isomers are not industrially relevant, and less prevalent in nature.[4]

Only carbon dioxide (CO_2) is considered as a supercritical solvent in this work. Most studies focus on CO_2 as a solvent for SCFF of FAEs, particularly in the processing of fish oil esters for the food and pharmaceutical industry.[6] This is due to CO_2 being a generally regarded as safe (GRAS) solvent, making it highly suitable for the processing of food products.[18]

With regards to thermodynamic modelling, two relatively simple equations of state (EOSs) are considered: predictive Peng-Robinson as a model that has been applied to FAE + supercritical solvent systems by several authors[19–21] and modified Sanchez-Lacombe as an alternative model that has not been applied to these types of systems before.

1.4. Thesis Structure

Chapter 2 focusses on the production and application of fatty acid esters, highlighting their commercial significance, and then discusses the process of supercritical fluid fractionation. **Chapter 3** discusses high-pressure phase behaviour and thermodynamics, and collates all literature data available for the systems investigated in this work. **Chapter 4** then presents the experimental methodology followed to measure the phase behaviour data. Chapter 5, 6, and 7 discuss the results of the investigation, and link back to Objectives 1, 2, and 3 respectively. **Chapter 5** focusses on the binary systems, **Chapter 6** on the ternary systems, and **Chapter 7** considers the thermodynamic modelling. **Chapter 8** summarises the conclusions of the study, and provides recommendations for further work.

CHAPTER 2:
Supercritical Fluid Fractionation of Fatty Acid Esters

Fatty acid esters as derived from lipid sources are the components of interest in this work. This chapter discusses their properties and production routes, and highlights their application and relevance as high-value chemicals. An overview is also given of the separation technologies that have been investigated or applied to the processing of fatty acid ester products. This leads to a discussion of supercritical fluid fractionation, motivating the selection of a suitable solvent, as well as the utility of phase behaviour data in the evaluation of supercritical processes.

2.1. FAE Structure

Esters are organic molecules containing an ester-bond functional group, which is most commonly formed through an esterification reaction of an alcohol with a carboxylic acid.[22] Various reaction schemes exist, with and without catalysis, using acids, bases, or other compounds as activators. A basic reaction scheme is illustrated in Equation 2.1[23]:

$$R1\!-\!OH \; + \; \text{(carboxylic acid)} \; \longrightarrow \; \text{(ester)} \; + \; H_2O \qquad\qquad 2.1$$
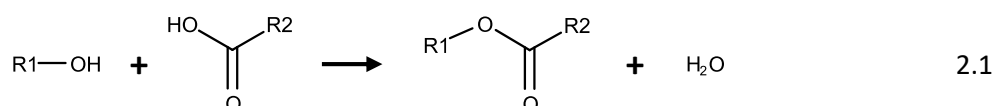
where $R1$ and $R2$ represent any organic constituent. In the case of fatty acid esters (FAEs), $R2$ is a long-chain alkyl or alkenyl group, whilst $R1$ can be a variety of groups – most commonly a methyl or ethyl group for the purposes of this investigation. A shorthand notation for referring to FAEs is introduced:

$$XY\!:\!Z$$
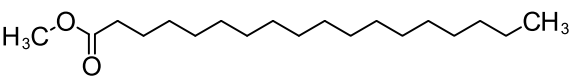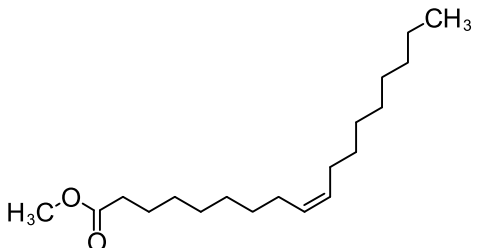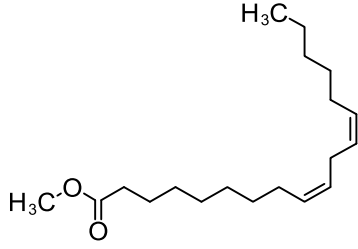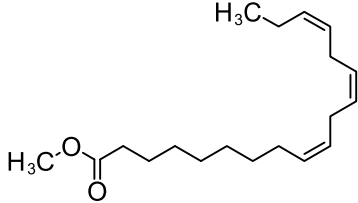
where X is a letter denoting the alkyl group attached to the oxygen atom of the ester bond (M for a methyl group, E for an ethyl group), Y is a number denoting the number of carbon atoms in the fatty acid hydrocarbon backbone $R2$, and Z is a number indicating the number of C=C double bonds present in $R2$. Following this notation methyl stearate is referred to as M18:0, as it is the product of the esterification of methanol with octadecanoic acid.

FAEs without C=C bonds are saturated, while unsaturated FAEs possess one (monounsaturated) or more (polyunsaturated) C=C bonds. An additional descriptor can be provided for unsaturated FAEs in

2. Supercritical Fluid Fractionation of Fatty Acid Esters

the form of the ω-number.[24] The ω-number denotes the position of the first C=C bond when counting from the terminal end of the fatty acid hydrocarbon backbone. In this way, methyl oleate can be denoted by M18:1 ω-9. Table 2.1 provides a summary of the structure and properties of the most relevant members of the C_{18}-family of fatty acid methyl esters (FAMEs).[25] Only the *cis*-isomers (having the hydrogen atoms of the C=C bond on the same side) of the unsaturated FAMEs are considered, as they are more industrially relevant than their *trans*-isomer counterparts.[4]

Table 2.1: Summary of the structure and properties of C_{18} FAMEs. Melting point and boiling point data from Lide.[25]

Component	Properties		Structure
Methyl Stearate M18:0	M [g·mol⁻¹]	298.51	
	Melting Point	39.1°C	
	Boiling Point	443°C	
Methyl Oleate M18:1 ω-9	M [g·mol⁻¹]	296.50	
	Melting Point	-19.9°C	
	Boiling Point	218.5°C	
Methyl Linoleate M18:2 ω-6	M [g·mol⁻¹]	294.48	
	Melting Point	-35°C	
	Boiling Point	-	
Methyl Linolenate M18:3 ω-3	M [g·mol⁻¹]	292.46	
	Melting Point	-	
	Boiling Point	-	

FAMEs are thermally labile compounds, which means that they are susceptible to degradation at high temperatures.[12] This limits the range of possible operating temperatures, which in turn limits viable unit operations for FAME processing. The unsaturated FAMEs in particular have a decreased heat resistance, and have an increased susceptibility to oxidation.[12]

Pillar et al.[12] investigated the thermal decomposition of FAMEs with thermogravimetric analysis (TGA) and pressure differential scanning calorimetry (PDSC) in the context of lubricants. They found that an increasing level of unsaturation resulted in a decrease in the degradation onset temperature. Table 2.2

provides a summary of the results obtained. It can be seen that in an oxidising atmosphere, FAMEs should not be processed above 100 °C.

Table 2.2 Summary of thermal degradation temperatures for C_{18} FAMEs. Data from Pillar et al.[12]

Compound	T_{onset} (TGA) [˚C]	T_{onset} $(PDSC)$ [˚C]
Methyl Stearate	176	207
Methyl Oleate	167	174
Methyl Linoleate	159	136
Methyl Linolenate	154	121

Shin et al. tested the thermal stability of FAMEs in supercritical methanol,[13] which is a non-oxidising atmosphere. It was found that at pressures of 23 MPa, thermal degradation occurred above 325 °C, where the main degradation reactions were isomerisation, hydrogenation, and pyrolysis. The presence of degradation products has a severe impact on the properties and quality of a processed FAME product,[12] thus it is imperative to avoid conditions that will lead to these reactions taking place. Since it might not be possible to guarantee the complete absence of oxygen in processing steps, it would be ideal to process FAMEs at temperatures as close to ambient as possible. This would also reduce the energy costs.

2.2. FAE Application and Significance

FAEs as derivatives of fatty acids are a convenient form of processing where the fatty acid is the final product, but there are also a variety of applications where the FAE is the final product or serves as the feedstock for another production process.

2.2.1. Biologically active compounds

Fatty acids are biologically active compounds that can influence cellular metabolism and are involved in cell membranes, thus playing a role in health and disease risk. In a comprehensive review of the effects of fatty acids on human health, Calder[4] concluded that the consumption of *trans* fatty acids should be eliminated, and the consumption of even-numbered saturated fatty acids (such as stearic acid) should be reduced. Furthermore, he recommends an increased comsumption of unsaturated *cis* fatty acids (such as the C_{18}-acids: oleic acid, linoleic acid, and linolenic acid), particularly eicosapentaenoic acid (EPA, 20:5 ω-3) and docosahexaenoic acid (DHA, 22:6 ω-3). Replacing common saturated fatty acids with their unsaturated counterparts has been shown to lower LDL cholesterol, which is associated with decreased risk for heart disease. Additionally, polyunsaturated fatty acids have been found to play an important role in human bone marrow health.[26]

2. Supercritical Fluid Fractionation of Fatty Acid Esters

Fish oils are major sources of these healthier, more unsaturated fatty acids. These oils typically contain a distribution of fatty acids, however, including less healthy saturated fatty acids. In order improve the quality of the oil for human consumption, it is desired to enrich the oil in certain fatty acids (typically the longer-chain, more unsaturated compounds).[3] Figure 2.1 provides examples of the fatty acid profiles of some extracted fish oils. It can be seen that fish oils typically contain high amounts of 16:0, 18:1, and 20:5 fatty acids, with the C_{18}-family of fatty acids making out the centre of the carbon number distribution present in the oil.
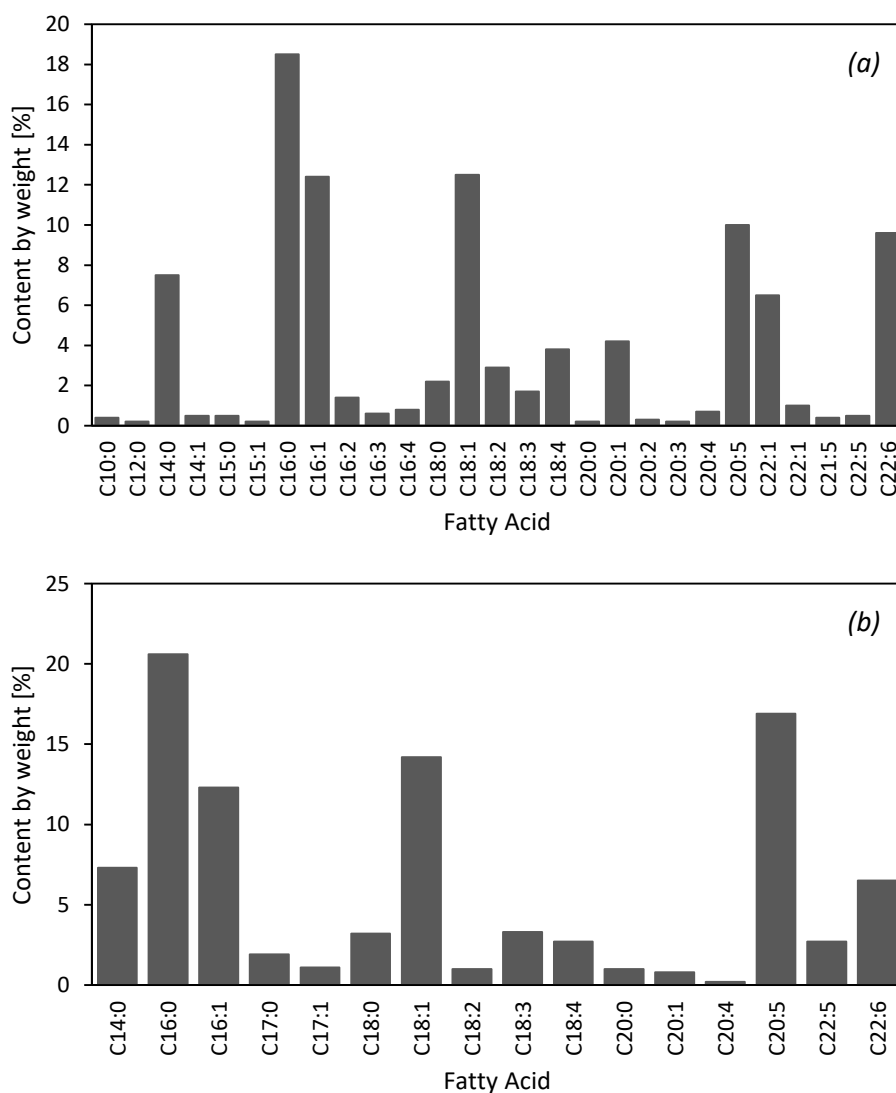
Figure 2.1: Typical fatty acid profiles of extracted fish oils. (a) Fatty acid profile of a sand eel oil quantified by Staby et al.[27] (b) Fatty acid profile of sardine oil quantified by Aarthy et al.[28]

2.2.2. Niche applications

FAEs are also used in a number of smaller-scale industries. Oleic acid derivatives in particular can be used as biodegradable lubricants for metalworking processes, or for processes where it is necessary to prevent lubricant loss. These types of lubricant are environmentally friendly, show low aquatic toxicity,

and can be produced via the enzymatic esterification of vegetable oils with a variety of alcohols from C_2 to C_5.[29]

FAEs can also be used as feedstock for the production of unsaturated fatty alcohols such as oleyl alcohol produced from methyl oleate. These fatty alcohols find application in detergents, pharmaceuticals, cosmetics, and antifoaming agents.[30,31] Other uses for FAEs include applications such as the use of seed-oil derived FAEs as a solvent in car shampoos and hydraulic oils.[32]

2.2.3. Biodiesel

Biodiesel is an environmentally friendly alternative to more traditional fossil fuels, and consists primarily of FAMEs, having the advantage of direct use in current diesel combustion engines without the need for modification.[33] Biodiesel is produced mainly from vegetable oils and waste cooking oils. Concerns about food security has led to increased interest in the production of biodiesel from algal lipids.[34] The composition of the biodiesel is highly dependent on the source, however, and much work is required to optimise the FAME yield and profile in order to produce biodiesel that meets legislative standards.[35] FAEs derived from non-biodiesel sources can be used as biodiesel additives to improve low-temperature behaviour.[32]

2.3. FAE Production Processes

FAEs are most commonly produced via the transesterification of triglyceride oils. These oils are mainly obtained from natural products, and need to be extracted before transesterification can be performed.[3,34]

2.3.1. Extraction of triglyceride oils

Triglycerides are large lipid molecules consisting of a glycerol backbone, with three fatty acids (long-chain carboxylic acids) bonded to the backbone with ester-bonds. Triglycerides are a major source of fatty acids, and a variety of natural sources contain lipid fractions containing valuable fatty acids. These include: fish[3,24,36] and fishery waste and byproducts,[5] other marine animals such as crustaceans[37] and cephalopods,[38] macroalgae and microalgae,[5,24,39,40] plants and seeds and their waste and byproducts,[5,24,41,42] and even waste cooking oil.[34] The triglyceride oil is contained in natural matrices such as the tissue of fish and marine organisms, inside microalgal cells, or contained within solid plant and vegetable structures. This requires the extraction of the triglycerides before further processing.

Traditional extraction techniques like Soxhlet extraction have been replaced by more environmentally friendly techniques such as pressurised liquid extraction and supercritical fluid extraction (SCFE). SCFE

2. Supercritical Fluid Fractionation of Fatty Acid Esters

is widely used, particularly with CO_2 as the supercritical solvent, and has been the subject of much study.[5,43,44]

Extraction processes frequently result in the co-extraction of other biological compounds. These may be valuable components such as astaxanthin and other carotenes found in marine organisms,[37] tocopherols and other vitamins found in fish and plant oils,[3,45] and phytosterols, biopesticides, and pharmaceutical ingredients found in plant materials.[5,44]

Conversely, unwanted compounds such as cholesterol may also be co-extracted.[38] Further separation may thus be required to remove these compounds from the triglyceride oil, whether they are serve as value-added products or as impurities. Once an oil fraction containing primarily triglycerides has been obtained, it can serve as a feedstock for the production of FAEs.

2.3.2. Transesterification

The fatty acid constituents of triglycerides can vary in chain length and degree of unsaturation and a variety of triglycerides can be present in source organisms.[3,35] Combined with the fact that triglycerides are much less soluble in processing solvents than free fatty acids or FAEs,[46] separating the constituent fatty acids from the glycerol backbone improves the selectivity and efficiency of processes to concentrate the oil in desirable fatty acid compounds.[3] Triglycerides can accordingly be converted into free fatty acids or FAEs for further processing.

FAEs are the focus of this work, and enjoy improved solubility in processing solvents compared to fatty acids.[47] They are produced from triglyceride oils via a transesterification reaction with an alcohol. This breaks the ester bonds between the glyceride backbone and the fatty acids, and forms new ester bonds between the fatty acids and the alcohol. A typical transesterification of a triglyceride with methanol is illustrated in Equation 2.2[23]:

$$2.2$$
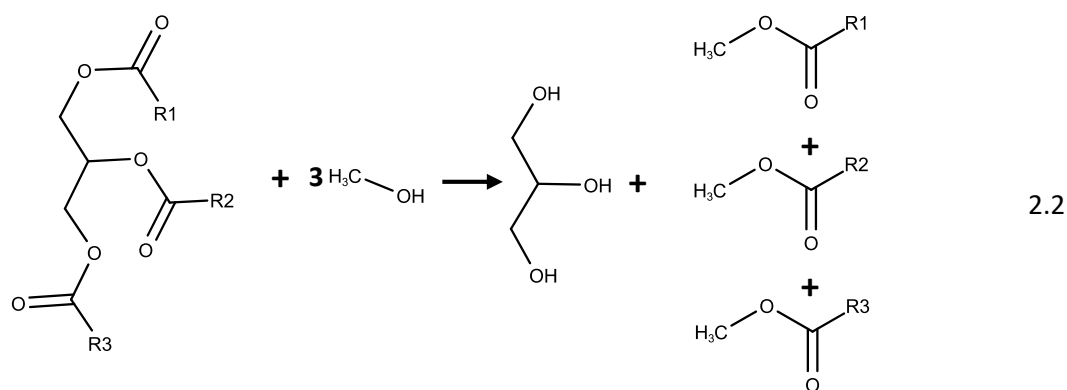
where $R1$, $R2$, and $R3$ represent the fatty acid hydrocarbon chains, and can be identical or dissimilar.

The transesterification can be conducted via several routes, such as chemical alcoholysis using methanol or ethanol and catalyst,[42] or treatment with supercritical methanol or ethanol.[13] Another route that has received attention is the biocatalytic conversion of oils into FAEs making use of enzymes such as lipases. The enzyme can catalyse both the cleavage of the triglyceride ester bonds as well as the formation of new ester bonds.[28,34,42]

2.4. FAE Separation Strategies

The previous discussions regarding the application and production of FAEs highlight two features of the edible oil industry:

i. There exists a large degree of variability in FAE mixtures produced from animal and plant sources due to differences in diet, environment, and genetics between species and between members of the same species. FAE mixtures have a distribution of compounds of varying hydrocarbon chain length and degree of unsaturation.

ii. The composition of the produced FAE mixture is a determining factor in the quality of the final product, as the distribution in chain length and degree of unsaturation directly controls whether the oil is of value for the intended application.

There is thus a need for separation strategies capable of separating or concentrating a FAE mixture in compounds with the desired chain length and degree of unsaturation to deliver an appropriate and on-specification product that possesses the required properties for the intended application.

2.4.1. Distillation

Distillation is a well-established separation technology that relies on differences in boiling points to separate liquid mixtures.[8] Nonvolatile components like FAEs require high temperatures for distillation, which is not feasible for thermally labile molecules.

An alternative technique is vacuum distillation, where the operating temperatures are reduced by operating under low pressures. This technique has been used to fractionate FAEs, mainly based on their molecular weight. Despite operation close to vacuum, this process still requires temperatures of about 250 ˚C. This may thermally degrade the FAEs, particularly the polyunsaturated fractions, resulting in isomerization and oxidation.[24] Aside from the risk of thermal degradation, vacuum distillation does not appear to be able to fractionate FAE mixtures on the basis of their degree of unsaturation.

Rose and Schrodt measured binary equilibrium data for the methyl oleate + methyl stearate system,[48] and their results at 199 °C are shown in Figure 2.2. It can be seen that there is little enrichment of

2. Supercritical Fluid Fractionation of Fatty Acid Esters

methyl oleate (M18:1) in the vapour phase. Additionally, Haley and McCabe[49] modelled the same system with the GC-SAFT-VR model, which is purely predictive. They found a pressure-minimum azeotrope at 200 °C, which would render separation by distillation infeasible. However, this azeotrope has not been observed experimentally.
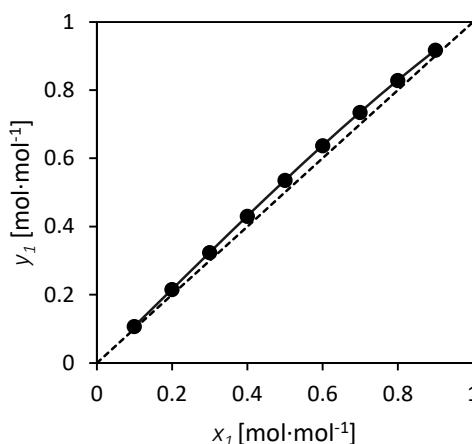
Figure 2.2: Binary equilibrium data for the M18:1 (1) + M18:0 (2) system at 199 °C, taken from Rose and Schrodt.[48]

Short-path distillation is another technique that could be utilised, as it makes use of lower temperatures. It is, however, difficult to separate high molecular mass fatty acids as the separation becomes less feasible with an increase in molecular mass.[36] Furthermore, this technique does not appear to be able to fractionate FAEs based on the degree of unsaturation according to the work of Gray and Cawley.[50] They measured the elimination temperature curves for the C_{18}-family of FAMEs, which displayed significant overlap. Short-path distillation could be utilised to fractionate a FAE mixture by chain length, as their elimination temperatures show a greater degree of variation with increasing chain length.

2.4.2. Crystallisation

Crystallisation techniques have found use as valuable pre-concentrating or post-processing steps for use in conjunction with other separation techniques.[3] The solubility of FAEs in organic solvents is a function of molecular mass and degree of unsaturation. This can be exploited in a low-temperature crystallisation operation to cause some esters to crystallise out, whilst the rest remain in solution, allowing for separation by filtration or centrifugation.

Generally, longer chain esters are less soluble than shorter chain esters, saturated esters are less soluble than monounsaturated esters, monounsaturated esters are less soluble than polyunsaturated esters, and *trans* isomers are less soluble than *cis* isomers. Low-temperature crystallisation can thus be used to fractionally crystallize FAEs based on chain length and degree of unsaturation. Lower

temperatures tend to yield concentrates of higher polyunsaturated fatty acid esters, but such low temperatures can pose operational challenges, especially on a large-scale process. Solvents such as hexane, acetone, and methanol are commonly used, and crystallisation temperatures of -10 °C to -80 °C have been investigated.[36]

Urea complexation is another crystallization technique that can be used. Urea can form complexes with FAEs, and the complexation occurs more readily depending on the geometry of the molecule. Saturated, straight-chain esters are more readily complexed by the urea, whilst unsaturated FAEs, particularly the polyunsaturated components due to the steric effect of *cis* C=C bonds, remain in solution. The fraction that complexes with the urea crystallizes upon cooling and can then be filtered out, leaving behind a non-ureacomplexing fraction concentrated in unsaturated FAEs. The urea complexation process allows operation at higher temperatures than the low-temperature crystallisation process, above 0 °C.

The operation also requires a solvent. Water is the ideal choice due to its low toxicity, but can be problematic for applications involving biodiesel. Other potential solvents include ethanol, methanol, acetonitrile, and even supercritical CO_2.[36]

Potential drawbacks of crystallisation processes can include the use of large amounts of solvent,[38] and the use of potentially hazardous solvents that can be problematic for the processing of oils intended for human consumption. These can be avoided by selecting the appropriate solvent and urea concentrations for the intended application and scale of processing.

2.4.3. Chromatography

Chromatographic methods involve passing a fluid solvent (the mobile phase) over a solid stationary phase. The compounds to be separated can either be dissolved in the fluid phase or adsorbed onto the stationary phase. The interaction of the solutes with the mobile and stationary phases causes separation if the various compounds have different interactions.

Supercritical chromatography has been used to separate FAEs based on both molecular mass as well as degree of unsaturation. Supercritical CO_2 is used as the solvent with the addition of entrainers such as ethyl acetate to enhance extraction. The stationary phase consists of $AgNO_3$-doped silica gel beads or resins. High-pressure liquid chromatography can also be employed.

Chromatographic techniques can achieve high recoveries and product purities, but their use is generally limited to analytical or preparative applications due to difficulties with scale-up for commercial application. The use of a supercritical fluid as solvent mitigates concerns of the use of large

2. Supercritical Fluid Fractionation of Fatty Acid Esters

amounts of hazardous solvents, but there are concerns over the presence of toxic silver residues in the extract fractions.[6,16,17,24,38,47]

2.4.4. Supercritical fluid fractionation

Not only can supercritical fluids be used to extract the triglyceride oil from natural matter, or as a solvent for the transesterification reaction, but these fluids can also be used to separate the resultant mixture of FAEs into various fractions via the process of supercritical fluid fractionation (SCFF).

Work done by Brunner and coworkers[6,7,10] and Nilsson et al.[51] have demonstrated the ability of supercritical CO_2 to fractionate fish oil FAEEs based on the hydrocarbon chain length, successfully producing concentrates of high-value polyunsaturated FAEEs, especially in conjunction with a pre-processing step of urea crystallisation. The ability of SCFF to separate mixtures of equal-length FAEs based on degree of unsaturation is unclear, as most studies have focussed on the fractionation of multicomponent mixtures of non-synthetic extracted oils. This allows the effect of chain-length on the separation to overshadow that of degree of unsaturation, as the effect of chain length is estimated to be larger.[46]

SCFF has several advantages, such as trivial separation of the solvent from the extract, trivial solvent recycle, and operation at mild process temperatures. SCFF requires operation at high pressures which can influence economic considerations, as it increases the production cost. Despite this, SCFF operations can process large amounts of fluid with relatively small pieces of equipment,[44] and can also be used to further refine extracted oils by removing unwanted components such as cholesterol and excess vitamin E.[36] SCFF is thus an attractive separation technique for FAE fractionation.

2.5. Supercritical Fluids

The importance of separation processes in the refining of fatty acid ester oils of commercial interest has been established, and the attractiveness of supercritical fluid fractionation (SCFF) as a strategy to adjust the composition or concentrate the oil in more valuable compounds has been highlighted. This brings the focus to supercritical fluids as the solvent used in SCFF processes.

A supercritical fluid is defined as a fluid at conditions above its critical point. That is, both the pressure and temperature of the fluid must be above its critical pressure and critical temperature. The supercritical region is illustrated in Figure 2.3. This region is characterised by the disappearance of the meniscus between the gas and liquid phases, resulting in one fluid phase that cannot be completely described as either a gas or a liquid.[8,52,53]
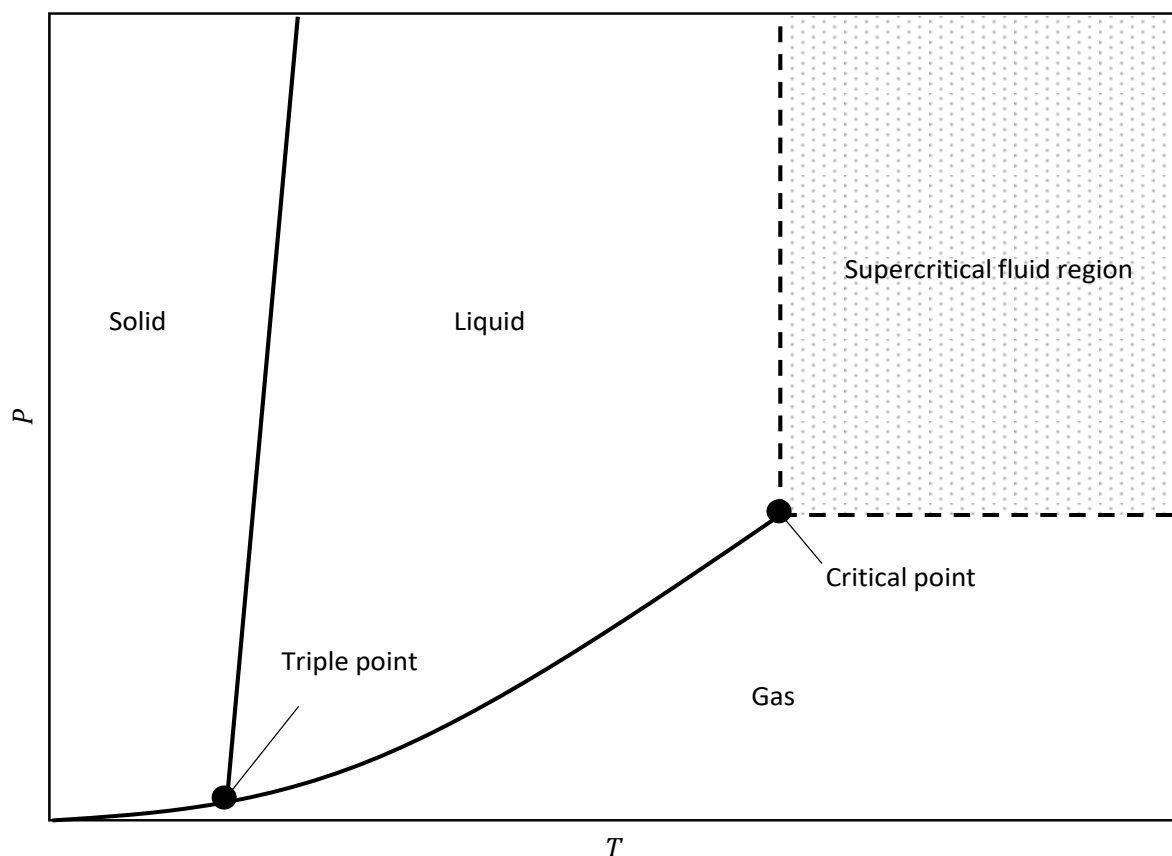
Figure 2.3: Pure-component pressure-temperature diagram. Reproduced from McHugh & Krukonis.[53]

The pressure-density diagram for CO_2 provided in Figure 2.4 illustrates two important benefits of operating a solvent in its supercritical region. The first benefit is the increased solvent power at these conditions resulting from the change in fluid density.[43,53] As can be seen in Figure 2.4, liquid-like densities can be obtained at high pressures and temperatures above the critical temperature of the solvent.[6] The increased density significantly increases the frequency and probability of solute-solvent interactions, allowing a supercritical solvent to interact much more strongly with solute molecules than at conditions far away from the critical point of the solvent.[53] This means that the strength of intermolecular interactions between solvent and solute molecules plays a determining role in the solubility of a solute in a supercritical fluid.

2. Supercritical Fluid Fractionation of Fatty Acid Esters
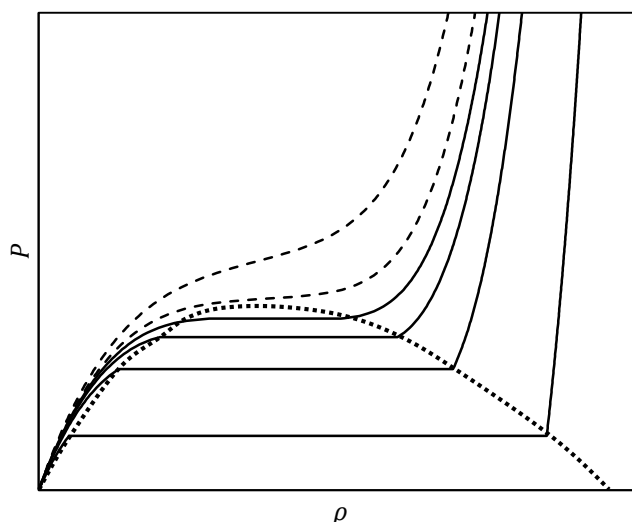
Figure 2.4: Illustrative Pressure-density diagram for pure CO_2. (—) Isotherms at temperatures below the critical temperature; (---) Isotherms at temperatures above the critical temperature; (•••) Vapour-liquid dome. Drawn with data obtained from the NIST database.[54]

The second benefit of a supercritical solvent is the tunability of the solvent.[6,8] Inspection of Figure 2.4 shows that just above the critical temperature of the solvent, the density is sensitive to changes in pressure and temperature. Since the density is related to the solvent power, this means that the solubility of a solute can be effectively manipulated by adjusting the process conditions of pressure and temperature. This feature allows for the efficient downstream separation of solute from solvent, as a simple reduction in pressure can render the solute virtually insoluble in the solvent.[43]

Another property of supercritical solvents is that they maintain the high diffusivity and low viscosity of a gas.[8,43] This property decreases the mass transfer resistance and allows supercritical processes to approach equilibrium with relative speed.

2.6. The SCFF Process

Most SCFF processes consist of at least two major units: the extractor, and the separator. The extractor contacts the liquid feed with the supercritical solvent, allowing the more soluble solutes to be preferentially dissolved and separated from the less soluble components. The extract is then sent to the separator, which separates the top product into a liquid extract product and a recovered gaseous solvent.

A multistage, countercurrent operation is the most efficient, and is necessary for separation of mixtures with relatively low separation factors, or for components that dissolve in the solvent, but do not preferentially distribute to the solvent-rich phase. This is generally the case for FAE fractionation.[6]

Figure 2.5 shows a basic SCFF process where the extractor is a multistage high-pressure packed column. The extractor is operated in a stripping mode, with the liquid feed fed at the top, and the solvent fed at the bottom. The upwards flowing solvent strips the more soluble components from the downward flowing liquid, with the completely stripped liquid raffinate exiting the bottom of the column. The simplest separator scheme makes use of pressure reduction (a temperature increase can also be used) to separate the extract from the solvent. This is accomplished with an expansion valve (the expansion can also be multistage), followed by a separator vessel to de-entrain the liquid extract. The recovered solvent is recompressed and recycled to the extractor column. Depending on the process the raffinate can also be flashed to remove any excess dissolved solvent.[6,8,43]
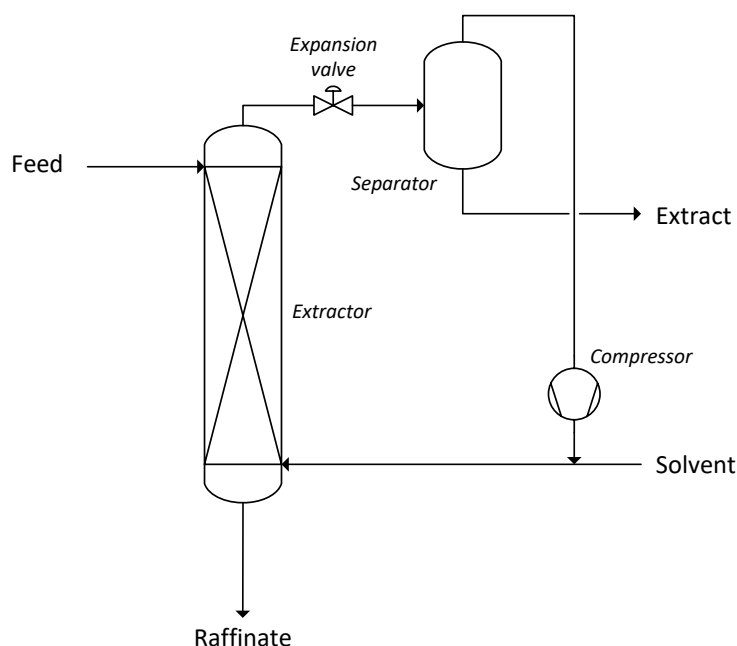
Figure 2.5: Simplified diagram of a SCFF process operating in pure stripping mode. Adapted from Seader et al.[8]

This base process can be modified in several ways. It is possible to reflux a portion of the extract after it leaves the separator, as in a distillation operation, with the feed fed at an intermediate point in the column. The column section below the feed then operates in the stripping manner, and the section above the feed operates in a rectification mode, where the liquid reflux absorbs more of the less soluble compounds from the upwards travelling solvent.[6,8] This type of process is shown in Figure 2.6.

2. Supercritical Fluid Fractionation of Fatty Acid Esters
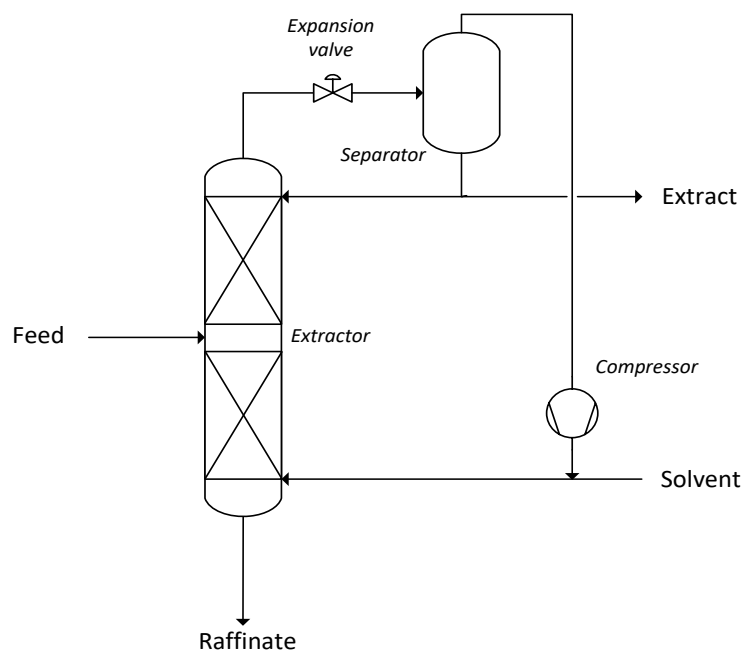
Figure 2.6: Process diagram of a SCFF process with reflux. Adapted from Brunner.[6]

It is also possible to utilise the presence of temperature and pressure profiles over the length of the column to effect the fractionation of multicomponent mixtures – allowing different fractions to be withdrawn as side streams.[44,55]

Design considerations for SCFF equipment are similar to low-pressure distillation equipment. Care should be taken to ensure adequate wetting of the packing, as well as to avoid flooding (entrainment of the liquid in the solvent). An important difference between SCFF equipment and traditional distillation equipment is the higher density of the upward-flowing fluid. Assuming that the required data are available, traditional design calculation procedures such as the height equivalent to a theoretical plate (HETP) method can also be applied to the design of SCFF columns.[6,44]

The higher operating pressures contributes to the capital cost, especially of the extractor and the separator. Another main contribution to the separation cost is the energy requirement of recompressing the recycled solvent.[6,56] Economy of scale is an important factor in SCFF plants, as higher capacity plants tend to have lower production costs, making them economically comparable to more traditional low-pressure separation technologies, however the higher price might be overlooked for small-scale operations due to SCFF being the only way to effect the separation or to adhere to regulatory requirements (particularly for processes involved in the pharmaceutical and food industries) as is often the case for FAE processing.[56,57]

2.7. Solvent Selection

The selection of a supercritical solvent for a SCFF process is made on the grounds of several factors. These include: cost, safety, product application, solute solubility, dependence of phase behaviour on pressure and temperature, regulatory requirements, as well as limitations imposed by the nature of the solutes.[6] There are three principal solvents that have been investigated for the processing of FAEs, namely carbon dioxide, ethane, and propane.[7,58]

Table 2.3 summarises the critical properties of these solvents. It can be seen that propane has a substantially higher critical temperature than CO_2 and ethane. This makes it less suitable for the handling of the thermally labile polyunsaturated FAEs, since a SCFF process would operate at a temperature above the critical temperature of the solvent due to the increased solvent power and tunability near the critical point.

Table 2.3: Critical properties of relevant solvents for FAE separation. Data from Seader et al.[8]

Solvent	Critical Temperature [K]	Critical Pressure [bar]	Critical Density [kg·m^{-3}]
CO_2	304	73.8	468
Ethane	305	48.8	203
Propane	370	42.4	217

Schwarz et al. measured phase behaviour data for the members of the homologous series of FAEEs in supercritical ethane and propane.[58] They found significantly lower pressures than for the same FAEEs in supercritical CO_2, due to the observed lower critical pressures of ethane and propane when compared to CO_2. However, significant research has been done on the use of supercritical CO_2 to fractionate or concentrate FAEs and a variety of other biological compounds for use in the nutraceutical and pharmaceutical industry.[7,10,27,43] CO_2 as solvent allows for mild operating conditions, is inexpensive, non-toxic, non-flammable, inert, readily recoverable, and has GRAS status according to the FDA.[3,6,18,43]

The behaviour and selectivity of a supercritical solvent can be enhanced by adding an entrainer. The entrainer can be a liquid or gas at ambient conditions and is usually added in small amounts. Shimizu & Abbott investigated the entrainer effect for CO_2 as supercritical solvent by using the Kirkwood-Buff theory.[59] This theory is assumption-free, and has been demonstrated to be robust. They found that for CO_2 + solute + entrainer systems, the solubility enhancement can be attributed to strong solute-entrainer interactions, and not interactions with the solvent, or density changes of the solvent. Ethanol and methanol are popular entrainers for the SCFE of lipids and other biologically active compounds from natural materials.[37,60] It has been suggested that ethane or propane might make suitable

2. Supercritical Fluid Fractionation of Fatty Acid Esters

entrainers in CO_2 for the fractionation of FAEs, due to their lower phase transition pressures as pure solvents.[58] Staby and Mollerup commented that the use of entrainers would increase the capacity (or vapour-loading) of FAEs in CO_2, but would decrease the selectivity.[3]

The safe and benign nature of CO_2 combined with its low critical temperature motivates its use as the supercritical solvent of choice in this study.

2.8. Feasibility

The feasibility of a SCFF process rests on the ability of the solvent to be more selective for the desired solute(s) than for the undesired solute(s). The selectivity can thus be used to quantify the separation potential of a SCFF process. This can be applied in the form of the relative solubility α_{ij}, as shown in Equation 2.3:[6]

$$\alpha_{ij} = \frac{y_i/x_i}{y_j/x_j}$$
2.3

where y is the mass fraction solute in the vapour phase, and x is the mass fraction solute in the liquid phase at equilibrium. A value close to one for the relative solubility indicates that a mixture will be difficult or impossible to separate. A value larger than one indicates that component i is selectively extracted into the vapour phase, whilst a value smaller than one indicates that component j is selectively extracted into the vapour phase. The calculation of this parameter requires phase equilibrium data.

The selectivity is based on the distribution of individual components between the phases, and distribution coefficients K_i can also be calculated to investigate the separability, shown in Equation 2.4:[6]

$$K_i = \frac{y_i}{x_i}$$
2.4

Ideally K_i should be larger than K_j, with both distribution coefficients not close to one. For heavier long-chain components such FAE mixtures, distribution coefficients for C_{14} to C_{22} ethyl esters in CO_2 have been found to be quite low, making the separation between such components relatively tedious, as the separability decreases with decreasing difference in chain length.[7,10] The calculation of the distribution coefficients also requires phase equilibrium data.

Another important consideration that ties in with the distribution coefficient, is the solute loading in the solvent-rich phase, which can be determined from phase behaviour data. Lower concentrations of the extracted components in the solvent-rich vapour phase require larger amounts solvent to maintain the production rate. Processing and recycling higher flowrates of solvent can lead to high capital and

operating costs, due to an increase in column diameter, and the higher compression cost of the solvent recycle. The solvent compression cost in particular has been found to not conform with the economy of scale.[56]

Chapter 2 has shown that supercritical CO_2 is the ideal solvent for the application of FAE fractionation, and that the design and analysis of such a process requires phase behaviour data for the C_{18} FAME systems to be studied.

CHAPTER 3:
High-Pressure Phase Behaviour

Chapter 2 discussed the performance of supercritical fluid fractionation processes. The performance of SCFF is dependent on the properties, behaviour, and interactions of the solvent + solute systems to be separated, as well as the process conditions such as pressure and temperature. The design and operation of SCFF processes thus rely on knowledge of the phase behaviour and thermodynamics of the relevant systems, as such data is of critical importance not only for the direct application of design calculations such as estimation of the number of theoretical stages, but also for the fitting of thermodynamic models to predict key design properties. Additionally, knowledge of phase behaviour is necessary for the identification of viable process conditions, and the quantification of distribution coefficients and relative solubilities. Accordingly, there is significant value in the measurement of reliable phase equilibrium data.[3,6,9,11]

In Chapter 3, the high-pressure phase behaviour of binary and ternary systems is discussed as it relates to FAE + CO_2 systems. This is followed by a discussion of the techniques for the measurement of high-pressure phase equilibrium data. An evaluation of the available literature data for the FAME + CO_2 systems to be studied in this work is also provided.

3.1. Thermodynamics and System Classification

3.1.1. Binary systems

Binary solvent + solute mixtures can be classified into six different types according to the classification of van Konynenburg and Scott,[61] of which the first five types were determined from the van der Waals equation of state.[52] Bolz et al.[62] developed an alternative classification scheme that focusses on the phase behaviour features present in a given system, rather than focussing on distinct types of systems. This scheme will not be considered here, however.

Section 3.1.1 is given as a summary of treatments on the topic by McHugh and Krukonis, Clifford, and De Loos.[52,53,63] The details and features of the different types of systems are first described, followed by a summary to discuss the classification to FAE + CO_2 systems specifically.

3.1.1.1. Type I systems

Type I phase behaviour is the most trivial, and will serve as a starting point for the discussion. Consider a binary solvent + solute system at a temperature below the critical temperature of both components. The phase behaviour can be illustrated on a pressure-composition plot, as illustrated in Figure 3.1 (a).

3. High-Pressure Phase Behaviour

A mixture A at a pressure p will split into a liquid phase and a vapour phase with compositions x and y, respectively.
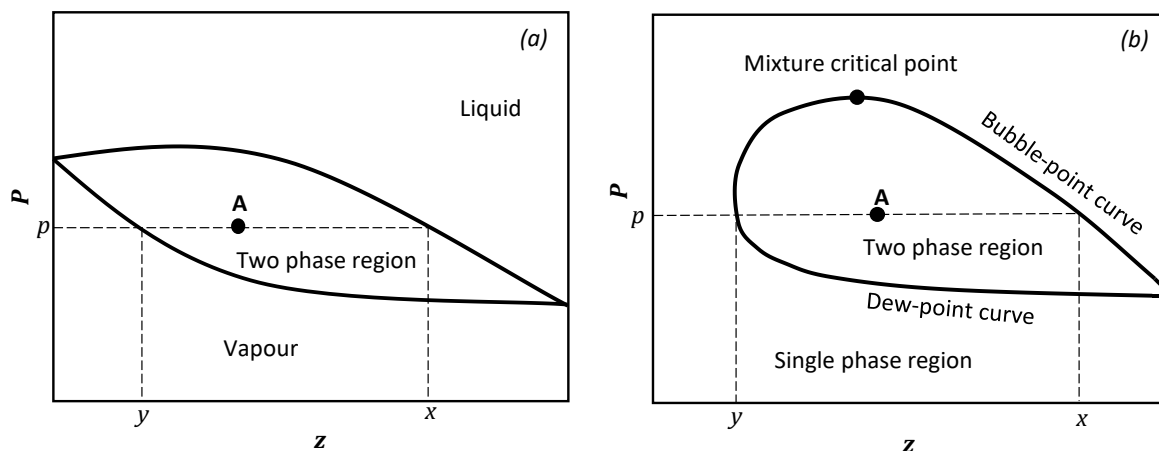
Figure 3.1: Pressure-composition diagram for a binary Type I mixture. (a) At a temperature below the critical temperature of both components. (b) At a temperature between the critical temperatures of the solvent and solute. Adapted from McHugh & Krukonis.[53]

Now, consider the same system at a temperature above the critical temperature of the solvent, but below the critical temperature of the solute. The pressure-composition diagram at these conditions is shown in Figure 3.1 (b). The vapour-liquid envelope has pulled away from the pure solvent side of the composition axis diagram. The bubble and dew point curves join at the mixture critical point, where both phases critically merge, having identical properties such as density and viscosity. The horizontal tie-line at a composition of A will function similarly as in Figure 3.1 (a). This is the region where a SCFF process will operate as discussed in section 2.5.

The phase behaviour in the whole pressure-temperature-composition space can be represented in a P-T-x prism. This construction is illustrated in Figure 3.2. Points A and B represent the critical points of the solvent and solute respectively. The dashed line is the vapour-liquid critical curve, and represents the locus of mixture critical points, joining the solvent vapour pressure curve to the solute vapour pressure curve. This illustrates why the vapour-liquid envelope pulls away from the pure solvent side, as at temperatures between A and B, a vertical isotherm does not cross the vapour pressure curve of the solvent, but does still cross the vapour pressure curve of the solute. Beyond the critical point of A, the equilibrium shifts from a vapour-liquid (VL) envelope to a fluid-liquid (FL) envelope, since the lighter component is now supercritical.
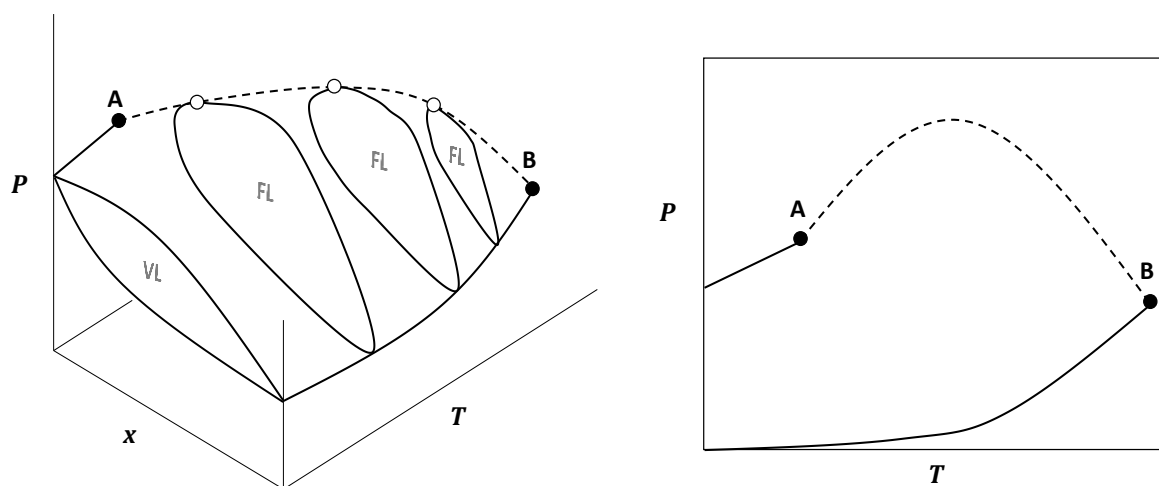
Figure 3.2: P-T-x and P-T diagrams for a Type I binary mixture. Adapted from McHugh & Krukonis.[53]

Type I behaviour is generally found in systems where components have similar sizes or interactions.[53] This includes systems of members of the same homologous series where the size difference is not too large, as well as systems of methane and shorter *n*-alkanes.[53,63] FAE + CO_2 systems are highly asymmetric, and thus unlikely to exhibit Type I behaviour.

Asymmetry in a system can give rise to deviations from Type I behaviour as a result of enthalpic and/or entropic interactions between the components.[53] These deviations are generally in the form of regions where liquid-liquid equilibria or vapor-liquid-liquid equilibria occur.[53,63]

3.1.1.2. Type II systems

Type II systems are similar to Type I systems with the only difference being the occurrence of a three-phase liquid-liquid-vapour (LLV) curve, and a two-phase liquid-liquid (L_1L_2) dome where the condensed phase splits into two liquid phases. This is shown in Figure 3.3. The P-T plot is characterised by a liquid-liquid (L_1L_2) critical curve. This curve defines the locus of points where the two liquid phases critically merge into one liquid phase and intercepts the three-phase line at the upper critical end point (UCEP). The L_1L_2 critical curve does not necessarily have a positive slope.[63]

3. High-Pressure Phase Behaviour
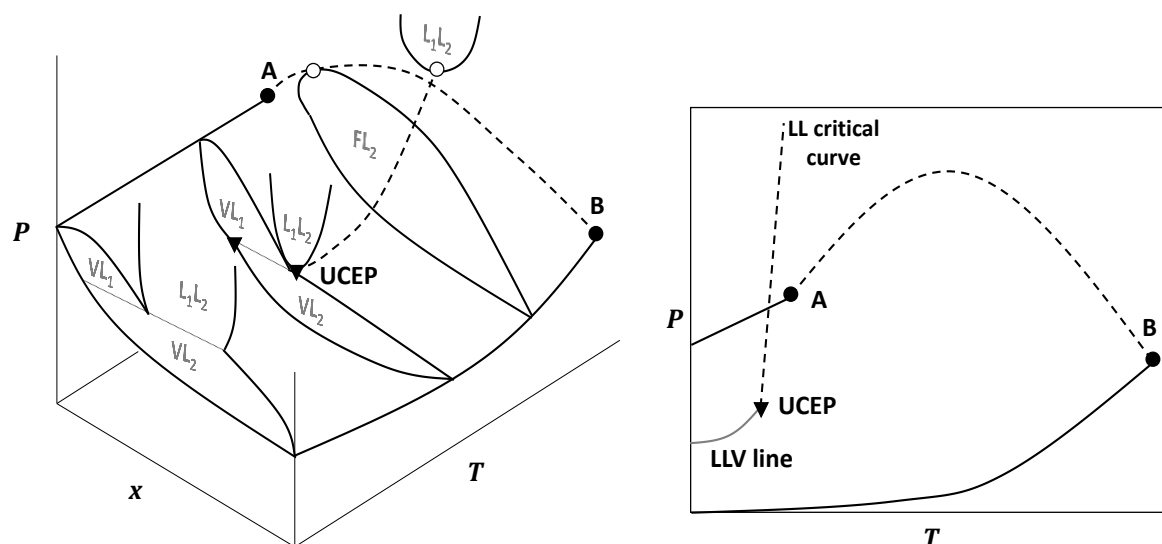
Figure 3.3: P-T plot for a Type II binary mixture. Adapted from McHugh & Krukonis.[53]

Figure 3.3 also shows the P-T-x prism, where it is seen that as temperature increases, the composition difference between the two liquid phases on the LLV line decreases until the UCEP is reached. At higher temperatures the liquid-liquid dome detaches from the vapour-liquid envelope, until the critical temperature of A is reached. Here the vapour-liquid envelope detaches from the pure solvent axis, as for Type I systems, with the only difference being the continued presence of the floating liquid-liquid dome at increasingly higher pressures as the temperature increases. In the case of a negative slope for the L_1L_2 critical curve, the liquid-liquid dome closes at the top with a liquid-liquid critical point on the L_1L_2 curve, instead of the liquid-liquid region stretching to infinite pressure as shown in Figure 3.3. This closed liquid-liquid dome then reduces as the temperature increases until it disappears at the UCEP.

Type II behaviour is found in systems exhibiting some asymmetry, such as the binary systems of CO_2 + $C_6 - C_{12}$ *n*-alkanes.[63] The asymmetry of FAE + CO_2 systems in general could lead to the low-temperature LLE behaviour found in Type II systems, but the C_{18} FAMEs specifically may be too large when compared to the C_{12} *n*-alkane upper limit.

3.1.1.3. Type V systems

Further increasing the asymmetry leads to Type V behaviour. These systems also have two critical curves, similar to Type II systems. A liquid-liquid (L_1L_2) critical curve connects the lower critical endpoint (LCEP) to the critical point of component B. This curve is the locus of points where two liquid phases critically merge into one. A vapour-liquid (VL_1) critical curve connects the critical point of component A to the UCEP. This curve is the locus of points where a vapour phase and liquid phase critically merge into one.
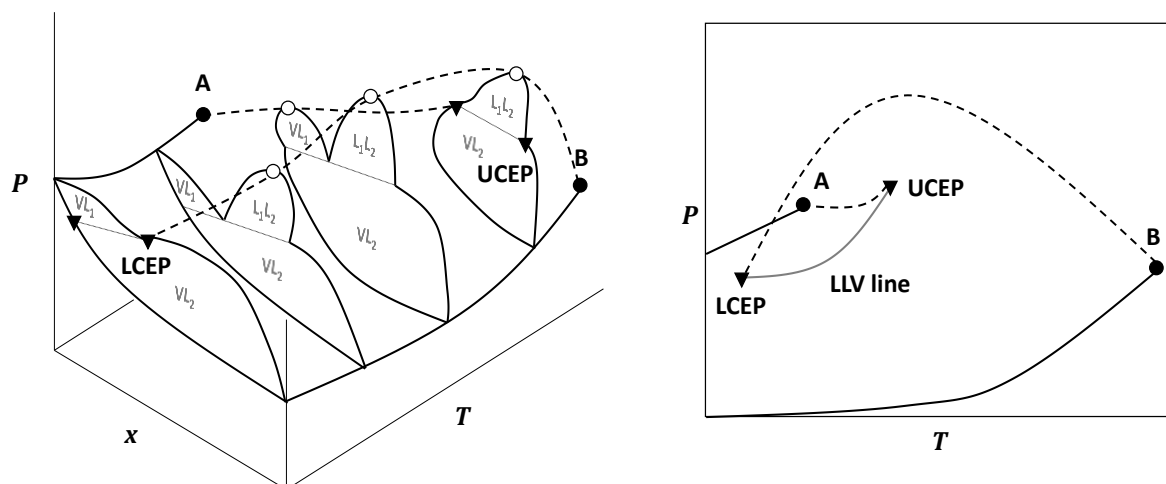
Figure 3.4: P-T-x and P-T plot for a type V binary mixture. Adapted from De Loos.[63]

The LCEP temperature is the lowest temperature where two liquid phases can coexist in the system, and is also the lowest temperature where the three-phase region exists. Above this temperature a liquid-liquid dome forms in the P-x section. Similarly, the UCEP is the highest temperature where the three-phase region can exist, and denotes the disappearance of the vapour-liquid (VL_1) dome. Beyond the UCEP the phase envelope becomes a regular two-phase fluid-liquid (FL_2) region.

Type V behaviour is found in the methane + *n*-hexane and ethane + eicosane systems, the latter having a particular degree of asymmetry. This makes Type V behaviour a candidate for FAE + CO_2 systems.

3.1.1.4. Type IV systems

Type IV systems have similar asymmetry to Type V systems. They exhibit a combination of the behaviour of Type II and Type V systems. As can be seen in Figure 3.5, there is a low-temperature LLV branch like that found in Type II systems. This LLV branch terminates in an UCEP where the low-temperature liquid-liquid dome disappears. There is also a high-temperature LLV branch like that found in Type V systems, where the three-phase LLV region is bounded by a LCEP and an UCEP. This means that the P-T-x prism for a Type IV system would start off as that of a Type II system, and then transition into that of a Type V system at higher temperatures.

3. High-Pressure Phase Behaviour
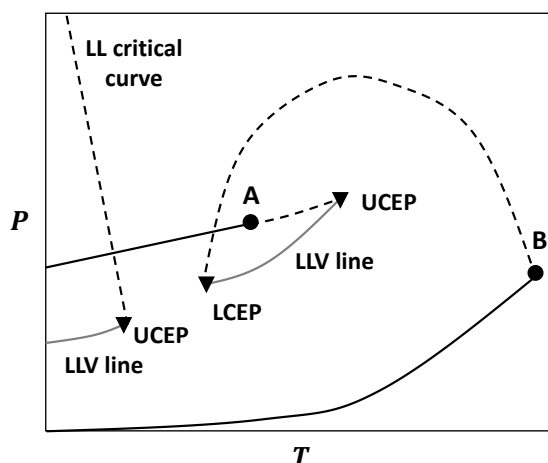
Figure 3.5: P-T plot of a binary type IV system. Adapted from De Loos.[63]

It is possible for the low-temperature liquid-liquid regions found in Type II and Type IV systems to be concealed by a solid-liquid equilibrium surface. This means that Type II systems can mistakenly be classified as Type I, and Type IV systems can mistakenly be classified as Type V systems.

This type of phase behaviour is observed in the CO_2 + tridecane system for example.[63] Type IV behaviour is thus also a candidate for FAE + CO_2 systems, although the level of asymmetry in the C_{18}-FAME systems may lead to even larger deviations from Type I behaviour.

3.1.1.5. Type III systems

Substantial asymmetry between components can lead to Type III behaviour. Here, the two critical curves intersecting the three-phase line LLV found in Type IV systems merge into one curve and the two branches of the LLV line merge into one low-temperature line. The dominant critical curve can have a variety of shapes, possessing pressure maxima and/or minima, as well as potentially having a temperature minimum. The curve shown in Figure 3.6 exhibits both a pressure maximum and minimum. The other variants of the critical curves result in what is referred to as gas-gas equilibria, and are more prevalent in systems with smaller components, such as the He + Xe system.
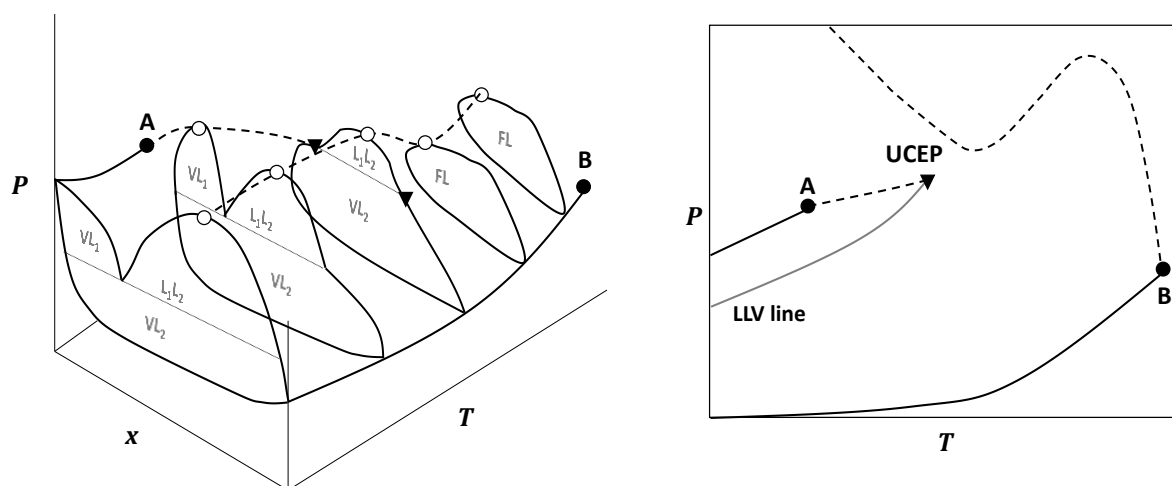
Figure 3.6: P-T-x and P-T plot for a type III binary system. Adapted from De Loos.[63]

The behaviour illustrated in Figure 3.6 is observed in the propane + triphenylmethane system.[63] The case of the dominant critical curve having a temperature minimum is observed for the CO_2 + tetradecane system.[63] Type III behaviour is thus also a candidate for FAE + CO_2 systems, particularly the C_{18} FAMEs.

3.1.1.6. Type VI systems

Type VI systems exhibit a three-phase equilibrium with a L_1L_2 dome that appears at the LCEP, and then disappears at the UCEP, as shown in Figure 3.7. Beyond the UCEP the behaviour is similar to Type I systems. Type VI systems can also have an additional L_1L_2 critical curve with a pressure minimum instead of a pressure maximum, and is found in systems exhibiting high-pressure immiscibility.
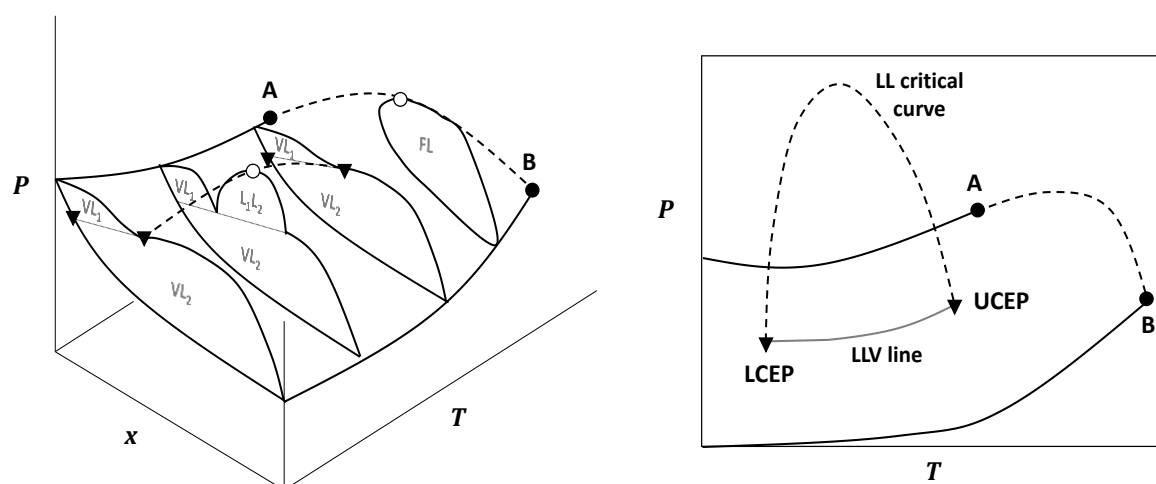
Figure 3.7: P-T-x and P-T plot for a type VI binary system. Adapted from De Loos.[63]

This type of phase behaviour is present in systems with complex interactions such as certain water-containing systems.[63] This makes it an unlikely candidate for FAE + CO_2 systems.

3. High-Pressure Phase Behaviour

3.1.1.7. Summary

So far, Type II, Type, V, Type, IV, and Type III behaviours have been suggested for the FAE + CO_2 systems in general. Specifically, Types IV and V, and particularly Type III behaviours are candidates for the C_{18} FAMEs investigated in this work. It is difficult to conclusively classify systems, as a large amount of experimental data over a large range of pressures and temperatures may be required.

Juntarachat et al.[21] investigated the homologous series of saturated ethyl esters in CO_2 by modelling them with the predictive Peng-Robinson equation of state. The results are presented in Figure 3.8, and show the progression of the different types of phase behaviour with increasing molecular size. It can be seen that the model predicts one LCEP for the E5:0 − E10:0 esters, corresponding to Type II behaviour. Increasing the asymmetry of the FAEE + CO_2 system further leads to the prediction of three critical endpoints between the E10:0 and E12:0 esters, which corresponds to Type IV behaviour. For the esters beyond E12:0 a single UCEP is predicted, corresponding to Type III behaviour. This range includes the E18:0 ester, and thus it is likely that the C_{18} FAMEs will exhibit Type III behaviour.
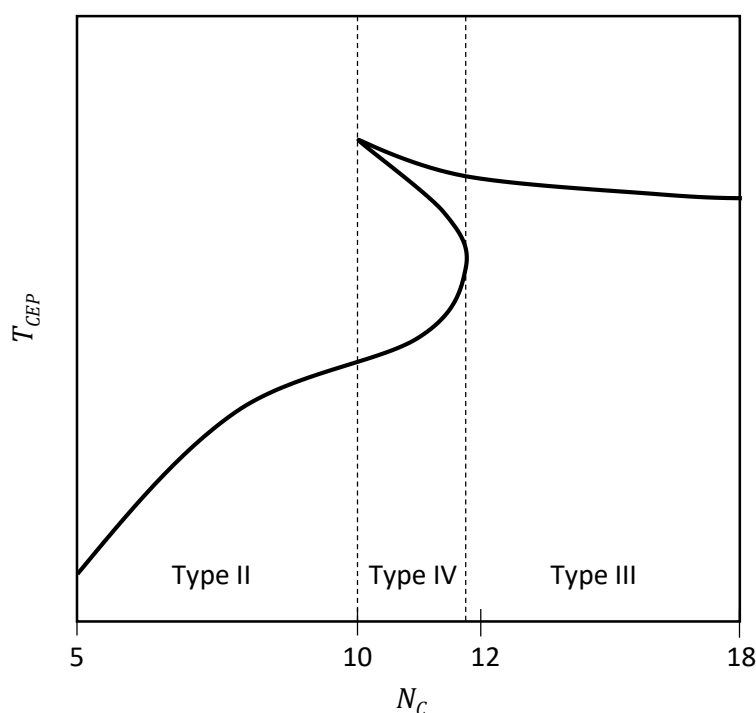
Figure 3.8: Critical end point temperature (T_{CEP}) as a function of the carbon number (N_C) of saturated ethyl esters as predicted by the predictive Peng-Robinson equation of state. Redrawn from Juntacharat et al.[21]

Soto et al. modelled the M18:1 + CO_2 system with the GCA-EOS.[64] The model successfully predicted data measured by Inomata et al.,[65] and predicted VLLE behaviour at 10 °C, which had not been experimentally observed.

Staby et al. measured data for fish oil ethyl esters in CO_2 and also found VLLE behaviour at 10 °C.[27] At 40 °C (above the critical temperature of CO_2, 31 °C) the VL_1-envelope had disappeared, and the L_1L_2-

dome had transitioned into a FL-dome. This behaviour is illustrated in Figure 3.9. The UCEP for this system appears to be between 10 °C and 40 °C. This indicates that fish oil FAEE + CO_2 systems can be classified as either Type IV, Type V, or Type III, which supports the predictive modelling results of Juntarachat et al.
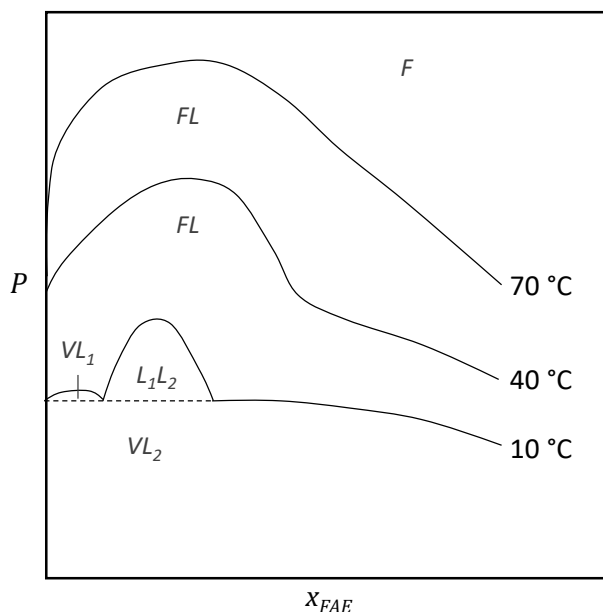
Figure 3.9: Illustrative behaviour of a fish oil FAE + CO_2 system. Adapted from Staby et al.[27] The oil consisted of 51.1 % by mass E16:0, E16:1, E18:1, and E20:5, with the remainder being made up of small amounts of a distribution of several FAEEs ranging from $C_{10} - C_{22}$.

3.1.2. Ternary systems

Bluma and Deiters[66] followed an approach similar to van Konynenburg and Scott[61] to classify the phase behaviour of ternary mixtures. They also used the Van Der Waals equation of state to generate the different phase diagrams. Their phase diagram constructions were based on the assumption of equally sized molecules, however, and may be of limited application to highly asymmetric systems like FAE + CO_2 mixtures. This classification scheme is also highly complex, and so the behaviour of ternary solvent + solute A + solute B systems will be discussed according to the types of interactions found between solute A and solute B to illustrate the salient features.

3.1.2.1. Systems with ideal interactions

Ternary systems where solute A and solute B have similar sizes and functional groups, and thus have similar or like interactions, exhibit the simplest type of phase behaviour.[67] This type of behaviour is illustrated in Figure 3.10. The system is represented as an isothermal P-x-x-x prism for the hypothetical solvent + solute A + solute B system, where solute A is less soluble than solute B, as can be seen in the higher pressures of the solvent + solute A binary equilibrium curve.

3. High-Pressure Phase Behaviour

The curve connecting the mixture critical points of the constituent binaries shows a monotonic increase as the composition changes from predominantly solute B to predominantly solute A. This critical curve defines the locus of critical points for mixtures with a constant solute-solute ratio or reduced mass fraction solute w^{red}.

Figure 3.10 also provides more detailed sections of the heterogenous phase surface at different pressures. As pressure increases isothermally, the size of the two-phase region decreases until the mixture critical pressure of solute B is reached. At this point the two-phase region pulls away from the binary solvent + solute B axis. The remaining two-phase region continues to decrease in size until the mixture critical pressure of the solvent + solute A system is reached. From this point on, the system remains in a homogenous single phase regardless of composition.
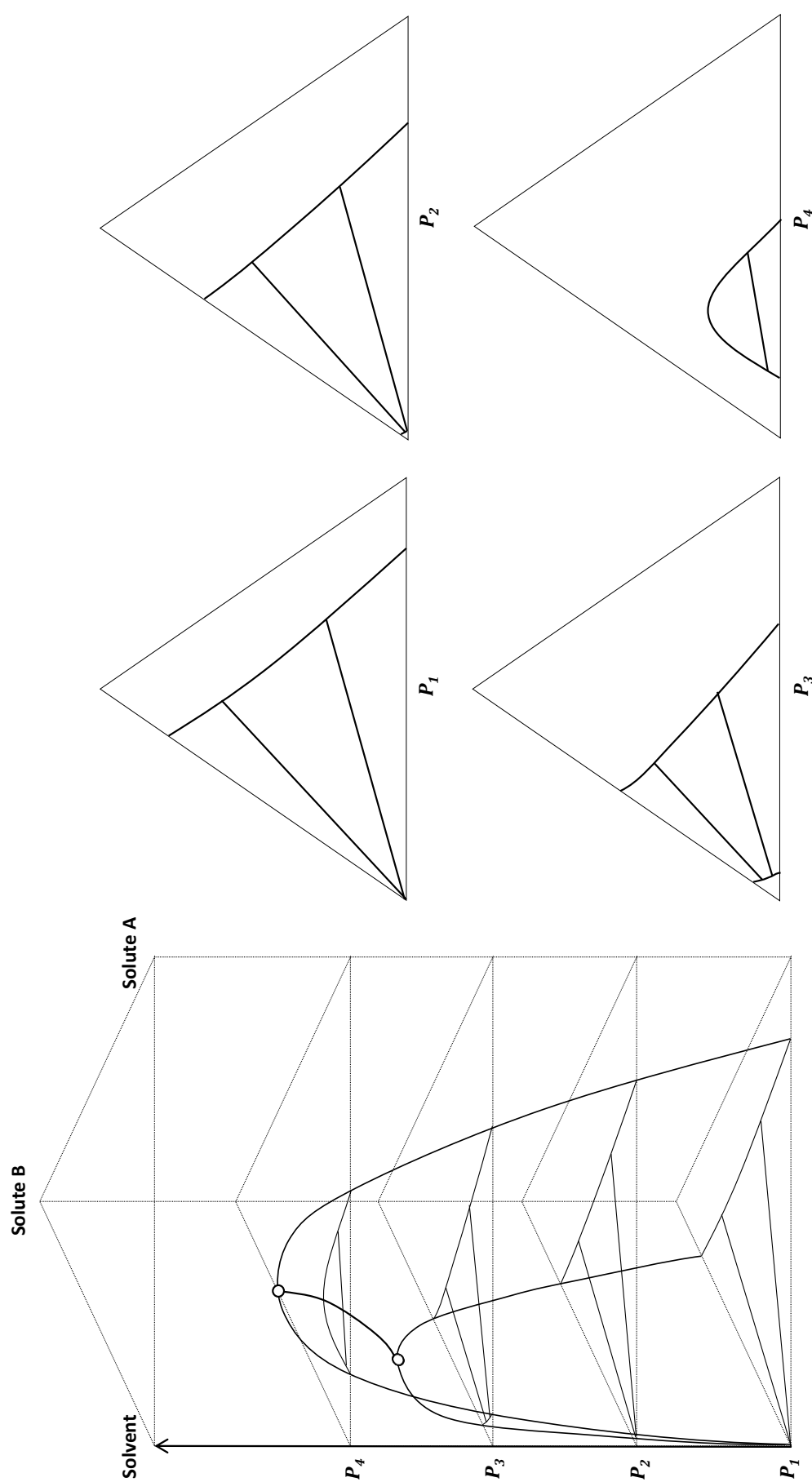
Figure 3.10: P-x-x prism showing high-pressure phase behaviour for an ideal ternary system at a constant temperature. P_1 to P_4 designate isobaric sections of the heterogenous equilibrium surface. (O) Mixture critical point of constituent binary solvent + solute systems. Adapted from Pöhler.[68]

3. High-Pressure Phase Behaviour

3.1.2.2. Systems with nonideal interactions

In ternary systems where solute molecules have more asymmetry in their size and functional groups, and thus have dissimilar or unlike interactions, more complex phase behaviour can be found.[67,69,70] Scheidgen and coworkers have thoroughly investigated the complex phenomena and phase behaviours that can be found in such systems.[68–71]

Figures 3.11 and 3.12 illustrate two types of deviation from the ideal ternary behaviour discussed in section 3.1.2.1. Figure 3.11 shows the isothermal behaviour of a system where the critical curve exhibits a pressure minimum. The pressure minimum is the result of cosolvency effects that cause a mixture of solute A and solute B to be more soluble in the solvent than either pure solute.[69]

This cosolvency causes the two-phase region to become pinched as the pressure increases isothermally, eventually causing the two-phase region to separate into two distinct heterogenous regions. The presence of a pinch point and the accompanying region of total miscibility between the two separated two-phase regions are important features to be aware of for industrial SCFF applications.[69]

Figure 3.12 shows the isothermal behaviour of a system where the critical curve exhibits a pressure maximum. The pressure maximum gives rise to an island system, where a mixture of solute A and solute B is less soluble in the solvent than either pure solute.[70] Increasing the pressure isothermally in an island system eventually causes the two-phase region to completely detach from the binary system axes, resulting in an immiscibility island. The immiscibility island disappears once the pressure exceeds the pressure maximum of the critical curve.

Cosolvency effects are generally present in systems where the solute components have significant size differences and dissimilar functional groups, such as CO_2 + 1-alkanol + alkane systems.[69] Island systems are generally found in systems where the solute components are similar and polar, and have small differences in their critical pressures, such as CO_2 + carboxylic acid + 1-alkanol systems.[70] The C_{18} FAMEs investigated in this study have similar functional groups and molecular sizes, and are not strongly polar. This makes it unlikely that differences in unsaturation between these components will give rise to either of the complex ternary phase behaviours discussed in this section. Considering this, it is expected that ternary systems containing CO_2 and two C_{18} FAMEs differing only in degree of unsaturation will exhibit the ideal ternary phase behaviour described in section 3.1.2.1.
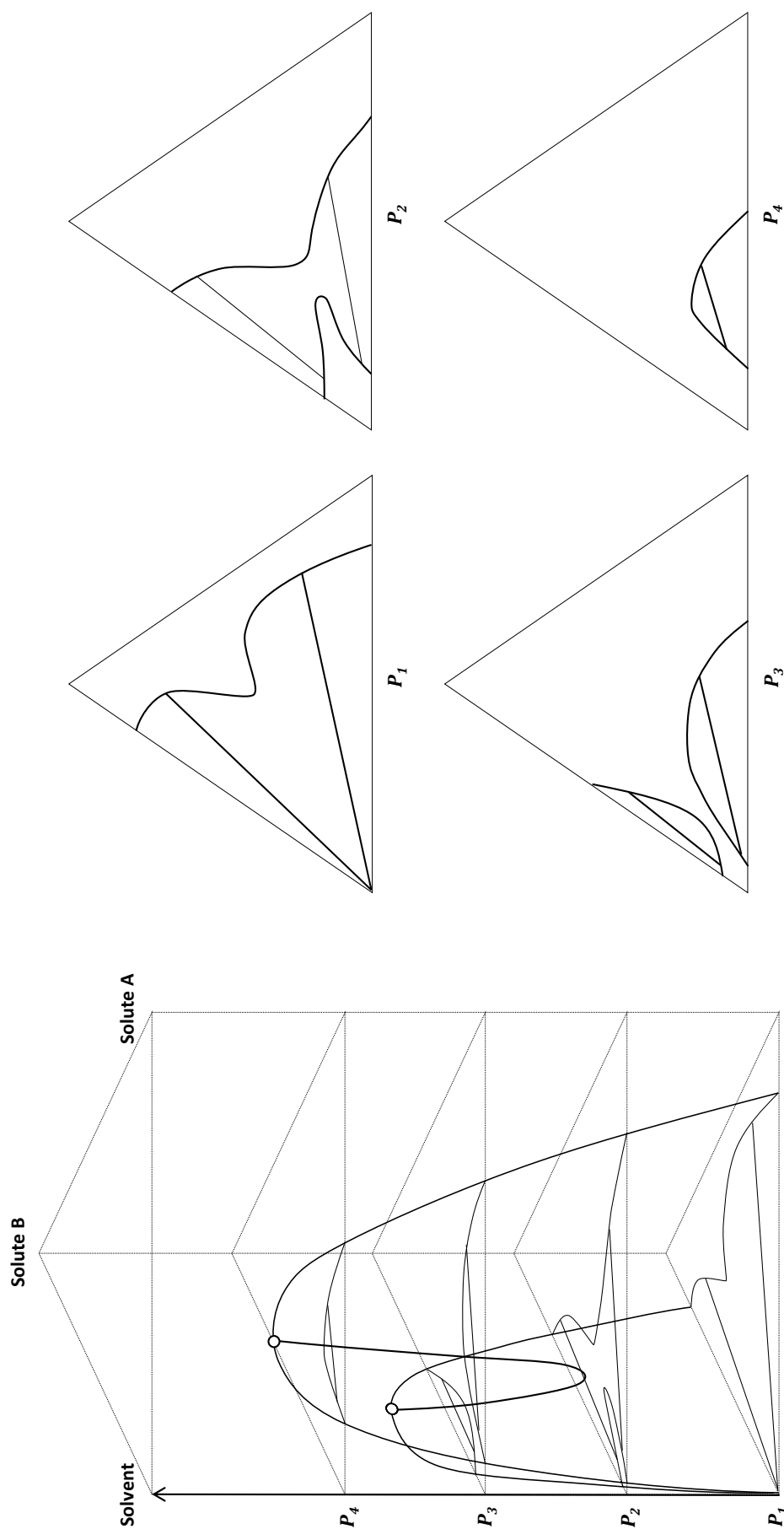
Figure 3.11: P-x-x prism showing high-pressure phase behaviour for a nonideal ternary system with a pressure minimum at a constant temperature. P_1 to P_4 designate isobaric sections of the heterogenous equilibrium surface. (○) Mixture critical point of constituent binary solvent + solute systems. Adapted from Scheidgen and Schneider.[69]

3. High-Pressure Phase Behaviour
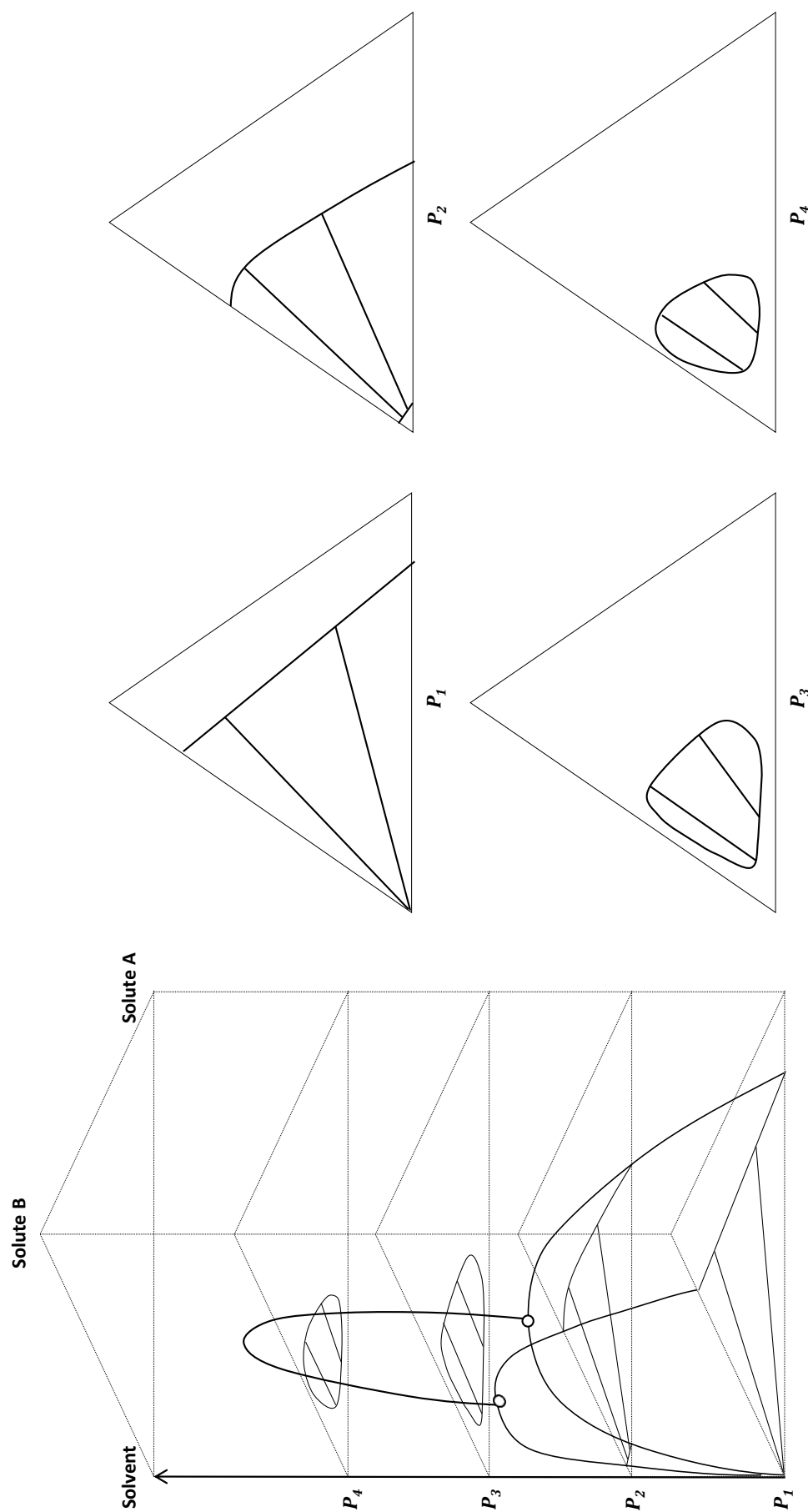
Figure 3.12: P-x-x prism showing high-pressure phase behaviour for a nonideal ternary system with a pressure maximum at a constant temperature. P_1 to P_4 designate isobaric sections of the heterogenous equilibrium surface. (O) Mixture critical point of constituent binary solvent + solute systems. Adapted from Scheidgen and Schneider.[70]

3.2. Measurement of High-Pressure Phase Behaviour

Numerous techniques have been used to study the phase behaviour of fluid systems at high pressure. Dohrn and coworkers proposed a classification method focusing on the characteristic sources of error, which forms the basis of the discussion of measurement techniques in this section.[9] Such a classification system is useful when considering which method to select for data measurement, as an understanding of the main sources of experimental error is vital to the generation of reliable equilibrium data.

Measurement techniques can broadly be classified into two categories: analytical, or synthetic. In analytical methods the compositions of coexisting phases are measured, whereas synthetic methods require the preparation of a mixture of known composition, followed by the determination of the phase transition point. These two measurement philosophies are illustrated in Figure 3.13. If correctly applied, all methods of measurement should result in the same phase behaviour data.
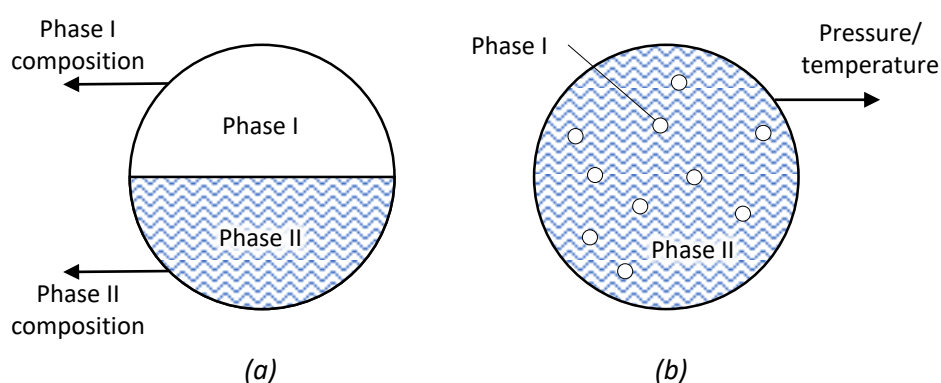
Figure 3.13: Measurement techniques for high-pressure phase behaviour data. (a) Analytical methods. Determine the compositions of coexisting phases at specified pressure and temperature. (b) Synthetic methods. Determine the pressure or temperature where an incipient second phase forms at fixed composition and temperature or pressure.

3.2.1. Analytical methods

The advantage of analytical methods are that tie-line data can be directly generated, making them suitable for the investigation of multicomponent systems – the drawback being the added complexity and labour involved with the analysis. The main sources of error in analytical methods are related to the analytical determination of the phase compositions and any related sampling that may be required. Figure 3.14 illustrates the classification scheme for analytical methods, omitting the isobaric sampling method, as this application is limited to lower pressures.[9]

3. High-Pressure Phase Behaviour

Figure 3.14: Classification of analytical methods for high-pressure phase equilibria measurements. Adapted from Dohrn et al.[9]

Phase compositions can be determined directly through the analysis of samples, or more indirectly, by making use of non-invasive analytical methods such as spectroscopic techniques: infrared, NMR (nuclear magnetic resonance) and X-ray scattering, for example. Spectroscopic methods are expensive and may not be able to distinguish between all the components in a mixture, which may rule it out as an option for certain multicomponent systems. Gravimetric techniques also avoid the need for sampling, but require density and volume data for the phases that may make it difficult to implement.[9]

The two main sampling techniques are isothermal, and isobaric-isothermal. Isobaric-isothermal methods rely on constant flow of one or more components through the system, necessarily requiring relatively large amounts of material. This can make experiments costly if working with high-value compounds.[9]

Isothermal methods can be further classified based on the method used to promote equilibrium, and the method used to extract the sample. The equilibration time can be reduced by agitating the system via stirring, rocking, or recirculation of the liquid phase, vapour phase, or both. Magnetic stirring is preferred over motor-driven stirring, as it does not penetrate the cell physically, reducing the likelihood of leakages. Phase recirculation can greatly improve the mass transfer, but these techniques may also require larger amounts of material, which can be a drawback when working with high-value components. Recirculation also has the advantage of simplifying sampling and the measurement of additional data such as density.[9]

Sampling has several challenges associated with it, such as a pressure drop in the cell and loss of material causing a shift in the equilibrium. This can be circumvented by taking small samples via capillary tubes, or specific valves or valve systems. Capillaries can be adjusted to alter the sampling height, making the equipment more versatile as it can cater to varying experimental conditions and more easily sample from multiphase systems such as vapour-liquid-liquid equilibria. Valve systems such as the ROLSI™ (rapid on-line sampler injector) can also be adjusted to change the sampling height, and can be connected to the analytical instrument directly, facilitating the analysis.

Capillaries can have significant pressure drops causing the sample to split into two phases if not properly designed. Other techniques of reducing the pressure drop in the system include adjusting the cell volume to maintain a constant pressure, blocking off the majority of the cell contents from the sample, and taking samples from recirculation lines. Alternatively, sampling methods that do not require the cell to remain under pressure can be used, such as in situ or material-loss analysis methods.[9]

3.2.2. Synthetic methods

Synthetic methods generate bubble-point or dew-point data, and avoid the complexity related to sampling and analysis whilst foregoing the measurement of tie-line data. This makes them more suitable to binary mixtures, or to initial multicomponent studies, as these methods can still provide phase boundary data and be used to identify the presence of potential solute-solute interactions. Synthetic methods generally require smaller volumes of material, which is beneficial when investigating high-value compounds. The main sources of error in synthetic methods are related to the synthesis of the loading mixture, and to the method used to detect the phase transition. Figure 3.15 illustrates the classification scheme for synthetic methods.

3. High-Pressure Phase Behaviour

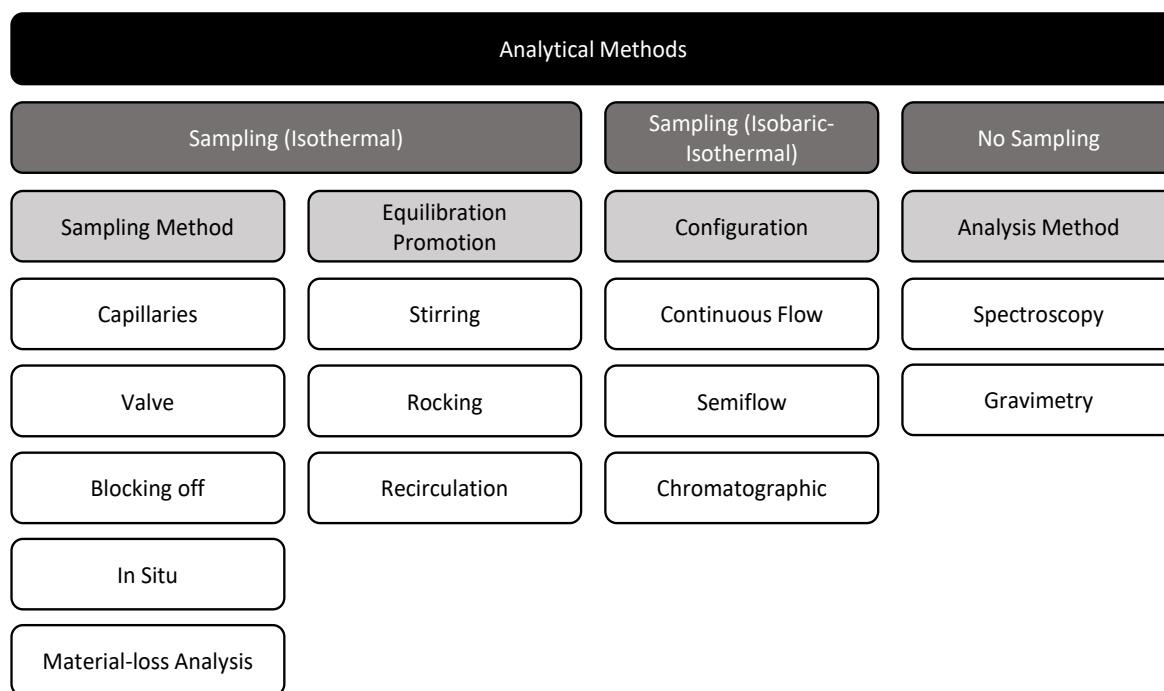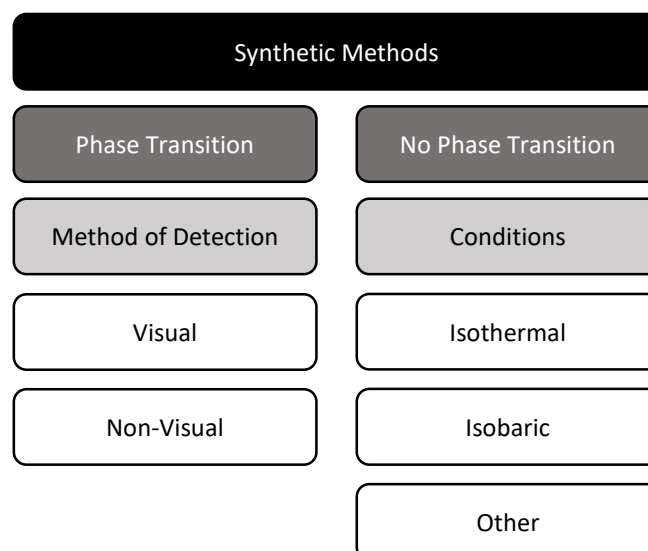*Figure 3.15: Classification of synthetic methods for high-pressure phase equilibria measurements. Adapted from Dohrn et al.[9]*

Synthetic methods can broadly be classified based on whether or not a phase transition is detected. For the "no phase transition" methods, determination of the phase boundary relies on knowledge of phase-density data and the calculation of phase compositions with models or material balances. This makes them problematic to apply to systems that are difficult to model, or where sufficient density data are not known.

Methods where a phase transition is detected, can be grouped according to the method used to detect the phase transition. Non-visual methods make use of indirect techniques such as plots of physical properties (pressure-volume plots, for example, exhibit a slope discontinuity at the transition point), or detection via non-visible radiation such as infrared or X-ray transmission. These methods are highly suited to applications where visual methods are impossible, or as additional checks to confirm the visual detection.

Visual methods rely on the real-time detection of a phase transition by means of transmitted or reflected visible light. These methods have the advantage of providing the observer with more direct knowledge of what is happening inside the cell, which is very useful for troubleshooting, as the observer can see potential contaminants and areas of poor mixing for example, and take corrective action if possible. The success of visual measurements is dependent on the ability of the observer to correctly identify a phase transition. This makes it important that each transition be observed repeatedly, and that the observer measures and compares validation data to literature to ensure that phase transitions are correctly observed.

In summary, several measurement techniques are available to the researcher. The synthetic-visual method is particularly attractive for both binary and multicomponent systems, as it can generate data

in the entire compositional space efficiently both in terms of time and resources. The only downside is the inability to measure the compositions of coexisting phases.

3.3. Available Literature Data

Literature data for the C_{18} FAME systems investigated in this work were collected, as well as data for certain relevant related systems. The data is discussed in terms of phase behaviour observations and potential shortcomings, highlighting the motivation for the experimental measurements conducted in this work.

3.3.1. Binary systems

Binary FAME + CO_2 data were collected for the systems investigated in this work, and are summarised in Table 3.1.

Table 3.1: Summary of collected literature data for binary C_{18} FAME + CO_2 systems.

System	Temperature [˚C]	Measurement Technique	Reference
Methyl stearate + CO_2	40, 50, 60, 70	Analytical	Inomata et al.[65]
Methyl oleate + CO_2	40, 50, 60, 70	Analytical	Inomata et al.[65]
	40, 60	Analytical	Zou et al.[72]
	40, 60	Analytical	Yu et al.[73]
	40, 60	Analytical	Chang et al.[74]
	40, 60, 80	Analytical	Fang et al.[45]
	40, 50, 60	Synthetic	Crampon et al.[75]
Methyl linoleate + CO_2	40, 60	Analytical	Zou et al.[72]
	40, 60	Analytical	Chang et al.[74]
	40, 70	Analytical	Adams et al.[76]

3. High-Pressure Phase Behaviour

Data for the M18:0 (1) + CO_2 (2) system is shown in Figure 3.16. It can be seen that there is a gap in the data in the critical region. Data in this region is notoriously difficult to measure, particularly with the analytical setup used by Inomata, et al.[65] since sampling is difficult when both phases have similar densities and are close to merging into one phase. It can also be seen that the phase transition pressure increases monotonically with increasing temperature.
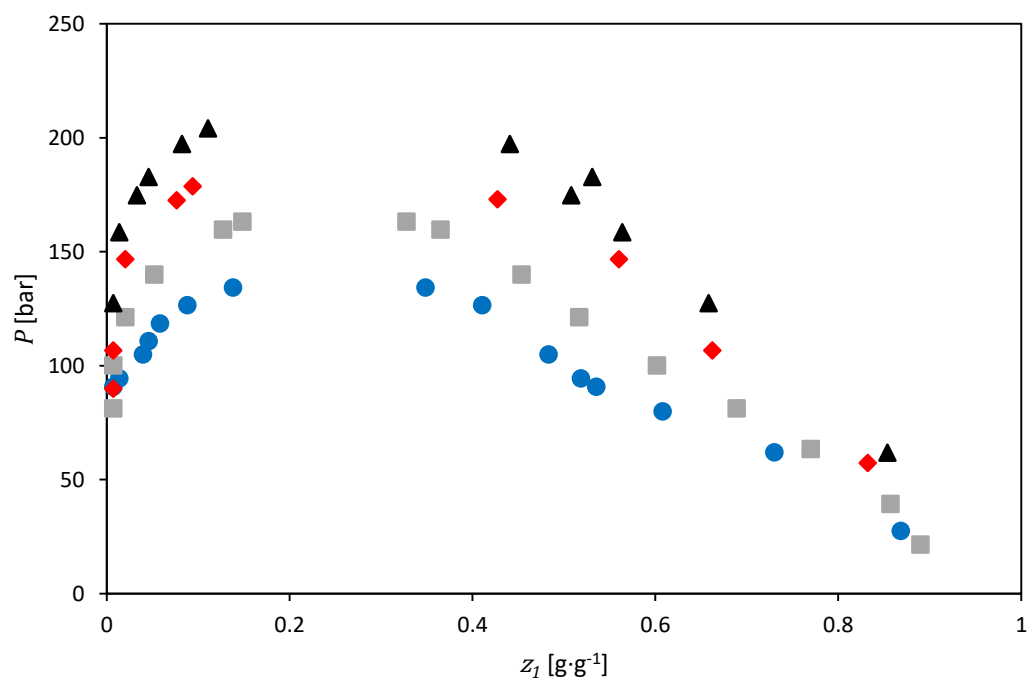
Figure 3.16: Binary phase behaviour of the M18:0 (1) + CO_2 (2) system. Data from Inomata et al.[65] (●) T = 40 °C; (■) T = 50 °C; (◆) T = 60 °C; (▲) T = 70 °C.

Data for the M18:1 (1) + CO_2 (2) system is shown in Figure 3.17 at 60 °C. It can be seen that there is less data in the critical region that on the dew-point or bubble-point curves. There is some disagreement between literature data sets. The data measured by Inomata et al.,[65] Crampon et al.,[75] and Yu et al.[73] show good agreement over the entire composition range. However, the data measured by Zou et al.[72] show deviations from the data of the other authors on both the dew-point and bubble-point sides. The data measured by Chang et al.[74] and Fang et al.[45] show good agreement on the dew point curve, but deviate from the bubble point curves of the other authors.
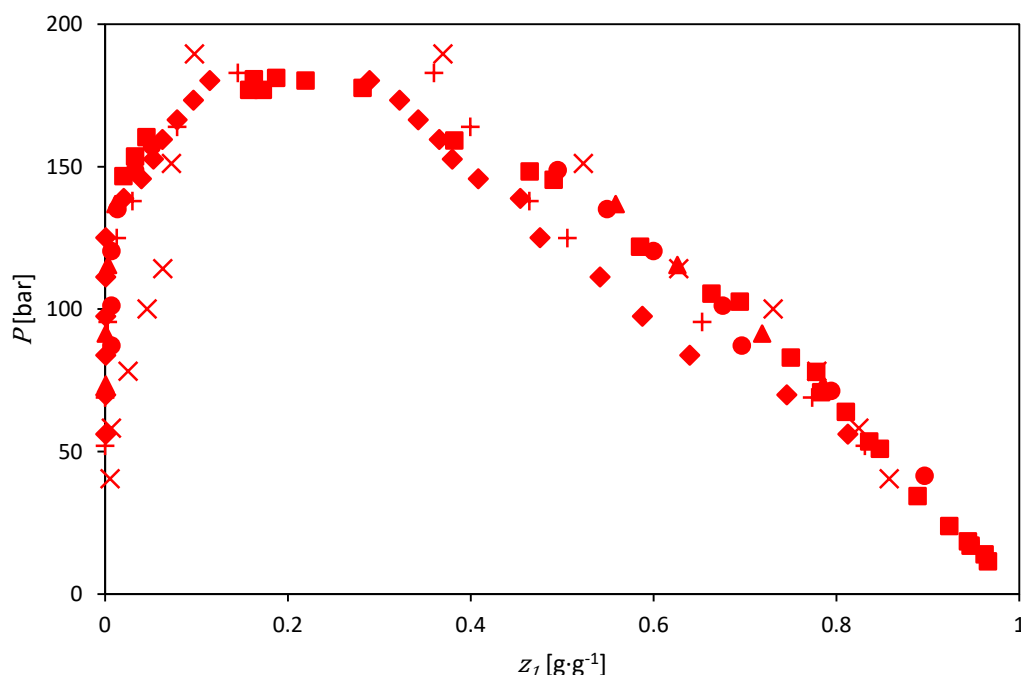
Figure 3.17: Binary phase behaviour of the M18:1 (1) + CO_2 (2) system at 60 °C. (●) Inomata et al.[65]; (■) Crampon et al.[75]; (▲) Yu et al.[73]; (x) Zou et al.[72]; (◆) Chang et al.[74]; (+) Fang et al.[45]

In the first group of authors, Inomata et al. and Yu et al. made use of an analytical experimental method (where the major source of error lies in the composition), whilst Crampon et al. made use of a synthetic experimental method (where the major source of error lies in the reported phase transition pressure). These data sets show very good agreement with one another, and the use of different experimental methods lends them credibility. Liong et al. commented on the discrepancy in dew-point curve data between Inomata et al. and Zou et al., stating that entrainment of liquid droplets in the solvent-rich phase may have resulted in the data by Zou et al. predicting higher solubility of M18:1 in CO_2.[77] Similar discrepancies can be seen in the data at 40 °C.

3. High-Pressure Phase Behaviour

Data for the M18:2 (1) + CO_2 (2) system is shown in Figure 3.18 for 40 °C. It can again be seen that there is a gap in the data in the critical region. It can also again be seen that there are large discrepancies between the data from different sources. The data measured by Zou et al.[72] show similar deviations to that in the M18:1 + CO_2 system. It is likely that the deviation is in the composition and not the pressure, since an analytical method was used, where the main source of uncertainty lies in the determination of the composition.
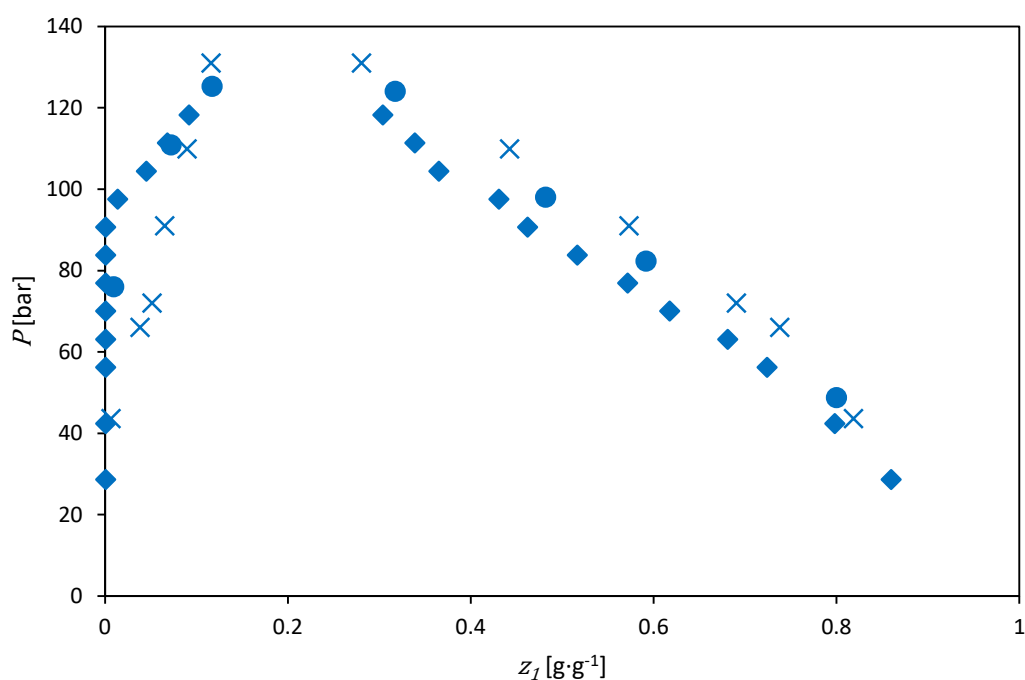
Figure 3.18: Binary phase behaviour for the M18:2 (1) + CO₂ (2) system at 40 °C. (●) Adams et al.[76]; (x) Zou et al.[72]; (◆) Chang et al.[74]

All the binary C_{18} FAME + CO_2 systems display a monotonic increase in the phase transition pressure, indicating an absence of temperature inversions (the occurrence of nonmonotonic changes in phase transition pressure with increasing temperature). Differences in the phase transition pressures mean differences in solubility, which can indicate fractionability of a mixture, in the absence of solute-solute interactions. A comparative plot of the binary phase behaviour data in literature at 40 °C is given in Figure 3.19. Comparison of the binary data measured by Inomata et al.[65] for the M18:0 + CO_2 and M18:1 + CO_2 systems provide the best suggestion of solubility differences between saturated and unsaturated C_{18} FAMEs. However, it is clear that due to the significant deviations present in the literature data, and the absence of any critical region data for M18:0 + CO_2 and M18:2 + CO_2, no reliable conclusions can be drawn about the influence of unsaturation on the solubility of C_{18} FAMEs in supercritical CO_2.
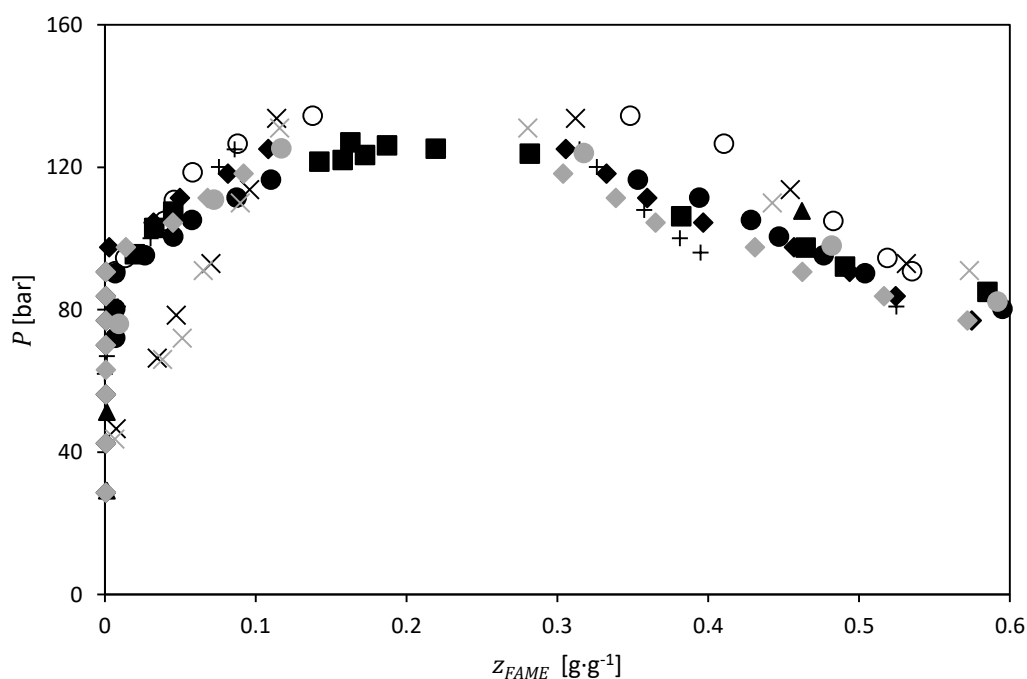
Figure 3.19: Comparison of the phase behaviour for binary FAME + CO_2 systems of C_{18} FAMEs in the literature at 40 °C. For M18:0: (O) Inomata et al.[65]; For M18:1: (●) Inomata et al.[65]; (■) Crampon et al.[75]; (▲) Yu et al.[73]; (x) Zou et al.[72]; (◆) Chang et al.[74]; (+) Fang et al.[45] For M18:2: (●) Adams et al.[76]; (x) Zou et al.[72]; (◆) Chang et al.[74]

3. High-Pressure Phase Behaviour

It has been shown that FAEEs and FAMEs show similar phase behaviour in CO_2, with only slight solubility differences being reported.[78] In order to further investigate the effect of unsaturation on FAE phase behaviour, literature data for binary FAEE + CO_2 systems in the C_{18}-ester family were collected and are displayed in Figure 3.20. The data for the FAEEs suggests some degree of solubility difference between components with differing degrees of unsaturation, but the lack of any data in a large composition range make it difficult to draw any firm conclusions.
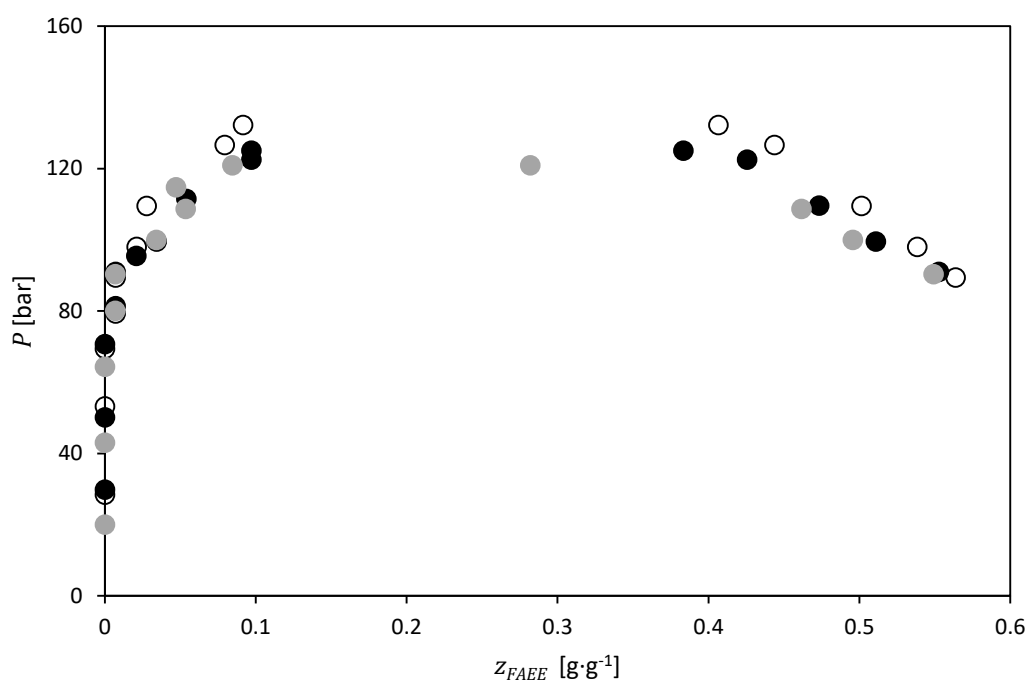
Figure 3.20: Comparison of the binary phase behaviour of C_{18} FAEEs in CO_2 at 40 °C. Data from Bharath et al.[78] (○) M18:0; (●) M18:1; (◐) M18:2.

3.3.2. Ternary systems

Very little data for ternary CO_2 + FAME + FAME systems with the C_{18} FAMEs investigated in this work are found in the literature. One set of data was measured by Zou and coworkers for the CO_2 + M18:1 + M18:2 system at 40 °C and 60 °C, for three different reduced weight franctions w^{red}.[79] The reduced weight fraction is defined as the solvent-free fraction of one solute in a hypothetical solute A + solute B + solvent mixture:

$$w_A^{red} = \frac{x_A}{x_A + x_B}$$

3.1

Each tie-line was measured at a different pressure, and there were no ternary bubble point and dew point curves available, so it is difficult to plot meaningful isobaric-isothermal diagrams for analysis. Inspection of the compositions of coexisting phases indicates that there is little selectivity between

M18:1 and M18:2 in CO_2. No ternary CO_2 + FAME + FAME data could be found in the open literature for systems containing M18:0 and an unsaturated C_{18} FAME.

3.3.3. Motivation for further investigation

The literature data gathered for the binary systems has been found to significantly deviate from each other, as well as having gaps in certain composition ranges, particularly the critical region. This motivates the need for the measurement of consistent data with a rigorous analysis of the measurement uncertainty.

In order to investigate the influence of unsaturation on the VLE of mixtures of esters, data is required for systems containing CO_2 and a mixture of equal-length FAMEs with differing degrees of unsaturation. It was also shown in section 2.8 that ternary VLE data are necessary to perform relative solubility calculations, and to investigate the compositions of coexisting phases containing the components to be separated. No data for such systems were found in the open literature. This motivates the need to measure ternary high-pressure VLE data. The measurement of VLE data is complex and time-consuming, and considerable value can be gained from the supplementary measurement of ternary high-pressure bubble-point and dew-point (HPBDP) data.

Accordingly, after inspection of the available data in the literature, the following data will be measured:

- Binary HPBDP data was measured with a synthetic-visual method for the systems CO_2 + M18:0, M18:1, and M18:2 to resolve the inconsistencies in literature data.
- Ternary HPBDP data was measured with a synthetic-visual method for the ternary CO_2 + M18:0 + M18:1 system to generate phase boundary data and investigate solute-solute interactions. This system is ideal for the investigation of the influence of unsaturation on C_{18} FAME phase behaviour.
- High-pressure VLE data was measured with an analytical isothermal sampling method for the same ternary system to investigate the compositions of coexisting phases.

CHAPTER 4:
Materials & Methods

Chapter 3 established the need for the measurement of phase behaviour data for systems containing C_{18} FAMEs and CO_2. Chapter 4 provides a discussion of the materials and methodology employed in the measurement of the phase behaviour data, as well as brief summaries of the experimental uncertainty.

4.1. Materials

FAMEs were obtained from Sigma-Aldrich, and are summarized in Table 4.1. Quoted purities are those supplied by Sigma-Aldrich. Additionally, high-purity CO_2 from Air Products was used as a solvent. All ester compounds were analysed with gas chromatography (GC) and no impurity peaks could be detected.

Table 4.1: Summary of components used in this investigation.

Component	Product Code	Purity
Methyl Stearate (M18:0)	S5376	99 %
Methyl Oleate (M18:1)	311111	99 %
Methyl Linoleate (M18:2)	L1876	99 %
Carbon Dioxide	K243C	99.995 %

4.2. Measurement of HPBDP Data

4.2.1. Equipment

Two high-pressure synthetic-visual cells were used to measure the binary and ternary bubble and dew point data. Both cells are of similar construction. The larger cell has a maximum volume of about 80 mL,[80] whilst the smaller cell has a maximum volume of about 45 mL.[81] Bubble points were measured on the small cell to reduce the amount of solute used, whilst dew points were measured on the large cell. A schematic drawing of the cells is given in Figure 4.1.

4. Materials & Methods
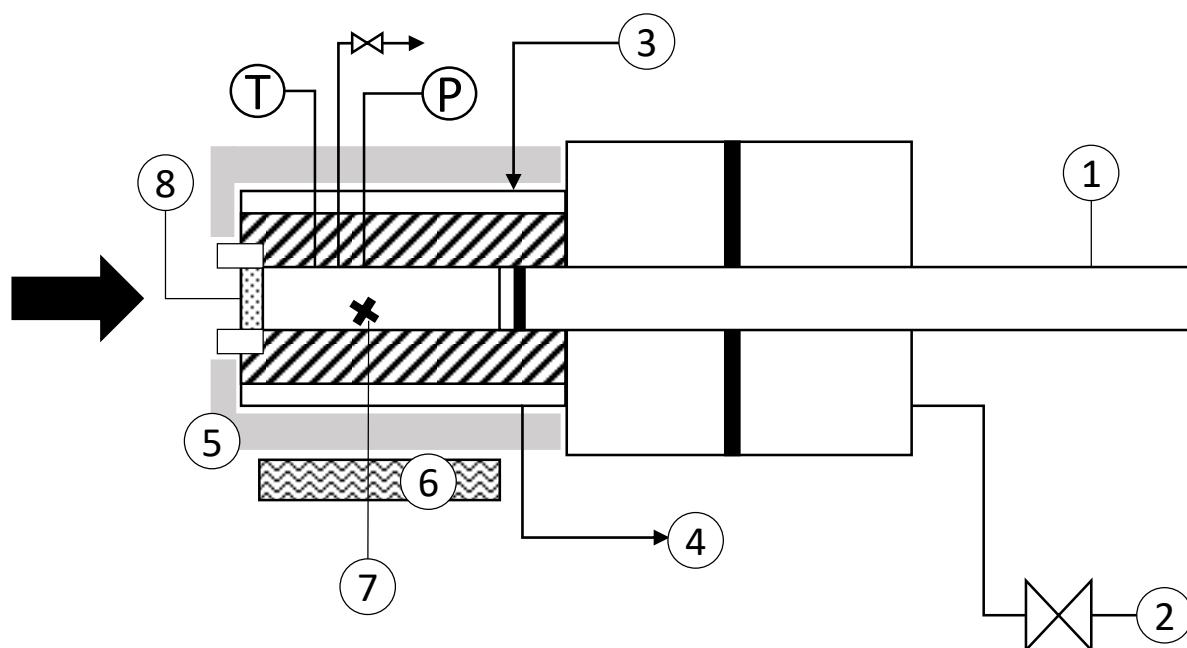
Figure 4.1: Schematic representation of the static synthetic cells used in this work. 1: Piston shaft. 2: Nitrogen source. 3: Heating fluid in. 4: Heating fluid out. 5: Insulation. 6: Magnetic stirrer. 7: Stirrer bar. 8: Sight glass.

The cells are of the variable volume type, where the pressure is controlled by means of a piston connected to a nitrogen cylinder. A Vernier calliper can be attached to the piston to measure the displacement. The cells have OneHalf20 pressure transducers for pressure measurement which were calibrated against a deadweight pressure tester. The calibration data can be found in Appendix B.

Temperature measurements were made by inserting a Pt-100 probe into a thermo-well in the cell wall. The temperature in the cells was controlled by circulating water from a heated bath through the jacket around the cell. The cells were surrounded with glass wool insulation to reduce temperature gradients, and a magnetic stirrer was placed underneath to allow for continuous mixing of the cell contents.

The cells have SITEC sapphire sight glasses to allow for visual detection of phase transitions. This was accomplished by means of a light source and camera connected to a medical endoscope. The endoscope was positioned at the sight glass and the video image was displayed on a computer screen. This allowed phase transitions to be observed from the recorded image in real time. The cells are rated to 300 bar and 200 ˚C. A detailed discussion of their construction was given by Schwarz and Nieuwoudt.[81]

4.2.2. Procedure

The experiment consists of three main steps: loading, measurement, and cleaning. The cell is loaded with the stirrer bar and a weighed-off amount of solute. The piston is attached and sealed. The solvent is loaded from the main cylinder into the solvent gas bomb. The gas bomb is attached to the cell via a manifold with an attached pressure gauge and vacuum line. The cell is flushed with solvent to remove

most of the air in the cell, and is then evacuated with the vacuum line. The gas bomb is then detached and emptied to the desired amount of solvent. Once the bomb is reattached, the valves can be opened to allow solvent to flow into the cell. A hairdryer is used to heat up the gas bomb, manifold, and connecting lines to ensure no liquid solvent remains and to achieve a maximum loading. The valves are closed and the temperature and pressure of the manifold is noted with an infrared thermometer and a pressure gauge respectively. This was used to quantify the amount of solvent lost that remained in the manifold and connecting lines. Knowing the pressure of the manifold and connecting lines, and knowing the temperature of the manifold, NIST[54] data was used to determine the density of solvent in the manifold. This was then used in conjunction with the manifold volume (determined by calibration) to calculate the mass of solvent lost during the loading procedure. The heating bath is then set to the required temperature, and the cell is insulated, the magnetic stirrer positioned and switched on, and the endoscope positioned and adjusted. The pressure is increased to obtain a single fluid phase.

Once thermal equilibrium has been reached (about 45 minutes), the measurements can commence. The pressure is carefully lowered until a phase transition is observed. The pressure, temperature, and visual phenomenon is noted. The cell is recompressed to a single phase, and this process is repeated until the transition point has been observed three times within a range of 0.2 bar. The water bath is set to the next temperature and the measurement procedure is repeated until all temperatures are completed.

At the end of the experiment the heating bath is switched off and the pressure on the piston is removed completely. A solute loading can be reused in order to conserve expensive components if it is a solid under ambient conditions. If the solute loading is to be reused, the cell is left over-night to cool down, allowing the solute to crystallise. The gas can then be unloaded carefully through the valve, and the cell vacuumed to make sure no solvent is left in the cell. Future experiments simply require reloading a different amount of solvent to obtain a different solute fraction. FAMEs have very low vapour pressures at ambient conditions, and thus it is believed that potential losses during this procedure are negligible.

If the loading is not to be reused, the cell is allowed to cool to 50 ˚C. The contents are unloaded into an Erlenmeyer flask by carefully opening the valve. The captured solute can also be stored and reused later if it is a single component. The piston is then removed, and the cell is then rinsed with isopropanol and methanol to dissolve any remaining solute. The cell is then blown dry with compressed air. Rinsing and drying is repeated until the cell is visibly clean. Refer to Appendix A.1 for the detailed experimental procedure.

4. Materials & Methods

4.2.3. Results processing

The phase transition pressures measured will not be at the exact nominal temperature investigated, due to the cells being in an ambient environment. Pressure-temperature correlations at fixed composition can be plotted in order to predict the phase transition pressure at the exact desired temperature. This method has been shown to be reliable for a variety of supercritical solute + solvent systems.[81] A second order polynomial can be fitted to the observed pressure-temperature data for a given solute mass fraction in the form given by Equation 4.1:

$$P = AT^2 + BT + C \qquad\qquad 4.1$$

Initially, A is set to zero. Three criteria are then used to evaluate the suitability of this correlation to predict the phase transition pressure[82]:

$$R^2 > 0.980 \qquad\qquad 4.2$$

$$\left|P_{predicted} - P_{measured}\right| \leq 2\ bar \qquad\qquad 4.3$$

$$\frac{\left|P_{predicted} - P_{measured}\right|}{P_{measured}} \times 100 \leq 2\ \% \qquad\qquad 4.4$$

If setting A to zero does not satisfy these criteria, the correlation is redone including A in the fit, and the correlations are retested. Another benefit of this method is that it becomes possible to compare measured data to literature data not measured at the same temperatures, as long as the literature data was measured at temperatures within the range that the correlation was determined for.

4.2.4. Verification

The equipment and procedure for measuring HPBDP data was verified by measuring six points for the 1-octanol (1) + CO_2 (2) system. This system was measured by several authors in the temperature range planned for this investigation.[80,83,84] Two bubble points, two dew points, and two near-critical points were measured. These points are shown in Figure 4.2. It can be seen that the data measured shows good agreement with literature. This illustrates the confidence in the experimental method, as well as the ability of a visual method to correctly identify the various phase transitions. The measured verification data can be found in Appendix D.
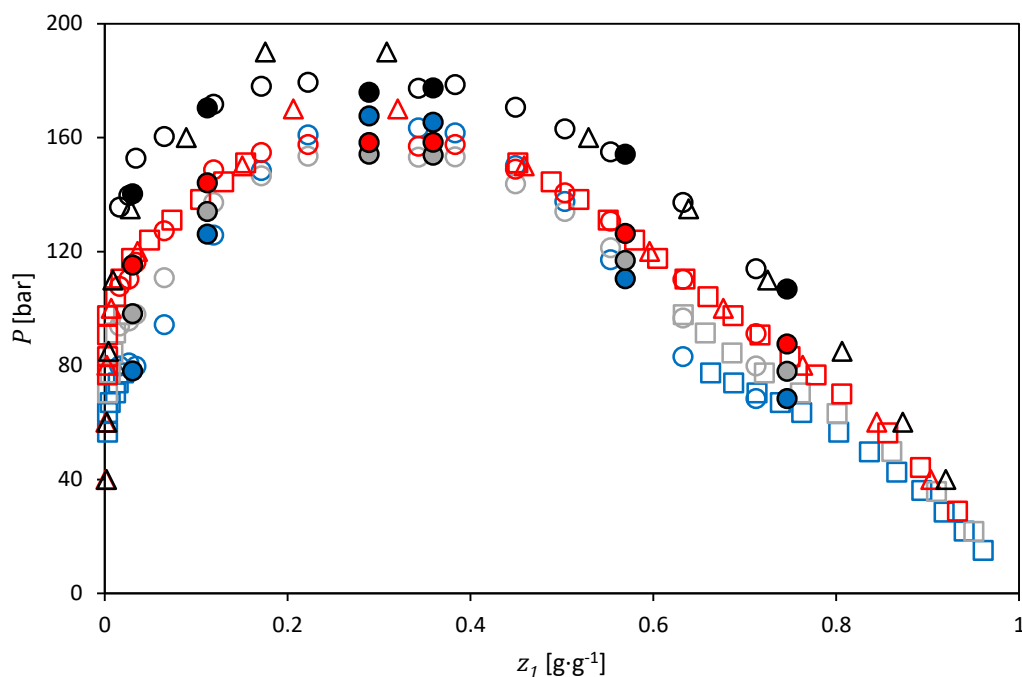
Figure 4.2: Pressure (P) versus solute fraction (z_1) plot of the measured verification points and literature data for the 1-octanol (1) + CO_2 (2) system. This work: (●) T = 35 °C; (●) T = 45 °C; (●) T = 55 °C; (●) T = 75 °C. Literature data: (○) Fourie et al.[80]; (□) Chang et al.[83]; (Δ) Weng & Lee.[84]

4.2.5. Uncertainty

The uncertainty in measurements was determined by following the GUM (*Guide to the expression of uncertainty in measurement*) guidelines to calculate standard uncertainties for all quoted values by propagating uncertainty from the measured variables to the calculated variables.[85] This section briefly explains the factors considered during the uncertainty analysis. Refer to Appendix C for a detailed discussion of the approach and calculations involved.

4.2.5.1. Standard uncertainty in the phase transition pressure

The phase transition pressure was measured with a OneHalf20 mercury-capillary transducer. The transducer was calibrated with a deadweight tester. Table 4.2 provides a summary of the sources of uncertainty accounted for in the quoted experimental phase transition pressure, as well as the method used to determine the uncertainty contribution. The pressure transducer calibration data can be found in Appendix B.1, and a detailed uncertainty report can be found in Appendix C.

4. Materials & Methods

Table 4.2: Overview of the sources of uncertainty in the quoted phase transition pressure.

Component source of uncertainty	Method of determination
Indicated pressure	Calculated from sensor specifications
Pressure correction	Calculated from pressure calibration results
Pressure fluctuation	Observed experimentally
Sensor hysteresis	Calculated from pressure calibration results
Error associated with synthetic-visual method	Calculated from comparison of measured verification data with literature data
Effect of temperature on the phase transition	Calculated through a P-T sensitivity analysis
Effect of composition on the phase transition	Calculated through a P-x sensitivity analysis

4.2.5.2. Standard uncertainty in the solute fraction

Table 4.3 provides a summary of the sources of uncertainty accounted for during the determination of the uncertainty in the solute mass fractions z_1 reported in this work. The GC calibration data and manifold volume calibration data can be found in Appendices B.3 and B.2 respectively. Detailed uncertainty reports are provided in Appendix C.

Table 4.3: Overview of the sources of uncertainty in quoted mass fractions.

Component source of uncertainty	Method of determination
Measured initial and final masses	Calculated from scale specifications
Mass of CO_2 lost during loading	Calculated from uncertainty in manifold volume and CO_2 density
Manifold volume	Calculated from volume calibration data
CO_2 density	Calculated through propagation of uncertainty with the Redlich-Kwong EOS
Manifold temperature	Determined from infrared thermometer specifications
Impurity of stock solutes	Calculated from reported purity of purchased components
Reuse of recovered solute (ternary systems)	Propagation of error from mass balance and GC calibration

4.2.5.3. Standard uncertainty in the temperature

The temperature was measured with a Pt100 handheld temperature probe. The probe was calibrated by WIKA Instruments (Pty) Ltd. The standard uncertainty in the measured cell temperature was calculated by combining the uncertainty associated with the indicated temperature, and the uncertainty associated with the temperature correction from the probe calibration data. The

temperature calibration data and certificates can be found in Appendix B.4. and detailed uncertainty reports are provided in Appendix C.

4.2.5.4. Summary of HPBDP standard uncertainties

A brief summary of the standard uncertainties associated with the HPBDP measurements are provided in Table 4.4. A detailed accounting of the uncertainty values can be found in Appendix C.

Table 4.4: Summary of the standard uncertainties and standard uncertainty ranges in the temperature (T), phase transition pressure (P), total solute fraction (z_1), and reduced weight fraction on a solvent-free basis (w_1^{red}) for all the HPBDP data measured in this work.

System	$u(T)$ [°C]	$u(P)$ [bar]	$u(z_1)$ [g·g⁻¹]	$u(w_1^{red})$ [g·g⁻¹]
M18:0 (1) + CO$_2$ (2)	0.2	0.7 - 1.8	0.0001 - 0.0056	
M18:1 (1) + CO$_2$ (2)	0.2	0.7 - 1.8	0.0001 - 0.0051	
M18:2 (1) + CO$_2$ (2)	0.2	0.7 - 1.8	0.0003 - 0.0048	
M18:0 (1) + M18:1 (2) + CO$_2$ (3) at w_1^{red} = 0.237 g·g⁻¹	0.3	1.0 - 1.6	0.0001 - 0.0070	0.011
M18:0 (1) + M18:1 (2) + CO$_2$ (3) at w_1^{red} = 0.501 g·g⁻¹	0.3	1.0 - 1.5	0.0002 - 0.0077	0.001
M18:0 (1) + M18:1 (2) + CO$_2$ (3) at w_1^{red} = 0.772 g·g⁻¹	0.3	1.0 - 1.5	0.0001 - 0.0057	0.011

4.3. Measurement of High-Pressure VLE Data

4.3.1. Equipment

An analytical view-cell similar in principle to the synthetic-visual cells was used to measure VLE data for the ternary system. The cell has a volume of 75 to 125 mL, and is rated for 300 bar and 150 ˚C. A diagram of the cell is given in Figure 4.3 (front cross-section). The main difference between this cell and previous ones, is the addition of ROLSI™ (Rapid Online Sampler Injector) samplers (R1 and R2 in Figure 4.3) to sample the vapour and liquid phases simultaneously and send them to an on-line GC for analysis of samples. The cell is placed in a forced-convection oven in addition to the jacketed heating water circulation. This virtually eliminates any temperature gradients. The reader is referred to various works by Fourie and coworkers for further detail about the construction and function of the VLE cell.[86–89] Temperature and pressure calibration data can be found in Appendix B.

4. Materials & Methods
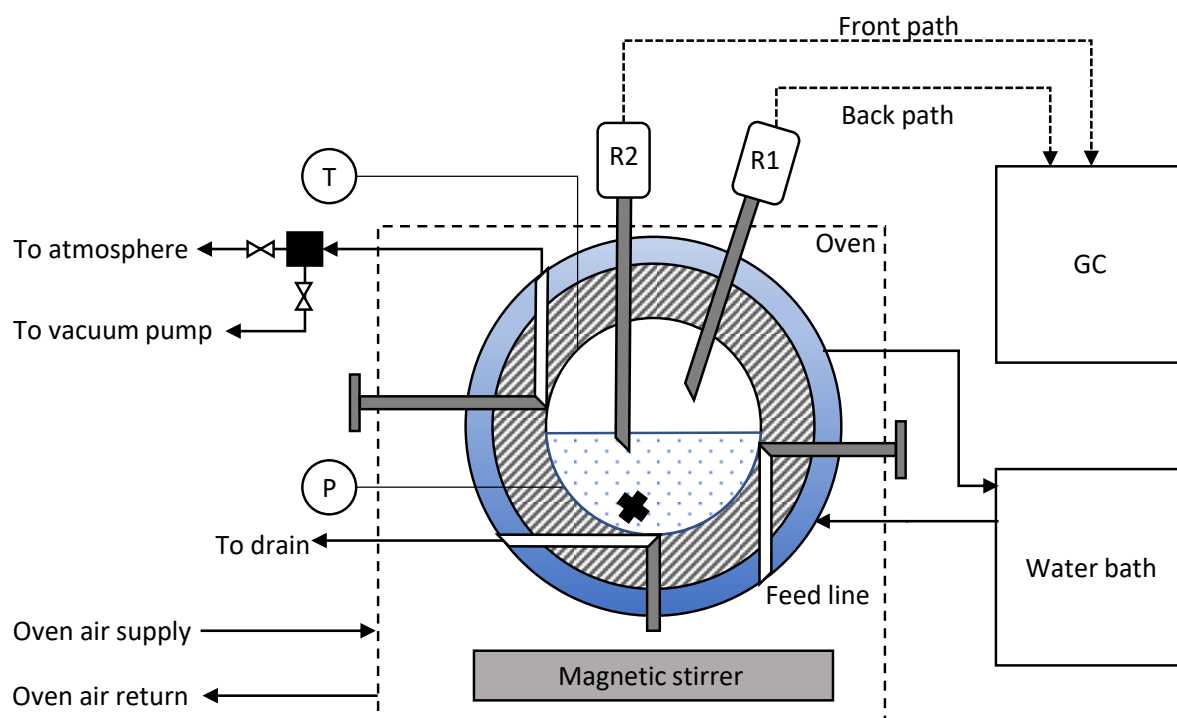
Figure 4.3: Schematic representation of static-synthetic high-pressure cell, front cross-sectional view.

In this work, ROLSI R1 was used to sample both phases for operational reasons. The cell has previously been operated in this manner.[88] The ROLSI samplers have automatic sampling timers that were adjusted to allow for different sampling rates and sizes. The back and front pathways are heated and insulated, and transfer the samples to the GC inlets via helium carrier gas.

The GC system is shown schematically in Figure 4.4. Samples enter through either the front inlet or back inlet to either columns C-1 or C-2. These are the solute columns, and are designed to separate the heavy components. The CO_2 solvent, however, does not interact with the stationary phases in these columns and rapidly moves through.

Initially the valves are in the "open" position, allowing the CO_2 to be transported to columns C-3 and C-4. These are the solvent columns, and they elute to the thermal conductivity detector (TCD) in order to analyse the solvent. Columns C-3 and C-4 have different lengths, allowing analysis on the same detector for both pathways due to the staggered elution.

Once the CO_2 has entered the solvent columns, the valves switch to the "closed" position, and allow the eluted solute compounds through to the flame ionisation detectors (FID) for analysis. The valve system protects the solvent columns from being damaged by the heavy compounds that would interact strongly with the stationary phase. The fourth port on each of the valves is connected to an auxiliary carrier gas supply. This ensures constant flow of gas throughout the columns, regardless of valve position, to protect the columns from thermal damage. As only one ROLSI was used for sampling,

only one analysis pathway was used. The unused pathway is greyed out in Figure 4.4 (front inlet, C-2, C-4, back FID). GC calibration data can be found in Appendix B.
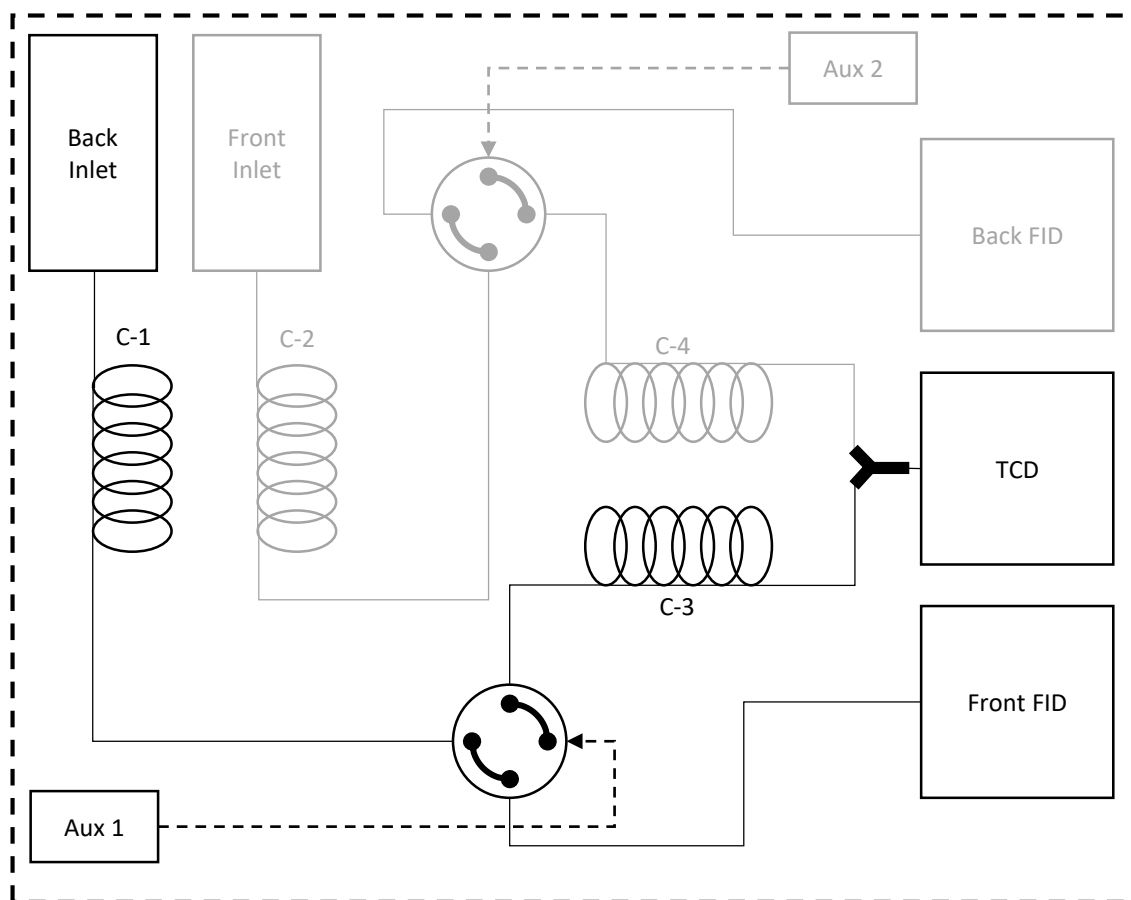
Figure 4.4: Schematic representation of the modified on-line GC system setup. The analysis path that was not used in this work is greyed out (front inlet, C-2, C-4, back FID). Pneumatic 4-way valves are shown in the "closed" position.

Table 4.5 summarises the columns used for the sample analysis. The difference in length between the two solvent columns should be noted, the CO_2 has a retention time in C-3 of about double that of C-4.

Table 4.5: Summary of columns used in the on-line GC setup.

Column	Use	Model	Dimensions		
			Length [m]	*I.D. [mm]*	*Film Thickness [μm]*
C-1	Solute	Zebron ZB-WAX	30	0.53	0.50
C-2	Solute	Zebron ZB-WAX	30	0.25	0.25
C-3	Solvent	Agilent HP-PLOT/Q	30	0.53	40
C-4	Solvent	Agilent HP-PLOT/Q	15	0.53	40

4.3.2. Procedure

The cell is loaded with the stirrer and the piston is attached and sealed. The liquid solute mixture with a predetermined composition is loaded via syringe through the feed line (about 23 mL). The dedicated vacuum line is used for flushing and degassing. The solvent is loaded from a custom gas bomb, in a similar fashion to the synthetic-visual cells. The oven can then be closed by attaching the insulating

4. Materials & Methods

outer plates to the enclosure. The water bath and forced-convection oven is set to the correct temperature setpoints, and the pressure in the cell is set to the desired pressure with the nitrogen cylinder connected to the piston.

The contents of the cell are then allowed to reach equilibrium under constant agitation. Equilibrium is assumed after the contents of the cell have been agitated under pressure and at temperature overnight, with both the pressure and temperature remaining stable, with the liquid and vapour phases clear of entrained bubbles or droplets, and in the absence of any transitional phases.

Once equilibrium has been reached, the agitation is switched off. Time is allowed for the liquid-vapour interface to stabilise, and any nonvisible entrained particles to settle out. Automatic sample sequences are set up to purge the sampling needles until the peaks level out on the GC.

Once the sampling needles and lines have been purged the setup is ready for sampling. Four or five repeat samples are taken per phase. After four consistent GC sampling runs have been conducted, the temperature and/or pressure can be set to the next point, and the measurement procedure repeated. Cleaning of the cell is done similarly to the synthetic-visual cells. Refer to Appendix A for the detailed experimental procedure.

4.3.3. Analytical technique development

The on-line GC analysis of extracted samples for the M18:0 + M18:1 + CO_2 system proved to be more complex than the analysis of the systems that were previously investigated with the experimental setup. Both methyl stearate and methyl oleate have similar retention times even when using the most optimal column configuration and temperature program. This is not a problem on a normal GC setup where samples are made by hand and injected. However, for on-line analyses of an equilibrium cell at high pressure, and with the addition of a carbon dioxide solvent that cannot be analysed on the same detector, the situation changes.

4.3.3.1. Identification of extra-column effects

Initial M18:0 + M18:1 mixture injections revealed excessive band-broadening and fronting effects, causing severe peak overlap, as illustrated in Figure 4.5. It was determined that the pneumatic valves and stainless-steel connecting tubing constitute a large amount of dead volume for samples that need to travel from the wax-column to the FID. This was tested by temporarily bypassing the valves and connecting lines, which resulted in FAME peaks eluting with perfect resolution and separation. With the valves, however, the peaks could not be completely resolved, though they maintained characteristic shapes when compared to single-component injections. The valves and tubing used

already had minimised volumes, so the analysis problem could not be solved by eliminating the dead volume with substituted parts.

Extra-column effects
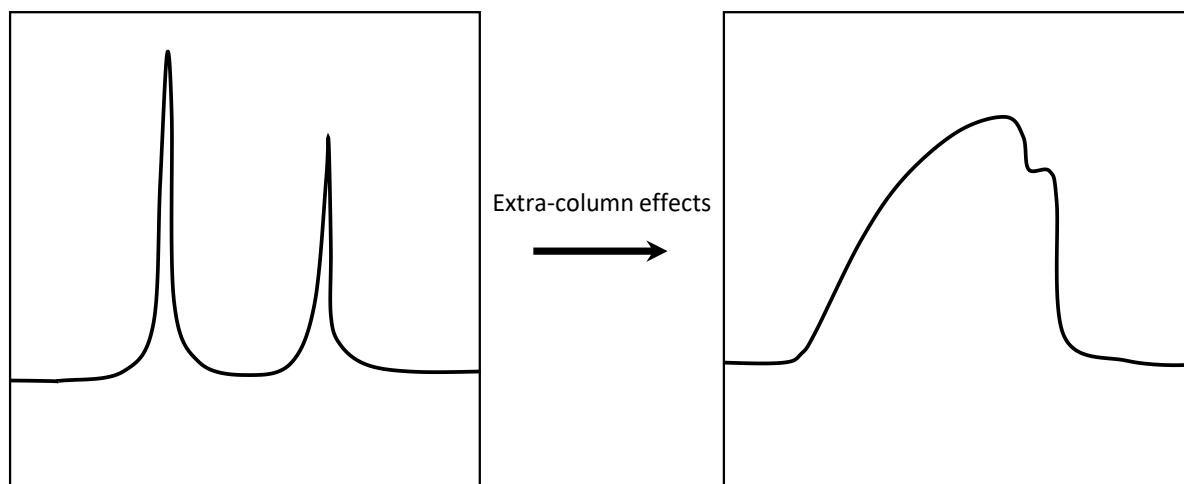
Figure 4.5: Illustration of typical extra-columns effects on analyses in this work.

4.3.3.2. Asymmetric-system effects in on-line sampling

The analysis was further complicated by the inability of the GC setup to simultaneously detect the carbon dioxide peaks on the TCD as well as semi-resolved ester peaks on the FID for the liquid-phase samples. Liquid samples were analysed at a split ratio of 80:1 instead of the 20:1 ratio that was used for the vapour samples. This was done to reduce column overload from the ester-rich liquid phase. This worked antagonistically with the CO_2 analysis, since the liquid phase is CO_2-poor, and further reducing the size of the sample sent to the detectors made the CO_2 peaks on the TCD undetectable.

The inability to directly analyse the amount of CO_2 in a liquid sample required an alternative approach to phase composition determination. Novak et al. discusses several methods for evaluating tie-line compositions without direct analysis of the coexisting phases in the measurement of LLE data.[90] These types of methods require knowledge of the binodal curve (or, more generally the curve of incipient phase formation). The binodal curve (or bubble-point, or dew-point curves) defines the locus of points where equilibrium compositions exist. This means that, having knowledge of the binodal curve, it is possible to determine the tie-line compositions by only measuring one or two additional variables to specify the system and determine the compositions. Applying this method to the determination of the liquid phase composition thus required ternary bubble-point data (which had already been measured) and an additional variable. The GC analysis could not detect the CO_2, but it could detect the two ester compounds, meaning that analysing a liquid-phase sample provided the mass ratio of the esters in the liquid phase. This was used in conjunction with the bubble-point data to calculate the location of the coexisting liquid-phase composition, as shown in Figure 4.6. Knowing the bubble-point curve, and the mass ratio of solutes, the liquid composition must lie on the intersection of the constant solute-solute

4. Materials & Methods

ratio line (CSSRL) with the bubble-point curve in order to satisfy the equilibrium condition and mass balance.
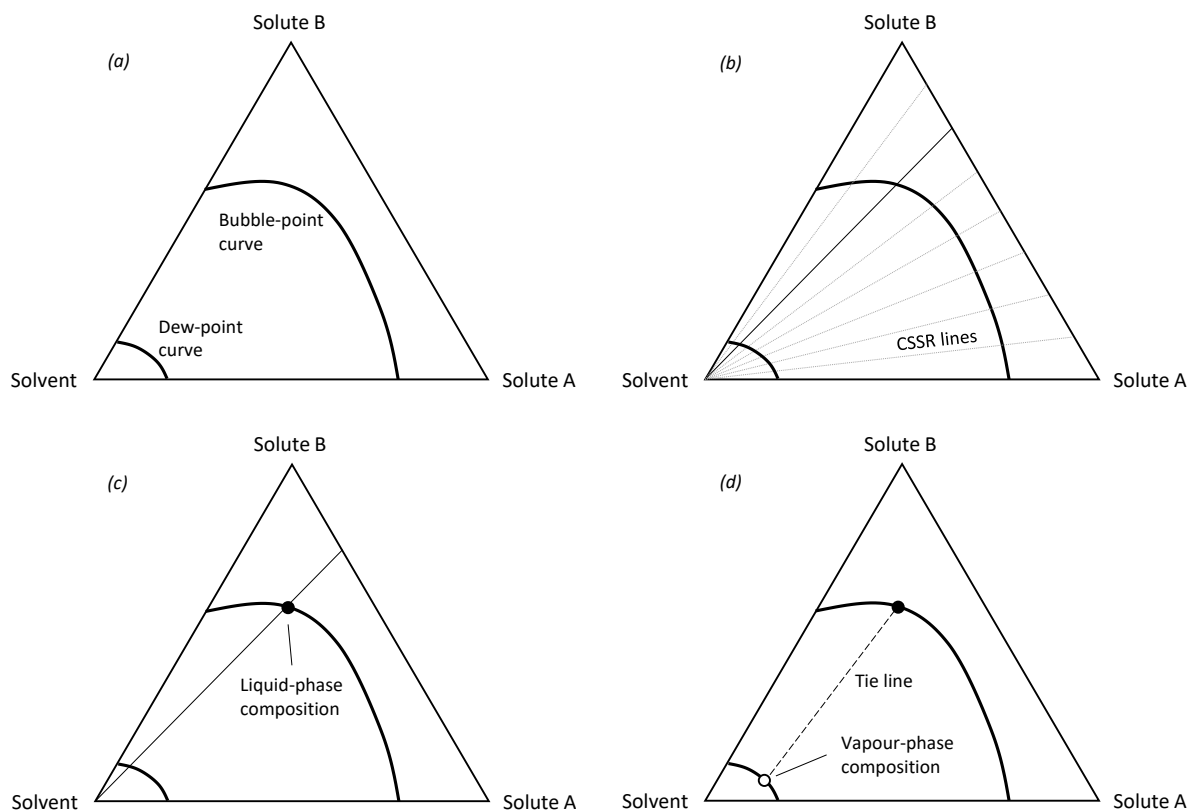
Figure 4.6: Determination of the liquid-phase composition via a nondirect method. (a) Find/measure bubble-point data. (b) Determine solute-solute ratio and identify relevant CSSRL. (c) Liquid composition point is the intersection of the CSSRL and the bubble-point curve. (d) Measure vapour composition to determine tie line.

This means that in order to obtain the liquid point on a VLE tie-line, only the ratio of the esters needs to be determined. This requires a method of processing the overlapping peak signal obtained from the GC. Similarly, the determination of the vapour point on a VLE tie-line requires the determination of the individual masses of esters, since the CO_2 can be directly analysed.

4.3.3.3. Peak deconvolution

Felinger describes a variety of methods that can be used to resolve or deconvolute overlapping peaks.[91] These include signal-derivative analysis for integration-boundary detection, curve fitting, and application of neural networks. Other methods, such as principal component regression, are not appropriate for this application, as they are either better-suited to more symmetrical peaks, or they require that the peak shape not change with composition.[91] This was not the case for the highly asymmetric peaks observed in this work. In order to test the deconvolution methods, a series of known FAME mixture samples were made and analysed using both the 20:1 and 80:1 split ratio methods. Five samples, 40 %, 45 %, 50 %, 55 %, and 60 % g·g^{-1} M18:0 were made and analysed multiple times on the two analysis methods to generate a set of training and validation data for various deconvolution

procedures. Figure 4.7 shows how the convoluted peak shape changes with increasing M18:0 content whilst the M18:1 content remains constant. Additionally, standard single-component GC calibration curves were constructed for both methods and both components. These can be found in Appendix B.
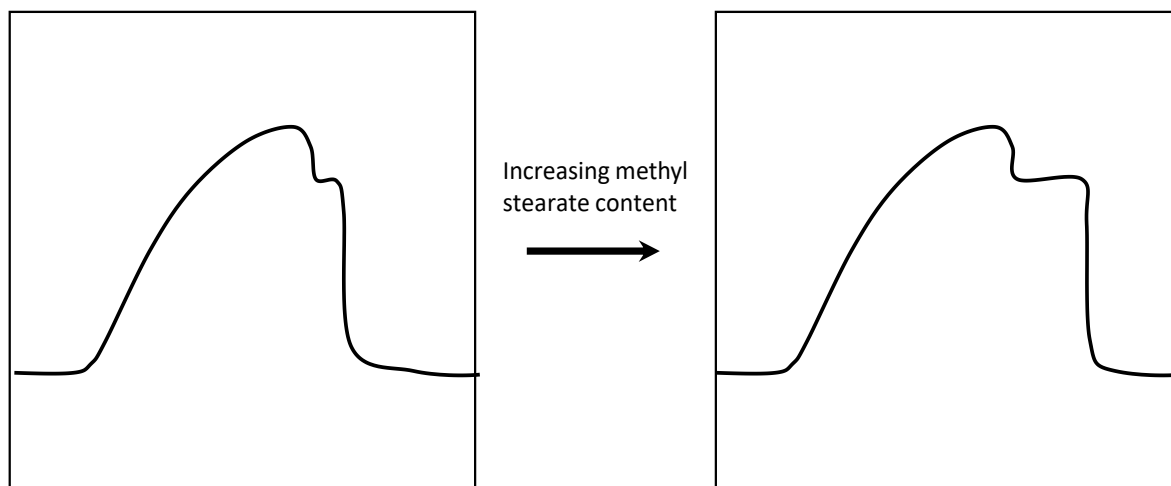
Figure 4.7: Illustration of the effect of methyl stearate content on the eluting ester peaks on the FID.

4.3.3.4. Peak deconvolution – curve fitting

Three deconvolution methods were attempted. Curve fitting is a more fundamental approach to peak deconvolution. Under the assumption that the convoluted peak is the linear sum of the individual component peaks, and knowing the number of overlapping peaks beforehand, one can fit a suitable model to single-component injections. If there are relationships between the model parameters, this can be exploited to reduce the number of unknowns in subsequent regressions on overlapped peaks.[91] Firstly, a suitable model had to be found. The Haarhoff-van der Linde model (HVDL model) is based on the mass balance of an injected sample, including broadening effects, which makes it ideal to apply to asymmetrical peaks in overloaded systems.[91] The model in the form used by Le Saux et al. is given in Equation 4.5 as a function of the time t[92]:

$$
f(t) = \frac{\dfrac{a_0 a_2^2}{a_1 a_3}\left[\dfrac{1}{a_2\sqrt{2\pi}}\exp\left(-\dfrac{(t-a_1)^2}{2a_2^2}\right)\right]}{\dfrac{1}{\exp\left(\dfrac{a_1 a_3}{a_2^2}\right)-1} + \dfrac{1}{2}\left[1 + \mathrm{erf}\left(\dfrac{t-a_1}{a_2\sqrt{2}}\right)\right]}
\tag{4.5}
$$

where a_0 is the peak area, a_1 is the centre point of the Gaussian component, a_2 is the standard deviation of the Gaussian component, and a_3 is a measure of the distortion of the peak. The HVDL model was found to adequately correlate the single-component peaks of both M18:1 and M18:0, as is illustrated in Figure 4.8.

4. Materials & Methods
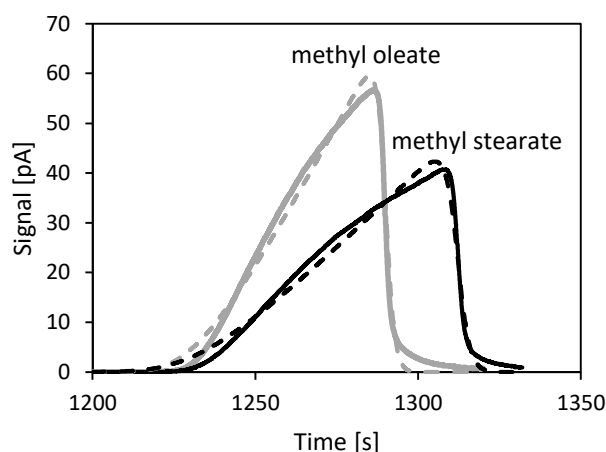
Figure 4.8: Single-component peaks for methyl oleate and methyl stearate with Haarhoff-van der Linde model fits. Solid lines are experimental data, dashed lines are model fits.

However, it was found that linear summations of the peaks modelled to single-component data could not predict the convoluted peak. Felinger describes that, under column overload conditions, the interactions of two components cannot be disregarded.[91] The HVDL model would thus need to be directly fitted to the generated mixture data. To that effect, regressions were performed in MATLAB®, in order to determine the four parameters for each mixture sample in the training data set. The known masses were plotted against the adjusted deconvoluted area A' (where a_0 is the deconvoluted area) to generate a calibration curve. The calibration curves are shown in Figure 4.9.
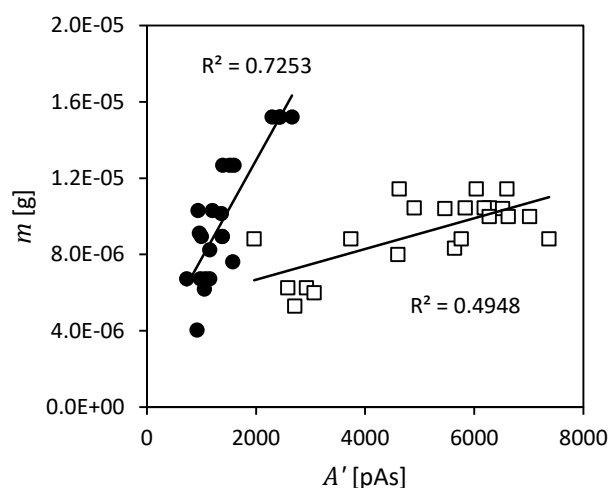
Figure 4.9: Calibration curve for deconvoluted area using the Haarhoff-van der Linde curve-fitting approach. (●) M18:0; (□) M18:1.

To summarise, the curve-fitting approach was applied to samples by performing a nonlinear regression in MATLAB® to determine the eight parameters of the Haarhoff-van der Linde model that result in two

deconvoluted ester peaks. The component peak areas were then used together with the calibration curves of the respective components to calculate the masses of each ester present in the sample.

4.3.3.5. Peak deconvolution – integration bounding

Integration bounding is a technique that is used in chromatography to calculate the areas of overlapping peaks. The limit to where the first component's area is integrated, and the point from which the second component's area is integrated, needs to be determined. This method is commonly used for the case of slightly overlapping peaks, as the determination of the integration boundary is trivial.[91] For peaks with a larger degree of overlap, the derivatives of the time-domain response signal can provide valuable information.[93] The first and second derivatives of a chromatographic signal with overlapping peaks have distinct features. The first derivative has four alternating maxima and minima, whilst the second derivative has five alternating maxima and minima. The location of these extrema in the derivative can provide information on where one peak stops and another peak begins.[91,93]

First and second derivatives were calculated numerically from the mixture sample signal data by using finite central difference formulae, given in Equations 4.6 and 4.7[94]:

$$f'(x_i) = \frac{f(x_{i-2}) - 8f(x_{i-1}) + 8f(x_{i+1}) - f(x_{i+2})}{12h} \qquad 4.6$$

$$f''(x_i) = \frac{-f(x_{i-2}) + 16f(x_{i-1}) - 30f(x_i) + 16f(x_{i+1}) - f(x_{i+2})}{12h^2} \qquad 4.7$$

The numerical calculation method was not satisfactory for the second derivative, as excessive noise was present, so it was decided to make use of the first derivative. The location of the first minimum was taken as the integration boundary. Figure 4.10 provides an example signal and its first derivative. All four first derivative maxima and minima can be identified. In order to accurately determine the location of the minimum, the derivative was plotted, and MATLAB®'s manual input function $ginput$ was used to manually read in the point.

4. Materials & Methods
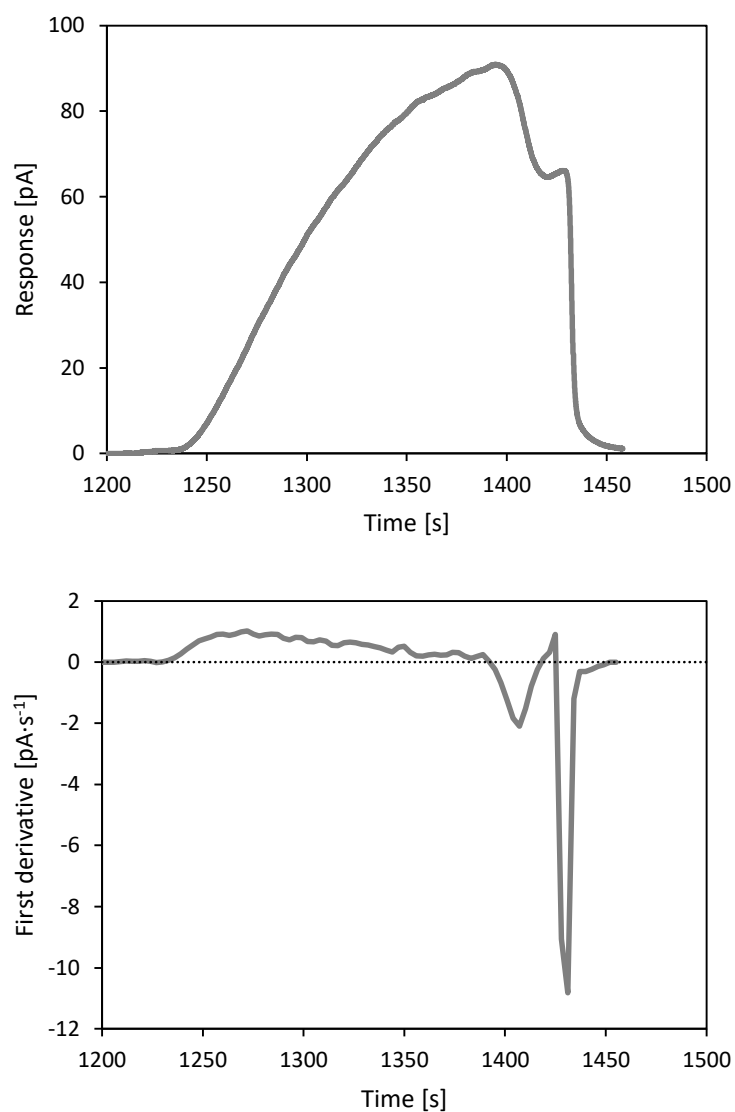
Figure 4.10: Response signal of an ester mixture sample, and the numerical first derivative of the signal.

After the integration boundary was identified for a sample, the component areas were calculated by numerical integration with the trapezium rule. This provided a set of ester mass vs deconvoluted ester area data that was used to construct calibration curves. The calibration curves are provided in Figure 4.11.
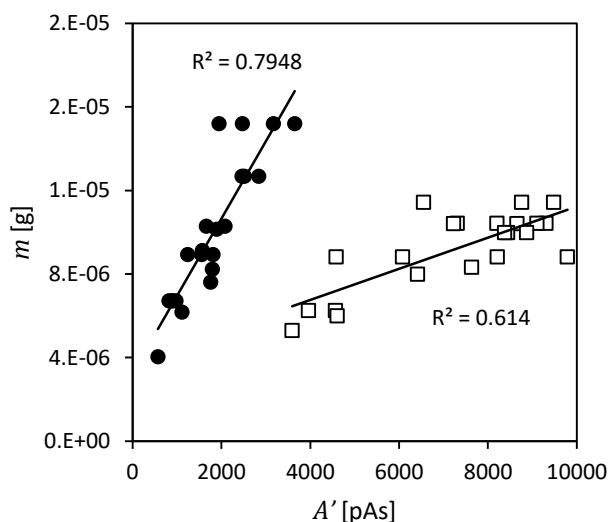
Figure 4.11: Calibration curves for the integration-bounding method. (●) M18:0; (□) M18:1.

4.3.3.6. Peak deconvolution – neural network

Neural networks lend themselves to the solution of large or complex problems where little fundamental knowledge is available. They can also be applied to highly nonideal systems if more fundamental approaches have failed. Gallant et al. employed an artificial neural network to solve the chromatographic deconvolution problem.[95] Their approach entailed making use of the second derivative of the response signal to extract features that are sent as inputs to the neural network. The neural network then produces an output of the parameters required to model the two resolved peaks as the sum of two Gaussian functions. This approach had to be modified for application to the nonideal chromatography in this work.

As was previously discussed, the numerical calculation of the second derivative of the signal was insufficient for feature extraction purposes, so the method was instead based on the first derivative of the signal. A similar approach to that used in the integration-bounding method was followed for the feature extraction. The last three of the four extrema were selected as features, both the time, as well as the detector response at that time for each feature. The feature extraction is shown in Figure 4.12. This procedure was carried out in MATLAB® with the use of the $ginput$ function to ensure accurate detection of extrema. The result was six feature values, three times and three detector responses.

4. Materials & Methods
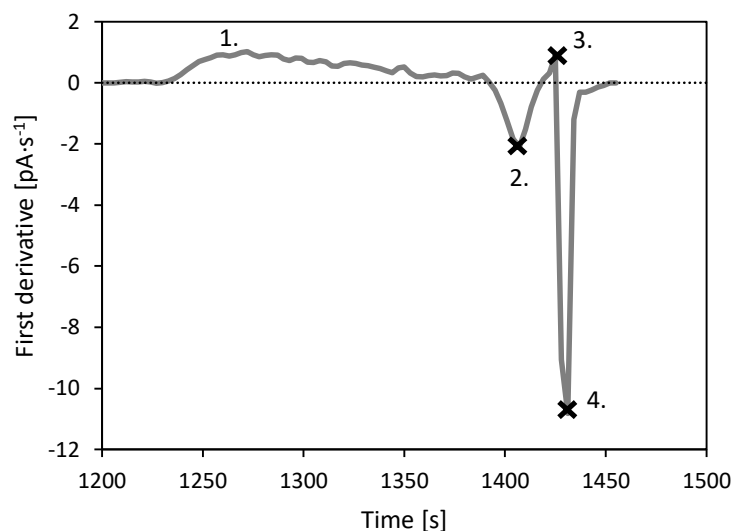
Figure 4.12: Feature extraction from the first derivative of the response signal for the neural network approach to peak deconvolution. First derivative extrema are numbered, with the selected features marked with a cross.

In order to ensure that the neural network responded only to the shape of the composite peak, and not its size, the features were nondimensionalised before being placed in the feature vector $\boldsymbol{F}$ as shown in Equation 4.8[95]:

$$\boldsymbol{F} = \begin{bmatrix} round\left(d \cdot \dfrac{t_1 - t_b}{w}\right) \\ round\left(d \cdot \dfrac{c_1}{c_{max}}\right) \\ \vdots \\ round\left(d \cdot \dfrac{t_3 - t_b}{w}\right) \\ round\left(d \cdot \dfrac{c_3}{c_{max}}\right) \end{bmatrix} \qquad 4.8$$

where t_i is the feature time, c_i is the detector response at time t_i, t_b is the breakthrough time of the signal – i.e. the time the peak starts to elute, w is the signal length – i.e. the length of time it takes for the peak from start to end of elution, c_{max} is the maximum detector response for the overlapped signal, and d is the discretisation, taken as 100 here. As outputs, the neural network was trained to provide a vector containing two nondimensionalised areas. Training data was nondimensionalised by dividing the individual peak area (back-calculated from the known component mass in the mixture with the single-component calibration curves) by the total area of the composite peak. The neural network was created and trained with the MATLAB® neural network application in the *Statistics and Machine Learning Toolbox*. The network was created with ten hidden layers.

To summarise, a neural network was trained to deconvolve overlapped chromatographic peaks by receiving nondimensionalised peak features identified with a first derivative approach, and to provide

the resolved, dimensionless area of each individual peak. These areas were then scaled back to the correct area unit by multiplication with the total composite peak area, and used with the single-component calibration curves to calculate the mass of each ester present in the sample.

4.3.3.7. Selection of a deconvolution method

In order to evaluate which deconvolution method to select, a cross-validation approach was used. Cross-validation is a statistical resampling method that is used to determine the test error rate, i.e. a measure of the error associated with a model that is independent of the data used to fit the model. Cross-validation methods are useful when there is a limited set of data to use for both training and validation of the model.[96] The test error rate is a useful quantity when selecting a model for a given application.

In particular, a k-fold cross-validation approach was used. This approach entails dividing the data set into k partitions or folds. The model is then fitted k times, each time leaving out one of the folds in the fitting process.[96] For each of the k fits, the mean squared error (MSE) or mean absolute percentage error ($MAPE$) is calculated, according to Equations 4.9 and 4.10[96]:

$$MSE_k = \frac{1}{n}\sum_{i=1}^{n}\left(y_i - f(x_i)\right)^2 \qquad\qquad 4.9$$

$$MAPE_k = \frac{100}{n}\sum_{i=1}^{n}\left|\frac{y_i - f(x_i)}{y_i}\right| \qquad\qquad 4.10$$

where $f(x_i)$ is the predicted output value for input x_i in fold k, and y_i is the actual output value for data point i in fold k. These values can be averaged across all folds to provide an estimate of the test error rate for comparative purposes, or for uncertainty analyses.[96]

For the samples analysed on the 20:1 split ratio method, the three deconvolution methods were evaluated on the basis of the predicted component masses vs actual sample masses, with the methyl stearate and methyl oleate masses being evaluated individually. The plot of the average $MAPE$ on the basis of mass for the cross-validation procedure is shown in Figure 4.13. The total data set contained 22 samples, resulting in 4 folds, containing 5, 5, 6, and 6 samples respectively. It can be seen that on average all three methods performed equally well for the prediction of the methyl oleate mass in the samples. However, large differences were observed for the prediction of the methyl stearate mass. The integration-bounding method performed the best, with an average $MAPE$ of 13.7 %, followed by the neural-network method at 27.2 %, and the curve-fitting method at 37.0 %.

4. Materials & Methods
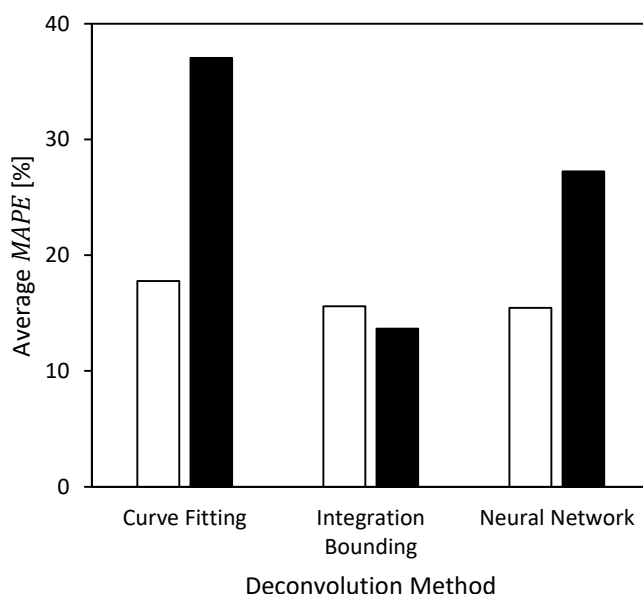
Figure 4.13: Cross-validation results for the three investigated peak deconvolution methods for both methyl stearate and methyl oleate for the 20:1 split ratio method. (□) M18:1; (■) M18:0.

Considering the results of the cross-validation, the integration-bounding method was selected, specifically the model trained in fold 3. The final calibration curve parameters are provided in Table 4.6. In order to quantify the uncertainty in the calculation of the ester masses in a sample, the MSE was calculated based on all the data sets, and then recast as a standard uncertainty $u^2(m)$ for use in error propagation calculations according to the GUM procedures.

Table 4.6: Final calibration parameters for the integration-bounding method for the analysis of vapour-phase samples with the 20:1 split ratio method.

Component	Slope β [g·pAs^{-1}]	Intercept α [g]	MSE [g^2]	$u^2(m)^a$ [g^2]
Methyl oleate	6.887e-10	4.353e-6	1.101e-12	1.55e-13
Methyl stearate	3.664e-9	3.559e-6	1.586e-12	1.85e-13
*[a] The **MSE** was recast as a standard uncertainty with the formula $u^2(m) = \frac{MSE}{n}$ where n = 22.*[85]				

The data for the 80:1 split ratio method used to analyse liquid-phase samples was not as easily modelled by the deconvolution procedures outlined thus far, resulting in calibration curves with low R^2 values. The only feasible approach was the implementation of a neural network. A neural network identical in procedure to that of the 20:1 split ratio method was employed, with the only difference being that the network was trained to provide the mass ratio of esters instead of separate areas, as the ratio is all that is needed for the cloud-point calculation of tie-lines. The ratio r_{21} of methyl oleate (component 2) mass to methyl stearate (component 1) mass was used. The method was cross-validated with the k-fold procedure in order to determine the test error for uncertainty calculations. The data set consisted of 25 samples, and cross-validation was performed with 5 folds containing 5

samples each. The results of the validation procedure are given in Figure 4.14. It can be seen that fold 5 performed the best, with an $MAPE$ of 10.5 %, followed by fold 3 with an $MAPE$ of 15.5 %.
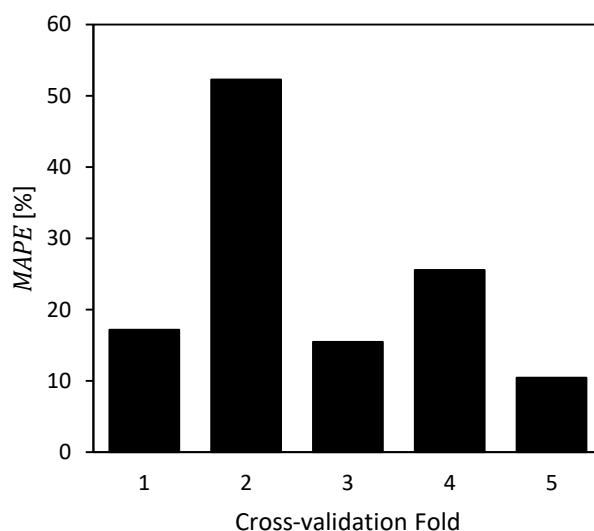
Figure 4.14: Cross-validation results for the analysis of liquid-phase samples using a neural network to determine the ester mass ratio.

Considering the results of the cross-validation, the neural network trained on fold 3 was selected. This was done despite fold 5 having a lower test error rate, since the network for fold 3 always predicted correctly whether r_{21} was above or below 1, which the network for fold 5 was not always able to do. In phase-equilibrium measurements, it is very important to know the relative amounts of components distributed in the phases, so the ability of the fold 3 network to correctly predict a majority of one component over the other was prioritised above the slightly higher error rate. The standard uncertainty in the predicted r_{21} was taken as the average MSE across data sets in all folds, to provide for a more conservative estimate, and was found to be $u^2(r_{21})$ = 0.090 $g^2{\cdot}g^{-2}$.

4.3.4. Verification

Verification of the analytical method of ternary VLE measurement was conducted by measuring data for the CO_2 + n-dodecane (n-C_{12}) + 1-decanol (1-$C_{10}OH$) system. This system was previously measured by Fourie with the newly constructed analytic setup. The results are shown in Figure 4.15. It can be seen that the measured data shows good agreement with literature. The measured verification data can be found in Appendix D.

4. Materials & Methods
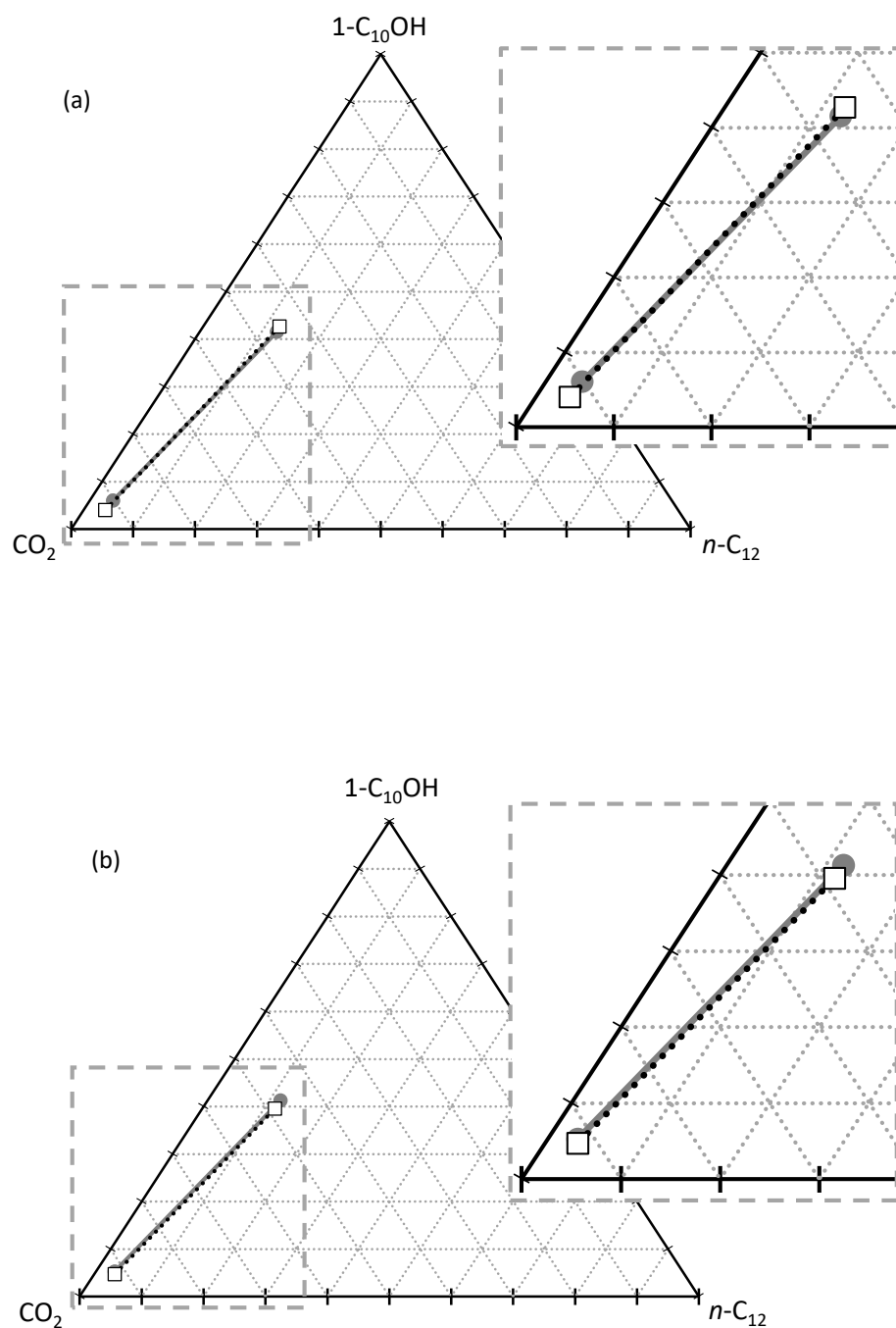
Figure 4.15: VLE verification data for the CO_2 + $1-C_{10}OH$ + $n-C_{12}$ system. (a) 55 °C and 123 bar. (b) 75 °C and 157 bar. (●) Verification data; (□) Data from Fourie.[89]

4.3.5. Uncertainty

The same approach to the determination of uncertainty was used for the VLE data as for the HPBDP data, as outlined in Appendix C.

4.3.5.1. Standard uncertainty in the pressure

The standard uncertainty in pressure was determined from the pressure calibration data. Since the pressure was controlled, and was not an output measurement in these experiments, no other contributions to the pressure uncertainty were present.

4.3.5.2. Standard uncertainty in the compositions of coexisting phases

The calculation of the standard uncertainty in the equilibrium compositions was a necessarily complex process, as uncertainty is introduced by the procedure of calibrating the GC, as well as by the actual sample analysis procedure and the subsequent peak deconvolution.

Uncertainty was introduced by the calibration curves, due to random variation, uncertainty associated with the injection volume, uncertainty associated with the preparation of the calibration sample, and uncertainty in the peak areas that were adjusted with a bubble flow test. This uncertainty was accounted for by doing repeat injections, repeat bubble flow tests, and by calculating error propagation from the microsyringe and scale specifications.

Uncertainty was also introduced during the analysis procedure from the combined effects of the calibration curves, the analysis-run bubble flow tests, the peak area adjustment, and the deconvolution procedure. This was accounted for by taking repeat samples and analysing them, as well as by error propagation from the calibration uncertainty, bubble flow tests, and area adjustment.

Finally, uncertainty was also contributed by the effect of pressure and temperature on the compositions of coexisting phases.

4.3.5.3. Standard uncertainty in temperature

The temperature was measured with a Pt100 dedicated temperature probe attached to the cell. The probe was calibrated by WIKA Instruments (Pty) Ltd. The standard uncertainty in the measured cell temperature was calculated by combining the uncertainty associated with the indicated temperature, and the uncertainty associated with the temperature correction from the probe calibration data. The temperature calibration data and certificates can be found in Appendix B.4. and detailed uncertainty reports are provided in Appendix C.

4. Materials & Methods

4.3.5.4. Summary of HPVLE standard uncertainties

Table 4.7 provides a brief summary of the standard uncertainty in the measured HPVLE data for the ternary M18:0 (1) + M18:1 (2) + CO_2 (3) system. A detailed accounting of the uncertainty values can be found in Appendix C.

Table 4.7: Summary of the standard uncertainties and uncertainty ranges in the temperature (T), pressure (P), liquid phase composition (x_i), and vapour phase composition (y_i) at three different temperatures for the M18:0 (1) + M18:1 (2) + CO_2 (3) system.

T [°C]	$u(T)$ [°C]	$u(P)$ [bar]	$u(x_1)$ [g·g⁻¹]	$u(x_2)$ [g·g⁻¹]	$u(x_3)$ [g·g⁻¹]	$u(y_1)$ [g·g⁻¹]	$u(y_2)$ [g·g⁻¹]	$u(y_3)$ [g·g⁻¹]
35.0	0.3	0.3	0.0179 - 0.0289	0.0494 - 0.0730	0.0511 - 0.0685	0.0061 - 0.0111	0.0037 - 0.0101	0.0087 - 0.0208
55.0	0.3	0.3	0.0259 - 0.0301	0.0593 - 0.0742	0.0555 - 0.0691	0.0024 - 0.0100	0.0020 - 0.0055	0.0035 - 0.0142
75.0	0.3	0.3	0.0245 - 0.0276	0.0587 - 0.0702	0.0557 - 0.0659	0.0023 - 0.0043	0.0020 - 0.0046	0.0037 - 0.0086

CHAPTER 5:
Phase Behaviour of Binary FAME + CO_2 Systems

Binary HPBDP data were measured for three FAME + CO_2 systems containing the C_{18}-series methyl esters with varying degrees of unsaturation. Chapter 5 presents the measured data for each system, comparing it to available literature data. This is followed by a comparison of the three systems with each other, and the presentation of a hypothesis to explain the observed behaviour.

5.1. Methyl Stearate + CO_2

Phase transition data for the M18:0 (1) + CO_2 (2) system is shown in Figure 5.1. The data table and P-T correlations can be found in Appendix D.1. It can be seen that the phase transition pressure increases monotonically with an increase in temperature, as expected from literature. It can also be seen that the measured data shows good agreement with the literature data,[65] addressing the gap in the critical region that was present in literature.
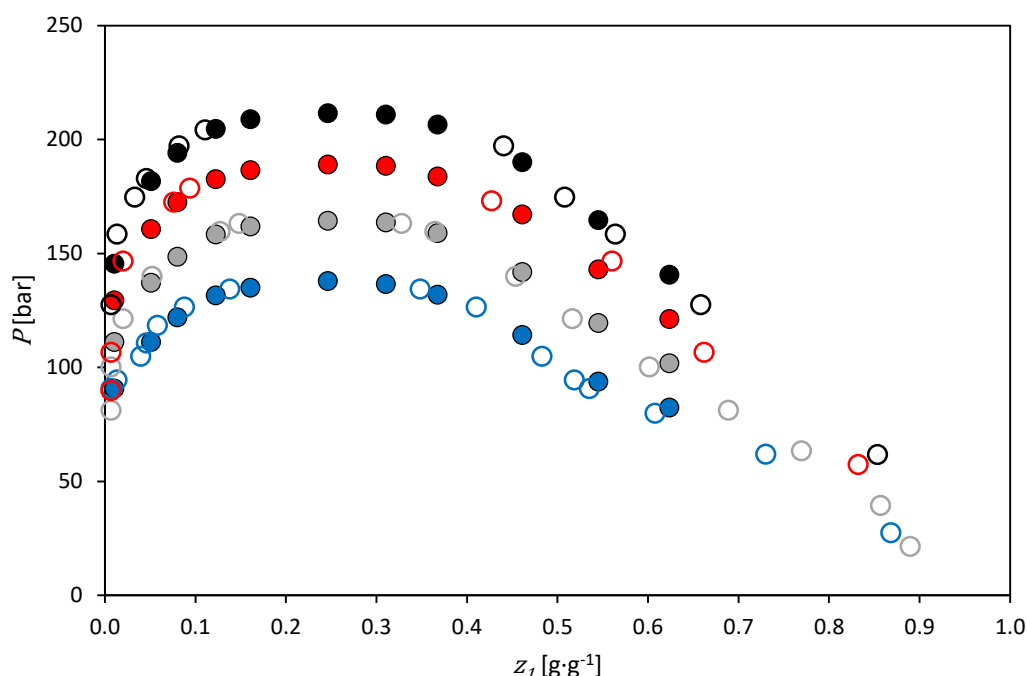
Figure 5.1: Phase transition pressures (P) as a function of solute mass fraction (z_1) at various temperatures (T) for the M18:0 (1) + CO₂ (2) system. This work: (●) T = 40 °C; (●) T = 50 °C; (●) T = 60 °C; (●) T = 70 °C. Literature: (○) Inomata et al.[65] u_{min} (z_1) = 0.0001 g·g⁻¹ and u_{max}(z_1) = 0.0056 g·g⁻¹; u_{min}(P) = 0.7 bar and u_{max}(P) = 1.8 bar; error bars are smaller than markers.

5. Phase Behaviour of Binary FAME + CO$_2$ Systems

It can also be seen from Figure 5.1 that at 40 °C there is a slight inflection in the solubility curve close to z_1 = 0.55 g·g^{-1}, particularly when compared to the data at higher temperatures, which exhibit a more linear trend in this region. This inflection is even more prominent at 35 °C where the data were originally measured. This supports the observation of Staby et al.[27] that fish oil FAE + CO$_2$ systems have an UCEP (disappearance of a VLLE region) above ambient temperature close to the critical temperature of CO$_2$ of 31 °C. It would thus not be optimal to run a SCFF column at temperatures below 35 °C, as the presence of three phases in the column could interfere with the operation.

5.2. Methyl Oleate + CO$_2$

Phase transition data for the M18:1 (1) + CO$_2$ (2) system is shown in Figure 5.2. The data table and P-T correlations can be found in Appendix D.1. This system exhibits the same behaviour as the M18:0 + CO$_2$ system with regards to the influence of temperature, and agrees well with the data measured by Inomata et al.,[65] Crampon et al.,[75] and Yu et al.[73] The data measured by Zou et al.,[72] Chang et al.,[74] and Fang et al.[45] deviate strongly from the other author's data and that measured in this work, as discussed in section 3.3.1.
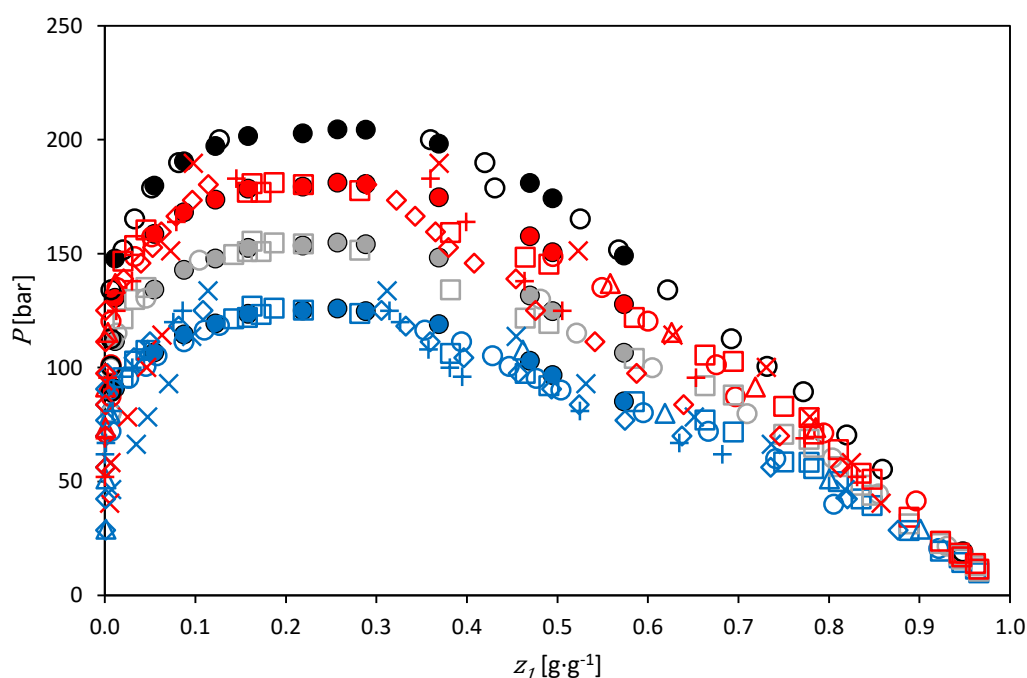
Figure 5.2: Phase transition pressures (P) as a function of solute mass fraction (z_1) at various temperatures (T) for the M18:1 (1) + CO$_2$ (2) system. This work: (●) T = 40 °C; (●) T = 50 °C; (●) T = 60 °C; (●) T = 70 °C. Literature: (○) Inomata et al.[65]; (□) Crampon et al.[75]; (Δ) Yu et al.[73]; (X) Zou et al.[72]; (◊) Chang et al.[74]; (+) Fang et al.[45]. u_{min} (z_1) = 0.0001 g·g^{-1} and $u_{max}(z_1)$ = 0.0051 g·g^{-1}; $u_{min}(P)$ = 0.7 bar and $u_{max}(P)$ = 1.8 bar; error bars are smaller than markers.

5.3. Methyl Linoleate + CO$_2$

Phase transition data for the M18:2 (1) + CO$_2$ (2) system is shown in Figure 5.3. The data table and P-T correlations can be found in Appendix D.1. It can be seen that the data follows a similar trend and shape as the M18:0 + CO$_2$ data, and agrees well with the limited amount of data measured by Adams et al.[76] The data from Chang et al.[74] deviates strongly from the observed trends on the bubble point curve, and the data from Zou et al.[72] tends to deviate on the dew point curve. These authors' data have been identified to consistently deviate from that measured by other authors as well as the data measured in this work. Given the rigorous approach to the calculation of experimental uncertainty in this work, it is believed that the data measured here is acceptably accurate. The data measured for the M18:2 + CO$_2$ system in this work thus reinforces the data measured by Adams et al. and expands it over a wider temperature range, with more points in the critical region.
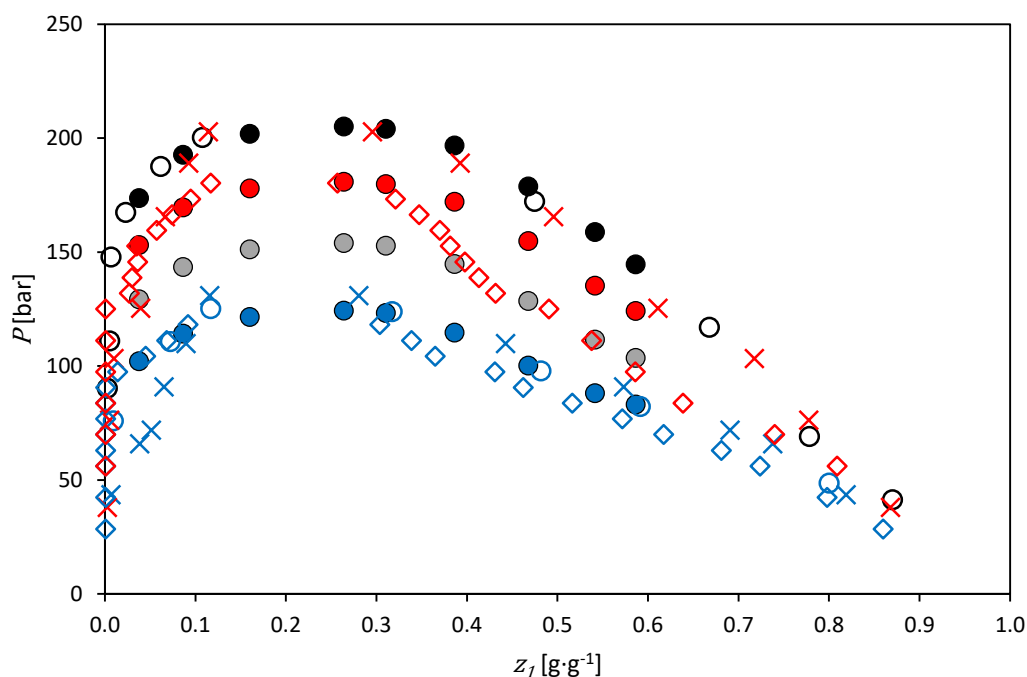
Figure 5.3: Phase transition pressures (P) as a function of solute mass fraction (z_1) at various temperatures (T) for the M18:2 (1) + CO$_2$ (2) system. This work: (●) T = 40 °C; (●) T = 50 °C; (●) T = 60 °C; (●) T = 70 °C. Literature: (O) Adams et al.[76]; (X) Zou et al.[72]; (◊) Chang et al.[74] u_{min} (z_1) = 0.0003 g·g^{-1} and $u_{max}(z_1)$ = 0.0048 g·g^{-1}; $u_{min}(P)$ = 0.7 bar and $u_{max}(P)$ = 1.8 bar; error bars are smaller than markers.

5.4. Comparison of Binary Data

An initial step in determining whether components can be fractionated with a supercritical fluid, is to compare binary solubility data in the relevant supercritical fluid. Ignoring possible solute-solute interactions, this can provide a qualitative indication of mixture fractionation potential. It can also highlight regions of interest for further study of mixture phase behaviour. The binary HPBDP data

5. Phase Behaviour of Binary FAME + CO_2 Systems

measured in this work for M18:0, M18:1, and M18:2 in CO_2 are compared at 35 °C and 75 °C in Figure 5.4.
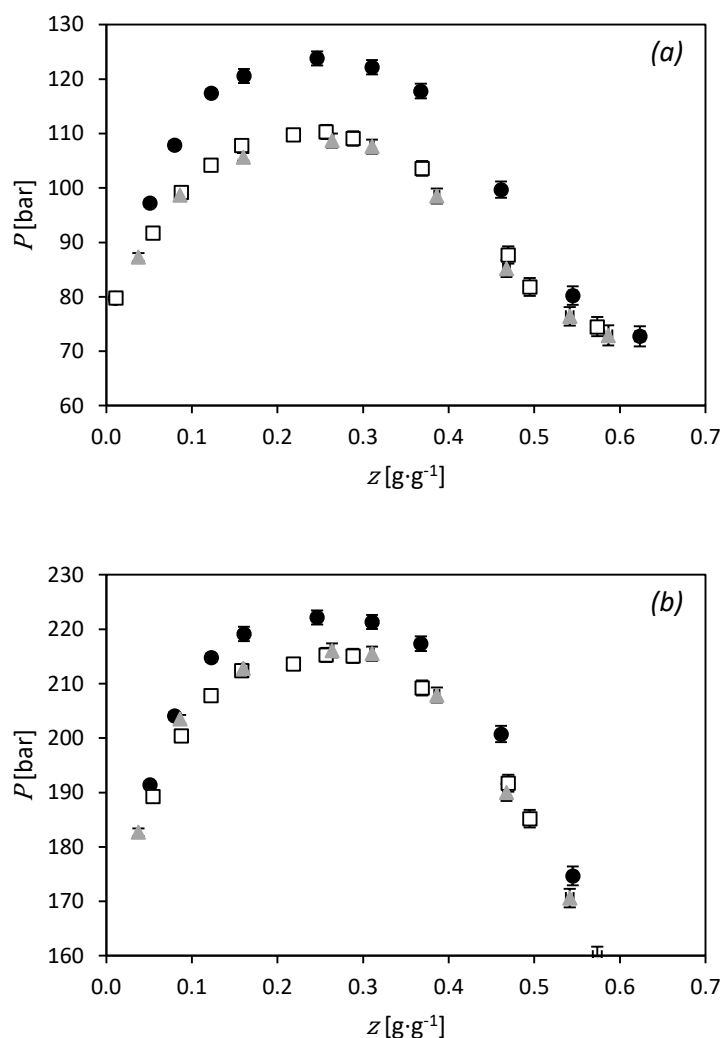
Figure 5.4: Comparison of the phase transition pressures (P) as a function of the solute mass fraction (z) of M18:0, M18:1, and M18:2 in CO_2. (a) T = 35 °C; (b) T = 75 °C. (●) M18:0; (□) M18:1; (▲) M18:2.

In the temperature range 35 – 75 °C, the phase behaviour of M18:1 and M18:2 shows no solubility differences within the experimental uncertainty of 1.8 bar. There is, however, a noticeable difference in solubility between the saturated M18:0 and the two unsaturated FAMEs. The maximum solubility difference is about 10 bar in the critical region at 35 °C, and decreases as the solute fraction z moves away from the critical region. As the temperature increases, the solubility difference decreases.

The observed solubility differences can potentially be explained by investigating the intermolecular forces and steric effects present in the systems. Linear long-chain saturated hydrocarbons tend to experience a correlation of molecular order (CMO) – molecules will orient themselves with nearby molecules to ensure better energetic contact, resulting in stronger attractive forces due to the smaller

distance between molecules.[97] Molecules experiencing the CMO-effect thus have high packing densities. This CMO-effect decreases with increasing temperature and increases with increasing chain length.[98]

Conversely, the presence of *cis* C=C bonds in a hydrocarbon backbone causes a reduced rotational degree of freedom (rotation about the π-bond would break it),[99] and an increased molecular cross-sectional area (due to the bend induced in the molecule by the *cis* C=C bond)[15], which results in weaker attractive forces as a result of the increased distance between molecules.[100] Molecules with *cis* C=C bonds thus have lower packing densities than their saturated counterparts.

The weakening of attractive forces does not take place in the case of *trans* C=C bonds. A *trans* C=C bond does not introduce a bend in the hydrocarbon chain of the molecule,[22] and thus does not influence the packing density and attractive forces to the extent that a *cis* C=C bond does, since the *trans* isomer will behave more like the saturated form of the molecule.[4]

FAEs are long-chain compounds, particularly the high-value FAEs found in fish oils (generally in the C_{14} – C_{22} range).[7] The majority of these compounds are thus made up of a hydrocarbon chain as opposed to the relatively small ester functional group. This means that dispersion forces are the most important intermolecular force for FAEs, and that the CMO arguments developed for alkanes can potentially be applied to them.

The CMO-argument can be supported by inspecting the melting point data for some C_{18} FAMEs, shown in Figure 5.5. As the number of *cis* C=C bonds – or the degree of unsaturation – increases, the melting point temperature decreases. This is due to the steric effect of the *cis* C=C bonds resulting in weaker attractive forces and a reduced packing density of the molecules, resulting in a lower energy barrier to the solid-liquid transition.[100] The lack of any C=C bonds in M18:0, coupled with the CMO-effect, results in a high packing density of the molecules, leading to a higher energy barrier to the solid-liquid transition, and a higher melting point temperature.

5. Phase Behaviour of Binary FAME + CO_2 Systems
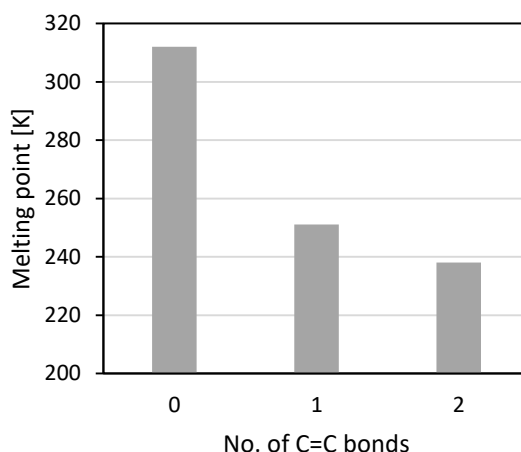
Figure 5.5: Melting points of the C_{18} FAMEs as a function of the number of the cis *C=C bonds in the hydrocarbon backbone. Data from Lide.[25]*

It is believed that a similar CMO-argument can be used to explain the phase behaviour of the C_{18} FAMEs in supercritical CO_2. M18:0 has consistently higher phase transition pressures than the unsaturated C_{18} FAMEs. The CMO-effect and resultant high packing density could cause M18:0 to resist being dissolved by CO_2 due to the stronger attractive forces, whereas the steric effect and resultant low packing density of M18:1 and M18:2 may facilitate their dissolution in CO_2 when compared to a saturated FAME.

Why does M18:2 not have lower phase transition pressures than M18:1, despite having a larger molecular cross-sectional area and lower packing density? Considering the melting point data in Figure 5.5 again, it can be seen that the transition from saturated to monounsaturated results in a 60.9 K reduction in the melting point temperature. The addition of another C=C bond results in only a 13.1 K reduction in the melting point temperature. This suggests that the effect of a reduced packing density in the transition from monounsaturated to polyunsaturated is not as large as the effect of the loss of the CMO and subsequent large drop in the packing density in the transition from saturated to unsaturated. Thus, supercritical CO_2 cannot distinguish between M18:1 and M18:2 to the degree that it can distinguish between M18:0 and the unsaturated FAMEs.

The solubility difference between M18:0 and the unsaturated FAMEs is dependent on temperature, decreasing as the temperature increases. At higher temperatures the CMO-effect on M18:0 would be reduced, lowering the phase transition pressures relative to M18:1 and M18:2, and narrowing the solubility difference.

Figure 5.6 shows a plot of the phase transition pressures for the homologous series of saturated ethyl esters in supercritical CO_2 as a function of hydrocarbon chain length N_C at a constant ester fraction of 0.16 mol·mol^{-1} and a constant temperature of T = 40 °C. It can be seen that the phase transition pressure increases with a slightly increasing gradient as N_C increases.

A higher transition pressure indicates an increased resistance of solute molecules to being dissolved by solvent molecules (or a decreased solubility). Stronger intermolecular forces between solute molecules can decrease this solubility. Dispersion forces increase with increasing chain length, which accounts for the increasing pressure with increasing chain length. However, dispersion forces increase linearly with chain length.[101]

Assuming that the phase transition pressure is an indication of the intermolecular forces holding molecules together in the condensed state, there must be an additional contribution to cause the nonlinear trend observed. The CMO-effect could account for this. As the molecular order increases with increasing chain length, it would contribute increasingly to the attractive forces, resulting in higher phase transition pressures. This would explain the increasing gradient trend observed in Figure 5.6. A similar trend in the phase transition pressure was observed by Schwarz[102] for the C_{10} to C_{16} ethyl esters at higher temperatures. This investigation into the homologous series of alkyl esters further supports the hypothesis of the CMO explaining the phase behaviour of the C_{18} FAMEs.
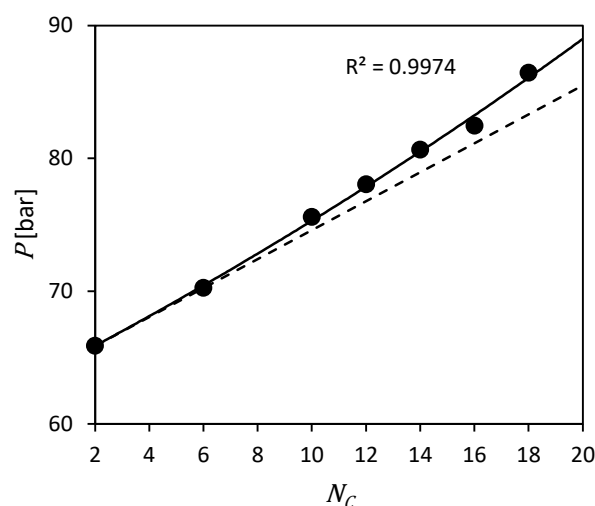
Figure 5.6: Plot of phase transition pressure (P) at a constant ester mole fraction of 0.16 mol·mol^{-1} and temperature T = 40 °C for saturated ethyl ester (1) + CO₂ (2) systems as a function of the number of carbon atoms in the hydrocarbon backbone (N_C). The solid curve represents a trendline with an increasing gradient. The dashed line represents a straight line between the two data points with the lowest N_C. Data from Borges et al.,[103] Hwu et al.,[104] Schwarz,[102] Crampon et al.,[75] and Bharath et al.,[78] with consultation of the data review collections by Dohrn and coworkers[105–107]

The influence of the solvent-solute interactions on the phase behaviour was investigated by calculating dipole-quadrupole potentials Γ_{12} for the pairs M18:0 (1) + CO₂ (2) and M18:1 (1) + CO₂ (2), after Equation 5.1[101]:

$$\Gamma_{12} = -\frac{\mu_1^2 Q_2^2}{kT(4\pi\varepsilon_0)^2 r^8}$$

5.1

5. Phase Behaviour of Binary FAME + CO$_2$ Systems

where μ_1 is the dipole moment of component 1, Q_2 is the quadrupole moment of component 2, k = 1.38e-23 J·K^{-1} is Boltzmann's constant, T is the absolute temperature, ε_0 = 8.854e-12 C^2·J^{-1}·m^{-1} is the dielectric permittivity of vacuum, and r is the intermolecular distance.

The results of the calculations are shown in Table 5.1. It can be seen that Γ_{12} for the two molecule pairs are very similar, particularly when considering the calculated uncertainty in Γ_{12} for the M18:0 + CO$_2$ pair, which was found to be 0.04e-96$\frac{1}{r^8}$, as propagated from the uncertainty in $\mu_{M18:0}$. This suggests that the intermolecular interactions between CO$_2$ and saturated FAMEs, and CO$_2$ and FAMEs containing C=C bonds are not meaningfully different, and are thus unlikely to be responsible for the observed phase behaviour differences.

Table 5.1: Calculation of dipole-quadrupole potentials between C$_{18}$ FAMEs and CO$_2$ at T = 298 K. Data from Exner & Bapcum,[108] Abboud & Notario[109] via Stenutz,[110] and Gray & Gubbins.[111]

Quantity	M18:0 (1) + CO$_2$ (2)	M18:1 (1) + CO$_2$ (2)
μ_1 [C·m]	5.20e-30	5.34e-30
Q_2 [C·m^2]	-1.43e-39	-1.43e-39
$\Gamma_{12}(r)$ [J]	-1.09e-96$\frac{1}{r^8}$	-1.15e-96$\frac{1}{r^8}$

It is expected that similar differences in the phase behaviour between saturated and unsaturated FAMEs would be observed for other longer-chain esters slightly below and above the C$_{18}$ esters, due to the similar natures of the systems and the similar differences in their geometries. It is possible that CO$_2$ may start to distinguish between unsaturated FAMEs where the difference in the degree of unsaturation exceeds that between M18:1 and M18:2.

5.5. Summary

Without taking solute interactions into account, it appears that supercritical CO$_2$ cannot distinguish between monounsaturated FAMEs and polyunsaturated FAMEs of equal chain length. This suggests that supercritical carbon dioxide would not be able to fractionate equal-length unsaturated FAMEs from each other. Contrastingly, supercritical carbon dioxide can distinguish between saturated and unsaturated FAMEs of equal chain length, albeit at a diminished capacity at higher temperatures. This suggests that supercritical carbon dioxide may be able to fractionate equal-length saturated and unsaturated FAMEs. Further study into mixture phase behaviour is warranted in order to quantify the solubility difference and evaluate the separation feasibility.

CHAPTER 6:
Phase Behaviour of the Methyl Stearate + Methyl Oleate + CO_2 System

In Chapter 5, it was shown that there is a solubility difference between M18:0 and M18:1 in supercritical CO_2. This was further investigated by the measurement and analysis of ternary phase behaviour data for this system. Chapter 6 discusses the measured ternary HPBDP data and how the presence of both esters influence the phase behaviour, the measured ternary VLE data and relative solubility trends, and ends with comments on the experimental challenges associated with the measurement of phase equilibrium data for highly asymmetric systems.

6.1. Ternary HPBPDP Data

Ternary HPBPDP data were measured for three M18:0 (1) + M18:1 (2) + CO_2 (3) systems, each with a different reduced mass fraction M18:0 on a solvent-free basis, w_1^{red}. The data tables and unprocessed data can be found in Appendix D, and a detailed discussion of the uncertainty can be found in Appendix C.

A comparison of the three ternary systems with each other and with the binary data at 35 °C is presented in Figure 6.1 at w_1^{red} = 0, 0.237, 0.501, 0.772, and 1 g·g^{-1}. It can be seen that as w_1^{red} increases from zero to one, there is a general trend of an increase in the phase transition pressure. The same trend was found at higher temperatures, but is more difficult to observe visually since the solubility difference of M18:0 and M18:1 decreases with increasing temperature. This means that the experimental uncertainty can increasingly obscure the trend as the proximity of the phase transition pressure curves increases. The investigated systems do not exhibit any cosolvency in the measured conditions, as the phase transition pressures of the mixtures lie between that of the pure components. This suggests an absence of solute-solute interactions that would give rise to complex phase behaviour.

6. Phase Behaviour of the Methyl Stearate + Methyl Oleate + CO_2 System
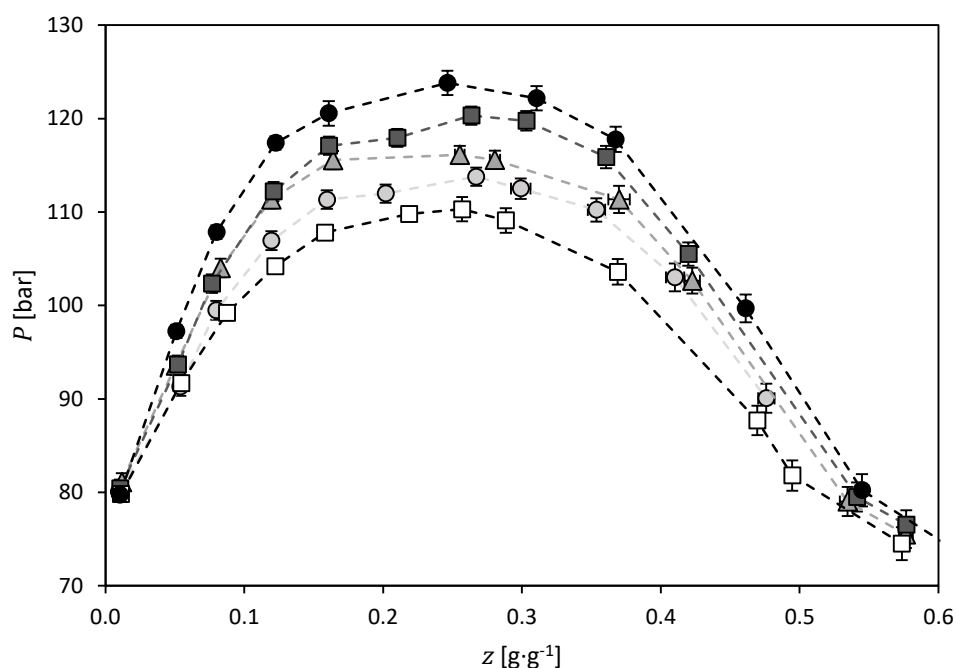
Figure 6.1: Comparison of the phase transition pressures (P) as a function of the total solute fraction (z) for M18:0 (1) and M18:1 (2) mixtures in CO_2 (3) measured in this work at 35 °C. ($\square$) w_1^{red} = 0 g·g⁻¹; ($\bullet$) w_1^{red} = 0.237 g·g⁻¹; ($\triangle$) w_1^{red} = 0.501 g·g⁻¹; ($\blacksquare$) w_1^{red} = 0.772 g·g⁻¹; ($\bullet$) w_1^{red} = 1 g·g⁻¹. Data points are connected with lines as a guide for the eye.

The observations made from Figure 6.1 can be further investigated by plotting the phase transition pressure versus w_1^{red} at different temperatures and total solute fractions z. These plots are provided in Figure 6.2 for three different values of z, corresponding to vapour-like (z = 0.1 g·g⁻¹), liquid-like (z = 0.5 g·g⁻¹), and critical regions (z = 0.3 g·g⁻¹). The plots for T = 35 °C are highlighted for a clearer indication of the observed trend, since this is the temperature where the largest solubility difference between M18:0 and M18:1 was observed. It can be seen, as in Figure 6.1, that the phase transition pressure of the mixture increases with increasing M18:0 content with a reasonably linear trend.
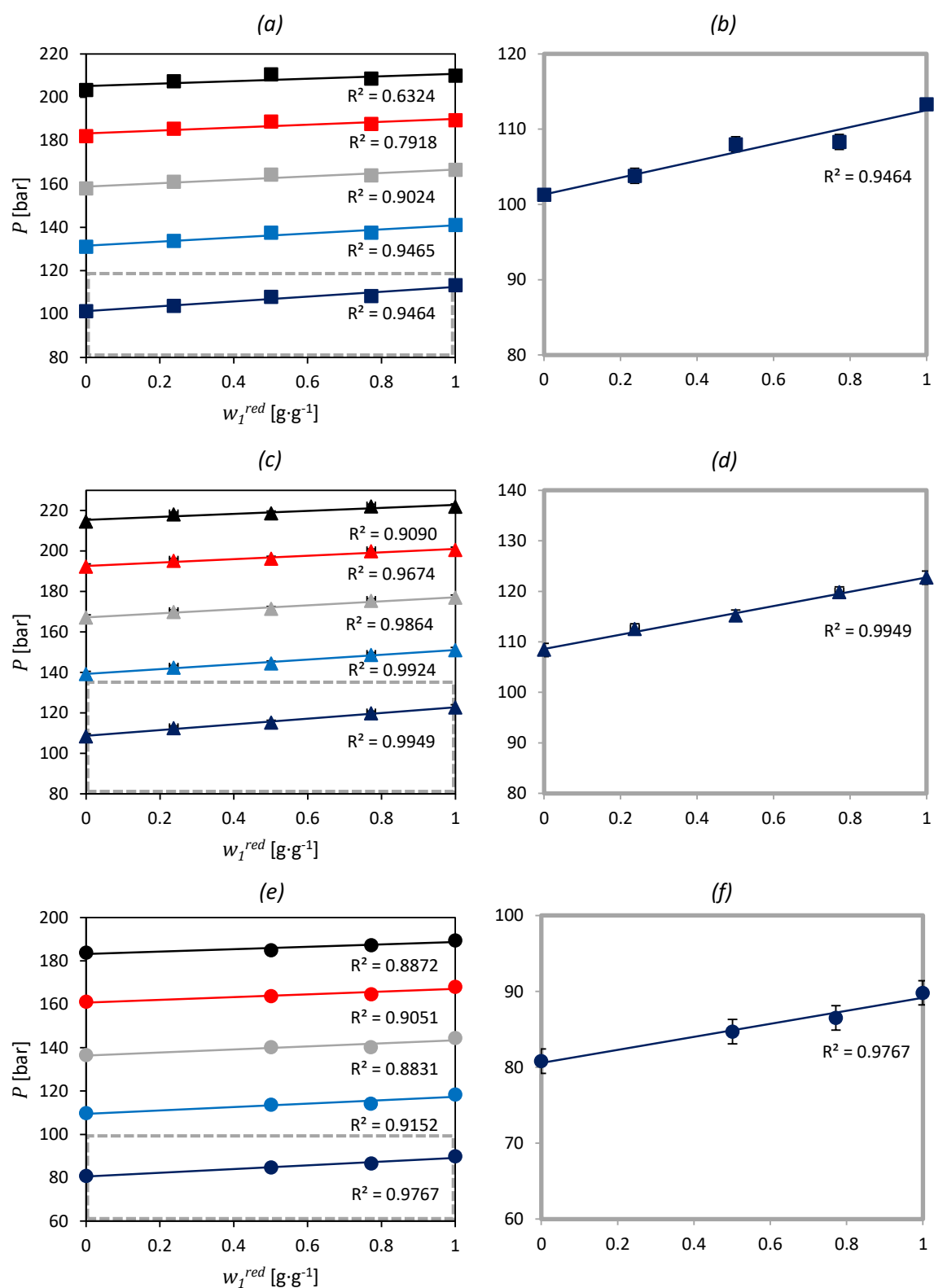
Figure 6.2: Plots of the phase transition pressure (P) as a function of solvent-free mass fraction M18:0 (w_1^{red}) for the ternary M18:0 (1) + M18:1 (2) + CO_2 (3) system. (a) z = 0.1 g·g^{-1}; (c) z = 0.3 g·g^{-1}; (e) z = 0.5 g·g^{-1}. (b), (d), and (f) provide enlarged sections of (a), (c), and (d) respectively. Temperatures investigated: (●) T = 308 K; (●) T = 318 K; (●) T = 328 K; (●) T = 338 K; (●) T = 348 K.

6. Phase Behaviour of the Methyl Stearate + Methyl Oleate + CO_2 System

The ternary HPBDP data indicate that a mixture of M18:0 and M18:1 is always more soluble in supercritical CO_2 than pure M18:0, and always less soluble than pure M18:1. This is likely due to the CMO-effect discussed in Section 5.4. It is possible for a molecule like M18:1 to have a steric effect on the CMO of M18:0 due to its larger molecular cross-sectional area and lower packing density.[97]

M18:1 could thus break the CMO between the M18:0 molecules by shielding them from each other and preventing them from orienting themselves and packing closely. This results in weaker attractive forces between the components in the mixture, decreasing the resistance of M18:0 to being dissolved. The result is a lower phase transition pressure for the mixture. This effect also places an upper limit on the solubility. A given mixture of M18:0 and M18:1 cannot have a higher solubility (lower phase transition pressure) than pure M18:1, since the presence of M18:1 cannot reduce the packing density of the mixture beyond the case of there being only M18:1. This is in agreement with the observations in Figure 6.2, as the phase transition pressure increases monotonically as the M18:1-content decreases.

6.2. Ternary VLE Data

Investigation of the measured ternary HPBDP data indicated that steric effects and the correlation of molecular order likely influence the phase behaviour of the M18:0 (1) + M18:1 (2) + CO_2 (3) system. HPBDP data, however, does not provide information on the distribution of solutes between the vapour and liquid phases.

To that end, VLE data were measured for the ternary system to investigate the FAME distribution between coexisting phases at temperatures of 35 °C, 55 °C, and 75 °C respectively. Four pressures were investigated for each temperature, with the exception of 75 °C, since reliable sampling became impractical at the highest pressure. This will be discussed further in Section 6.3. Pressures were selected to be in the region where the largest solubility differences between the binary systems were observed, ranging from pressures below to slightly above the total solubility pressure of M18:1 at each temperature. The loaded feed mixture had an approximate composition of w_1^{red} = 0.5 g·g⁻¹. The tabulated tie-line data can be found in Appendix D, and a detailed discussion of the experimental uncertainty can be found in Appendix C.

The measured VLE data and bubble-point and dew-point curves determined from the HPBDP data are presented in Figures 6.3 to 6.5. It can be seen that the experimentally determined tie-lines compare well with the measured dew-point curves.
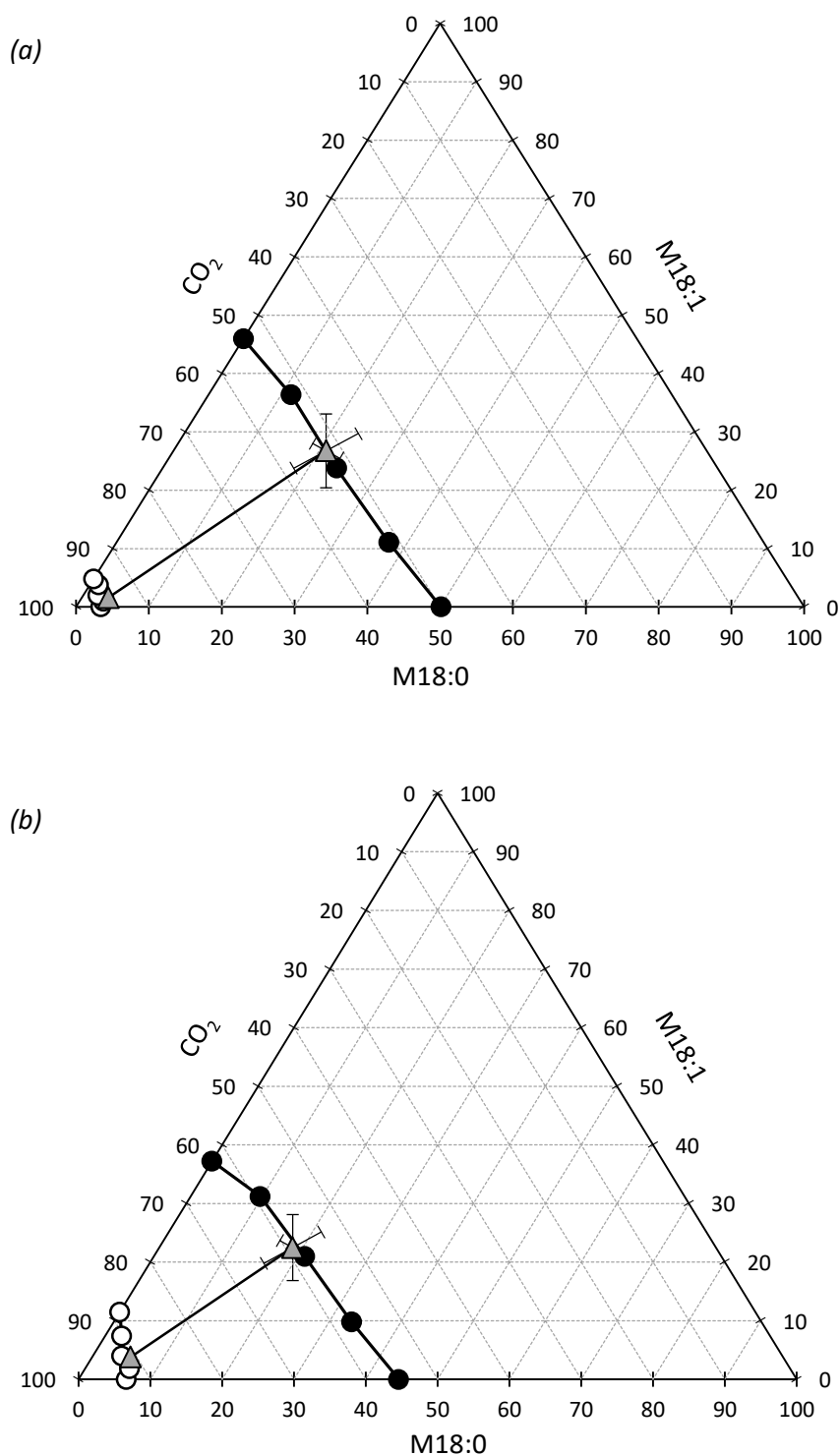
Figure 6.3: Ternary VLE data in weight percent for the M18:0 (1) + M18:1 (2) + CO$_2$ (3) system at 35 °C. (●) Bubble-point curve compiled from HPBDP data measured in this work; (○) Dew-point curve compiled from HPBDP data measured in this work; (▲) VLE tie-line measured in this work. (a) P = 90.0 bar; (b) P = 103.4 bar; (c) P = 110.4 bar; (d) P = 113.1 bar. Uncertainties are of similar size to markers where not visible. (Continues…).

6. Phase Behaviour of the Methyl Stearate + Methyl Oleate + CO₂ System
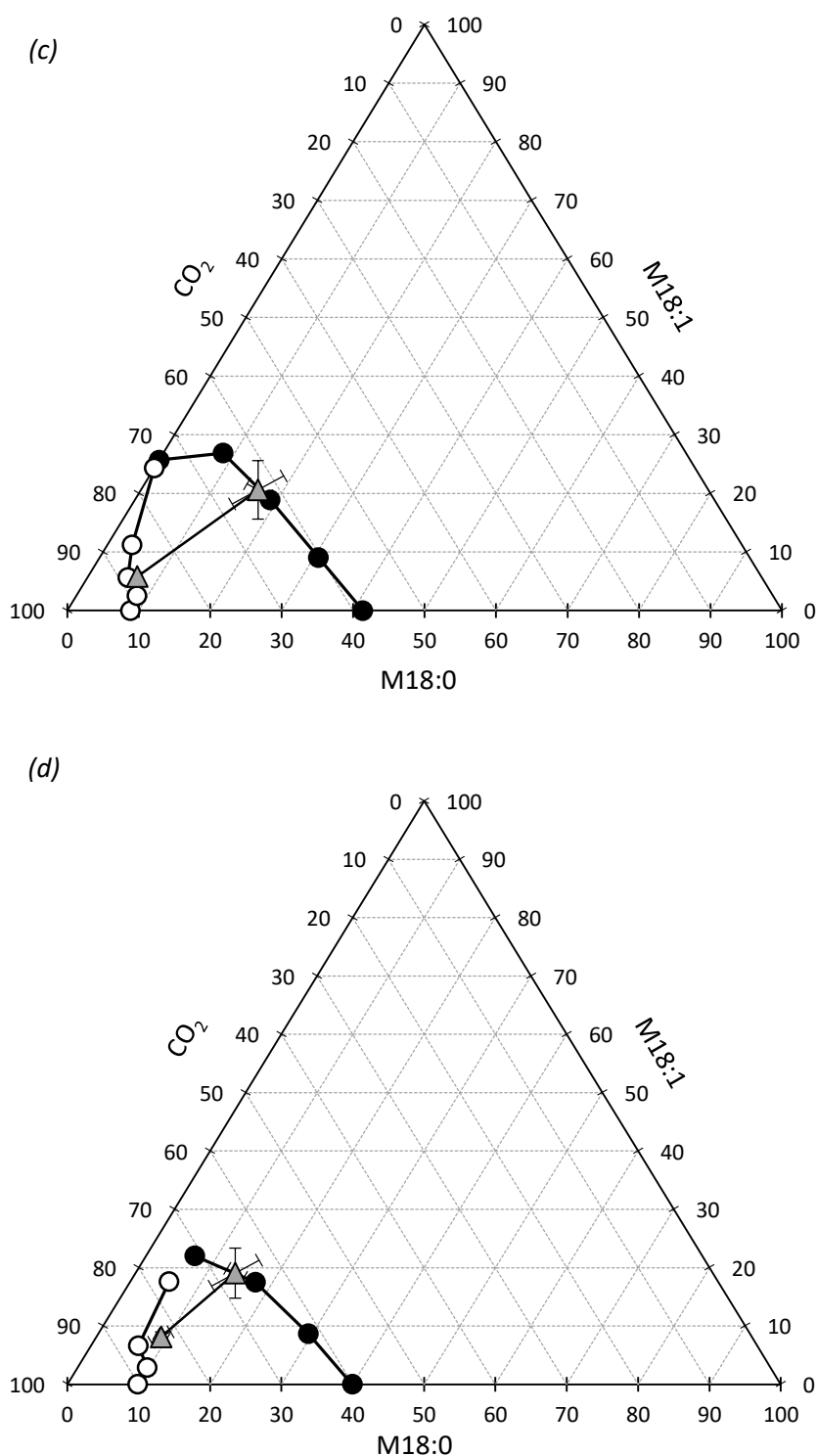
Figure 6.3(continued): Ternary VLE data in weight percent for the M18:0 (1) + M18:1 (2) + CO₂ (3) system at 308 K. (●) Bubble-point curve compiled from HPBDP data measured in this work; (O) Dew-point curve compiled from HPBDP data measured in this work; (▲) VLE tie-line measured in this work. (a) P = 90.0 bar; (b) P = 103.4 bar; (c) P = 110.4 bar; (d) P = 113.1 bar. Uncertainties are of similar size to markers where not visible.
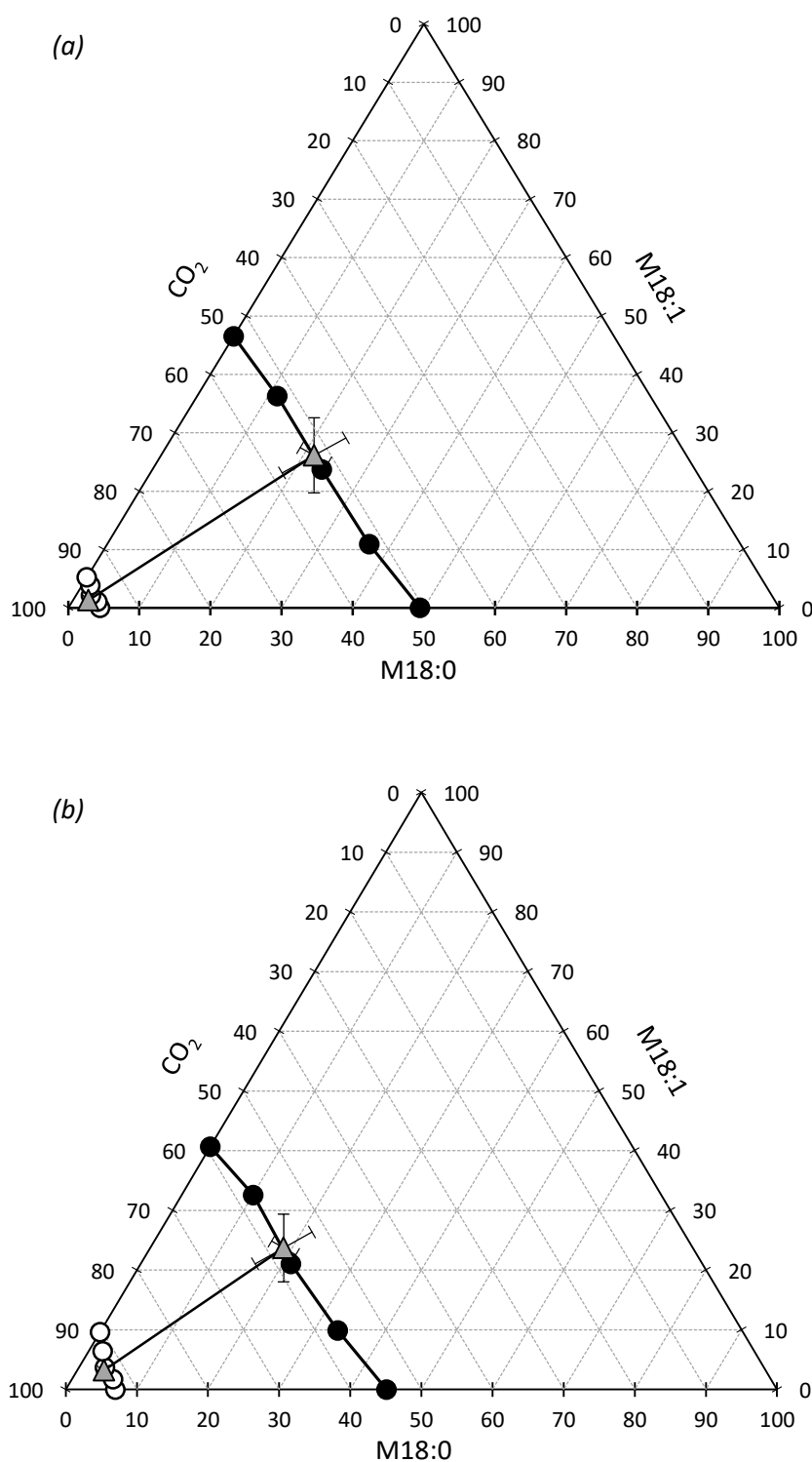
Figure 6.4: Ternary VLE data in weight percent for the M18:0 (1) + M18:1 (2) + CO₂ (3) system at 328 K. (●) Bubble-point curve compiled from HPBDP data measured in this work; (○) Dew-point curve compiled from HPBDP data measured in this work; (▲) VLE tie-line measured in this work. (a) P = 146.1 bar; (b) P = 157.4 bar; (c) P = 165.9 bar; (d) P = 168.5 bar. Uncertainties are of similar size to markers where not visible. (Continues…).

6. Phase Behaviour of the Methyl Stearate + Methyl Oleate + CO$_2$ System
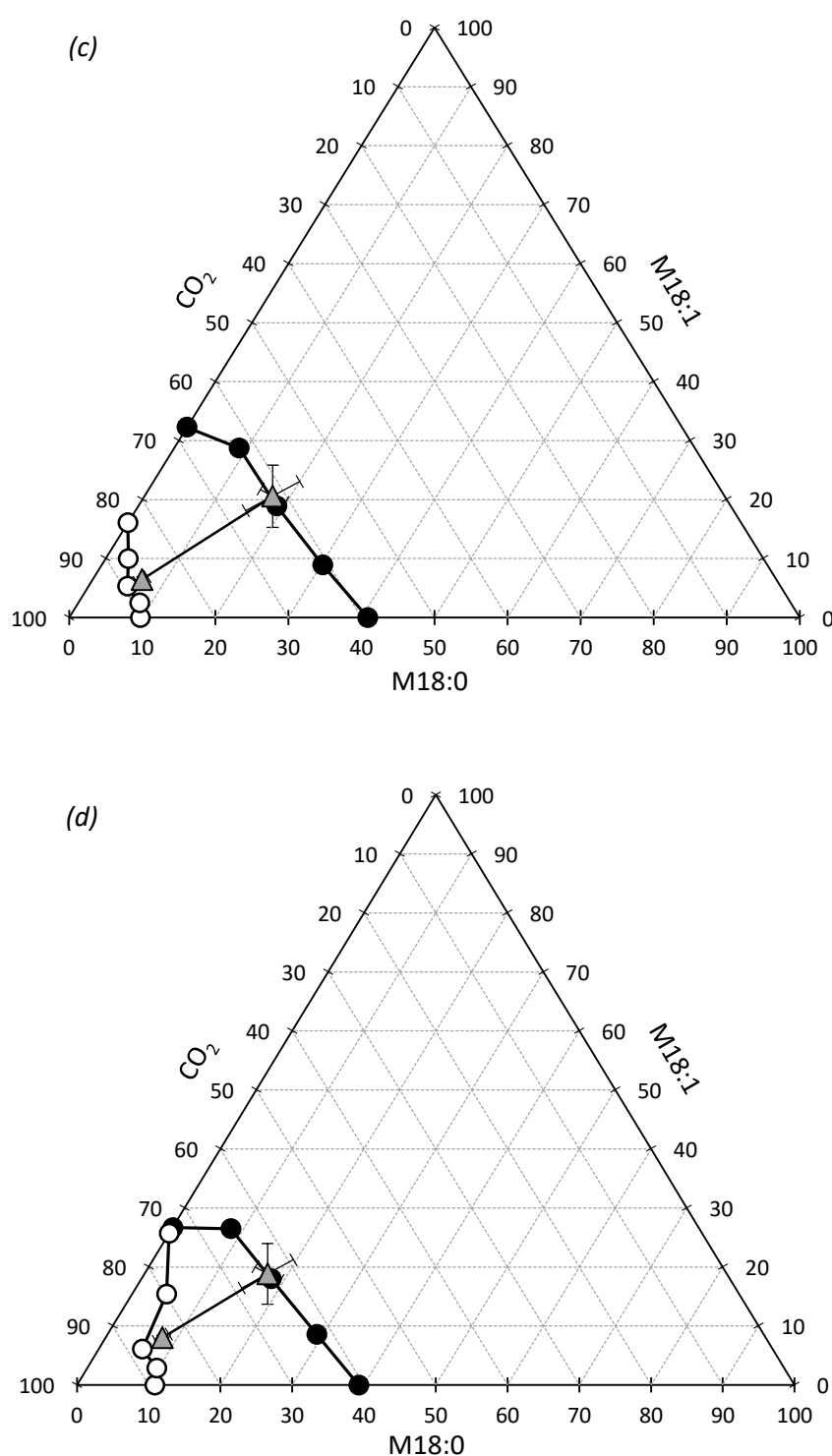
Figure 6.4(continued): Ternary VLE data in weight percent for the M18:0 (1) + M18:1 (2) + CO$_2$ (3) system at 328 K. (●) Bubble-point curve compiled from HPBDP data measured in this work; (○) Dew-point curve compiled from HPBDP data measured in this work; (▲) VLE tie-line measured in this work. (a) P = 146.1 bar; (b) P = 157.4 bar; (c) P = 165.9 bar; (d) P = 168.5 bar. Uncertainties are of similar size to markers where not visible.
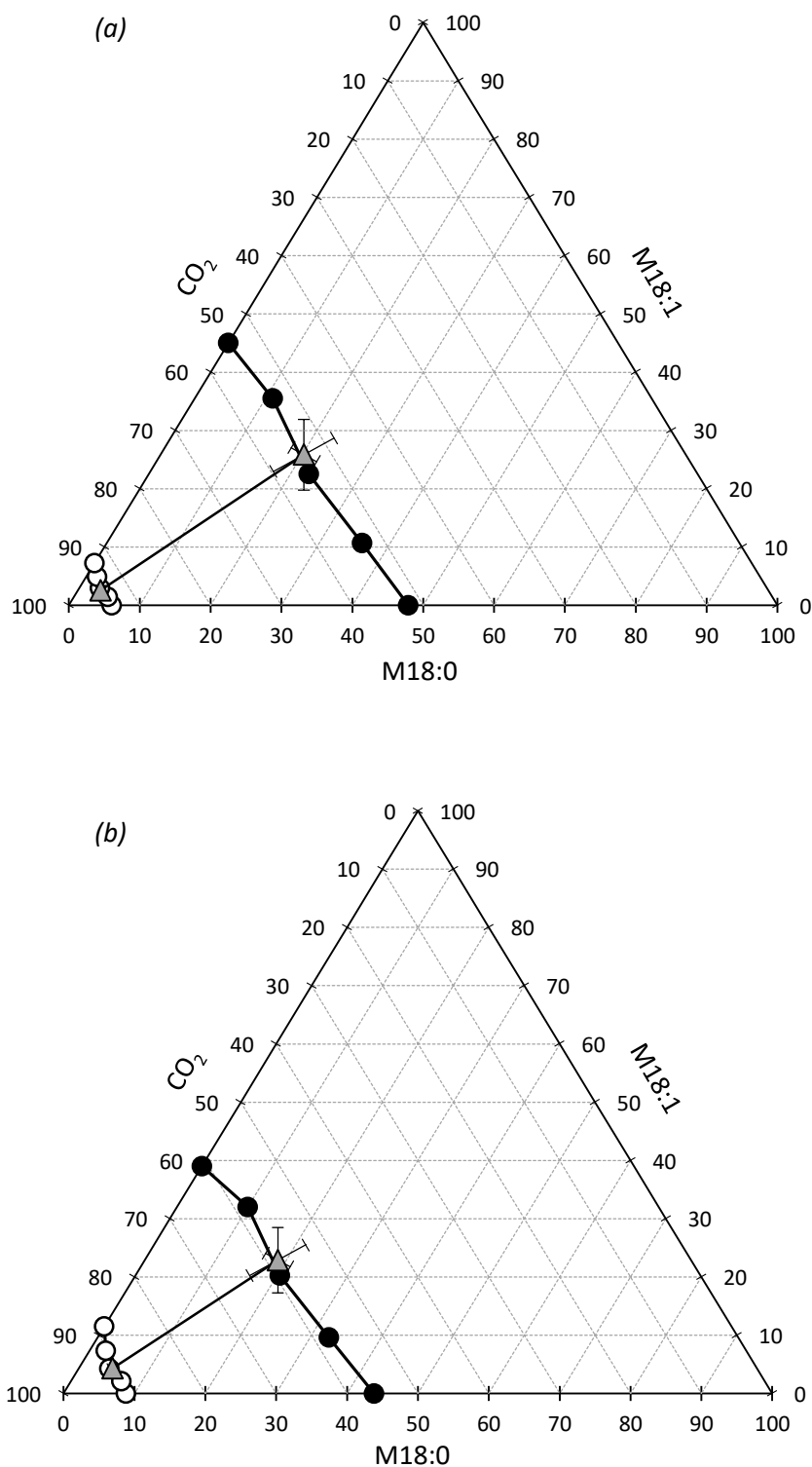
Figure 6.5: Ternary VLE data in weight percent for the M18:0 (1) + M18:1 (2) + CO₂ (3) system at 348 K. (●) Bubble-point curve compiled from HPBDP data measured in this work; (○) Dew-point curve compiled from HPBDP data measured in this work; (▲) VLE tie-line measured in this work. (a) P = 196.2 bar; (b) P = 206.6 bar; (c) P = 214.3 bar. Uncertainties are of similar size to markers where not visible. (Continues…).

6. Phase Behaviour of the Methyl Stearate + Methyl Oleate + CO₂ System
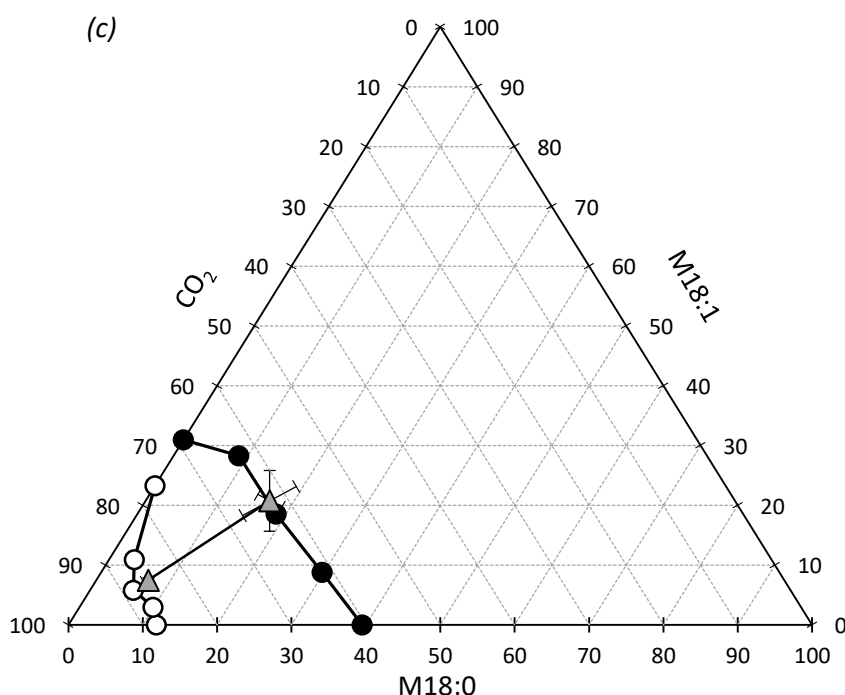
Figure 6.5(continued): Ternary VLE data in weight percent for the M18:0 (1) + M18:1 (2) + CO₂ (3) system at 348 K. (●) Bubble-point curve compiled from HPBDP data measured in this work; (○) Dew-point curve compiled from HPBDP data measured in this work; (▲) VLE tie-line measured in this work. (a) P = 196.2 bar; (b) P = 206.6 bar; (c) P = 214.3 bar. Uncertainties are of similar size to markers where not visible.

Inspection of Figures 6.3 to 6.5 confirms the absence of complex ternary phase behaviour under the conditions investigated, as it can be seen that the isobaric-isothermal plots are similar in appearance to the simple phase behaviour described in section 3.1.2.1 where the solutes have ideal interactions. This confirms the hypothesis in section 3.1.2.1 that unsaturation does not lead to sufficiently dissimilar interactions in FAEs to cause pressure minima or maxima in the ternary critical curves.

It can also be seen that, at constant temperature, an increase in pressure leads to an increase in the FAME-content of the vapour phase, and an increase in the CO_2-content of the liquid-phase, resulting in a smaller two-phase region. This is due to the increase in density at higher pressures causing the system to near the critical pressure, where the similar densities cause the two phases to merge into one phase.

The phase envelope gradually pulls away from the M18:1 + CO_2 axis as the pressure increases. This happens when the mixture critical pressure of pure M18:1 in CO_2 is exceeded, since the M18:1 + CO_2 binary has a lower mixture critical pressure than the M18:0 + CO_2 binary.

The relative solubility α_{12} (as defined in section 2.8) can be used to evaluate the separability of the M18:0 (1) + M18:1 (2) + CO_2 system.

Figure 6.6 provides the relative solubility data as a function of pressure for the measured VLE data. There is a trend of the relative solubility decreasing down to one with increasing pressure – a result of the approach to the mixture critical pressure, as was observed in Figures 6.3 to 6.5. It can also be seen that all the calculated α_{12}-values are greater than one. This indicates that, according to the measured VLE data, M18:0 is preferentially extracted into the vapour phase relative to M18:1.
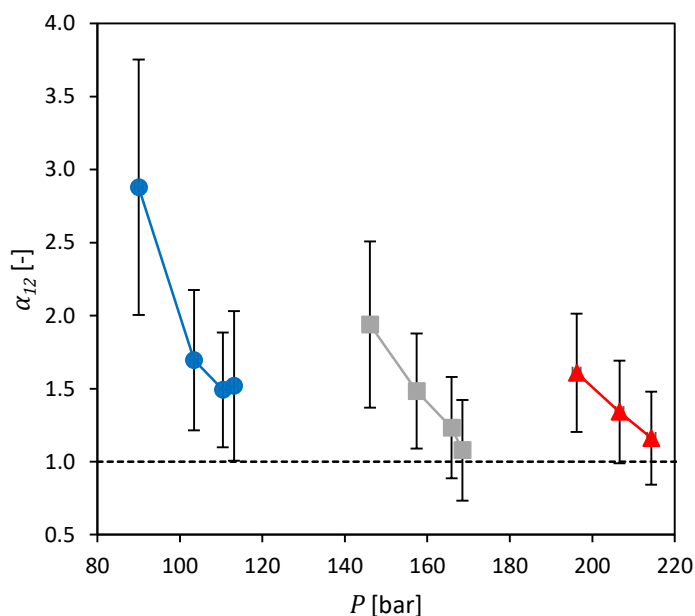
Figure 6.6: Relative solubility (α_{12}) as a function of pressure (P) for the M18:0 (1) + M18:1 (2) + CO_2 (3) system as calculated from the measured VLE data in this work. (●) T = 35 °C; (■) T = 55 °C; (▲) T = 75 °C.

The preferential extraction of M18:0 into the vapour phase relative to M18:1 is counterintuitive when considering the binary HPBDP data, which indicated that M18:0 is less soluble in supercritical CO_2 on its own than M18:1, and the ternary HPBDP data, which indicated that there are no nonideal interactions like cosolvency present that would influence the relative solubility.

The CMO-effect that was used to explain the influence of unsaturation on the phase behaviour observed in the measured HPBDP data may also be used to attempt to explain this phenomenon. It was previously suggested that M18:1 has a CMO-breaking effect due to the lower packing density induced by the *cis* C=C bond. This would prevent the dense packing of the M18:0 molecules by increasing the distance between them, effectively shielding them from one another, resulting in reduced attractive forces. This reduction in the close packing of M18:0 may allow CO_2 to better penetrate the condensed phase and dissolve the M18:0 to a greater extent at a given pressure and temperature. This would increase the distribution of M18:0 into the vapour phase relative to the M18:1 molecules.

6. Phase Behaviour of the Methyl Stearate + Methyl Oleate + CO$_2$ System

However, it should be noted in Figure 6.6 that there is considerable uncertainty present in the calculated α_{12}-values. This is the result of a thorough accounting of the propagation of uncertainty from the measured VLE data and the significant experimental difficulties encountered in generating the data. This uncertainty places a measure of doubt on any observation and conclusion based on the relative solubility data.

It is thus believed that the uncertainty associated with the experimental determination of the VLE tie-lines overestimates the true selectivity, and potentially even incorrectly suggests that α_{12} is greater than one. Although the CMO-effect can be used to explain that the presence of M18:1 might increase the distribution of M18:0 to the vapour phase (an increase in the distribution coefficient K_1), and that relative to K_2 this would cause α_{12} to increase, this does not necessarily mean that the increased K_1 would exceed the value of K_2 and thus result in a α_{12}-value greater than one.

This can be investigated further by inspecting relative solubility data for a multicomponent mixture of fish oil FAEEs (C$_{14}$ to C$_{22}$) as presented in Figure 6.7. Riha and Brunner[7,10] grouped together equal-length FAEEs to determine the relative solubilities on the basis of chain length.
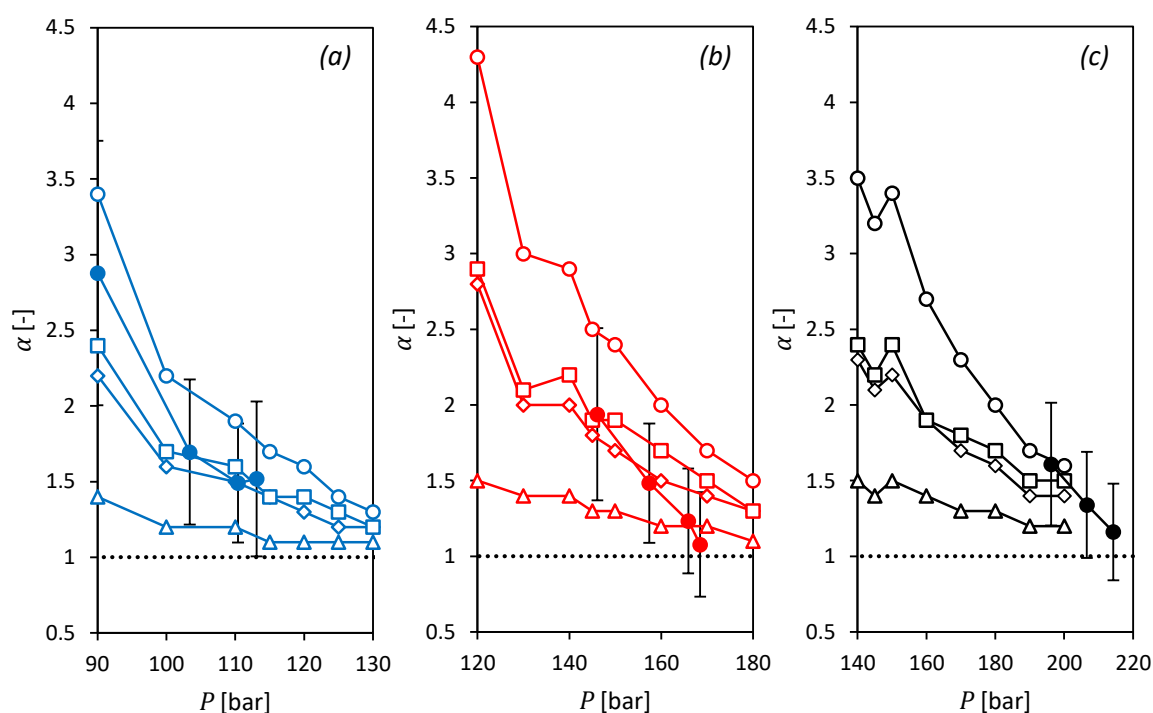
Figure 6.7: Comparison of the relative solubility (α) as a function of pressure (P) determined in this work with that determined from VLE measurements of a multicomponent mixture of C$_{14}$ to C$_{22}$ ethyl esters by Riha and Brunner.[7,10] (○) $\alpha_{C_{14}/C_{20}}$; (◊) $\alpha_{C_{16}/C_{20}}$; (Δ) $\alpha_{C_{18}/C_{20}}$; (□) $\alpha_{C_{18}/C_{22}}$. (a) Literature data at T = 40 °C, with α measured in this work (●) at T = 35 °C; (b) Literature data at T = 60 °C, with α measured in this work (●) at T = 55 °C; (c) Literature data at T = 70 °C, with α measured in this work (●) at T = 75 °C.

It can be seen that, at constant temperature, the relative solubility decreases as the difference in chain length decreases. The data indicates good selectivity between the C_{14} and C_{20} esters, and poor selectivity between the C_{18} and C_{20} esters. It can also be seen that similar selectivities are obtained between the C_{16} and C_{20}, and the C_{18} and C_{22} esters. This is the result of both groups having the same chain length difference of 4 methylene groups.

The relative solubilities α_{12} determined in this work are compared with the relative solubilities found by Riha and Brunner at similar temperatures. It can be seen that the α_{12}-values found in this work are similar to the $\alpha_{C_{16}/C_{20}}$-values obtained from the multicomponent mixture. This indicates that the selectivity between M18:0 and M18:1 and the selectivity between C_{16} and C_{20} ethyl esters should arise from reasonably similar differences in their solubilities in CO_2.

Figure 6.8 shows a comparison of the binary phase behaviour data for a variety of FAE + CO_2 systems at 40 °C. The data for the C_{20} ester is not complete, but it can be seen that the maximum solubility difference between E16:0 and E20:5 is at least about 50 bar. The maximum solubility difference between M18:0 and M18:1, however, is about 10 bar. This supports the argument that the experimentally determined tie-lines in this work overestimate the true α_{12}-values, since it is unlikely that a system with a 50 bar solubility difference would have the same selectivity as a system with a 10 bar solubility difference.
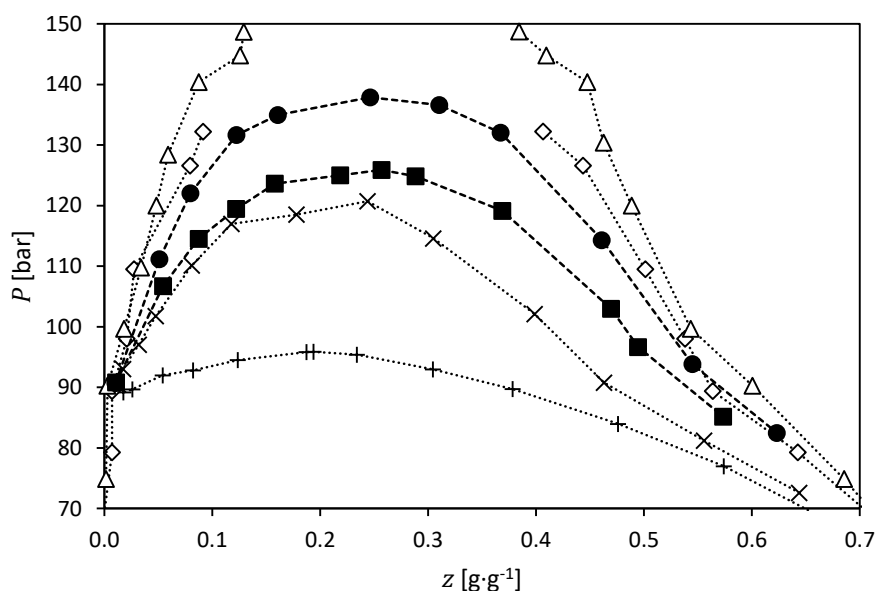
Figure 6.8: Phase transition pressures (P) as a function of the total solute fraction (z) for a variety of FAE + CO_2 systems at 40 °C. (+) E14:0 + CO_2 data from Schwarz[102]; (X) E16:0 + CO_2 data from Schwarz[102]; (■) M18:1 + CO_2 data measured in this work; (●) M18:0 + CO_2 data measured in this work; (◊) E18:0 + CO_2 data from Bharath et al.[78]; (Δ) E20:5 + CO_2 data from Bharath et al.[78]

6. Phase Behaviour of the Methyl Stearate + Methyl Oleate + CO_2 System

From Figure 6.8 it can also be seen that there may be a solubility difference between E18:0 and E20:5 of similar size to that between M18:0 and M18:1. Comparing this to the data in Figure 6.7, it suggests a significantly lower range of α_{12} (between 1 and 1.5) than seen in the experimentally determined data. This further supports the argument that the uncertainty in the α_{12}-values have led to their overestimation.

6.3. Experimental Challenges

The measurement of the HPBDP data in this work did not experience many challenges, since the synthetic-visual method is well-established and reliable if applied with care. The measurement of high-pressure VLE data is not trivial,[112] however, and becomes particularly challenging for highly asymmetric systems like the system measured in this work. The difficulty related to the analysis of samples was discussed in Section 4.3.3. This discussion will focus on visual observations made during the equilibration and sampling procedures. Similar challenges were experienced by Fourie.[89]

6.3.1. Sampling

Disturbance of the equilibrium condition during sampling is a well-documented issue, as changes in the equilibrium cell volume during sampling can cause a shift in the equilibrium state – which is normally confirmed through the observation of constant temperature and pressure.[9,112] However, even if the temperature and pressure remain constant to within the instrument resolution during sampling, some disturbances may occur that can only be detected through visual observation.[89]

Sampling of the vapour phase often caused the formation of a mist of liquid droplets settling down throughout the vapour volume of the equilibrium cell, as shown in Figure 6.9. Fourie[89] used the term *global mist formation* to describe the phenomenon, which was particularly prevalent at the lowest temperature of 35 °C. The settling out of the fine mist droplets could be accelerated by light, brief stirring – followed by a rest period before the next sample. The sample GC analysis duration of 25 min allowed for ample time to reach a stable state before extracting the next sample.

Figure 6.9: View of the equilibrium cell for VLE measurement at 35 °C: (a) before vapour sampling; (b) after vapour sampling.

6.3.2. Near-critical mixture measurements

The VLE measurement for the fourth pressure at 75 °C could not be performed due to the unstable nature of the phase behaviour close to the mixture critical pressure. Constant pressure fluctuations and the sudden formation of dispersed liquid droplets in the vapour phase made reliable and representative sampling of the phases impossible.

Additionally, McHugh & Krukonis[53] report that near the mixture critical point, small changes in the pressure or temperature can cause significant changes in the relative volumes of the two phases, further complicating the measurement of reliable equilibrium data. This lack of stability can be seen in Figure 6.10, which displays the visual observations made for the M18:0 + M18:1 + CO_2 system at 75 °C.

In Figure 6.10 (a), the system is at 217.6 bar, after being compressed to the one-phase region. The dark-red colour is indicative of critical opalescence near the mixture critical point. Critical opalescence is the result of short-range fluctuations in the fluid density near the critical point. These fluctuations occur over distances to the order of the wavelength of visible light. The fluid then scatters reflected and transmitted light, resulting in interesting optical phenomena.[52,53]

In Figure 6.10 (b) the pressure has been decreased to 216.4 bar, close to the desired measurement pressure, with the magnetic stirring still on. The dark-yellow colour is an indication of continued proximity to the mixture critical point. The phase transition has occurred, and it can be seen that a large phase volume change took place in just a 1.2 bar pressure drop. Additionally, the liquid phase is murky with entrained vapour bubbles, whilst a mist of liquid droplets is entrained in the vapour phase. This is mostly a result of the stirring.

6. Phase Behaviour of the Methyl Stearate + Methyl Oleate + CO$_2$ System

In Figure 6.10 (c) the stirring has been switched off. This caused a 0.1 bar drop in pressure. The pressure drop after switching off the stirrer was observed repeatedly at these conditions. This pressure is only 2 bar above the pressure of the previous measurement.

In Figure 6.10 (d) the entrained phases have settled out after a period of time, leaving the liquid phase clear. The pressure showed constant fluctuations of about 0.2 bar, which caused the formation of fine liquid droplets at the top of the view cell. The droplets could not be avoided or removed, and had long settling times due to the similar densities of the two phases near the critical point. This prevented the measurement of equilibrium data at these conditions.

(a) P = 217.6 bar　　　　　*(b) P = 216.4 bar*

(c) P = 216.3 bar　　　　　*(d) P = 216.3 bar*
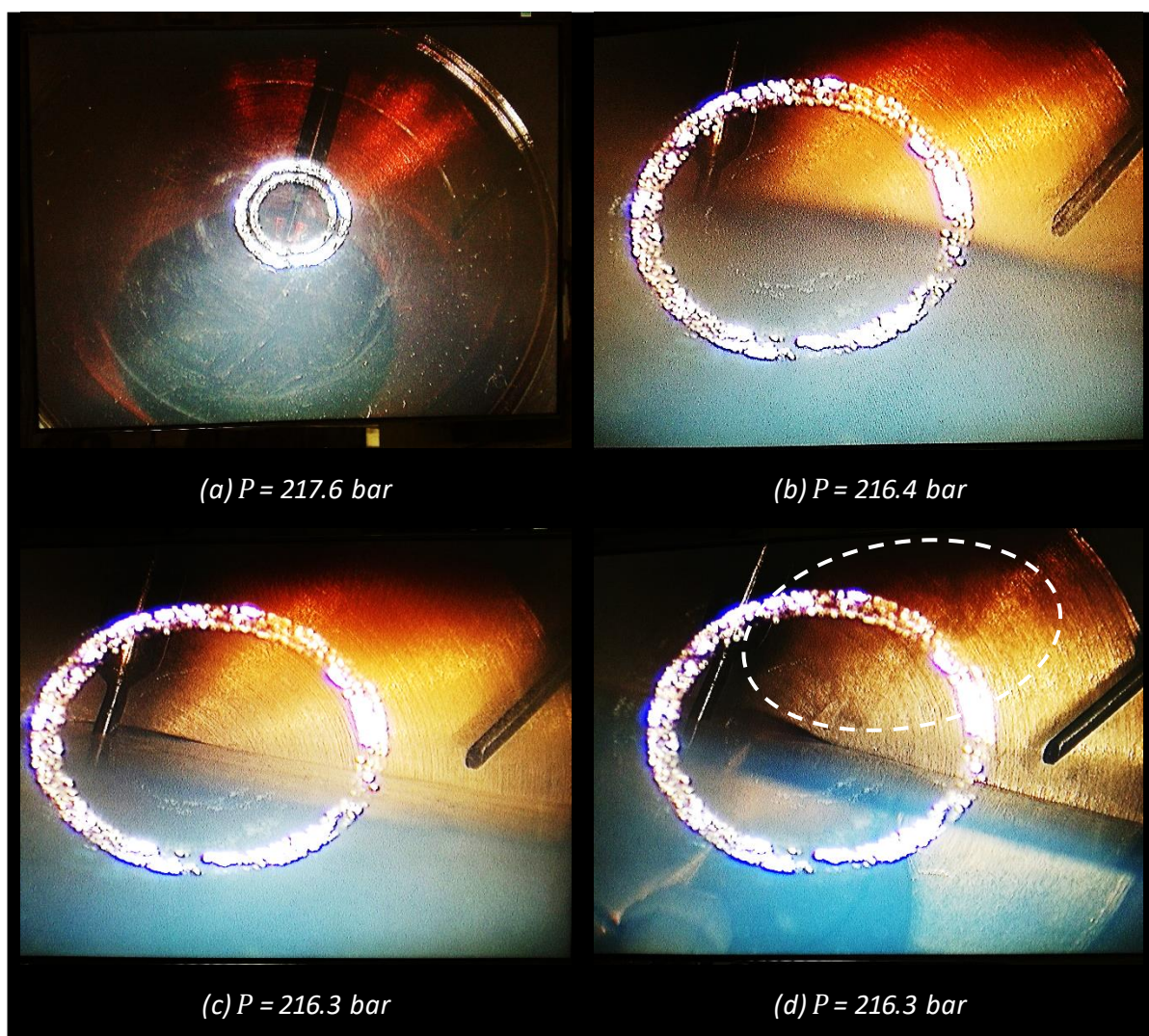
Figure 6.10: Observations of the ternary M18:0 + M18:1 + CO$_2$ system at 75 °C near the mixture critical point. (a) P = 217.6 bar; just above mixture critical point. (b) P = 216.4 bar; slightly below mixture critical pressure. (c) P = 216.3 bar; stirring off. (d) P = 216.3 bar; liquid phase clear of entrained bubbles, fine mist of droplets settling down from top of view cell.

The measurement of high-pressure VLE data is complex and challenging, with many sources of uncertainty in measurements, particularly for systems with high asymmetry. This means it is not the ideal measurement method for binary systems, where synthetic-visual methods can be used with great

success, generating data more quickly, with fewer sources of uncertainty, and with the possibility of fully measuring the critical region.

For ternary and higher mixtures, however, synthetic-visual methods cannot fully describe the phase behaviour, and equilibrium studies become necessary. The challenges experienced in this work for the measurement of high-pressure VLE for a highly asymmetric system highlight the importance of a rigorous approach to the quantification of the uncertainty involved in phase equilibria measurements, as well as applying the correct analysis methodology to effectively measure VLE for high-asymmetry systems.

6.4. Summary

The high-pressure phase behaviour data measured for the M18:0 + M18:1 + CO_2 system indicated that there are no nonideal solute interactions in the system caused by the unsaturation of M18:1. The measurement of the VLE data was challenging and imparted considerable uncertainty to the calculated relative solubility.

The uncertainty in the measured relative solubility data has two implications. Firstly, it is difficult to make conclusive statements about the values of the relative solubility and the implication thereof on the selectivity of supercritical CO_2 for the separation of M18:0 and M18:1.

Secondly, VLE data are important for making design calculations for separation processes. Uncertainty in the VLE data will thus influence design calculations, and the confidence of calculated design parameters, which can have serious process implications due to potential overdesign or underdesign.[9]

SCFF design variables have been found to be very sensitive to uncertainty when the relative solubility is less than 1.5[47] – and given the experimental uncertainty and discussion in section 6.2, many α_{12} values measured in this work may fall in or near this range.

Thermodynamic modelling can potentially reduce the dependence on experimental data, and may be preferred over the costly, complex, and time-consuming nature of high-pressure VLE measurement for asymmetric systems like the M18:0 + M18:1 + CO_2 system investigated in this work.

CHAPTER 7:
Thermodynamic Modelling

Chapter 6 highlighted the difficulty of measuring high-pressure VLE data for asymmetric systems. Considerable experimental effort could be reduced or avoided altogether if the phase behaviour of these systems could be predicted by thermodynamic models. Additionally, the modelling of phase equilibria is a useful tool for the development and design of separation processes,[113] and it is thus valuable to be able to predict or describe the phase behaviour of relevant systems with little or no experimental input. Chapter 7 discusses the application of two simple predictive or semi-predictive equations of state to the modelling of the FAME + CO_2 systems investigated in this work.

7.1. Theory

Pressure-explicit cubic-type equations of state (EOSs) lend themselves to the computation of high-pressure and near-critical phase behaviour, since they rely on critical properties to calculate pure-component parameters.[8,113,114]

An EOS can be predictive or correlative. Predictive EOSs rely on pure-component data or group contribution methods to calculate model parameters, which allow the prediction of phase behaviour data without the need for experimental data.

Correlative models require experimental data to fit parameters (often binary interaction parameters, BIPs) in order to compute phase behaviour successfully. Experimental data may however still be necessary for the fitting of group-contribution methods in predictive models.

Two relatively simple EOSs are investigated for the modelling of C_{18} FAME + CO_2 systems: predictive Peng-Robinson (PPR) and modified Sanchez-Lacombe (MSL). PPR is purely predictive, and is selected as a model that has previously been applied to FAE + CO_2 with success.[19] MSL can be applied predictively or correlatively, and is selected as a model that is not based on modifications of the van der Waals EOS (such as Peng-Robinson, Soave-Redlich-Kwong, etc.), but instead is based on the Lattice-Fluid Theory, and has not yet been applied to FAE + CO_2 systems in the open literature.

7. Thermodynamic Modelling

7.1.1. Predictive Peng-Robinson

The Peng-Robinson (PR) EOS was developed as a modification of the van der Waals EOS to better predict liquid phase densities.[115] It has found success in the calculation of phase behaviour in the critical region at high pressures, making it suitable for application to supercritical systems.[8,113] The base EOS is given in Equation 7.1[115]:

$$P = \frac{RT}{v - b_m} - \frac{a_m}{v^2 + 2b_m v - b_m^2} \tag{7.1}$$

The mixture parameters a_m and b_m are calculated from pure component parameters a_i and b_i. These can be found from Equations 7.2 to 7.5, only requiring knowledge of the pure component critical properties, acentric factors, and the equilibrium temperature[115]:

$$b_i = 0.07780 \frac{RT_c}{P_c} \tag{7.2}$$

$$a_i = 0.45724 \frac{R^2 T_c^2}{P_c} \left[1 + m_i \left(1 - \sqrt{\frac{T}{T_c}} \right) \right]^2 \tag{7.3}$$

$$m_i = 0.37464 + 1.54226\omega_i - 0.26992\omega_i^2, for\ \omega_i < 0.491 \tag{7.4}$$

$$m_i = 0.379642 + 1.48503\omega_i - 0.164423\omega_i^2 + 0.016666\omega_i^3, for\ \omega_i > 0.491 \tag{7.5}$$

In order to calculate the mixture parameters from the pure component parameters a mixing rule is required. The predictive Peng-Robinson (PPR) EOS is an attempt to select mixing rules that allow the calculation of binary interaction parameters (BIPs) from group-contribution methods, entirely avoiding the need for experimental phase behaviour measurements to regress the BIPs. This method is based on the use of excess energy functions (normally used in activity coefficient models, as opposed to PVT EOSs) to calculate the BIPs k_{ij}.[116] The approach makes use of classical mixing rules, as shown in Equations 7.6 and 7.7[116]:

$$a_m = \sum_{i=1}^{N} \sum_{j=1}^{N} x_i x_j \sqrt{a_i a_j} (1 - k_{ij}) \tag{7.6}$$

$$b_m = \sum_{i=1}^{N} x_i b_i \tag{7.7}$$

where k_{ij} is a temperature-dependent BIP that is calculated from the group-contribution method detailed in Equations 7.8 to 7.12 as developed by Abdoul et al.[117]:

$$k_{ij}(T) = \frac{[E_{ij}(T) - \Delta_{ij}(T)]}{\Theta_{ij}(T)} \tag{7.8}$$

$$E_{ij}(T) = -\frac{1}{2}\sum_{k=1}^{Ng}\sum_{l=1}^{Ng}(\alpha_{ik} - \alpha_{jk})(\alpha_{il} - \alpha_{jl})A_{kl}\left(\frac{298.15}{T}\right)^{\frac{B_{kl}}{A_{kl}}-1} \qquad 7.9$$

$$\Delta_{ij}(T) = (\delta_i - \delta_j)^2 \qquad 7.10$$

$$\Theta_{ij}(T) = 2\delta_i\delta_j \qquad 7.11$$

$$\delta_i(T) = \sqrt{a_i}/b_i \qquad 7.12$$

Where Ng is the number of unique groups present and a_{ik} is the fraction of molecule i occupied by group k. A_{kl} and B_{kl} are the group interaction parameters, where $A_{kl} = A_{lk}$ and $B_{kl} = B_{lk}$. In order to apply the PPR model to the modelling of fish oil ester + CO_2 systems, Jaubert and coworkers regressed the group interaction parameters for the ester group -COO- with other relevant groups (-CH_3, -CH_2-, CO_2, and -CH= – whose interaction parameters among themselves had been determined previously by Abdoul et al.[21]).[19–21] These parameters are given in Tables 7.1 and 7.2

Table 7.1: Group interaction parameters A_{kl} (in J·cm⁻³) for the PPR EOS as taken from Jaubert et al.[19]

	-CH₃	-CH₂-	CO₂	-CH=	-COO-
-CH₃	0				
-CH₂-	26.76	0			
CO₂	150.37	140.08	0		
-CH=	25.83	19.85	32.60	0	
-COO-	328.05	355.16	-305.4	-1750.04	0

Table 7.2: Group interaction parameters B_{kl} (in J·cm⁻³) for the PPR EOS as taken from Jaubert et al.[19]

	-CH₃	-CH₂-	CO₂	-CH=	-COO-
-CH₃	0				
-CH₂-	46.11	0			
CO₂	176.05	270.77	0		
-CH=	39.46	47.38	-3.43	0	
-COO-	1297.09	1347.19	-603.94	-2608.25	0

Equation 7.12 contains the pure-component energy and volume parameters a_i and b_i, and thus k_{ij} is dependent on the critical properties of the components involved. The thermally labile FAMEs investigated in this work decompose before their critical points are reached, and these are thus purely hypothetical quantities. In order to apply the PPR EOS as used by Jaubert and coworkers, it is necessary to use the same critical properties used in the regression of the group-contribution parameters. The estimated pure-component properties as used in this work are provided in Table 7.3.

7. Thermodynamic Modelling

Table 7.3: Estimated critical properties of the C₁₈ FAMEs investigated in this work as taken form Jaubert et al.[19]

Component	T_c [K]	P_c [bar]	ω [-]
M18:0	778.756	12.5288	0.9542
M18:1	774.093	12.7832	0.9445
M18:2	776.461	13.0469	0.9317

7.1.2. Modified Sanchez-Lacombe

The modified Sanchez-Lacombe (MSL) model is based on the Lattice-Fluid Theory. This allows the model to account for the long hydrocarbon chain of the FAME molecule, instead of approximating molecules as spheres like traditional EOSs such as PR. This is done by approximating the fluid as a three-dimensional lattice. Chain-like molecules can then be represented as a sequence of adjacent lattice sites. The MSL model can be written as a pressure-explicit EOS, and relies on critical properties to calculate the pure component parameters.[118] The MSL EOS is given in Equation 7.13[118]:

$$\frac{P}{RT} = \frac{1-d}{v} - \frac{d}{b}\ln\left(\frac{v-b}{v}\right) - \frac{a}{v^2 RT} \qquad 7.13$$

The Péneloux volume translation is used to calculate the actual molar volume from the molar volume used in the EOS, allowing for a more accurate prediction of phase densities[118]:

$$v_t = v + c \qquad 7.14$$

The calculation of the four mixture parameters is done via the mixing rules shown in Equations 7.15 to 7.18[118]:

$$a = \sum_{i=1}^{N}\sum_{j=1}^{N} x_i x_j M_i M_j a_{ij}(1 - k_{ij}) \qquad 7.15$$

$$b = \sum_{i=1}^{N} x_i M_i b_i \qquad 7.16$$

$$c = \sum_{i=1}^{N} x_i M_i c_i \qquad 7.17$$

$$d = \sum_{i=1}^{N} x_i M_i d_i \qquad 7.18$$

where x_i is a mole fraction, M_i is a molar mass, b_i, c_i, and d_i are the pure component EOS parameters, a_{ij} is a binary combination parameter, and k_{ij} is an optional correlative binary interaction parameter, which can be made temperature dependent.

Each of these parameters can in turn be calculated from a set of four parameters for each pure component, namely the lattice energy ε_i, the volume per lattice site v_i^*, the number of lattice sites per molar mass unit d_i, and the volume shift parameter per molar mass unit c_i.[118] The calculations for these parameters are shown in Equations 7.19 to 7.24 according to the parameterisation of Gauter and Heidemann[118,119]:

$$a_{ij} = \frac{d_i d_j \sqrt{\varepsilon_i \varepsilon_j}\left(v_i^* + v_j^*\right)}{2} \tag{7.19}$$

$$b_i = d_i v_i^* \tag{7.20}$$

$$c_i = 3.297 d_i - 0.1092 \tag{7.21}$$

$$d_i = \frac{d_i^*}{M_i} = \frac{-1.2952\omega_i^3 + 5.9404\omega_i^2 + 13.5698\omega_i + 5.1178}{M_i} \tag{7.22}$$

$$\varepsilon_i = \frac{RT_{c,i}\left(1 + \sqrt{d_i^*}\right)^2}{2d_i^*} \tag{7.23}$$

$$v_i^* = \frac{RT_{c,i}}{P_{c,i}}\left[\ln\left(\frac{1 + \sqrt{d_i^*}}{\sqrt{d_i^*}}\right) - \frac{\sqrt{d_i^*} - 0.5}{d_i^*}\right] \tag{7.24}$$

To summarise, The MSL EOS can be applied to a system of components, only requiring knowledge of the acentric factor ω, critical temperature T_c, critical pressure P_c, and molar mass M for each pure component.

7.2. Binary FAME + CO$_2$ Systems

Each of the binary FAME + CO$_2$ systems measured in this work were modelled with three models: predictive Peng-Robinson (PPR), modified Sanchez-Lacombe without a BIP (MSL), and modified Sanchez-Lacombe with a regressed, linearly temperature dependent BIP (MSLR). All calculations were performed in MS Excel with the VLXE|Blend software package.[120]

For PPR, the group-contribution method described in section 7.1.1 was used to calculate the k_{ij} values for each binary system at each temperature. These were found to vary linearly with temperature, and so an intercept $k_{ij}(a)$ and slope $k_{ij}(b)$ were determined for each system. For the MSLR correlations, regressions were performed using only the data measured in this work to determine $k_{ij}(a)$ and $k_{ij}(b)$ values. The objective function was of the form:

$$F_{OBJ} = \sum_{i=1}^{n} \frac{\left|P_{exp} - P_{calc}\right|}{P_{exp}} \tag{7.25}$$

7. Thermodynamic Modelling

All the BIPs used in this work are summarised in Table 7.4.

Table 7.4: Calculated (PPR) and regressed (MSLR) BIPs in the form $k_{ij}(T) = k_{ij}(a) + k_{ij}(b) \cdot T$, where T is in Kelvin.

System	PPR	MSLR
M18:0 + CO_2	$0.01130 + 0.00012T$	$0.00011 + 0.00042T$
M18:1 + CO_2	$-0.00077 + 0.00016T$	$0.19671 - 0.00017T$
M18:2 + CO_2	$-0.01180 + 0.00020T$	$0.10920 + 0.00009T$

A general overview of the modelling results is provided in Table 7.5 in the form of the calculated average absolute relative deviation (AARD) in pressure. It can be seen that MSL performed very poorly due to the lack of a BIP. Both PPR and MSLR performed similarly, except for the M18:2 + CO_2 system, where PPR provided a significant improvement. PPR also has the advantage over MSLR in that none of the measured data in this work were required in the calculations of the BIPs. The PPR model appears to better predict the phase behaviour as the degree of unsaturation increases.

Table 7.5: Calculated AARD in pressure for all models and binary systems investigated.

System	PPR	MSL	MSLR
M18:0 + CO_2	11.3 %	34.0 %	11.4 %
M18:1 + CO_2	7.1 %	30.7 %	7.0 %
M18:2 + CO_2	3.6 %	36.0 %	7.0 %

Figures 7.1 , 7.2 , and 7.3 show the modelling results for three binary systems. The results for the M18:0 (1) + CO_2 (2) system are shown in Figure 7.1. It can be seen that MSL performs poorly across all temperatures, severely underpredicting the pressures in most of the compositional range. The correlated MSLR improves the ability of the EOS to describe the phase behaviour at higher temperatures, with the performance still being quite low at the lower temperatures. Additionally, both the MSL and MSLR models fail to reproduce the position of the mixture critical point accurately. The PPR model provides a qualitatively correct prediction at all temperatures, although it underpredicts the pressure in the critical region. The PPR model also successfully predicts the position of the mixture critical point at all temperatures.

The modelling results for the M18:1 (1) + CO_2 (2) system are shown in Figure 7.2. As was seen from the AARD calculations, the MSL model is highly unsuccessful, both qualitatively and quantitatively. Similar observations can be made for this system and the M18:0 + CO_2 system, with the PPR and MSLR models providing better descriptions of the phase behaviour at higher temperatures. The PPR model underpredicts the pressure less for the M18:1 + CO_2 system than for the M18:0 + CO_2 system.
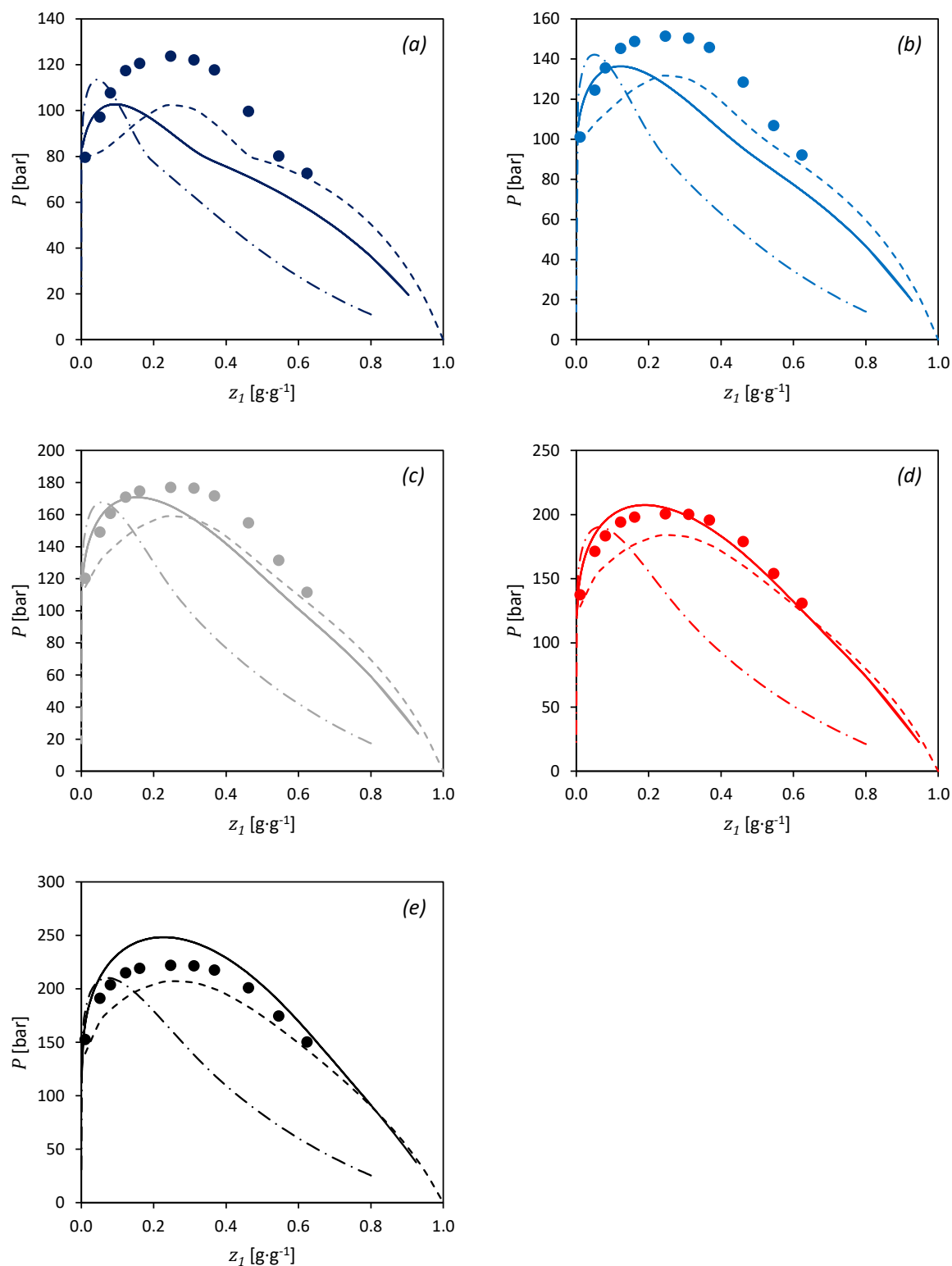
Figure 7.1: Modelling results of the phase transition pressure (P) as a function of the solute fraction (z) for the M18:0 (1) + CO$_2$ (2) system. (—) MSLR; (-··-) MSL; (---) PPR. (a) T = 35 °C; (b) T = 45 °C; (c) T = 55 °C; (d) T = 65 °C; (e) T = 75 °C.

7. Thermodynamic Modelling
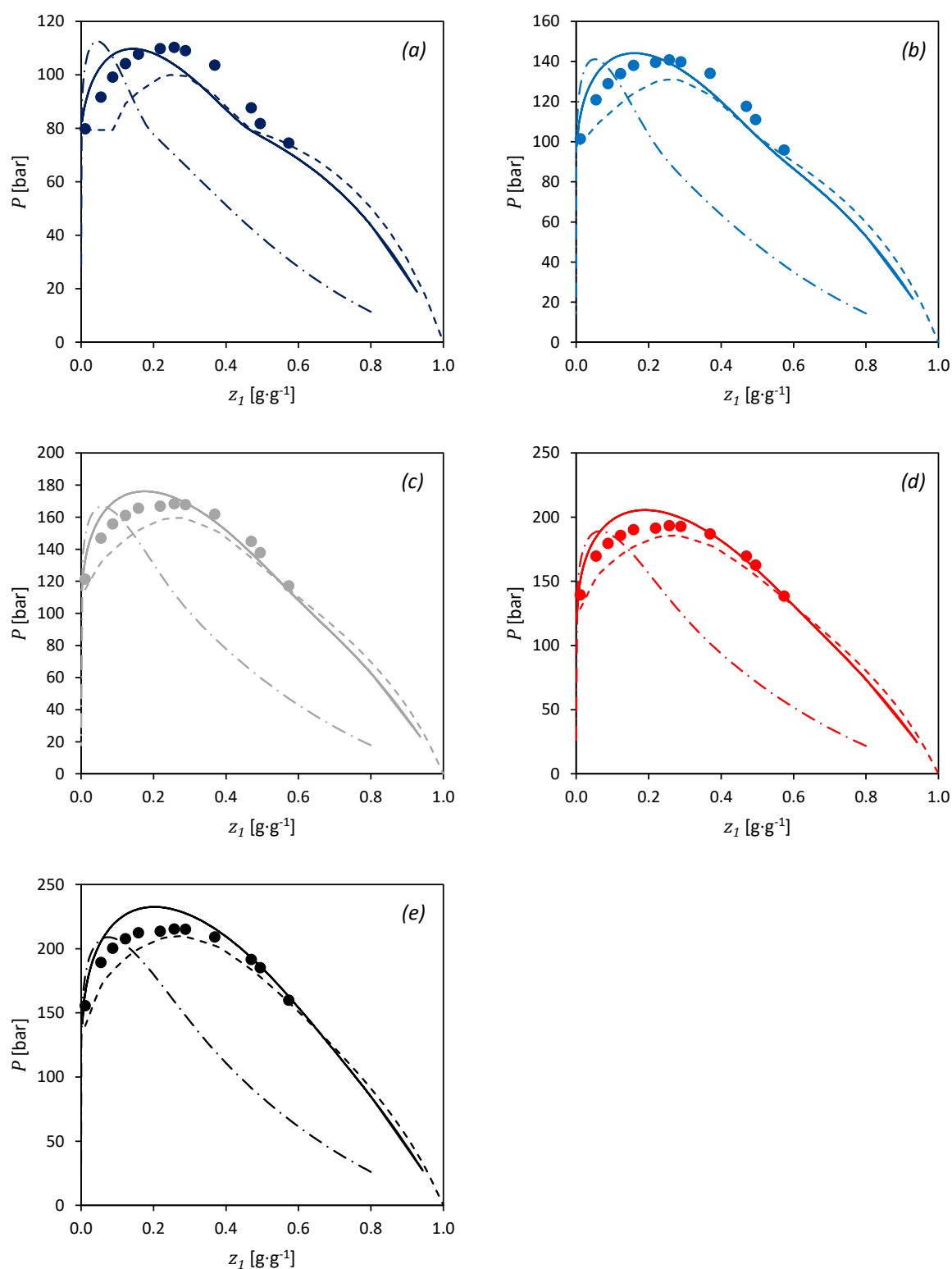
Figure 7.2: Modelling results of the phase transition pressure (P) as a function of the solute fraction (z) for the M18:1 (1) + CO_2 (2) system. (—) MSLR; (-··-) MSL; (---) PPR. (a) T = 35 °C; (b) T = 45 °C; (c) T = 55 °C; (d) T = 65 °C; (e) T = 75 °C.
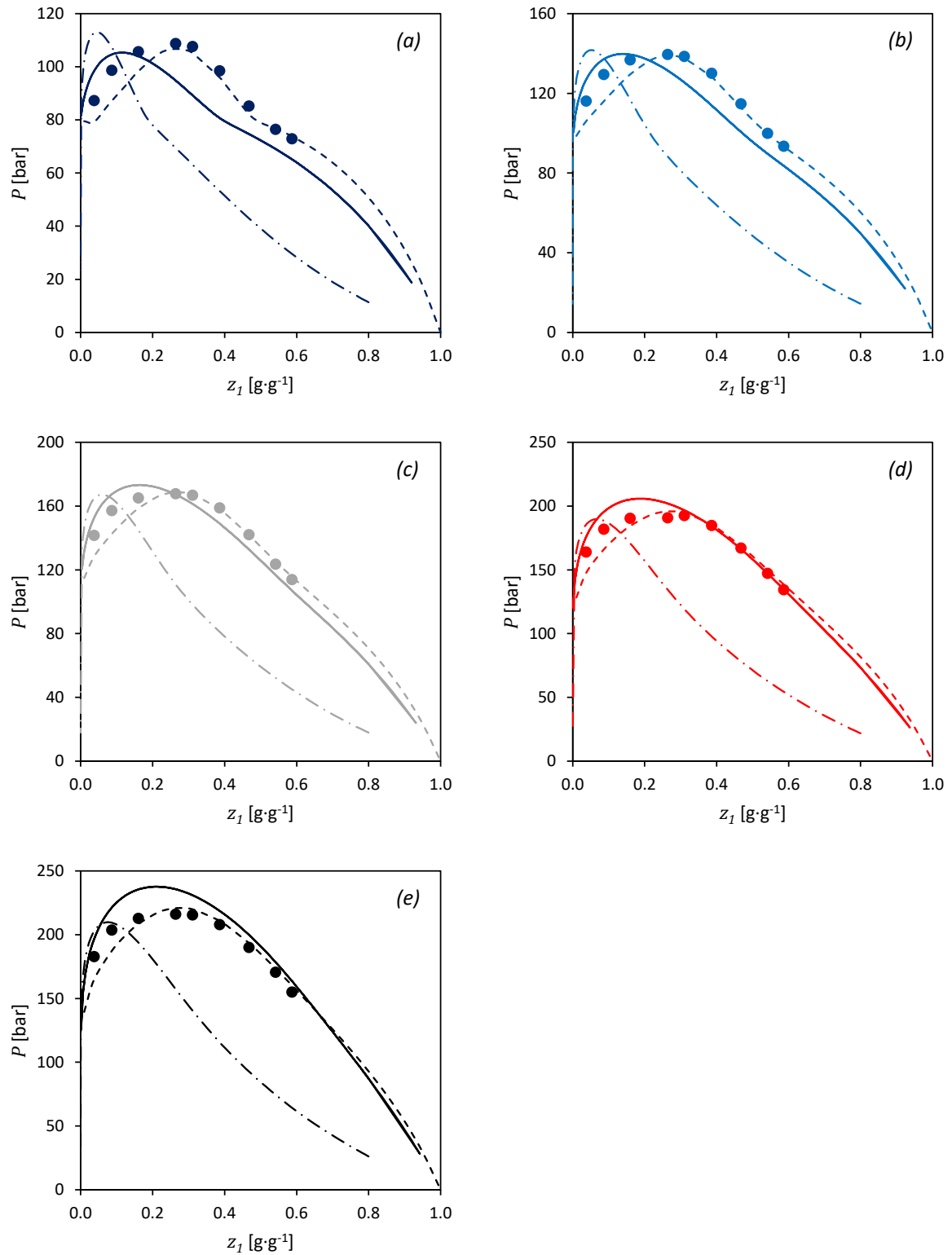
Figure 7.3: Modelling results of the phase transition pressure (P) as a function of the solute fraction (z) for the M18:2 (1) + CO_2 (2) system. (—) MSLR; (-··-) MSL; (---) PPR. (a) T = 35 °C; (b) T = 45 °C; (c) T = 55 °C; (d) T = 65 °C; (e) T = 75 °C.

7. Thermodynamic Modelling

The modelling results for the M18:2 (1) + CO_2 (2) system are shown in Figure 7.3. Again, similar results are obtained as for the other two systems. The PPR model notably provides a better prediction of the experimental data than for the other two systems, particularly for the bubble-point curve, and only slightly overpredicts the FAME-content of the vapour phase (even at low temperatures where models tend to struggle due to the proximity to the critical temperature of CO_2). The locations of the mixture critical points are also accurately reproduced.

Figure 7.4 provides a comparison between the PPR and MSLR models to illustrate their description of the influence of unsaturation on the phase behaviour of FAME + CO_2 systems. At 35 °C, the MSLR model calculates higher pressures for the unsaturated FAMEs. The PPR model is similarly incapable of replicating the trend of solubility with unsaturation that was observed experimentally. At 75 °C, the MSLR model correctly calculates higher pressures for the saturated component versus the unsaturated components. This pressure difference is larger than the experimentally observed one, however. The PPR model predicts the same trend regarding unsaturation as for 35 °C.
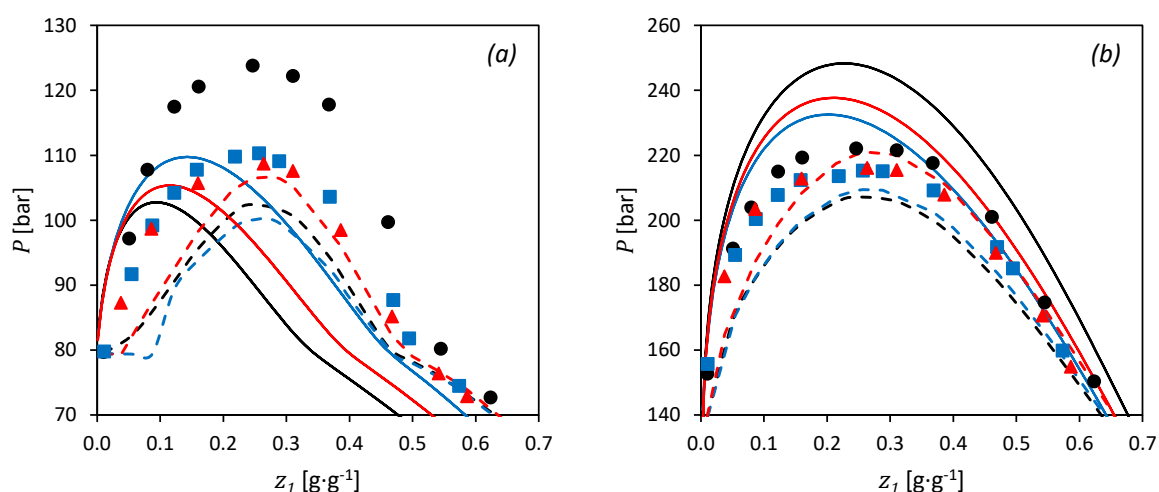
Figure 7.4: Comparison of PPR and MSLR for the description of the influence of unsaturation on FAME phase behaviour. (●) M18:0 + CO_2 data measured in this work; (■) M18:1 + CO_2 data measured in this work; (▲) M18:2 + CO_2 data measured in this work. (—) MSLR model; (---) PPR model. (a) T = 35 °C; (b) T = 75 °C.

Some general comments based on the modelling results of the binary systems can be made:

i. Relatively simple EOSs like PR and MSL require BIPs to adequately describe high-pressure phase behaviour of FAME + CO_2 systems.

ii. The location of mixture critical points is better described by PR than by MSL.

iii. The description of PR and MSL improves at higher temperatures further away from the critical temperature of the CO_2 solvent.

iv. MSLR better describes the vapour phase, whilst PR better describes the liquid phase.

v.   Neither model can accurately describe the influence of unsaturation on the phase behaviour of FAME + CO_2 systems.

The PPR model was found to perform the best, both quantitatively and qualitatively, and has been found to be an adequate tool for the description of the general phase behaviour of FAME + CO_2 systems by several authors.[19–21] Despite this, PPR has been shown here to be inadequate for the prediction of the influence of unsaturation on FAME + CO_2 phase behaviour, at least in its current form.

The model is highly dependent on the critical properties of the components involved, as these are used to estimate the k_{ij} values as well as directly in the phase equilibria calculations. For systems containing components with critical properties that cannot be measured experimentally, this poses a problem, as the ability of the model to predict phase behaviour becomes dependent on the method used to estimate the critical properties.

In this work, for example, the estimation method resulted in parameters that predicted the M18:2 + CO_2 phase behaviour more adequately, but resulted in less appropriate parameters for M18:0 and M18:1. The DIPPR database has a set of P_c, T_c, and ω for the C_{18}-family of FAMEs different to that used by Jaubert and coworkers to parameterise the PPR group-contribution BIP-estimation procedure.[121]

A comparison between the two sets is provided in Figure 7.5. It can be seen that there are differences between the M18:0 P_c-values and the unsaturated FAME T_c-values. However, both data sets still follow the same trend in P_c and T_c regarding the influence of unsaturation. With regards to the acentric factor ω, the two data sets follow different trends as the unsaturation increases, with the Jaubert et al. set having very similar values, and the DIPPR set having larger differences between different esters.
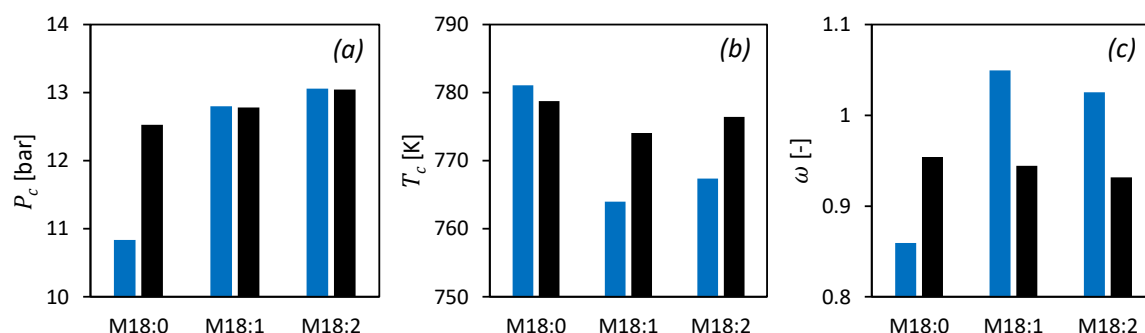
Figure 7.5: Comparison of two different sets of critical properties for the C_{18} FAMEs investigated in this work. (■) Properties taken form DIPPR[121]; (■) Properties taken from Jaubert et al.[19] as used in this work. (a) Critical pressure P_c; (b) Critical temperature T_c; (c) Acentric factor ω.

7. Thermodynamic Modelling

Considering the different trends in the acentric factors, and the differences in some of the other critical properties between the two data sets, it is possible that reregressing the A_{kl} and B_{kl} parameters for ester compounds by making use of the DIPPR critical properties may lead to better predictions for the phase behaviour with regards to the influence of unsaturation. Attempting this would take considerable effort and would not guarantee an improvement, however, and is beyond the scope of this investigation.

Alternatively, other models that do not rely on critical properties could be considered, such as those based on perturbation theory like the statistical associating fluid theory (SAFT) models. These EOSs usually require pure component data for determination of the parameters like liquid density data and vapour pressure data.[101]

7.3. Ternary Vapour-Liquid Equilibria

The PPR and MSLR models were applied to the modelling of the ternary M18:0 (1) + M18:1 (2) + CO_2 (3) system investigated in this work. For PPR, an additional ester-ester k_{ij} was calculated form the group-contribution method, and was found to be $k_{12}(T) = 0.00067 - 8.6856\text{e-}7 \cdot T$, where T is in Kelvin. No ester-ester BIP could be determined for MSLR, as there was no appropriate VLE data available for the M18:0 + M18:1 system (the data measured by Rose and Schrodt[48] was not sufficient for regression purposes, as it does not cover multiple temperatures, and was measured at a much higher temperature than investigated in this work). Accordingly, k_{12} was set to zero for MSLR. Furthermore, only the BIPs regressed from the binary data was used – no new parameters were fitted to the ternary data.

The results of the modelling are provided in Figures 7.6 to 7.8. Due to its general underprediction of the pressure in the binary systems, PPR predicts total solubility at most of the experimental pressures investigated in this work for the ternary VLE data. At the pressures where it does predict VLE, the size of the phase envelope is always underpredicted.

MSLR generally fares worse. Its poor description of the binary data results in entirely inadequate descriptions of the ternary behaviour, particularly at low temperatures and high pressures where the slope of the bubble-point curve deviates significantly from the experimental data. At 75 °C, however, the MSLR model provides a reasonable description of the phase envelope. Both models calculate tie-lines with different slopes to the experimental tie-lines.
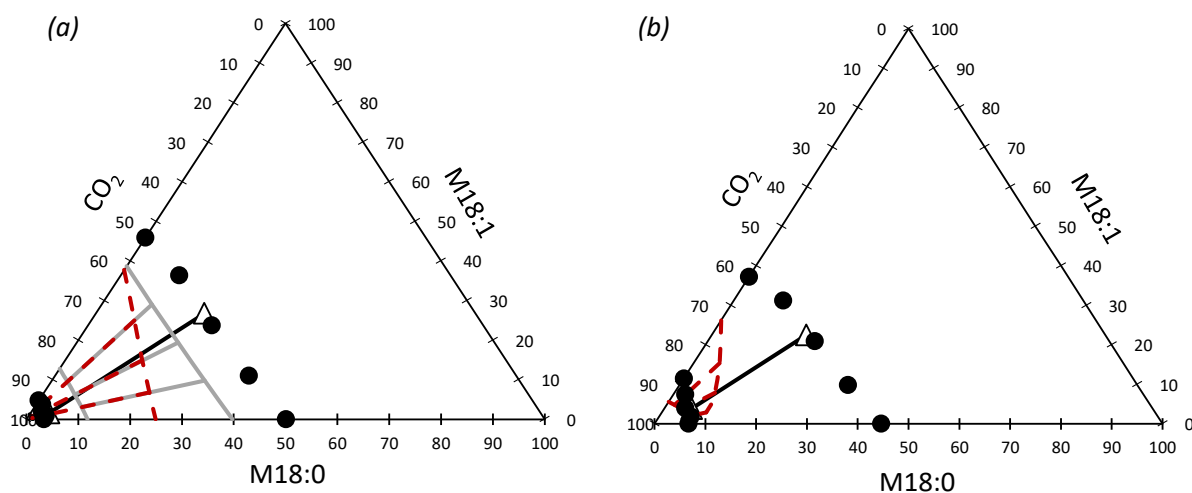
Figure 7.6: Thermodynamic modelling results for the ternary M18:0 + M18:1 + CO_2 system at 35 °C. (●) Ternary HPBDP data measured in this work; (Δ) Ternary VLE data measured in this work; (—) PPR; (---) MSLR. (a) P = 90.0 bar; (b) P = 103.4 bar.
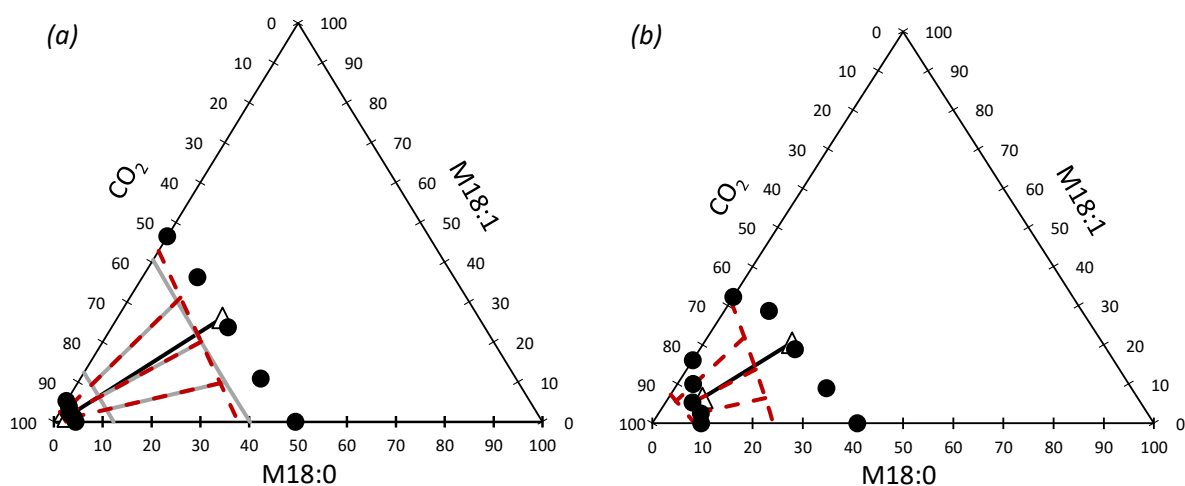
Figure 7.7: Thermodynamic modelling results for the ternary M18:0 + M18:1 + CO_2 system at 55 °C. (●) Ternary HPBDP data measured in this work; (Δ) Ternary VLE data measured in this work; (—) PPR; (---) MSLR. (a) P = 146.1 bar; (b) P = 165.9 bar.

7. Thermodynamic Modelling
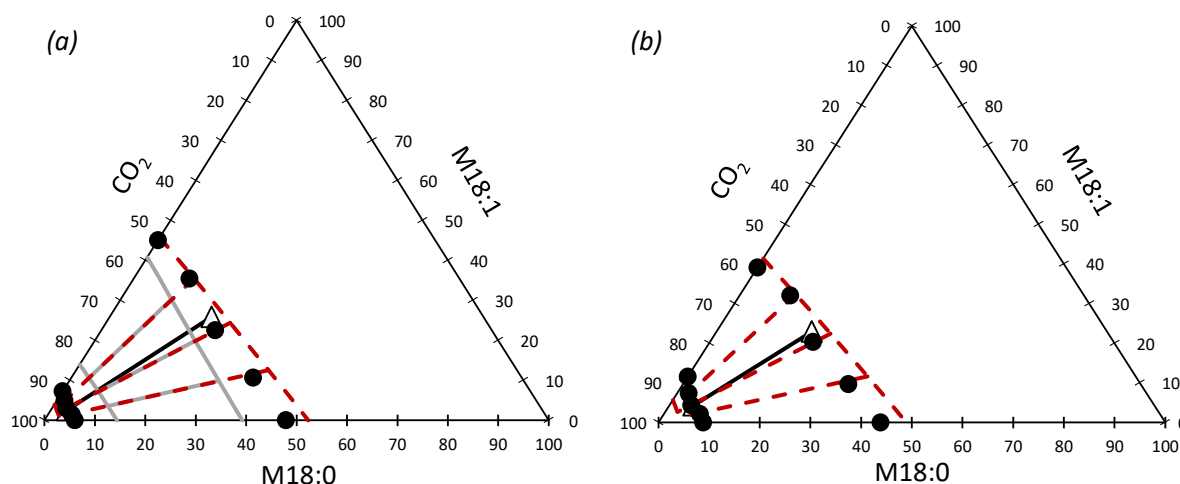
Figure 7.8: Thermodynamic modelling results for the ternary M18:0 + M18:1 + CO$_2$ system at 75 °C. (●)
Ternary HPBDP data measured in this work; (Δ) Ternary VLE data measured in this work; (—) PPR; (---) MSLR.
(a) P = 196.2 bar; (b) P = 206.6 bar.

A comparison of the measured and model-predicted relative solubilities is shown in Figure 7.9. It can be seen that the MSLR model predicts relative solubilities between 0.9 and 1.0. The model thus predicts that M18:1 is preferentially distributed to the vapour phase relative to M18:0, the opposite trend that was observed experimentally. This can also be seen in the difference between the experimental and model-predicted tie-line slopes. The PPR prediction of α_{12} is not shown, as it only predicted VLE at one pressure, and the tie-lines were coincident with the MSLR tie-lines.
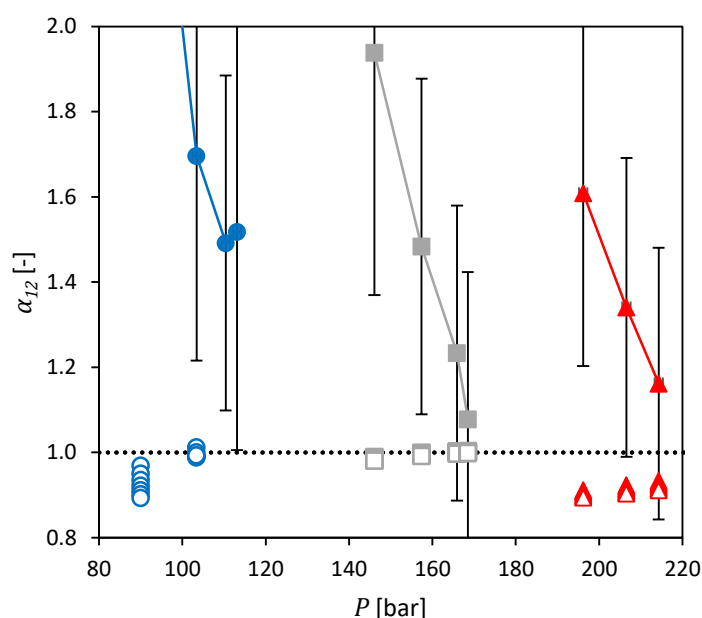
Figure 7.9: Measured and predicted relative solubility between M18:0 and M18:1 as a function of pressure.
(●) Measured data at T = 35 °C; (■) Measured data at T = 55 °C; (▲) Measured data at T = 75 °C; (○) MSLR
prediction at T = 35 °C; (□) MSLR prediction at T = 55 °C; (Δ) MSLR prediction at T = 75 °C.

The discussion in section 6.2 highlighted the uncertainty in the measured α_{12}-values, and the subsequent doubt involved in any interpretation of the results. It was also argued that the experimental relative solubility overestimates the true values, and that the observed α_{12}-values greater than one may even be erroneous. This argument lines up with the MSLR-predicted α_{12}-values, but due to the poor description of the influence of unsaturation on the binary HPBDP data by MSLR, as well as the poor description of the phase envelope of the ternary system at lower temperatures by MSLR, no meaningful conclusion can be drawn from this observation.

7.4. Summary

Considering the modelling performed on the systems investigated in this work, it is evident that simple PVT EOSs such as PPR and MSL in their current forms are not able to describe the influence of unsaturation on the phase behaviour of FAME + CO_2 systems, indicating that experimental measurement of multicomponent equilibrium data cannot be replaced by predictive modelling for these types of systems where there are small solubility differences between components with similar critical properties, particularly due to the unavailability of experimentally measured critical properties for thermally labile compounds.

CHAPTER 8:
Conclusions

The aim of this work was to investigate the ability of supercritical carbon dioxide to fractionate mixtures of fatty acid methyl esters (FAMEs) where the length of the hydrocarbon backbone remained constant, and the FAMEs only differed in their degrees of unsaturation. To that end, the phase behaviour of the C_{18}-family of FAMEs was investigated by measuring high-pressure phase behaviour data and analysing the data to determine the potential for supercritical fluid fractionation. This satisfied Objectives 1 and 2. Thermodynamic modelling with predictive EOSs provided insight into the ability of models to adequately describe the influence of unsaturation on long-chain molecules in high-pressure systems. This satisfied Objective 3.

8.1. Reviewing the Objectives

Objective 1: The influence of unsaturation on the phase behaviour of binary FAME + CO₂ systems

HPBDP data were measured for three binary C_{18} FAME + CO_2 systems with differing degrees of unsaturation. The measured data extended the available literature data by covering a larger temperature range (both lower and higher temperatures than available in literature), as well as providing data in the critical region that was not present in the literature data. The newly measured data combined with a rigorous uncertainty analysis resolves the discrepancy between some of the available literature data sets.

Inspection of the measured data indicates a difference in solubility (difference in phase transition pressures) between the saturated and unsaturated FAMEs in CO_2, with methyl stearate (M18:0) having a lower solubility (higher phase transition pressures) than the unsaturated FAMEs. The solubility difference was found to decrease with an increase in temperature. The two unsaturated FAMEs – methyl oleate (M18:1) and methyl linoleate (M18:2) – have indistinguishable phase behaviour in CO_2 at all temperatures investigated. The correlation of molecular order (CMO) is proposed as an explanation for the observed solubility trends, whereby the saturated M18:0 experiences molecular orientation for better energetic contact, increasing the packing density, resulting in stronger attractive forces and higher phase transition pressures. The unsaturated FAMEs have *cis* C=C bonds which alter their geometry and does not allow for the CMO to take place, causing them to have lower phase transition pressures.

8. Conclusions

Objective 2.1: The influence of unsaturation in ternary saturated FAME + unsaturated FAME + CO₂ systems on solubility

Ternary HPBDP measurements were conducted to further investigate the solubility difference between M18:0 and M18:1. A linearly increasing trend was found between the phase transition pressures and the reduced weight fraction M18:0 on a solvent free basis. This indicated an absence of cosolvency between the two solute compounds. According to the CMO, the *cis* C=C bond in M18:1 can cause it to act as an order-breaking molecule. This diminishes the capacity for nearby M18:0 molecules to orient themselves for better energetic contact, resulting in lower phase transition pressures for mixtures with a higher methyl oleate content.

Objective 2.2: The influence of unsaturation in ternary saturated FAME + unsaturated FAME + CO₂ systems on the compositions of coexisting phases

Ternary high-pressure vapour-liquid equilibrium (VLE) data were measured at 35 °C, 55 °C, and 75 °C and an overall solvent-free methyl stearate content of about 50 % by mass over a range of pressures. The compositions of coexisting phases were determined by sampling and analysis with an on-line gas-chromatography system.

The relative solubilities (distribution of M18:0 relative to the distribution of M18:1) were found to be greater than one, indicating a preferential extraction of M18:0 into the vapour phase relative to M18:1. This might be a result of the M18:1 shielding the M18:0 molecules from the effect of the CMO. The relative solubility decreased with increasing pressure, approaching one.

The results of the relative solubility analysis suggest that supercritical CO_2 is capable of fractionating a mixture of M18:0 and M18:1. However, a rigorous uncertainty analysis indicated that there is a large degree of uncertainty in the calculated relative solubilities due to difficulties with the analyses of the coexisting phases.

The determined uncertainty makes it difficult to conclusively comment on the influence of unsaturation on the selectivity and compositions of coexisting phases, and it is believed that the experimental relative solubility data overestimates the true values.

Objective 3: The ability of predictive models to describe the influence of unsaturation on the phase behaviour of FAMEs in CO₂

The data measured in this work were modelled with the predictive Peng-Robinson (PPR) and modified Sanchez-Lacombe (MSL) equations of state (EOSs). The PPR model outperforms the MSL model quantitatively and qualitatively for the binary systems, obtaining a good prediction for the M18:2 +

CO_2 system with an AARD of 3.6 %. For the other binary systems, however, the PPR EOS still underpredicted the phase transition pressures.

Both models were unable to describe the influence of unsaturation on the binary phase behaviour. Similarly, neither model was able to reproduce the measured ternary data. The modelling performed in this work thus illustrates that simple PVT EOSs in their current form are not suitable to develop and design separation processes for (FAME + CO_2)-type systems where it is important to capture the slight solubility difference between components with differing degrees of unsaturation, but similar hydrocarbon backbone lengths and thus having similar critical properties and molar weights.

Taking together the discussion of Objectives 1,2, and 3:

- There exists a definite solubility difference between saturated and unsaturated C_{18} FAMEs in supercritical CO_2.
- There are no complex, nonideal interactions present in the system that lead to effects like cosolvency or temperature inversions.
- The measurement of ternary VLE data was complicated by analytical difficulties leading to large uncertainties in the relative solubility data that cast doubt on any conclusions drawn from the data.
- Thermodynamic modelling revealed that both the PPR and MSL models are unable to correctly predict or describe the influence of unsaturation on binary and ternary C_{18} FAME phase behaviour.

8.2. Recommendations

A few recommendations are presented as a result of the work done in this investigation:

- Measurement of ternary and higher-order VLE data for highly asymmetric systems such as the one studied in this work should not be conducted with an on-line chromatographic method. The simultaneous analysis of light and heavy species on the same analytical equipment introduces a large degree of uncertainty that could be avoided by making use of other analytical methods. For example, flashing samples prior to analysis would allow the quantification of the amount of gaseous solvent via gravimetry,[65,78] avoiding the analysis of CO_2 chromatographically, which was the main complicating factor in the VLE experiments.

8. Conclusions

- In order to obtain conclusive quantitative results on the selectivity between M18:0 and M18:1 in supercritical CO_2, the ternary VLE data for the M18:0 + M18:1 + CO_2 system should be remeasured by making use of a more appropriate analytical method for high-asymmetry systems as previously discussed. This would provide a more conclusive indication of the relative solubility trends, and shed more light on the correlation of molecular order argument presented in this work.

- The experimental difficulties experienced in this work, and the results obtained from the uncertainty analysis reinforce the importance of propagating the uncertainty in measured quantities to calculated quantities. A study into the influence of the uncertainty in phase behaviour data on the design of supercritical fluid fractionation processes would invaluable.

- The modelling performed with the PPR EOS illustrated its difficulty in predicting the solubility difference between saturated and unsaturated C_{18} FAMEs. Since the critical properties used in the model for the thermally labile FAMEs require estimation as they cannot be measured, it is recommended to investigate the use of alternative sets of critical properties/estimation methods to regress the group-contribution parameters. A set of critical properties that better describes the differences between the FAMEs with differing degrees of unsaturation may allow a model to better distinguish between them. Alternatively, other models that do not require critical properties at all such as SAFT-type EOSs may be considered. The description of the influence of unsaturation may also be improved by directly regressing binary interaction parameters for the Peng-Robinson EOS from the measured data.

References

(1)   sustainability -- Britannica Academic https://www.britannica.com/science/sustainability (accessed Oct 15, 2019).

(2)   natural resource management -- Britannica Academic https://www.britannica.com/topic/natural-resource-management (accessed Oct 15, 2019).

(3)   Staby, A.; Mollerup, J. Separation of Constituents of Fish Oil Using Supercritical Fluids: A Review of Experimental Solubility, Extraction, and Chromatographic Data. *Fluid Phase Equilibria* **1993**, *91* (2), 349–386. https://doi.org/10.1016/0378-3812(93)85109-Y.

(4)   Calder, P. C. Functional Roles of Fatty Acids and Their Effects on Human Health. *J. Parenter. Enter. Nutr.* **2015**, *39* (1S), 18S-32S. https://doi.org/10.1177/0148607115595980.

(5)   Herrero, M.; Sánchez-Camargo, A. del P.; Cifuentes, A.; Ibáñez, E. Plants, Seaweeds, Microalgae and Food by-Products as Natural Sources of Functional Ingredients Obtained Using Pressurized Liquid Extraction and Supercritical Fluid Extraction. *TrAC Trends Anal. Chem.* **2015**, *71*, 26–38. https://doi.org/10.1016/j.trac.2015.01.018.

(6)   Brunner, G. Supercritical Fluids: Technology and Application to Food Processing. *J. Food Eng.* **2005**, *67* (1), 21–33. https://doi.org/10.1016/j.jfoodeng.2004.05.060.

(7)   Riha, V.; Brunner, G. Phase Equilibrium of Fish Oil Ethyl Esters with Supercritical Carbon Dioxide. *J. Supercrit. Fluids* **1999**, *15* (1), 33–50. https://doi.org/10.1016/S0896-8446(98)00130-2.

(8)   Seader, J. D.; Henley, E. J.; Roper, D. K. *Separation Process Principles: Chemical and Biochemical Operations*, 3rd ed.; John Wiley & Sons: Hoboken, 2011.

(9)   Dohrn, R.; Fonseca, J. M. S.; Peper, S. Experimental Methods for Phase Equilibria at High Pressures. *Annu. Rev. Chem. Biomol. Eng.* **2012**, *3* (1), 343–367. https://doi.org/10.1146/annurev-chembioeng-062011-081008.

(10)   Riha, V.; Brunner, G. Separation of Fish Oil Ethyl Esters with Supercritical Carbon Dioxide. *J. Supercrit. Fluids* **2000**, *17* (1), 55–64. https://doi.org/10.1016/S0896-8446(99)00038-8.

(11)   Brunner, G. Calculation of Phase Equilibria and Their Relation to Separation with Supercritical Fluids. *J. Supercrit. Fluids* **2018**, *134*, 2–11. https://doi.org/10.1016/j.supflu.2017.12.031.

(12)   Pillar, R.; Ginic-Markovic, M.; Clarke, S.; Matisons, J. Effect of Alkyl Chain Unsaturation on Methyl Ester Thermo-Oxidative Decomposition and Residue Formation. *J. Am. Oil Chem. Soc.* **2009**, *86* (4), 363–373. https://doi.org/10.1007/s11746-009-1358-7.

References

(13) Shin, H.-Y.; Lim, S.-M.; Bae, S.-Y.; Oh, S. C. Thermal Decomposition and Stability of Fatty Acid Methyl Esters in Supercritical Methanol. *J. Anal. Appl. Pyrolysis* **2011**, *92* (2), 332–338. https://doi.org/10.1016/j.jaap.2011.07.003.

(14) Fan, P.; Wang, Y.; Shen, J.; Jiang, L.; Zhuang, W.; Han, Y.; Zhang, H. Self-Assembly Behaviors of C_{18} Fatty Acids in Arginine Aqueous Solution Affected by External Conditions. *Colloids Surf. Physicochem. Eng. Asp.* **2019**, *577*, 240–248. https://doi.org/10.1016/j.colsurfa.2019.05.087.

(15) Hąc-Wydro, K.; Jędrzejek, K.; Dynarowicz-Łątka, P. Effect of Saturation Degree on the Interactions between Fatty Acids and Phosphatidylcholines in Binary and Ternary Langmuir Monolayers. *Colloids Surf. B Biointerfaces* **2009**, *72* (1), 101–111. https://doi.org/10.1016/j.colsurfb.2009.03.019.

(16) Ikushima, Y.; Arai, M.; Hatakeda, K.; Ito, S.; Saito, N.; Goto, T. Selective Extraction of a Mixture of Stearic, Oleic, Linoleic, and Linolenic Acid Methyl Esters with Supercritical Carbon Dioxide Using a Gas-Flow Method. *J. Chem. Eng. Jpn.* **1988**, *21* (4), 439–441. https://doi.org/10.1252/jcej.21.439.

(17) Ikushima, Y.; Saito, N.; Goto, T. Selective Extraction of Oleic, Linoleic, and Linolenic Acid Methyl Esters from Their Mixture with Supercritical Carbon Dioxide-Entrainer Systems and a Correlation of the Extraction Efficiency with a Solubility Parameter. *Ind. Eng. Chem. Res.* **1989**, *28* (9), 1364–1369. https://doi.org/10.1021/ie00093a014.

(18) Rozzi, N. L.; Singh, R. K. Supercritical Fluids and the Food Industry. *Compr. Rev. Food Sci. Food Saf.* **2002**, *1* (1), 33–44. https://doi.org/10.1111/j.1541-4337.2002.tb00005.x.

(19) Jaubert, J.-N.; Coniglio, L.; Denet, F. From the Correlation of Binary Systems Involving Supercritical CO_2 and Fatty Acid Esters to the Prediction of (CO_2–Fish Oils) Phase Behavior. *Ind. Eng. Chem. Res.* **1999**, *38* (8), 3162–3171. https://doi.org/10.1021/ie980783l.

(20) Jaubert, J.-N.; Coniglio, L.; Crampon, C. Use of a Predictive Cubic Equation of State To Model New Equilibrium Data of Binary Systems Involving Fatty Acid Esters and Supercritical Carbon Dioxide. *Ind. Eng. Chem. Res.* **2000**, *39* (7), 2623–2626. https://doi.org/10.1021/ie0000360.

(21) Juntarachat, N.; Privat, R.; Coniglio, L.; Jaubert, J.-N. Development of a Predictive Equation of State for CO_2 + Ethyl Ester Mixtures Based on Critical Points Measurements. *J. Chem. Eng. Data* **2014**, *59* (10), 3205–3219. https://doi.org/10.1021/je5002494.

(22) Silberberg, M. S. *Principles of General Chemistry*, 3rd ed.; McGraw-Hill: New York, 2013.

(23) Otera, J. *Esterification: Methods, Reactions, and Applications*, 1st ed.; Wiley-VCH: Weinheim, 2003.

(24) Mishra, V. K.; Temelli, F.; Ooraikul, B. Extraction and Purification of ω-3 Fatty Acids with an Emphasis on Supercritical Fluid Extraction—A Review. *Food Res. Int.* **1993**, *26* (3), 217–226. https://doi.org/10.1016/0963-9969(93)90056-O.

(25) Lide, D. R. *CRC Handbook of Chemistry and Physics*, 79th ed.; CRC Press: Boca Raton, FL, 1998.

(26) Pino, A. M.; Rodríguez, J. P. Is Fatty Acid Composition of Human Bone Marrow Significant to Bone Health? *Bone* **2019**, *118*, 53–61. https://doi.org/10.1016/j.bone.2017.12.014.

(27) Staby, A.; Forskov, T.; Mollerup, J. Phase Equilibria of Fish Oil Fatty Acid Ethyl Esters and Sub- and Supercritical CO_2. *Fluid Phase Equilibria* **1993**, *87* (2), 309–340. https://doi.org/10.1016/0378-3812(93)85034-J.

(28) Aarthy, M.; Saravanan, P.; Ayyadurai, N.; Gowthaman, M. K.; Kamini, N. R. A Two Step Process for Production of Omega 3-Polyunsaturated Fatty Acid Concentrates from Sardine Oil Using Cryptococcus Sp. MTCC 5455 Lipase. *J. Mol. Catal. B Enzym.* **2016**, *125*, 25–33. https://doi.org/10.1016/j.molcatb.2015.12.013.

(29) Dörmő, N.; Bélafi-Bakó, K.; Bartha, L.; Ehrenstein, U.; Gubicza, L. Manufacture of an Environmental-Safe Biolubricant from Fusel Oil by Enzymatic Esterification in Solvent-Free System. *Biochem. Eng. J.* **2004**, *21* (3), 229–234. https://doi.org/10.1016/j.bej.2004.06.011.

(30) Sarkar, B.; Sridhar, S.; Saravanan, K.; Kale, V. Preparation of Fatty Acid Methyl Ester through Temperature Gradient Driven Pervaporation Process. *Chem. Eng. J.* **2010**, *162* (2), 609–615. https://doi.org/10.1016/j.cej.2010.06.005.

(31) Pouilloux, Y.; Autin, F.; Piccirilli, A.; Guimon, C.; Barrault, J. Preparation of Oleyl Alcohol from the Hydrogenation of Methyl Oleate in the Presence of Cobalt–Tin Catalysts. *Appl. Catal. Gen.* **1998**, *169* (1), 65–75. https://doi.org/10.1016/S0926-860X(97)00344-X.

(32) Linko, Y.-Y.; Lämsä, M.; Wu, X.; Uosukainen, E.; Seppälä, J.; Linko, P. Biodegradable Products by Lipase Biocatalysis. *J. Biotechnol.* **1998**, *66* (1), 41–50. https://doi.org/10.1016/S0168-1656(98)00155-2.

(33) Savaliya, M. L.; Dhorajiya, B. D.; Dholakiya, B. Z. Current Trends in Separation and Purification of Fatty Acid Methyl Ester. *Sep. Purif. Rev.* **2015**, *44* (1), 28–40. https://doi.org/10.1080/15422119.2013.872126.

(34) Mittelbach, M. Fuels from Oils and Fats: Recent Developments and Perspectives. *Eur. J. Lipid Sci. Technol.* **2015**, *117* (11), 1832–1846. https://doi.org/10.1002/ejlt.201500125.

(35) Ramos, M. J.; Fernández, C. M.; Casas, A.; Rodríguez, L.; Pérez, Á. Influence of Fatty Acid Composition of Raw Materials on Biodiesel Properties. *Bioresour. Technol.* **2009**, *100* (1), 261–268. https://doi.org/10.1016/j.biortech.2008.06.039.

References

(36)   Shahidi, F.; Wanasundara, U. N. Omega-3 Fatty Acid Concentrates: Nutritional Aspects and Production Technologies. *Trends Food Sci. Technol.* **1998**, *9* (6), 230–240. https://doi.org/10.1016/S0924-2244(98)00044-2.

(37)   Sánchez-Camargo, A. P.; Meireles, M. Â. A.; Ferreira, A. L. K.; Saito, E.; Cabral, F. A. Extraction of ω-3 Fatty Acids and Astaxanthin from Brazilian Redspotted Shrimp Waste Using Supercritical CO_2+Ethanol Mixtures. *J. Supercrit. Fluids* **2012**, *61*, 71–77. https://doi.org/10.1016/j.supflu.2011.09.017.

(38)   Liang, J.-H.; Hwang, L. S. Fractionation of Squid Visceral Oil Ethyl Esters by Short-Path Distillation. *J. Am. Oil Chem. Soc.* **2000**, *77* (7), 773–777. https://doi.org/10.1007/s11746-000-0123-4.

(39)   Fakhry, E. M.; El Maghraby, D. M. Fatty Acids Composition and Biodiesel Characterization of Dunaliella Salina. *J. Water Resour. Prot.* **2013**, *5* (9), 894–899. https://doi.org/10.4236/jwarp.2013.59091.

(40)   Schenk, P. M.; Thomas-Hall, S. R.; Stephens, E.; Marx, U. C.; Mussgnug, J. H.; Posten, C.; Kruse, O.; Hankamer, B. Second Generation Biofuels: High-Efficiency Microalgae for Biodiesel Production. *BioEnergy Res.* **2008**, *1* (1), 20–43. https://doi.org/10.1007/s12155-008-9008-8.

(41)   Salgın, Ul·.; Salgın, S.; Ekici, D. D.; Uludaŀ, G. Oil Recovery in Rosehip Seeds from Food Plant Waste Products Using Supercritical CO_2 Extraction. *J. Supercrit. Fluids* **2016**, *118*, 194–202. https://doi.org/10.1016/j.supflu.2016.08.011.

(42)   Ciftci, O. N.; Temelli, F. Continuous Biocatalytic Conversion of the Oil of Corn Distiller's Dried Grains with Solubles to Fatty Acid Methyl Esters in Supercritical Carbon Dioxide. *Biomass Bioenergy* **2013**, *54*, 140–146. https://doi.org/10.1016/j.biombioe.2013.03.031.

(43)   Raventós, M.; Duarte, S.; Alarcón, R. Application and Possibilities of Supercritical CO_2 Extraction in Food Processing Industry: An Overview. *Food Sci. Technol. Int.* **2002**, *8* (5), 269–284. https://doi.org/10.1106/108201302029451.

(44)   Reverchon, E.; De Marco, I. Supercritical Fluid Extraction and Fractionation of Natural Matter. *J. Supercrit. Fluids* **2006**, *38* (2), 146–166. https://doi.org/10.1016/j.supflu.2006.03.020.

(45)   Fang, T.; Goto, M.; Yun, Z.; Ding, X.; Hirose, T. Phase Equilibria for Binary Systems of Methyl Oleate–Supercritical CO_2 and α-Tocopherol–Supercritical CO_2. *J. Supercrit. Fluids* **2004**, *30* (1), 1–16. https://doi.org/10.1016/S0896-8446(03)00165-7.

(46)   Yu, Z.-R.; Singh, B.; Rizvi, S. S. H.; Zollweg, J. A. Solubilities of Fatty Acids, Fatty Acid Esters, Triglycerides, and Fats and Oils in Supercritical Carbon Dioxide. *J. Supercrit. Fluids* **1994**, *7* (1), 51–59. https://doi.org/10.1016/0896-8446(94)90006-X.

References

(47)   Espinosa, S.; Diaz, S.; Brignole, E. A. Thermodynamic Modeling and Process Optimization of Supercritical Fluid Fractionation of Fish Oil Fatty Acid Ethyl Esters. *Ind. Eng. Chem. Res.* **2002**, *41* (6), 1516–1527. https://doi.org/10.1021/ie010470h.

(48)   Rose, Arthur.; Schrodt, V. N. Vapor-Liquid Equilibria for the Methyl Oleate and Methyl Stearate Binary System. *J. Chem. Eng. Data* **1964**, *9* (1), 12–16. https://doi.org/10.1021/je60020a006.

(49)   Haley, J. D.; MCabe, C. Predicting the Phase Behavior of Fatty Acid Methyl Esters and Their Mixtures Using the GC-SAFT-VR Approach. *Fluid Phase Equilibria* **2016**, *411*, 43–52. https://doi.org/10.1016/j.fluid.2015.11.012.

(50)   Gray, E. L.; Cawley, J. D. The Influence of Structures on the Elimination Maximum - I: The Structure of Vitamin A2. *J. Biol. Chem.* **1940**, *134*, 397–401.

(51)   Nilsson, W. B.; Gauglitz, E. J.; Hudson, J. K.; Stout, V. F.; Spinelli, J. Fractionation of Menhaden Oil Ethyl Esters Using Supercritical Fluid CO_2. *J. Am. Oil Chem. Soc.* **1988**, *65* (1), 109–117. https://doi.org/10.1007/BF02542560.

(52)   Clifford, T. *Fundamentals of Supercritical Fluids*; Oxford University Press, 1999.

(53)   McHugh, M.; Krukonis, V. *Supercritical Fluid Extraction*, 2nd ed.; Butterworth-Heinemann, 1994.

(54)   Lemmon, E. W.; McLinden, M. O.; Friend, D. G. Thermophysical Properties of Fluid Systems. In *NIST Chemistry WebBook, NIST Standard Reference DatabaseNumber 69*; Lindstrom, P. J., Mallard, W. G., Eds.; National Institute of Standards and Technology: Gaithersburg, 2018.

(55)   Perretti, G.; Motori, A.; Bravi, E.; Favati, F.; Montanari, L.; Fantozzi, P. Supercritical Carbon Dioxide Fractionation of Fish Oil Fatty Acid Ethyl Esters. *J. Supercrit. Fluids* **2007**, *40* (3), 349–353. https://doi.org/10.1016/j.supflu.2006.07.020.

(56)   King, M. B.; Catchpole, O. J.; Bott, T. R. Energy and Economic Assessment of Near-Critical Extraction Processes. In *Extraction 90*; Batey, W., Ed.; Institution of Chemical Engineers, 1990; pp 165–186.

(57)   Perrut, M. Supercritical Fluid Applications: Industrial Developments and Economic Issues. *Ind. Eng. Chem. Res.* **2000**, *39* (12), 4531–4535. https://doi.org/10.1021/ie000211c.

(58)   Schwarz, C. E.; Schlechter, C.; Knoetze, J. H. High Pressure Phase Equilibria of Ethyl Esters in Supercritical Ethane and Propane. *J. Supercrit. Fluids* **2013**, *79*, 19–26. https://doi.org/10.1016/j.supflu.2013.02.023.

(59)   Shimizu, S.; Abbott, S. How Entrainers Enhance Solubility in Supercritical Carbon Dioxide. *J. Phys. Chem. B* **2016**, *120* (15), 3713–3723. https://doi.org/10.1021/acs.jpcb.6b01380.

References

(60)   Létisse, M.; Comeau, L. Enrichment of Eicosapentaenoic Acid and Docosahexaenoic Acid from Sardine By-Products by Supercritical Fluid Fractionation. *J. Sep. Sci.* **2008**, *31* (8), 1374–1380. https://doi.org/10.1002/jssc.200700501.

(61)   van Konynenburg, P. H.; Scott, R. L.; Rowlinson, J. S. Critical Lines and Phase Equilibria in Binary van Der Waals Mixtures. *Philos. Trans. R. Soc. Lond. Ser. Math. Phys. Sci.* **1980**, *298* (1442), 495–540. https://doi.org/10.1098/rsta.1980.0266.

(62)   Bolz, A.; Deiters, U. K.; Peters, C. J.; de Loos, T. W. Nomenclature for Phase Diagrams with Particular Reference to Vapour–Liquid and Liquid–Liquid Equilibria (Technical Report). *Pure Appl. Chem.* **1998**, *70* (11), 2233–2258. https://doi.org/10.1351/pac199870112233.

(63)   De Loos, T. W. Understanding Phase Diagrams. In *Supercritical Fluids: Fundamentals for Application*; Kiran, E., Levelt Sengers, J. M., Eds.; Kluwer Academic Publishers: Dordrecht, 1994; pp 65–89.

(64)   Soto, G.; Hegel, P.; Pereda, S. Supercritical Production and Fractionation of Fatty Acid Esters and Acylglycerols. *J. Supercrit. Fluids* **2014**, *93*, 74–81. https://doi.org/10.1016/j.supflu.2014.04.017.

(65)   Inomata, H.; Kondo, T.; Hirohama, S.; Arai, K.; Suzuki, Y.; Konno, M. Vapour—Liquid Equilibria for Binary Mixtures of Carbon Dioxide and Fatty Acid Methyl Esters. *Fluid Phase Equilibria* **1989**, *46* (1), 41–52. https://doi.org/10.1016/0378-3812(89)80273-0.

(66)   Bluma, M.; Deiters, U. K. A Classification of Phase Diagrams of Ternary Fluid Systems. *Phys. Chem. Chem. Phys.* **1999**, *1* (18), 4307–4313. https://doi.org/10.1039/A904863D.

(67)   Schneider, G. M. Physico-Chemical Properties and Phase Equilibria of Pure Fluids and Fluid Mixtures at High Pressures. In *Supercritical Fluids: Fundamentals for Application*; Kiran, E., Levelt Sengers, J. M., Eds.; Kluwer Academic Publishers: Dordrecht, 1994; pp 91–115.

(68)   Pöhler, H. Fluidphasengleichgewichte Binärer Und Ternärer Kohlendioxidmischungen Mit Schwerflüchtigen Organischen Substanzen Bei Temperaturen von 303 K Bis 393 K Und Drücken von 10 MPa Bis 100 MPa. PhD Dissertation, Ruhr-Universität Bochum, Bochum, 1994.

(69)   Scheidgen, A. L.; Schneider, G. M. Fluid Phase Equilibria of (Carbon Dioxide + a 1-Alkanol+ an Alkane) up to 100 MPa AndT=393 K: Cosolvency Effect, Miscibility Windows, and Holes in the Critical Surface. *J. Chem. Thermodyn.* **2000**, *32* (9), 1183–1201. https://doi.org/10.1006/jcht.1999.0590.

(70)   Scheidgen, A. L.; Schneider, G. M. Complex Phase Equilibrium Phenomena in Fluid Ternary Mixtures up to 100 MPa: Cosolvency, Holes, Windows, and Islands—Review and New Results. *Fluid Phase Equilibria* **2002**, *194–197*, 1009–1028. https://doi.org/10.1016/S0378-3812(01)00695-1.

(71) Scheidgen, A. Fluidphasengleichgewichte Binärer Und Ternärer Kohlendioxidmischungen Mit Schwerflüchtigen Organischen Substanzen Bis 100 MPa. PhD Dissertation, Ruhr-Universität Bochum, Bochum, 1997.

(72) Zou, M.; Yu, Z. R.; Kashulines, P.; Rizvi, S. S. H.; Zollweg, J. A. Fluid-Liquid Phase Equilibria of Fatty Acids and Fatty Acid Methyl Esters in Supercritical Carbon Dioxide. *J. Supercrit. Fluids* **1990**, *3* (1), 23–28. https://doi.org/10.1016/0896-8446(90)90046-O.

(73) Yu, Z.-R.; Rizvi, S. S. H.; Zollweg, J. A. Phase Equilibria of Oleic Acid, Methyl Oleate, and Anhydrous Milk Fat in Supercritical Carbon Dioxide. *J. Supercrit. Fluids* **1992**, *5* (2), 114–122. https://doi.org/10.1016/0896-8446(92)90028-I.

(74) Chang, C. J.; Lee, M.; Li, B.; Chen, P. Vapor–Liquid Equilibria and Densities of CO_2 with Four Unsaturated Fatty Acid Esters at Elevated Pressures. *Fluid Phase Equilibria* **2005**, *233* (1), 56–65. https://doi.org/10.1016/j.fluid.2005.04.008.

(75) Crampon, C.; Charbit, G.; Neau, E. High-Pressure Apparatus for Phase Equilibria Studies: Solubility of Fatty Acid Esters in Supercritical CO_2. *J. Supercrit. Fluids* **1999**, *16* (1), 11–20. https://doi.org/10.1016/S0896-8446(99)00021-2.

(76) Adams, W. R.; Zollweg, J. A.; Streett, W. B.; Rizvi, S. S. H. New Apparatus for Measurement of Supercritical Fluid-Liquid Phase Equilibria. *AIChE J.* **1988**, *34* (8), 1387–1391. https://doi.org/10.1002/aic.690340820.

(77) Liong, K. K.; Foster, N. R.; Ting, S. S. T. Solubility of Fatty Acid Esters in Supercritical Carbon Dioxide. *Ind. Eng. Chem. Res.* **1992**, *31* (1), 400–404. https://doi.org/10.1021/ie00001a054.

(78) Bharath, R.; Inomata, H.; Arai, K.; Shoji, K.; Noguchi, Y. Vapor-Liquid Equilibria for Binary Mixtures of Carbon Dioxide and Fatty Acid Ethyl Esters. *Fluid Phase Equilibria* **1989**, *50* (3), 315–327. https://doi.org/10.1016/0378-3812(89)80298-5.

(79) Zou, M.; Yu, Z. R.; Rizvi, S. S. H.; Zollweg, J. A. Fluid-Liquid Equilibria of Ternary Systems of Fatty Acids and Fatty Acid Esters in Supercritical CO_2. *J. Supercrit. Fluids* **1990**, *3* (2), 85–90. https://doi.org/10.1016/0896-8446(90)90012-B.

(80) Fourie, F. C. v. N.; Schwarz, C. E.; Knoetze, J. H. Phase Equilibria of Alcohols in Supercritical Fluids: Part I. The Effect of the Position of the Hydroxyl Group for Linear C_8 Alcohols in Supercritical Carbon Dioxide. *J. Supercrit. Fluids* **2008**, *47* (2), 161–167. https://doi.org/10.1016/j.supflu.2008.07.001.

(81) Schwarz, C. E.; Nieuwoudt, I. Phase Equilibrium of Propane and Alkanes: Part I. Experimental Procedures, Dotriacontane Equilibrium and EOS Modelling. *J. Supercrit. Fluids* **2003**, *27* (2), 133–144. https://doi.org/10.1016/S0896-8446(02)00232-2.

References

(82)   Latsky, C.; Kouakou, A. C.; Schwarz, C. E. Phase Equilibria of CO_2 with Components in the Light Naphtha Cut of Tyre Derived Oil. *J. Supercrit. Fluids* **2018**, *131*, 58–65. https://doi.org/10.1016/j.supflu.2017.08.016.

(83)   Chang, C. J.; Chiu, K.-L.; Day, C.-Y. A New Apparatus for the Determination of P–x–y Diagrams and Henry's Constants in High Pressure Alcohols with Critical Carbon Dioxide. *J. Supercrit. Fluids* **1998**, *12* (3), 223–237. https://doi.org/10.1016/S0896-8446(98)00076-X.

(84)   Weng, W. L.; Lee, M. J. Phase Equilibrium Measurements for the Binary Mixtures of 1-Octanol plus CO_2, C_2H_6 and C_2H_4. *Fluid Phase Equilibria* **1992**, *73* (1), 117–127. https://doi.org/10.1016/0378-3812(92)85042-7.

(85)   Working Group 1 of the Joint Committee for Guides in Metrology. Evaluation of Measurement Data – Guide to the Expression of Uncertainty in Measurement. 2008.

(86)   Fourie, F. C. v N.; Schwarz, C. E.; Knoetze, J. H. Analytic Setup for Multicomponent High-Pressure Phase Equilibria via Dual Online Gas Chromatography. *Chem. Eng. Technol.* **2015**, *38* (7), 1165–1172. https://doi.org/10.1002/ceat.201400643.

(87)   Fourie, F. C. v N.; Schwarz, C. E.; Knoetze, J. H. Analytic High-Pressure Phase Equilibria. Part II: Gas Chromatography and Sampling Method Development. *Chem. Eng. Technol.* **2016**, *39* (8), 1475–1482. https://doi.org/10.1002/ceat.201500633.

(88)   Fourie, F. C. van N.; Schwarz, C. E.; Knoetze, J. H. CO_2+n-Dodecane+3,7-Dimethyl-1-Octanol: High Pressure Experimental Phase Equilibria Data and Thermodynamic Modelling. *J. Supercrit. Fluids* **2017**, *130*, 105–117. https://doi.org/10.1016/j.supflu.2017.07.027.

(89)   Fourie, F. C. v. N. The High Pressure Phase Behaviour of Detergent Range Alcohols and Alkanes. PhD Dissertation, Stellenbosch University, 2018.

(90)   Novak, J. P.; Matous, J.; Rehak, K. Liquid-Liquid Equilibrium. In *Measurement of the Thermodynamic Properties of Multiple Phases*; Weir, R. D., De Loos, T. W., Eds.; International Union of Pure and Applied Chemistry, 2005; pp 177–200.

(91)   Felinger, A. *Data Analysis and Signal Processing in Chromatography*; Elsevier: Amsterdam, 1998.

(92)   Le Saux, T.; Varenne, A.; Gareil, P. Peak shape modeling by Haarhoff-Van der Linde function for the determination of correct migration times: A new insight into affinity capillary electrophoresis. *ELECTROPHORESIS* **2005**, *26* (16), 3094–3104. https://doi.org/10.1002/elps.200500029.

(93)   Grushka, Eli.; Israeli, Dror. Characterization of Overlapped Chromatographic Peaks by the Second Derivative. The Limit of the Method. *Anal. Chem.* **1990**, *62* (7), 717–721. https://doi.org/10.1021/ac00206a014.

(94)   Gilat, A.; Subramaniam, V. *Numerical Methods for Engineers and Scientists*, 3rd ed.; John Wiley & Sons, 2014.

(95)   Gallant, S. R.; Fraleigh, S. P.; Cramer, S. M. Deconvolution of Overlapping Chromatographic Peaks Using a Cerebellar Model Arithmetic Computer Neural Network. *Chemom. Intell. Lab. Syst.* **1993**, *18* (1), 41–57. https://doi.org/10.1016/0169-7439(93)80043-H.

(96)   James, G.; Witten, D.; Hastie, T.; Tibshirani, R. *An Introduction to Statistical Learning: With Applications in R*; Springer Science & Business Media, 2017.

(97)   Charlet, G.; Delmas, G. Thermodynamic Properties of Polyolefin Solutions at High Temperature: 1. Lower Critical Solubility Temperatures of Polyethylene, Polypropylene and Ethylene-Propylene Copolymers in Hydrocarbon Solvents. *Polymer* **1981**, *22* (9), 1181–1189. https://doi.org/10.1016/0032-3861(81)90130-0.

(98)   Fischer, E. W.; Strobl, G. R.; Dettenmaier, M.; Stamm, M.; Steidle, N. Molecular Orientational Correlations and Local Order in N-Alkane Liquids. *Faraday Discuss. Chem. Soc.* **1979**, *68* (0), 26–45. https://doi.org/10.1039/DC9796800026.

(99)   Keeler, J.; Wothers, P. *Chemical Structure and Reactivity: An Integrated Approach*; OUP Oxford, 2014.

(100)   Gocen, T.; Bayarı, S. H.; Guven, M. H. Effects of Chemical Structures of Omega-6 Fatty Acids on the Molecular Parameters and Quantum Chemical Descriptors. *J. Mol. Struct.* **2018**, *1174*, 142–150. https://doi.org/10.1016/j.molstruc.2018.04.075.

(101)   Kontogeorgis, G. M.; Folas, G. K. *Thermodynamic Models for Industrial Applications: From Classical and Advanced Mixing Rules to Association Theories*; John Wiley & Sons, 2010.

(102)   Schwarz, C. E. High Pressure Phase Equilibria of the CO_2/Saturated Ethyl Esters Homologous Series. *J. Chem. Eng. Data* **2018**, *63* (4), 1006–1020. https://doi.org/10.1021/acs.jced.7b00780.

(103)   Borges, G. R.; Junges, A.; Franceschi, E.; Corazza, F. C.; Corazza, M. L.; Oliveira, J. V.; Dariva, C. High-Pressure Vapor–Liquid Equilibrium Data for Systems Involving Carbon Dioxide + Organic Solvent + β-Carotene. *J. Chem. Eng. Data* **2007**, *52* (4), 1437–1441. https://doi.org/10.1021/je700125v.

(104)   Hwu, W.-H.; Cheng, J.-S.; Cheng, K.-W.; Chen, Y.-P. Vapor–Liquid Equilibrium of Carbon Dioxide with Ethyl Caproate, Ethyl Caprylate and Ethyl Caprate at Elevated Pressures. *J. Supercrit. Fluids* **2004**, *28* (1), 1–9. https://doi.org/10.1016/S0896-8446(03)00028-7.

(105)   Dohrn, R.; Peper, S.; Fonseca, J. M. S. High-Pressure Fluid-Phase Equilibria: Experimental Methods and Systems Investigated (2000–2004). *Fluid Phase Equilibria* **2010**, *288* (1), 1–54. https://doi.org/10.1016/j.fluid.2009.08.008.

References

(106) Fonseca, J. M. S.; Dohrn, R.; Peper, S. High-Pressure Fluid-Phase Equilibria: Experimental Methods and Systems Investigated (2005–2008). *Fluid Phase Equilibria* **2011**, *300* (1), 1–69. https://doi.org/10.1016/j.fluid.2010.09.017.

(107) Peper, S.; Fonseca, J. M. S.; Dohrn, R. High-Pressure Fluid-Phase Equilibria: Trends, Recent Developments, and Systems Investigated (2009–2012). *Fluid Phase Equilibria* **2019**, *484*, 126–224. https://doi.org/10.1016/j.fluid.2018.10.007.

(108) Exner, O.; Bapçum, A. Dipole Moments Induced in Larger Molecule. Long-Chain Aliphatic Esters. *Collect. Czechoslov. Chem. Commun.* **1982**, *47* (1), 29–34. https://doi.org/10.1135/cccc19820029.

(109) Abboud, J.-L. M.; Notario, R. Critical Compilation of Scales of Solvent Parameters. Part I. Pure, Non-Hydrogen Bond Donor Solvents. *Pure Appl. Chem.* **1999**, *71* (4), 645–718.

(110) Stenutz, R. Tables of Organic Chemistry. 2015.

(111) Gray, C. G.; Gubbins, K. E. *Theory of Molecular Fluids*; Oxford University Press: Oxford, 1984.

(112) Raal, J. D.; Mühlbauer, A. L. *Phase Equilibria: Measurement and Computation*; Taylor & Francis: Washington, 1998.

(113) Walas, S. M. *Phase Equilibria in Chemical Engineering*; Butterworth-Heinemann, 1985.

(114) Dahm, K. D.; Visco, D. P. *Fundamentals of Chemical Engineering Thermodynamics*; Cengage Learning, 2015.

(115) Peng, D.-Y.; Robinson, D. B. A New Two-Constant Equation of State. *Ind. Eng. Chem. Fundam.* **1976**, *15* (1), 59–64. https://doi.org/10.1021/i160057a011.

(116) Peneloux, A.; Abdoul, W.; Rauzy, E. Excess Functions and Equations of State. *Fluid Phase Equilibria* **1989**, *47* (2), 115–132. https://doi.org/10.1016/0378-3812(89)80172-4.

(117) Abdoul, W.; Rauzy, E.; Péneloux, A. Group-Contribution Equation of State for Correlating and Predicting Thermodynamic Properties of Weakly Polar and Non-Associating Mixtures: Binary and Multicomponent Systems. *Fluid Phase Equilibria* **1991**, *68*, 47–102. https://doi.org/10.1016/0378-3812(91)85010-R.

(118) Krenz, R. A.; Laursen, T.; Heidemann, R. A. The Modified Sanchez–Lacombe Equation of State Applied to Polydisperse Polyethylene Solutions. *Ind. Eng. Chem. Res.* **2009**, *48* (23), 10664–10681. https://doi.org/10.1021/ie801451a.

(119) Gauter, K.; Heidemann, R. A. A Proposal for Parametrizing the Sanchez–Lacombe Equation of State. *Ind. Eng. Chem. Res.* **2000**, *39* (4), 1115–1117. https://doi.org/10.1021/ie990800m.

(120) Laursen, T. *VLXE|Blend Version 9.3*.

References

(121)   Design Institute for Physical Property Data (U.S.); American Institute of Chemical Engineers; National Institute of Standards and Technology (U.S.). *DIPPR Chemical Database.*; BYU DIPPR, Thermophysical Properties Laboratory: Provo, UT, 1998.

(122)   Swanepoel, R. M. Improving the Fluid Phase-Boundary Predictions of (Solvent + LLDPE) Systems of Commercial Interest. PhD Dissertation, Stellenbosch University, 2020.

(123)   Spencer, C. F.; Danner, R. P. Improved Equation for Prediction of Saturated Liquid Density. *J. Chem. Eng. Data* **1972**, *17* (2), 236–241. https://doi.org/10.1021/je60053a012.

(124)   Li, C. C. Critical Temperature Estimation for Simple Mixtures. *Can. J. Chem. Eng.* **1971**, *49* (5), 709–710. https://doi.org/10.1002/cjce.5450490529.

(125)   Felder, R. M.; Rousseau, R. W. *Elementary Principles of Chemical Processes*, 3rd ed.; John Wiley & Sons: Hoboken, 2000.

APPENDIX A:
Detailed Experimental Procedure

A.1. Measurement of High-Pressure Bubble and Dew points

A.1.1. Loading

1. Inspect cell to ensure it is clean.

2. Rotate cell to a vertical position and add stirrer bar to cell.

3. Close the cell valve.

4. Weigh off the required amount of solute. Solid solutes are weighed off onto a weighing boat, whilst liquid solutes are weighed into a 50 mL beaker with a pipette.

5. Add the solute to the cell.

6. Use compressed air to remove any dust from the piston head. Move the piston shaft so that it is fully extended. Screw piston onto cell.

7. Tighten locknut on piston shaft to seal the cell.

8. Rotate cell to a horizontal position and insert PTFE scope guide into sight glass opening.

9. Insert endoscope fully into the PTFE scope guide.

10. Ensure that there is a seal on the cell outlet line. Attach the loading manifold to the cell outlet line. Figure A-1 shows a representation of the manifold.

A. Detailed Experimental Procedure
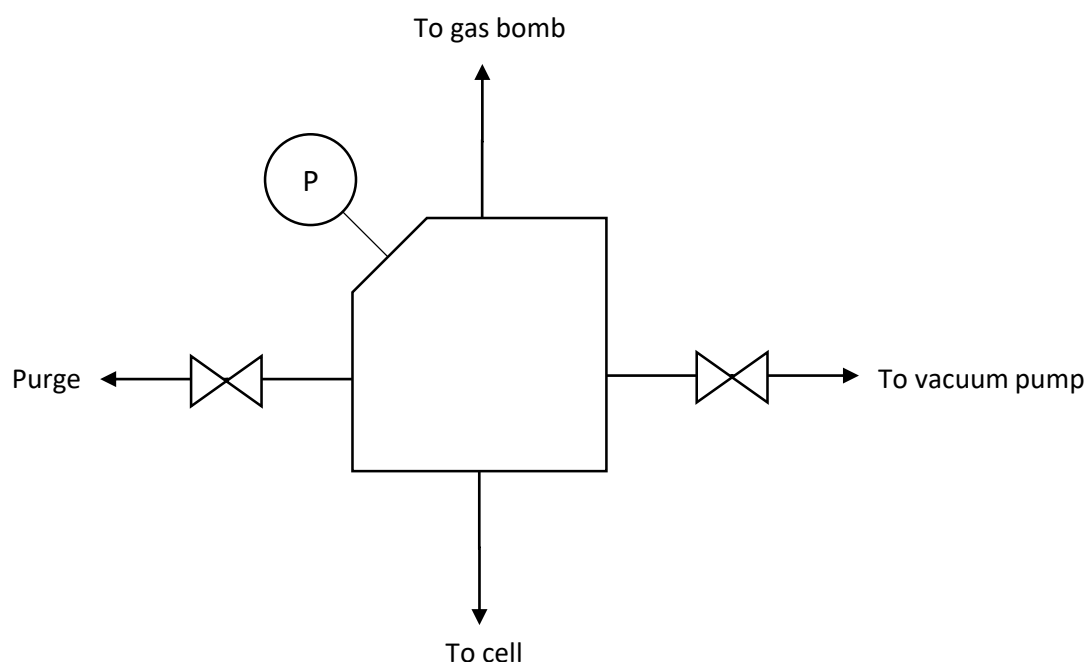
Figure A.1: Schematic representation of loading manifold

11. Remove gas bomb from the refrigerator and wipe off any condensation or ice crystals.

12. To load the gas bomb with CO_2, attach it to the CO_2 cylinder with both valves closed. Flush the connecting line by rapidly opening and closing the cylinder valve, and then loosening the nut to flush any gas out. Repeat this ten times.

13. Now open the cylinder valve. Open and close the top valve of the gas bomb to load the bomb with a purge. Release the purge by opening the bottom valve on the bomb. Do this twice.

14. Now open the top valve on the gas bomb for 20 seconds. Close the top valve, and then close the cylinder valve.

15. Before removing the bomb from the cylinder ensure that the cylinder valve is closed. Loosen the nut to let out the gas in the connecting line, and remove the bomb from the cylinder.

16. Weigh the bomb to make sure that it has been loaded with enough CO_2. Attach the bomb to the manifold, making sure that all valves on the bomb, manifold, and cell are closed.

17. Switch on the camera and the light source. Switch on the vacuum pump.

18. Position the endoscope for adequate visibility of the cell.

19. Switch on the manifold pressure gauge. Open the valve to the vacuum pump and hold for 5 seconds. Close the valve to the vacuum pump. Zero the pressure gauge on 0.0 bar absolute. Open the manifold purge valve to the atmosphere to check that the pressure gauge now reads 1.0 bar. Open the valve to vacuum until the pressure gauge reads zero. Then close the valve again.

20. Purge the cell with CO_2. This is done by quickly opening and closing the bottom valve on the gas bomb. Carefully open the cell inlet valve to load the cell with gas. Monitor this process on the camera display screen. Purge the cell by opening the manifold purge valve slowly until the pressure gauge reads close to 1.0 bar. Close the purge valve and the cell valve. Do this five times to ensure that no air remains in the cell.

21. Remove the gas bomb from the manifold. Weigh the bomb and note the mass. Vent gas from the bomb until the mass equals the desired loading of gas plus the empty bomb mass. The empty bomb mass is determined from experience.

22. Reattach the gas bomb to the manifold. Open the cell valve. Open the vacuum line valve to evacuate the cell to 0.0 bar. Close the vacuum line valve. Close the cell valve. Switch off the vacuum pump.

23. Plug in and ready the hairdryer. Open the bottom valve on the gas bomb. Open the cell inlet valve. Switch on the hairdryer. Use the hairdryer to heat up the gas bomb from top to bottom until the pressure reading stabilises. Close the bottom valve on the gas bomb. Now use the hairdryer to heat up the manifold and connecting lines until the pressure stabilises. Close the cell valve. This process ensures that no liquid CO_2 remains in the manifold or connecting lines, and allows loading the maximum amount of CO_2.

24. Use the infrared surface thermometer to note the temperature of the manifold, and simultaneously note the pressure of the manifold.

25. Vent the manifold by opening the purge valve.

26. Remove the gas bomb from the manifold, and remove the manifold from the cell. Switch off the manifold pressure gauge. Attach the blind nut to the cell outlet.

27. Weigh the gas bomb and note the mass.

28. Position the metal insulation enclosure around the cell, with the magnetic stirrer underneath. Switch on the magnetic stirrer, and confirm on the screen that the stirrer bar is stirring.

29. Set the water bath to the first temperature and switch it on. (Switch water bath pump on as well if necessary).

30. Insert the temperature probe into the thermo-well of the cell. Pack the glass fibre insulation into the enclosure as tightly as possible to ensure adequate insulation.

31. Attach the nitrogen line to the port on the piston. Open the nitrogen cylinder and increase the pressure on the regulator until the contents of the cell is compressed into a single phase. Do a last visual inspection of the screen to ensure that the stirrer bar is stirring adequately

A. Detailed Experimental Procedure

and that only one phase is present. Switch off the light source. The cell can now be left to attain thermal equilibrium. Allow about 45 min for this.

A.1.2. Measurement

1. Once the cell has reached thermal equilibrium, measurement can start. Switch on the light source. Reduce the pressure on the regulator in large increments until the phase transition is observed.

2. Recompress the contents of the cell to a single phase again.

3. Keep reducing the pressure, observing the phase transition, and recompressing in progressively smaller increments until the phase transition pressure can be determined to within about 0.2 to 0.3 bar repeatedly.

4. Recompress the cell contents to at least 20.0 bar above the phase transition pressure.

5. Set the water bath to the next temperature, and switch off the light source. Allow another 45 min for equilibration.

6. Repeat 1 – 5 until all points have been measured.

A.1.3. Cleaning

1. After all points have been measured, switch off the stirrer, water bath, light source, camera, and display screen. Remove all pressure from the cell by taking the pressure on the regulator to zero. Close the nitrogen cylinder.

2. Remove the nitrogen line form the piston.

3. Remove all insulation from the enclosure, and remove the enclosure and the magnetic stirrer.

4. Wait for the cell to cool down to 50 ˚C.

5. Once the cell is cool enough to work with, remove the temperature probe, PTFE scope guide, and the blind nut.

6. Rotate the cell to a 45˚ position with the outlet pointing down, and the piston pointing upwards.

7. Position the extractor above the cell.

8. Position an open bottle over the cell outlet to collect any solute for reuse, whilst using a small spanner to carefully open the cell outlet valve until the cell has been emptied.

9. Close the cell valve and rotate the cell to a vertical position.

10. Loosen the locknut on the piston shaft, and unscrew the piston from the cell. Lift off the piston and set it aside.

11. Rotate the cell to remove the stirrer bar, and return the cell to a vertical position.

12. Rinse the stirrer bar with isopropyl alcohol, followed by methanol, dry with paper towel, and place it in the storage container.

13. Fill the cell with isopropyl alcohol, open the valve, and allow the solvent to drain into a waste container.

14. Close the cell valve, fill with methanol, and again open the valve and allow drainage into a waste container.

15. Close the cell valve and rotate into a 45˚ position, with the sight glass pointing upwards.

16. Open the cell valve. Blow compressed air through the cell outlet. Blow compressed air into the cell opening.

17. Place a waste container under the cell opening. Rinse the inside of the cell with isopropyl alcohol. Blow the cell dry through the outlet and the opening.

18. Rinse the inside of the cell with methanol. Blow the cell dry through the outlet and the opening.

19. Roll up some paper towel and use it to dry the inside of the cell and sight glass until it is visibly dry.

20. Blow compressed air into the cell to check whether any liquid is still trapped in the crevices, particularly around the sight glass. If any wetness is observed, roll another piece of paper towel and repeat the process until the cell remains dry after blowing with compressed air.

21. Clean the piston head by rinsing with isopropyl alcohol and methanol. Blow dry with compressed air, and use a piece of paper towel dry between the piston head and PTFE seal.

22. Clean any glassware and weighing boats used by rinsing with isopropyl alcohol and methanol.

A.1.4. Pressure calibration

1. Rotate the cell to a vertical position, add the stirrer bar, and check that the cell valve is closed.

2. Completely fill the cell with water.

3. Attach the piston onto the cell. Tighten the locknut on the piston shaft to seal the cell.

4. Rotate the cell to a horizontal position and set up the cell for measurement as detailed in Appendix A.1.1 from Step 28. This includes insulating the cell and placing the magnetic stirrer. Do not attach the nitrogen line to the piston.

5. Switch on the camera, light source, and display screen.

6. Insert the PTFE scope guide into the sight glass, and then insert the endoscope into the guide. Confirm visually that there are no air bubbles present.

A. Detailed Experimental Procedure

7. Check that the calibrated dead weight tester dispenses oil. If necessary, load more oil from the reservoir by placing a finger over the outlet, turning the hand pump completely anti-clockwise, and then opening and closing the oil reservoir.

8. Check that the dead weight tester is level. Connect the tester to the cell valve.

9. Place 35 bar of weights onto the tester, and adjust the height with the help of the height gauge.

10. Set the water bath to the correct set point for the first temperature (35 ˚C), and switch on the magnetic stirrer.

11. Allow 45 min – 1 h for thermal equilibrium.

12. Remove the weights and all pressure from the tester by turning the hand pump anti-clockwise completely.

13. The dead weight tester platform corresponds to a 5 bar weight, and is the first point measured. Elevate the platform to the correct height using the height gauge whilst spinning the platform periodically so that it remains in motion. Record the indicated pressure and the indicated temperature.

14. Add the next weight, and whilst maintaining the spinning motion, adjust the height again. Record the pressure and temperature again.

15. Repeat step 14 until an applied pressure of 260 bar is reached. Note that it is important to only increase the weight so as to avoid hysteresis errors.

16. Once the 260 bar measurement has been made, add another weight to take it to 275 bar and adjust the height.

17. Now remove the top weight and lower the tester platform with the hand pump. Record the pressure and temperature. Maintain a spinning motion during measurement.

18. Repeat step 17 until all the weights have been removed, and all points recorded. Note that it is important to only decrease the weight so as to avoid hysteresis errors.

19. Repeat steps 12 to 18.

20. Repeat steps 10 to 19 for temperatures of 45 ˚C, 55 ˚C, 65 ˚C, and 75 ˚C.

21. Clean the cell as detailed in Appendix A.1.3.

A.1.5. Volume calibration

1. Set up the cell as for a loading detailed in Appendix A.1.1. but do not add any solute. Do not remove the manifold after loading, and reattach the gas bomb to the manifold after weighing the bomb after loading the CO_2. Do not pressurize the cell contents into a liquid phase. The volume calibration is only conducted at one temperature (55 ˚C).

2. Make sure to evacuate the manifold before starting the calibration.

3. Attach the electronic Vernier scale to the piston shaft and zero it – it is very important to do this before applying any pressure to the cell.

4. Once the cell is at thermal equilibrium, the measurements can start. Record the indicated cell pressure, the cell temperature, the manifold pressure, the manifold temperature, and the piston position (with the Vernier).

5. Now increase the pressure by adjusting the regulator on the nitrogen cylinder. Start with a 0.1 bar increase and record the required values.

6. Gradually increase the pressure increments, trying to not have the piston move more than 5 mm per increment, and recording the values.

7. Continue to do this until piston position does not change anymore.

8. Remove all pressure from the cell, and remeasure the "zero" point.

9. The volume of both the cell and the manifold will now be calibrated.

10. Repeat steps 4 to 8.

11. Clean the cell according to Appendix A.1.3.

A.2. Measurement of High-Pressure VLE Data

A.2.1. Loading

1. Switch on the vacuum pump, water bath, camera, and light source.

2. Clean out cell with compressed air.

3. Close the feed-line microvalve.

4. Insert magnetic stirrer bar into cell.

5. Position the piston into with the help of the lift.

6. Push piston into cell, and turn piston onto the thread.

7. Tighten the Teflon piston seal by tightening the locknuts on the piston shaft.

8. Set the water bath temperature to 35 °C.

9. Tighten ROLSI screws, and close the bottom microvalve.

10. Tighten the sight glass seal.

11. Open the vacuum pump line valve to draw vacuum in the cell. Check the pressure to ensure that vacuum is being drawn.

12. Close vacuum line.

13. Connect nitrogen line to piston.

14. Remove the feed-line microvalve.

15. Fill a syringe with about 23 mL of the premade mixture of solutes to be measured.

16. Insert the syringe into the feed line, and empty contents into the cell.

A. Detailed Experimental Procedure

17. Check the tip of the syringe for droplets before removing it.

18. Replace the feed-line microvalve.

19. Turn on the stirrer.

20. Load the solvent gas cylinder similarly to the gas bomb loading in section A.1.1.

21. Place the loaded cylinder on the stand and heat with the hairdryer. Wipe any condensation off.

22. Heat until pressure increases to about 250 bar.

23. Remove the stirrer plate.

24. Close the back microvalve.

25. Attach the gas cylinder to the bottom of the cell feed line.

26. Draw vacuum in the cell and cylinder connecting line.

27. Close the back microvalve to stop drawing vacuum.

28. Quickly open and close the gas cylinder valve to load the feed line with a CO_2 flush.

29. Open the feed-line microvalve to load the flush into the cell.

30. Vent the flush by opening and closing the back microvalve.

31. Close the feed-line microvalve.

32. Flush the cell with CO_2 a further three times.

33. Disconnect gas cylinder and replace the stirrer plate.

34. Draw vacuum and switch on stirring to ensure no CO_2 is dissolved in the solutes.

35. Close vacuum line and remove stirrer plate.

36. Reconnect the gas cylinder.

37. Draw vacuum and open the feed-line microvalve to remove air from the feed line.

38. Close the feed-line microvalve.

39. Open the gas cylinder whilst heating.

40. Carefully open the feed-line microvalve to load CO_2 into the cell.

41. Once the desired liquid-level has been reached, close the gas cylinder valve.

42. Close the feed-line microvalve.

43. Check all the valves to ensure they are closed tightly.

44. Tighten sight glass.

45. Place stirrer plate into position and place baffle plates in the enclosure.

46. Switch on stirrer.

47. Attach oven panels.

48. Connect the heating ducts to the oven enclosure.

49. Position scope to view cell contents.

50. Switch on the oven, and wait for it to stabilise.

A.2.2. Measurement

Setup

1. Adjust the pressure to the setpoint.

2. Switch on the GC in "sleep mode" to heat up the inlets, detectors, etc.

3. Switch on camera and light source.

4. Turn on the thermal regulators to heat the ROLSIs and transfer lines.

5. Switch on the data logger and its software.

6. Switch on the detectors when GC is ready.

7. Ensure that the ROLSI is in the correct position for vapour sampling. Always monitor the pressure when adjusting the ROLSI.

8. Zero the pressure data logger once the pressure has stabilised.

9. Switch of the stirrer and wait for the cell to be visually stable. There should not be a transitional phase, or entrained bubbles/droplets in the liquid and vapour phases respectively.

10. The pressure needs constant monitoring from now on. If it slightly drops or increases, set it back to the setpoint, stir a little, and check for visual stability.

Pre-purge

11. On the GC, set the sample info to the current date and sample name. Load the "slow purge" method and set: the oven time to 90 min, the gas saver off, and septum purge on.

12. On the ROLSI timer, set the close time to 2:3, and the open time to 0:18.

13. Start the ROLSI timer to start the pre-purge.

14. Allow the pre-purge to run until the peaks level out. Monitor the pressure.

15. Once the peaks have levelled out, stop the ROLSI timer.

16. When the last peak comes out, stop the run.

Slow purge

17. Load the "slow purge" method again, change the run name, the oven time to 90 min, switch off the gas saver, and switch on the septum purge.

18. Set the ROLSI timer close time to 2:30, and the open time to 0.18.

19. Start the ROLSI timer.

20. Run the method until the peaks level out. Monitor the pressure.

21. The setup is ready for sampling.

A. Detailed Experimental Procedure

Vapour sampling

22. Set the ROLSI timer close time to 0:04, and the open time to 0.29 (this setting should be lower at high pressures).

23. Load the analysis method on the GC, change the sample name, switch off the gas saver, and press apply.

24. Untick the valve setting – without pressing apply.

25. Just before the oven reaches the setpoint temperature, press apply to switch the valves and quickly start the ROLSI timer.

26. After taking one sample, stop the timer.

27. Perform bubble-flow tests.

28. Switch the gas saver on.

29. Let the analysis run finish.

30. Repeat steps 23 to 29 for four or five samples.

Liquid sampling

31. Adjust the ROLSI to allow liquid-phase sampling. Move the ROLSI incrementally, and alternate between lowering the one, and lifting the other, in order to keep the pressure stable.

32. If the pressure control was difficult, slightly stir, and wait for visual stability.

33. Repeat the slow purge and sampling steps. The liquid phase sampling uses a split ratio of 80:1, instead of 20:1. For the slow purge, set the ROLSI timer open time to 3:30, and the close time to 0.18. For the sampling, set the ROLSI timer open time to 0:04, and the close time to 0.25 (this value should decrease for higher pressures).

34. Repeat to obtain four or five liquid samples.

Shutdown

35. Load the "fast purge" method on the GC.

36. Turn off the detectors, but the keep oven hot.

37. Increase the thermal regulator temperatures on the regulator box to 300 °C, 240 °C, 300 °C, 240 °C, 300 °C.

38. Switch off the gas saver.

39. Leave the GC for 30 min – this allows the cleaning of the sampling and transfer lines.

40. Switch off the heating lines.

41. Load the "sleep mode" method. Leave on if measuring the next day, otherwise switch off the GC and convection oven.

42. Switch on the stirrer and set the pressure and/or temperature to the next setpoint.

43. Once the system is safe and stable, leave it overnight to reach equilibrium.

A.2.3. Cleaning

1. Once all points have been measured for the loaded mixture, release all pressure from the piston, and set the temperature to 35 °C.

2. Remove all oven plating, ducts etc. Also remove the baffle plates, stirrer plate, and spacers.

3. Release the CO_2 in the cell by opening the back microvalve and allowing the vapour to vent to the atmosphere. Close the back microvalve. Open the feed-line microvalve to ensure all pressure has been released.

4. Unload solutes by removing the piston and catching the solutes in a container. This is done to avoid blockage of the bottom microvalve due to solute crystallisation when unloading.

5. Remaining solute is cleaned out of the cell via simultaneous rinsing with acetone and application of compressed air. This needs to be done carefully to avoid damaging the ROLSI needles.

6. Wipe off the piston head with a wet acetone cloth.

7. Remove the sight glass to clean it properly.

8. Cleaning the feed-line microvalve by removing it and rinsing all the parts in acetone. Replace the O-rings, and PEEK back-up rings if necessary.

9. Replace all parts that had been removed and leave cell to dry.

A.2.4. Pressure calibration

1. Set up the cell as for a normal loading.

2. Completely lift out both ROLSIs to protect them from contact with oil and water. Cover ROLSI needle tips with small plastic bags.

3. Attach ROLSI replacement rods to the cell to maintain a seal without the presence of the ROLSI needles.

4. Remove the top vent line from the cell. Open the back microvalve.

5. Fill the cell with water through the top vent line.

6. Attach the oil feed line of the deadweight tester to the top vent line of the cell.

7. Follow normal pressure calibration procedures as outlined in section A.1.4.

APPENDIX B:
Calibration Data

B.1. Pressure Calibration

A pressure calibration was conducted for the synthetic-visual cells and the analytical VLE cell by means of a deadweight tester as detailed in Appendix A.1.4. The calibration experiments were conducted twice with increasing pressure, and twice with decreasing pressure. This allows for a statistical analysis of the results, and for the sensor hysteresis error to be quantified. The measured pressure is calculated by adding a pressure correction to the indicated pressure on the sensor, as shown in Equation B.1:

$$P_{meas} = P_{ind} + \varepsilon_P \qquad \text{B.1}$$

The purpose of the calibration is to model the pressure correction with a suitable function, and to use the measured calibration data to regress parameters for the function. The pressure correction incorporates the conversion from gauge pressure to absolute pressure. The functional form chosen is given by Equation B.2:

$$\varepsilon_P = \beta_4 P_{ind}^3 + \beta_3 P_{ind}^2 + \beta_2 P_{ind} + \beta_1 T_{ind} + \beta_0 \qquad \text{B.2}$$

where

β_i represents the linear regression parameters

P_{ind} is the indicated pressure in the cell

T_{ind} is the indicated temperature in the cell

The pressure correction was regressed separately for both the increasing and decreasing pressure experiments, and the parameters were averaged to obtain a general correction factor. The hysteresis variation is then addressed in the uncertainty analysis. The pressure correction is given by Equation B.3:

$$\varepsilon_P = \frac{\varepsilon_{iP} + \varepsilon_{dP}}{2} \qquad \text{B.3}$$

where

ε_{iP} represents the calibration performed with increasing pressure

ε_{dP} represents the calibration performed with decreasing pressure

The linear regression was performed with matrix algebra in MATLAB®. The results of the regression for the small cell is shown in Figure B.1. It can be seen that there is a large difference (up to about 3.5 bar) between the increasing and decreasing pressure cases. This illustrates the magnitude of the hysteresis

B. Calibration Data

error. The observed difference between Figure B.1 (a) and Figure B.1 (b) is due to the pressure transmitter having been replaced after breaking.
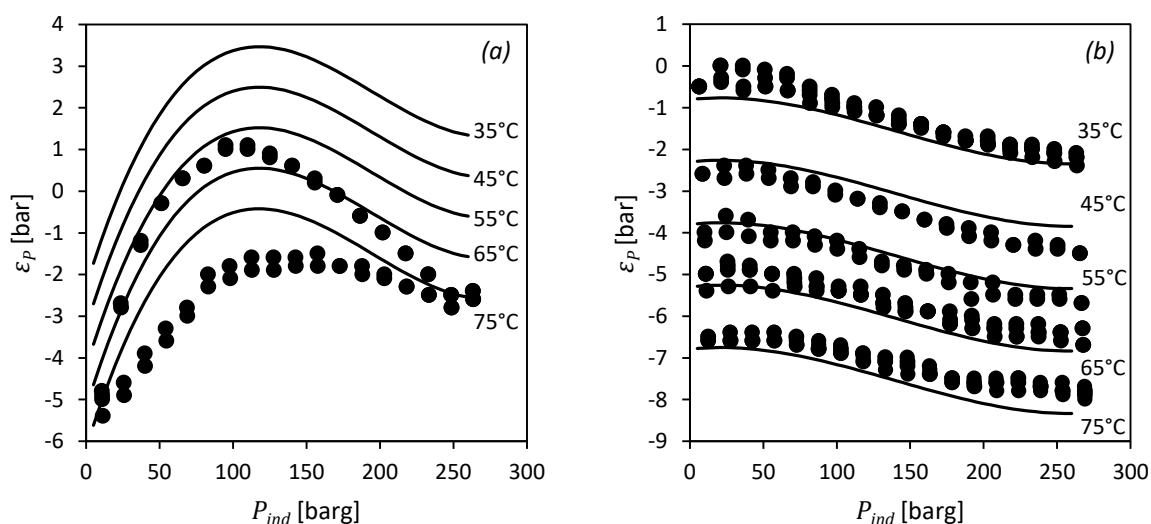
Figure B.1:Calibration curves for the pressure correction of the small cell. (a) 2018 calibration, data points only shown for T = 75°C; (b) 2019 calibration.

The calibration for the large cell is shown in Figure B.2 for all calibrated temperatures. The maximum hysteresis was determined to be 0.5 bar.
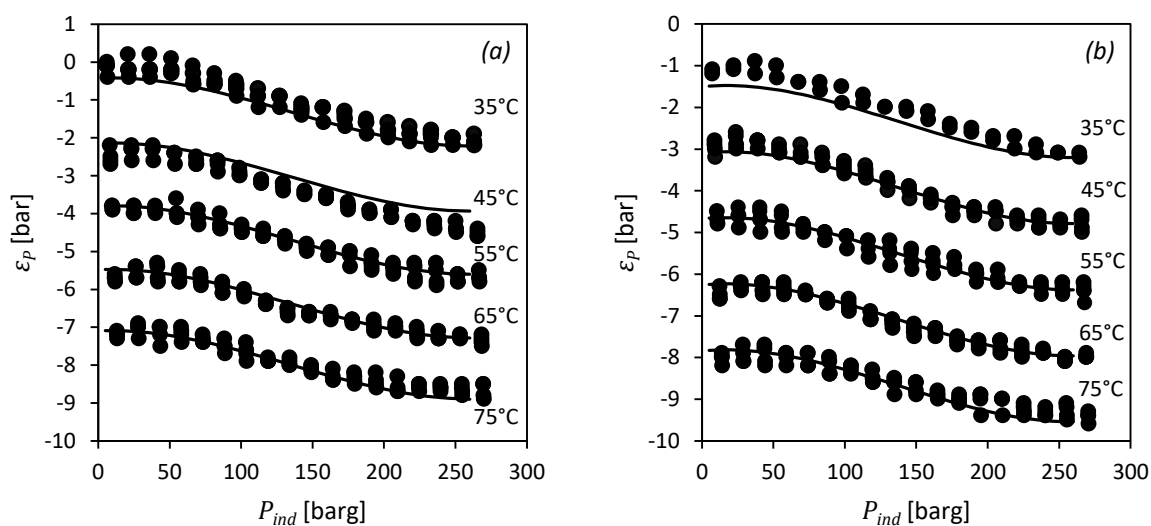
Figure B.2: Calibration curves for the pressure correction for the large cell. (a) 2018 calibration; (b) 2019 calibration.

The calibration of the VLE cell is shown in Figure B.3 for all calibrated temperatures.
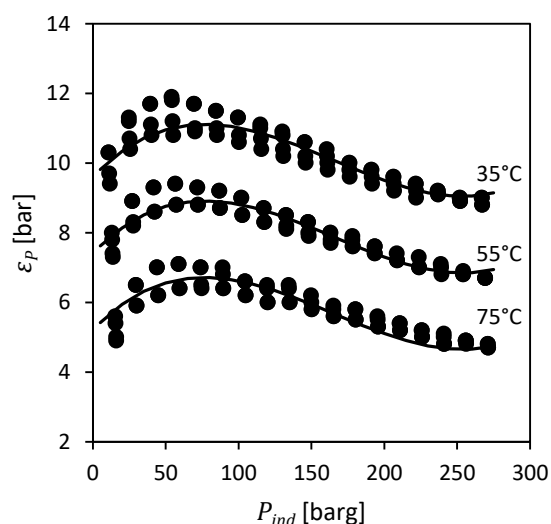
Figure B.3: Calibration curves for the pressure correction of the VLE cell.

Over the course of the experimental work the pressure transmitters were recalibrated. The large synthetic-visual cell was calibrated twice (once for the binary HPBPDP work, and once for the ternary HPBPDP work). The small synthetic-visual cell was similarly calibrated twice. The analytical VLE cell was calibrated once. The calibration parameters are presented in Table B.1 for the various calibration experiments.

Table B.1: Pressure correction calibration parameters for the synthetic-visual view cells.

Parameter	Small Cell (2018)	Large Cell (2018)	Small Cell (2019)	Large Cell (2019)	VLE Cell (2019)
β_4	1.19e-06	2.31e-07	2.38e-07	2.43e-07	7.44e-07
β_3	-6.95e-04	-9.34e-05	-9.97e-05	-1.01e-04	-3.69e-04
β_2	1.14e-01	1.79e-03	3.92e-03	3.17e-03	4.35e-02
β_1	-9.72e-02	-1.66e-01	-1.50e-01	-1.58e-01	-1.10e-01
β_0	1.12	5.23	4.44	4.04	1.35e+01

All pressure calibrations were performed with a deadweight pressure tester, which had been independently calibrated. The calibration certificate is provided on the following page.

B. Calibration Data

Unique Metrology

Eskom Research & Innovation Centre
Lower Germiston Road • Rosherville
P O Box 145296 • Bracken Gardens • 1452
Tel: 011 626 3808 • Cell: 083 254 3635 • Fax: 086 610 4196
Web: www.unimet.co.za

sanas
Calibration Laboratory
306   205

SANAS ACCREDITED CALIBRATION LABORATORY No 205

PRESSURE METROLOGY

CERTIFICATE OF CALIBRATION

Date of issue   :   25/02/2016

Certificate No   :   1602P6223-1

Technical Signatory

M Mathieson.

Page 1 of 4 pages.

The results of all measurements are traceable to the national measuring standards.

The values in this certificate are correct at the time of calibration. Subsequently the accuracy will depend on such factors as the care executed in handling and use of the device, and the frequency of use. Recalibration should be performed after the period so chosen to ensure that the instrument's accuracy remains within the desired limits.

This certificate is issued in accordance with the conditions of the accreditation granted by the South African National Accreditation System (SANAS). It is a correct record of the measurements made. This certificate may not be reproduced other than in full except with prior written approval of the issuing laboratory. Legal liability shall be limited to the cost of recalibration and or certification, but the applicant indemnifies Unique Metrology (Pty) Ltd against any consequential or other loss.

The South African National Accreditation System (SANAS) is a member of the International Laboratory Accreditation Cooperation (ILAC) Mutual Recognition Arrangement (MRA). This arrangement allows for the mutual recognition of technical test and calibration data by the member accreditation bodies worldwide. For more information on the Arrangement please contact www.ilac.org.

Unique Metrology

Eskom Research & Innovation Centre
Lower Germiston Road • Rosherville
P O Box 145296 • Bracken Gardens • 1452
Tel: 011 626 3808 • Cell: 083 254 3635 • Fax: 086 610 4196
Web: www.unimet.co.za

sanas
Calibration Laboratory
306   205

CERTIFICATE OF CALIBRATION

Page 2 of 4 pages.

Certificate Number	:	1602P6223-1
Calibration of a	:	Pressure Balance
Manufacturer & Type	:	Barnetts
Serial Number	:	3692/74
Calibrated for	:	Stellenbosch University, Stellenbosch.
Procedure Number	:	53-131
Date of Calibration	:	25/02/2016
Date of Issue	:	25/02/2016
Laboratory Environment	:	20.3 °C
Reference Standards	:	205-S-06 Budenberg 280D S/N 27702
	:	205-S-07 Budenberg Mass Set S/N 205-S-07
	:	205-S-10 Mass Set S/N 1406-01
	:	205-S-11 Mass Set S/N 1406-02

1. Procedure

The values of the pressure balance ring weights and of the weight of the piston assembly were determined by comparison against calibrated standard mass pieces.

The piston-cylinder assembly was balanced against a calibrated standard piston-cylinder assembly at several pressures within the normal working range. The effective area was determined and corrected to 20 °C assuming an increase in area of 22 ppm/°C rise in temperature.

2. Results

2.1 Weights

See next page for weight values.

Calibrated by : A Mathieson

Technical Signatory

B. Calibration Data

Unique Metrology

Eskom Research & Innovation Centre
Lower Germiston Road • Rosherville
P O Box 145296 • Bracken Gardens • 1452
Tel: 011 626 3808 • Cell: 083 254 3635 • Fax: 086 610 4196
Web: www.unimet.co.za
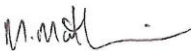
sanas
Calibration Laboratory
306   205

CERTIFICATE OF CALIBRATION

Certificate Number	:	1602P6223-1
Calibration of a	:	Pressure Balance
Manufacturer & Type	:	Barnetts

Page 3 of 4 pages.

2.1 Weights (cont)

Component marked		Nominal Value (kg)	Value measured (kg)	Uncertainty of measurement (g)	Error %
150 kPa	1	1.23371	1.23389	0.07	0.015
150 kPa	2	1.23371	1.23391	0.07	0.016
150 kPa	3	1.23371	1.23394	0.07	0.019
150 kPa	4	1.23371	1.23388	0.07	0.014
150 kPa	5	1.23371	1.23386	0.07	0.012
150 kPa	6	1.23371	1.23393	0.07	0.018
150 kPa	7	1.23371	1.23383	0.07	0.010
150 kPa	8	1.23371	1.23392	0.07	0.017
150 kPa	9	1.23371	1.23385	0.07	0.011
150 kPa	10	1.23371	1.23392	0.07	0.017
150 kPa	11	1.23371	1.23389	0.07	0.015
150 kPa	12	1.23371	1.23395	0.07	0.019
150 kPa	13	1.23371	1.23392	0.07	0.017
150 kPa	14	1.23371	1.23391	0.07	0.016
150 kPa	15	1.23371	1.23388	0.07	0.014
150 kPa	16	1.23371	1.23384	0.07	0.010
150 kPa	17	1.23371	1.23388	0.07	0.014
150 kPa	18	1.23371	1.23388	0.07	0.014
150 kPa	19	1.23371	1.23386	0.07	0.012
50 kPa	1	0.411237	0.411342	0.024	0.026
50 kPa	2	0.411237	0.411383	0.024	0.036
10 kPa	1	0.082247	0.082282	0.006	0.042
10 kPa	2	0.082247	0.082286	0.006	0.047
10 kPa	3	0.082247	0.082275	0.006	0.034
10 kPa	4	0.082247	0.082278	0.006	0.037
Piston Assy		Unknown	0.411942	0.022	

Calibrated by : A Mathieson

Technical Signatory

Unique Metrology

Eskom Research & Innovation Centre
Lower Germiston Road • Rosherville
P O Box 145296 • Bracken Gardens • 1452
Tel: 011 626 3808 • Cell: 083 254 3635 • Fax: 086 610 4196
Web: www.unimet.co.za

sanas
Calibration Laboratory
306   205

CERTIFICATE OF CALIBRATION

Certificate Number   :   1602P6223-1   Page 4 of 4 pages
Calibration of a   :   Pressure Balance
Manufacturer & Type   :   Barnetts

2.2 Piston-cylinder assembly

The effective area of the high-pressure piston-cylinder assembly was found to be expressible as

where

$A = A0(1 + \beta P)$
$A0 = 8.0641 \pm 0.0070$ mm²
$\beta = 3.92E\text{-}6 \pm 2.5E\text{-}6$ /MPa
P is the pressure in MPa.
The nominal value is 8.0645 mm².

3. Accuracy of pressure measurement.

When the pressure balance is used with the weight set supplied and after making suitable corrections for gravity, temperature and air buoyancy the total error in pressure measurement (ie the deviation from the nominal value) does not exceed 0.04% above 2 MPa.

4. Notes

The reference level for the pressure measurements was taken to be the base of the piston's cylinder.
The oil used for the calibration was a mineral oil of nominal density 870 kg/cm³.
The buoyancy volume was found to be negligible.

5. Uncertainty of Calibration

The reported uncertainty is based on a standard uncertainty multiplied by a coverage factor of k=2, which unless specifically stated otherwise, provides a confidence level of 95%, in accordance with the Guide to the expression of Uncertainty in Measurement, first edition, 1993.

6. Comments.

The weight set was marked with the serial number 3692/74.

Calibrated by : A Mathieson

Technical Signatory

B. Calibration Data

CMeTSA Pressure Metrology Course **FORMULAE AND REFERENCE VALUES**

MANOMETERS AND BAROMETERS

Principle:
$$P = h.\rho.g$$

Where P is pressure (Pa)
h is column height (m)
ρ is fluid density (kg m^{-3})
and g is the acceleration due to gravity (m s^{-2}).

THE PRESSURE BALANCE

The pressure is given from first principles by:

P	=	Force/Area

or

P	=	$\dfrac{mg}{A}$

Where m is the total mass (kg)
g is the acceleration due to gravity (m s^{-2}), and
A is the area of the PCU

Principle:
$$P = \frac{m.\left(1 - \dfrac{\rho_a}{\rho_m}\right).g}{A_{0,20}(1 + \beta P)(1 + \alpha(t - 20))}$$

General formula for pressure

$$P = \frac{\left\{\sum\left[m\left(1 - \dfrac{\rho_a}{\rho_m}\right)\right] - v\rho_f^{\circ}\right\}g + (\sigma\, c)}{A_{0,20}(1 + \beta P)[1 + \alpha(t - 20)]} + h\rho_f g$$

where the symbols have the usual meanings.

where

P	is the applied pressure
m	is the mass of the components of the load
ρ_a	is the density of the air
ρ_m	is the density of the mass m (which can be different for each component)
v	is the buoyancy volume ie the volume of the piston protruding into the oil 'below' the reference level
ρ_f	is the fluid density.
g	is the value of local gravity
σ	is the surface tension
c	is the circumference of the piston.
h	is the height difference
$A_{0,20}$	is the effective area of the PC assembly at zero applied pressure and a temperature of 20 °C.
β	is the pressure distortion coefficient.
α	is the area coefficient of thermal expansion
t	temperature of ambient or of piston.

Page 1 of 2

150

B.2. Volume Calibration

A volume calibration was performed on each cell in order to calculate the volume of the manifold and connecting lines, which is required to determine the amount of solvent lost during loading. The calibration is conducted according to the procedure in Appendix A.1.5, where the piston displacement and temperature is measured over a range of pressures for two cases: with the cell valve closed, and with the cell valve open to the manifold. The pressure and temperature can then be used to determine the density of the solvent (CO_2), by assuming no solvent is lost (thus meaning that the mass of solvent in the cell is known) and then calculating the density of the solvent by means of CO_2 data from the NIST database.[54] The density and assumed mass can then be used to determine the volume of solvent at each data point.

The volume was then plotted against the piston displacement for both cases and straight lines fitted to the data points. The intercepts of the lines represent the maximum volume. It then follows that the volume of the manifold is equal to the difference between the maximum volume with the valve open to the manifold, and the maximum volume with the valve closed to the manifold. Once this initial manifold volume has been obtained, the process was repeated by adjusting the assumption of no solvent lost (with a manifold volume, pressure, and temperature, the mass of solvent lost can be quantified). This will change the mass of solvent loaded, thus changing the volumes of each data point, which in turn will change calculated manifold volume. The calculations were iterated until the calculated manifold volume did not change to within a desired tolerance.

The calibration data is shown in Figure B.4. A volume of 6.569 mL and 5.657 mL was determined for the small and large cells respectively. The calculated standard uncertainties of the manifold volume were found to be 0.889 mL and 0.710 mL for the small and large cells respectively. Some of the data points for the large cell was not included in the regression since condensation occurred, as can be seen from the change in slope of the data points.

B. Calibration Data
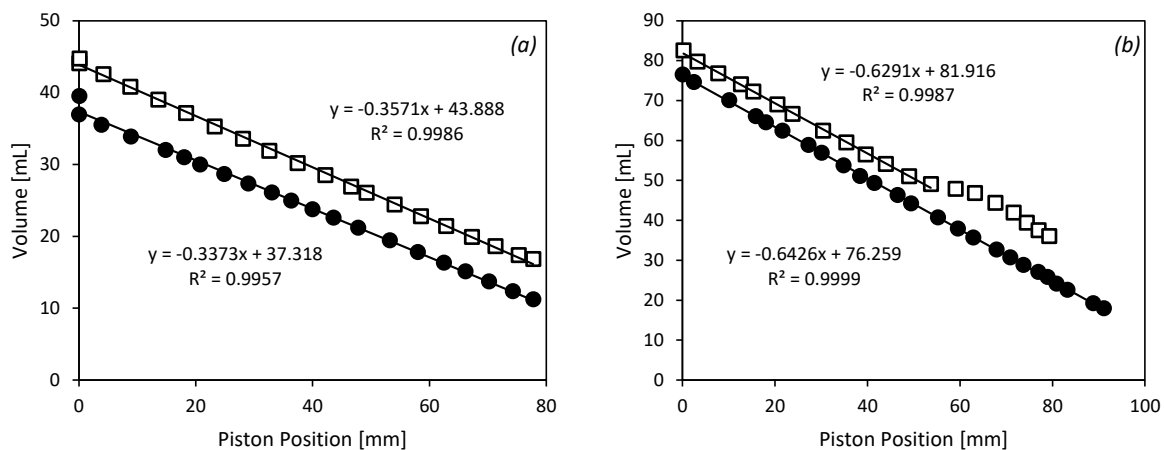
Figure B.4: Volume calibration curves. (●) Cell valve closed; (□) Cell valve open. (a) Small cell; (b) Large cell.

The uncertainty in the manifold volume was determined through Equation B.4 as derived by Swanepoel[122]:

$$u^2(V_{man}) = \frac{\beta^2}{3} L_\infty^2 \qquad \text{B.4}$$

where L_∞ is the maximum piston displacement (77.75 mm and 91.1 mm for the small and large cells respectively), and β is the difference between the slopes of the two volume calibration curves (0.0198 mL·mm^{-1} and 0.0135 mL·mm^{-1} for the small and large cells respectively).

B.3. Gas-chromatography Calibration

Aside from the on-line gas chromatography work, additional analyses were required to analyse the ester-mixture residue from the ternary HPBDP experiments for reuse in further experiments. This was done on a different GC than the high-pressure VLE work, to avoid the peak overlap problem. The GC had a similar WAX-column to the on-line GC. The calibration curves are presented in Figure B.5.
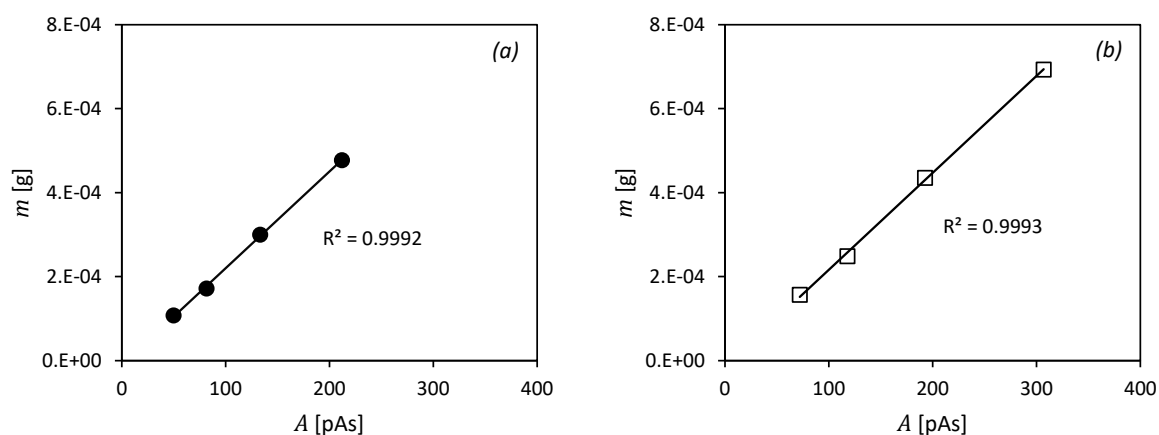
Figure B.5:Gas-chromatography calibration curves for nonequilibrium measurement analyses. (a) Methyl stearate; (b) Methyl oleate.

Standard single-component calibration curves were constructed for methyl stearate and methyl oleate for the 20:1 split ratio method. These are given in Figure B.6.
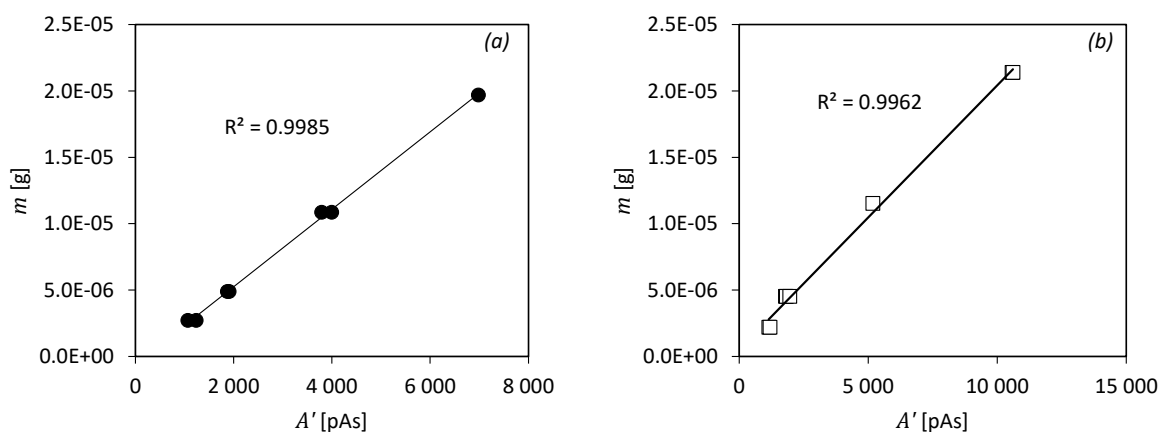
Figure B.6: GC-FID single-component calibration curves for the on-line chromatography work. (a) Methyl stearate; (b) Methyl oleate.

The injected masses were determined by injecting a known volume of a prepared sample of known composition and using the Riedel correlation to calculate the sample density, which could be used with the volume injected to determine the mass of each component injected. The Riedel correlation is provided in Equation B.5[123]:

B. Calibration Data

$$\rho_m = \rho_{c,m}\left[1 + (1.69 + 0.984\omega_m)\left(1 - \frac{T}{T_{c,m}}\right)^{\frac{1}{3}} + 0.85\left(1 - \frac{T}{T_{c,m}}\right)\right]$$

B.5

where ρ_m is the mixture density, $\rho_{c,m}$ is the mixture critical density, ω_m is the mixture acentric factor, and $T_{c,m}$ is the mixture critical temperature. In order to use the correlation, the mixture critical properties and acentric factor are required. These can be estimated with Li's method[124] (for $T_{c,m}$) and with Kay's rule[125] for the rest. These relations are provided in Equations B.6 to B.9:

$$T_{c,m} = \sum_{i=1}^{N} \Phi_i T_{c,i}$$

B.6

$$\Phi_i = \frac{x_i V_{c,i}}{\sum_{j=1}^{N} x_j V_{c,j}}$$

B.7

$$\rho_{c,m} = \frac{\bar{M}_m}{\sum_{i=1}^{N} x_i V_{c,i}}$$

B.8

$$\omega_m = \sum_{i=1}^{N} x_i \omega_i$$

B.9

where $T_{c,i}$ is the critical temperature of component i, Φ_i is the critical volume fraction of component i, $V_{c,i}$ is the critical volume of component i, N is the number of mixture components, $\bar{M}_m$ is the average mixture molar mass, x_i is the mole fraction of component i in the mixture, and ω_i is the acentric factor of component i. This correlation is appropriate for the calculation of the sample densities, as it was developed to calculate alkane densities, and the samples were dilute in the FAME components, consisting mostly of hexane.

The calibration curve for CO_2 on the 20:1 split ratio method for the vapour sample analyses is given in Figure B.7. The CO_2 was injected with a gastight syringe, which was filled from a flushed gas bomb fitted with a pressure gauge and a temperature probe. This allowed the mass of CO_2 injected to be determined with the ideal gas law.
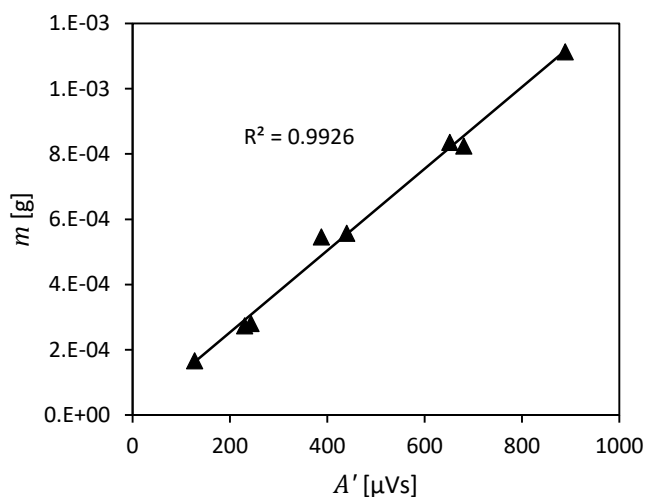
Figure B.7: GC-TCD CO$_2$ calibration curve for the on-line chromatography work.

B.4. Temperature Calibration

The temperature probes (a handheld Pt100 probe that was used in all synthetic-visual work, and a dedicated Pt100 probe attached to the high-pressure VLE cell) are calibrated yearly by WIKA, a SANAS accredited laboratory. This means that both probes had two different calibration certificates attached to them over the course of the experimental work. The VLE probe was only used under the certification of the 2018 calibration, and so only one certificate will be presented for it. The calibration certificates are presented below in the following pages in the order: handheld probe (2017), handheld probe (2018), VLE probe (2018).

The calibration results are summarised in Table B.2 for the temperature range investigated, namely 35 °C to 75 °C. The offset ε_T is the value that needs to be added to the indicated temperature in order to obtain the true temperature. The standard uncertainty $u(T)$ is the uncertainty associated with the calculated true temperature.

Table B.2: Summary of temperature probe calibration data.

Probe	ε_T [°C]	$u(T)$ [°C]
Handheld (2017)	0.0	0.2
Handheld (2018)	$0.0033T_{ind} - 0.015$	0.3
VLE (2018)	$0.0022T_{ind} + 0.5953$	0.3

B. Calibration Data

WIKA Instruments (Pty) Ltd South Africa

ilac-MRA   sanas
246/S1
346/S1

WIKA

SANAS Accredited Laboratory, No 346/S1
for
Temperature Metrology

Certificate Number   14-00000098

Certificate of Calibration

Calibration of a	PT 100 to Digital Thermometer
Manufacturer	Testo
Type	PT 100 Connected to Digital Thermometer Testo 720
Range	n/a
Serial number	**02753688 (Probe PT100 Loose 1)**
Tag number	**Handheld 1**
Customer	University Stellenbosch - Process Engineering
	Lab C301 , Process Engineering
	Banghoek , Stellenbosch
	7602
	South Africa
Customer Order No.	268623336
Number of pages of the certificate	Page 1 of 3
Date of calibration	13/07/2017

This calibration certificate documents the traceability to national standards and international standards, which realise the units of measurement according to the International System of Units (SI).

The South African National Accreditation System (SANAS) is a member of the International Laboratory Accreditation Cooperation (ILAC) for the Mutual Recognition Agreement. This arrangement allows for the mutual recognition of technical test and calibration data by the member's accreditation bodies worldwide. For more information on the MRA please consult www.ilac.org

The values in this certificate are correct at the time of calibration/certification. Subsequently the accuracy will depend on such factors as operating temperature, the care exercised in handling, frequency of use and its use under conditions other than specified by the manufacturer and/or conditions of calibration/certification. Recertification should be performed after a period that has been chosen by the user to ensure that the equipment's accuracy remains within the desired limits. The user is obliged to have the object recalibrated at these intervals.

The reported results are only valid for the object calibrated. Legal liability shall be limited to the cost of recalibration and or certification, but the applicant indemnifies WIKA INSTRUMENTS against any consequential or other loss.

This calibration certificate may not be reproduced other than in full except with the permission of the issuing laboratory. Calibration certificates without Technical Signatory's signature ana seal are not valid.

Seal	Date of Issue	Checked by SANAS Authorised Technical Signatory	Calibrated by Metrologist
	17/07/2017	Lyen EJ.	Shepherd J.

WIKA Instruments (Pty) Ltd
Unit 50-51 Gold Street , Northgate Business Park,
Maitland, 7405, Cape Town, South Africa
P.O. Box 475, Milnerton, 7435

Tel: (021) 511 8228
Fax: (021) 511 5866
email: capetown@wika.co.za

**WIKA Instruments (Pty) Ltd
South Africa**

page 2 of 3:   Date of calibration   13/07/2017   Certificate No.   14-00000098

Description of unit under test

Calibration of a   PT 100 to Digital Thermometer
Type   PT 100 Connected to Digital Thermometer Testo 720
Transmitter range & serial no.   n/a
Output signal   °C

Reference Standard and measurement conditions

The following measuring devices and references were used:

CTH 7000 S/N 020560/03 Cert 13-00000023 05/04/2017

The following uniformed temperature devices were used:

- Range   -20°C to 160°C   WIKA CTB9100 Stirred Liquid Bath, Medium : Silicone Oil M20

Environmental conditions

Ambient Temperature in °C   15   ± 1.5
Humidity %RH   52   ± 7

Place of calibration

WIKA Mobile Laboratory Cape Town Customer Premises

Calibration process

Method   by Comparison
Work instruction   LTW-003 r2 & LTW-005 r1 & LTW-006 r1

For calibration the following norm is used:
- DKD-R 5-1 Guideline for calibration of Resistance Thermometers by German Calibration Service "Deutscher Kalibrier Dienst"
(DKD) English translation Edition 02/2009

WIKA Instruments (Pty) Ltd   Tel.: (021) 511 9228
Unit 50-51 Gold Street , Northgate Business Park,   Fax: (021) 511 5868
Maitland, 7405, Cape Town, South Africa   email: capetown@wika.co.za
P.O Box 475, Milnerton, 7435

B. Calibration Data

**WIKA Instruments (Pty) Ltd
South Africa**

page 3 of 3: Date of calibration   13/07/2017   Certificate No. 14-00000098

Results

| Immersion depth (mm) | Reference Temperature °C | DUT | | | Displayed Temperature °C | Deviation Temperature °C | Uncertainty of Measurement ±°C |
		Indicated Reading Ω	Indicated Reading mV	Indicated Reading mA			
150	29.698	-	-	-	29.740	0.042	0.41
150	79.806	-	-	-	79.800	-0.006	0.41
150	139.867	-	-	-	140.000	0.133	0.41

The reported expanded uncertainty of measurement is stated as the standard uncertainty of measurement multiplied by the coverage factor k=2, which for a normal distribution corresponds to a coverage probability of 95,45%, the uncertainty of measurement has been estimated in accordance with the principles defined in the GUM, 'Guide to Uncertainty of Measurement, ISO, Geneva, 1993'.

Remarks

1. Standard used to convert resistance to temperature is IEC 60751:2008 and to convert millivolts to temperature is IEC 60584-1:2013

2. The deviation should be subtracted from the indicated temperature of the DUT to obtain the actual temperature.

Label

The calibration object is labelled, which shows the number of this calibration certificate, serial/tag number and the date of calibration.

-------------------END OF CERTIFICATE--------------------

The South African National Accreditation System (SANAS) is a member of the International Laboratory Accreditation Cooperation (ILAC) for the Mutual Recognition Agreement. This arrangement allows for the mutual recognition of technical test and calibration data by the member's accreditation bodies worldwide. For more information on the MRA please consult www.ilac.org

WIKA Instruments (Pty) Ltd
Unit 50-51 Gold Street, Northgate Business Park,
Maitland, 7405, Cape Town, South Africa
P.O. Box 475, Milnerton, 7435

Tel.: (021) 511 9228
Fax: (021) 511 5866
email: capetown@wika.co.za

WIKA Instruments (Pty) Ltd South Africa

SANAS Accredited Laboratory , No 346/S1
for
Temperature Metrology

Certificate Number | 14-00000553

Certificate of Calibration

This calibration certificate documents the traceability to national standards and international standards, which realise the units of measurement according to the International System of Units (SI).

Calibration of a	Digital Thermometer

The South African National Accreditation System (SANAS) is a member of the International Laboratory Accreditation Cooperation (ILAC) for the Mutual Recognition Agreement. This arrangement allows for the mutual recognition of technical test and calibration data by the member's accreditation bodies worldwide. For more information on the MRA please consult www.ilac.org

Manufacturer	Testo
Type	Digital
Range	-100 to 800 °C

The values in this certificate are correct at the time of calibration/certification. Subsequently the accuracy will depend on such factors as operating temperature, the care exercised in handling, frequency of use and its use under conditions other than specified by the manufacturer and/or conditions of calibration/certification. Recertification should be performed after a period that has been chosen by the user to ensure that the equipment's accuracy remains within the desired limits. The user is obliged to have the object recalibrated at these intervals.

Serial number	**02753688**
Tag number	**Probe PT Loose 1**
Customer	University Stellenbosch
	Lab C301 , Process Engineering
	Banghoek
	7602

The reported results are only valid for the object calibrated. Legal liability shall be limited to the cost of recalibration and or certification, but the applicant indemnifies WIKA INSTRUMENTS against any consequential or other loss.

	South Africa
Customer Order No.	287214194
Number of pages of the certificate	Page 1 of 3
Date of calibration	05/12/2018

This calibration certificate may not be reproduced other than in full except with the permission of the issuing laboratory. Calibration certificates without Technical Signatory's signature and seal are not valid.

Seal	Date of Issue	Checked by SANAS Authorised Technical Signatory	Calibrated by Metrologist
	21/01/2019	Shepherd J.	Shepherd J.

WIKA Instruments (Pty) Ltd
Unit 50-51 Gold Street , Northgate Business Park,
Maitland, 7405, Cape Town, South Africa
P.O. Box 475, Milnerton, 7435

Tel (021) 511 9228
Fax (021) 511 5866
email capetown@wika.co.za

B. Calibration Data

WIKA

WIKA Instruments (Pty) Ltd
South Africa

page 2 of 3:   Date of calibration   12/11/2018   Certificate No.   14-00000553

Description of unit under test

Calibration of a	Digital Thermometer
Type	Digital
Transmitter range & serial no.	-100 to 800 °C
Output signal	°C

Reference Standard and measurement conditions

The following measuring devices and references were used:

CTH 7000 S/N 020560/03 Cert 13-00000129 26/07/2018

The following uniformed temperature devices were used:

- Range   -20°C to 160°C   WIKA CTB9100 Stirred Liquid Bath, Medium : Silicone Oil M20

Environmental conditions

Ambient Temperature in °C	23 ± 1
Humidity %RH	52 ± 10

Place of calibration

WIKA Mobile Laboratory Cape Town Customer Premises

Calibration process

Method	by Comparison
Work instruction	LTW-005 r2 & LTW-006 r3

For calibration the following norm is used:
- DKD-R 5-1 Guideline for calibration of Resistance Thermometers by German Calibration Service "Deutscher Kalibrier Dienst"
(DKD) English translation Edition 02/2009

WIKA Instruments (Pty) Ltd   Tel (021) 511 8028
Unit 50-51 Gold Street , Northgate Business Park   Fax (021) 511 5866
Maitland, 7405 Cape Town, South Africa   email capetown@wika.co.za
P.O. Box 475, Milnerton, 7435

WIKA Instruments (Pty) Ltd
South Africa

page 3 of 3: Date of calibration   12/11/2018   Certificate No.   14-00000553

Results

Immersion depth (mm)	Reference Temperature °C	DUT			Displayed Temperature °C	Deviation Temperature °C	Uncertainty of Measurement ±°C
		Indicated Reading Ω	Indicated Reading mV	Indicated Reading mA			
145	19.991	-	-	-	19.94	-0.051	0.62
145	79.989	-	-	-	79.74	-0.249	0.62
145	139.991	-	-	-	140.16	0.169	0.62

The reported expanded uncertainty of measurement is stated as the standard uncertainty of measurement multiplied by the coverage factor k=2, which for a normal distribution corresponds to a coverage probability of 95,45%, the uncertainty of measurement has been estimated in accordance with the principles defined in the GUM, 'Guide to Uncertainty of Measurement, ISO, Geneva, 1993'.

Remarks

1. Standard used to convert resistance to temperature is IEC 60751:2008 and to convert millivolts to temperature is IEC 60584-1:2013

2. The deviation should be subtracted from the indicated temperature of the DUT to obtain the actual temperature.

Label

The calibration object is labelled, which shows the number of this calibration certificate, serial/tag number and the date of calibration.

-------------------END OF CERTIFICATE-------------------

WIKA Instruments (Pty) Ltd.
Unit 50-51 Gold Street   Northgate Business Park
Maitland 7405 Cape Town South Africa
P O Box 475 Milnerton 7435

Tel (021) 511 9228
Fax (021) 511 5866
email capetown@wika.co.za

B. Calibration Data

WIKA Instruments (Pty) Ltd South Africa

SANAS Accredited Laboratory , No 346/S1
for
Temperature Metrology

Certificate Number   14-00000555

Certificate of Calibration

Calibration of a	Pt 100 to Digital Indication
Manufacturer	Wika / Julabo
Type	PT 100 to Julabo Digital Indicator
Range	-80 to 450 °C
Serial number	**00296264**
Tag number	**Probe 13.EC**
Customer	University Stellenbosch
	Lab C301 , Process Engineering
	Banghoek
	7602
	South Africa
Customer Order No.	287214194
Number of pages of the certificate	Page 1 of 3
Date of calibration	05/12/2018

This calibration certificate documents the traceability to national standards and international standards, which realise the units of measurement according to the International System of Units (SI).

The South African National Accreditation System (SANAS) is a member of the International Laboratory Accreditation Cooperation (ILAC) for the Mutual Recognition Agreement. This arrangement allows for the mutual recognition of technical test and calibration data by the member's accreditation bodies worldwide. For more information on the MRA please consult www.ilac.org

The values in this certificate are correct at the time of calibration/certification. Subsequently the accuracy will depend on such factors as operating temperature, the care exercised in handling, frequency of use and its use under conditions other than specified by the manufacturer and/or conditions of calibration/certification. Recertification should be performed after a period that has been chosen by the user to ensure that the equipment's accuracy remains within the desired limits. The user is obliged to have the object recalibrated at these intervals.

The reported results are only valid for the object calibrated. Legal liability shall be limited to the cost of recalibration and or certification, but the applicant indemnifies WIKA INSTRUMENTS against any consequential or other loss.

This calibration certificate may not be reproduced other than in full except with the permission of the issuing laboratory. Calibration certificates without Technical Signatory's signature ana seal are not valid.

Seal	Date of Issue	Checked by SANAS Authorised Technical Signatory	Calibrated by Metrologist
	21/01/2019	Shepherd J	Shepherd J

WIKA Instruments (Pty) Ltd.
Unit 50-51 Gold Street , Northgate Business Park,
Maitland, 7405, Cape Town, South Africa
P.O. Box 475, Milnerton, 7435

Tel : (021) 511 9228
Fax: (021) 511 5866
email: capetown@wika.co.za

WIKA Instruments (Pty) Ltd
South Africa

page 2 of 3:   Date of calibration   05/12/2018   Certificate No.   14-00000555

Description of unit under test

Calibration of a	Pt 100 to Digital Indication
Type	PT 100 to Julabo Digital Indicator
Transmitter range & serial no.	-80 to 450 °C
Output signal	°C

Reference Standard and measurement conditions

The following measuring devices and references were used:

CTH 7000 S/N 020560/03 Cert 13-00000129 26/07/2018

The following uniformed temperature devices were used:

- Range   -20°C to 160°C   WIKA CTB9100 Stirred Liquid Bath, Medium : Silicone Oil M20

Environmental conditions

Ambient Temperature in °C	24 ± 1
Humidity %RH	54 ± 10

Place of calibration

WIKA Mobile Laboratory Cape Town Customer Premises

Calibration process

Method	by Comparison
Work instruction	LTW-005 r2 & LTW-006 r3

For calibration the following norm is used:
- DKD-R 5-1 Guideline for calibration of Resistance Thermometers by German Calibration Service "Deutscher Kalibrier Dienst"
(DKD) English translation Edition 02/2009

WIKA Instruments (Pty) Ltd   Tel (021) 511 9228
Unit 50-51 Gold Street Northgate Business Park,   Fax (021) 511 5866
Maitland, 7405 Cape Town, South Africa   email capetown@wika.co.za
P O Box 475, Milnerton, 7435

B. Calibration Data

WIKA Instruments (Pty) Ltd
South Africa

page 3 of 3: Date of calibration 05/12/2018 Certificate No. 14-00000555

Results

| Immersion depth (mm) | Reference Temperature °C | DUT | | | Displayed Temperature °C | Deviation Temperature °C | Uncertainty of Measurement ±°C |
		Indicated Reading Ω	Indicated Reading mV	Indicated Reading mA			
145	19.993	-	-	-	19.41	-0.583	0.60
145	79.992	-	-	-	79.08	-0.912	0.60
145	139.991	-	-	-	138.72	-1.275	0.60

The reported expanded uncertainty of measurement is stated as the standard uncertainty of measurement multiplied by the coverage factor k=2, which for a normal distribution corresponds to a coverage probability of 95,45%, the uncertainty of measurement has been estimated in accordance with the principles defined in the GUM, 'Guide to Uncertainty of Measurement, ISO, Geneva, 1993'.

Remarks

1. Standard used to convert resistance to temperature is IEC 60751:2008 and to convert millivolts to temperature is IEC 60584-1:2013

2. The deviation should be subtracted from the indicated temperature of the DUT to obtain the actual temperature.

Label

The calibration object is labelled, which shows the number of this calibration certificate, serial/tag number and the date of calibration.

--------------------END OF CERTIFICATE--------------------

The South African National Accreditation System (SANAS) is a member of the International Laboratory Accreditation Cooperation (ILAC) for the Mutual Recognition Agreement. This arrangement allows for the mutual recognition of technical test and calibration data by the member's accreditation bodies worldwide. For more information on the MRA please consult www.ilac.org

WIKA Instruments (Pty) Ltd
Unit 50-51 Gold Street, Northgate Business Park
Marland, 7405, Cape Town, South Africa
P O Box 475, Milnerton 7435

Tel. (021) 511 9208
Fax (021) 511 5666
email capetown@wika.co.za

B.5. Scale Calibration

CME METROLOGY

sanas
Calibration Laboratory
Lab no.1419

Po Box 99 Eppindust 7475, Cnr Riley & Brentford Streets, Beaconvale,Cape Town, Tel 021-931 1101 Fax 021-931 1126

Mass Laboratory
Certificate of Calibration

Calibration performed using measuring equipment traceable to National Measurement Standards

Mass Laboratory Standards: Serial Number: FA 005

Calibration Procedure: ML11
Page No.   1 of 1

Certificate Number:
M2779/1

Customer Details:
Calibration for: Stellenbosch University
Address: Department of Process Engineering
Cnr Bosmans & Banghoek Roads
Stellenbosch

Condition on receipt: Satisfactory
Calibration performed at: University of Stellenbosch
Location/Department: Room C307
Temperature(°C): Ambient
Type of Calibration: Full

Calibration Details:
Description: Balance
Type of Unit: Electronic
Serial Number: B648369370
Asset No: -
Make&Model: Ohaus Pioneer PA423C
Measuring Range: **Unit of**
Minimum: 0g   **Measure:**   g
Maximum: 400g
Resolution: 0.001g
Date received: N/a
Date of Calibration: 23/11/2017
Date of Issue: 27/11/2017
Requested recalibration date: N/a

Calibration Results

Nominal Test Position	Accuracy Test As Found	Accuracy Test As Left		
g	g	g	Repeatability	0.001g
			Mass Used	200g
0.5	0.500	0.500	Zero Error	0g
1	1.000	1.000	Off Centre Error	0.001g
2	2.000	2.000	*Mass Used*	100g
5	5.000	5.000	Sensitivity	0g
10	10.000	10.000	Linearity	0.002g
20	20.000	20.000		
50	50.000	50.000		
100	100.000	100.000		
200	200.000	200.000		
300	300.001	300.001		
400	400.002	400.002		
	Measurement Uncertainty @ 95% confidence level ±			0.002g

Remarks: None

Signatories: Technical Signatory: *F Arnold*   Calibrated by: *F Arnold*

MLBC Rev7 March 2017
End of Certificate

B. Calibration Data

CME METROLOGY

sanas Calibration Laboratory
Lab no.1419

Po Box 99 Eppindust 7475, Cnr Riley & Brentford Streets, Beaconvale,Cape Town, Tel 021-931 1101 Fax 021-931 1126

Mass Laboratory
Certificate of Calibration
Calibration performed using measuring equipment traceable to National Measurement Standards

Mass Laboratory Standards: Serial Number: FA 005

Calibration Procedure: ML11
Page No. **1 of 1**

Certificate Number: M2779/2

Customer Details:
Calibration for: Stellenbosch University
Address: Department of Process Engineering
Cnr Bosmans & Banghoek Roads
Stellenbosch

Condition on receipt: Satisfactory
Calibration performed at: University of Stellenbosch
Location/Department: Room C307
Temperature(°C): Ambient
Type of Calibration: Full

Calibration Details:
Description: Balance
Type of Unit: Electronic
Serial Number: 1127490444
Asset No: -
Make&Model: Ohaus Discovery
Measuring Range:
Minimum: 0g
Maximum: 200g
Resolution: 0.00001g/0.0001g
Date received: N/a
Date of Calibration: 23/11/2017
Date of Issue: 27/11/2017
Unit of Measure: g

Requested recalibration date: N/a

Calibration Results

Nominal Test Position g	Accuracy Test As Found g	Accuracy Test As Left g		
			Repeatability	0.0001g
			Mass Used	100g
0.1	0.10000	0.10000	Zero Error	0g
0.2	0.19998	0.19998	Off Centre Error	0.00004g
0.5	0.49999	0.49999	*Mass Used*	50g
1	0.99999	0.99999	Sensitivity	0g
2	1.99999	1.99999	Linearity	0.0002g
5	5.00000	5.00000		
10	10.00000	10.00000		
20	19.99999	19.99999		
50	50.00001	50.00001		
100	100.0000	100.0000		
200	200.0002	200.0002		

Measurement Uncertainty @ 95% confidence level ± 0.0001g up to 50g ±0.0004g above 50g

Remarks: None

Signatories:
Technical Signatory: *F Arnold*   Calibrated by: *F Arnold*

MLBC Rev7 March 2017
End of Certificate

CME METROLOGY

sanas
Calibration Laboratory
Lab no.1419

Po Box 99 Eppindust 7475, Cnr Riley & Brentford Streets, Beaconvale,Cape Town, Tel 021-931 1101 Fax 021-931 1126

Mass Laboratory
Certificate of Calibration

Calibration performed using measuring equipment traceable to National Measurement Standards

Mass Laboratory Standards: Serial Number: FA 006

Calibration Procedure: ML11
Page No. 1 of 1
Certificate Number:
M2779/3

Customer Details:
Calibration for: Stellenbosch University
Address: Department of Process Engineering
Cnr Bosmans & Banghoek Roads
Stellenbosch

Condition on receipt: Satisfactory
Calibration performed at: University of Stellenbosch
Location/Department: Room 307
Temperature(°C): Ambient
Type of Calibration: Full

Calibration Details:
Description: Balance
Type of Unit: Electronic
Serial Number: 4700032
Asset No: -
Make&Model: Precisa EP22204

Measuring Range: **Unit of**
Minimum: 0g   **Measure:** g
Maximum: 2000g
Resolution: 0.001g
Date received: N/a
Date of Calibration: 23/11/2017
Date of Issue: 27/11/2017
Requested recalibration date: N/a

Calibration Results

Nominal Test Position g	Accuracy Test As Found g	Accuracy Test As Left g		
			Repeatability	0.001g
			Mass Used	1000g
1	1.000	1.000	Zero Error	0g
2	2.000	2.000	Off Centre Error	0.003g
5	5.000	5.000	Mass Used	500g
10	9.999	9.999	Sensitivity	0g
20	19.999	19.999	Linearity	0.007g
50	49.999	49.999		
100	99.999	99.999		
200	199.999	199.999		
500	499.999	499.999		
1000	999.998	999.998		
2000	2000.005	2000.005		
Measurement Uncertainty @ 95% confidence level ±				0.01g

Remarks: None

Signatories: Technical Signatory: F Arnold   Calibrated by: F Arnold

MLBC Rev7 March 2017
End of Certificate

APPENDIX C:
Uncertainty Analysis

C.1. Procedure for the Evaluation of Experimental Uncertainty

The approach to the determination of experimental uncertainty was based on the framework described by the *Guide to the expression of uncertainty in measurement* (GUM)[85] as applied to the measurement of high-pressure phase equilibria by Swanepoel[122].

Due to the nature of experimental thermodynamics, it is often difficult, time-consuming, or expensive to replicate experiments a sufficient number of times for the determination of a reliable standard uncertainty in the form of a standard deviation of the mean of a series of measurements (referred to by the GUM as a Type A evaluation). A standard uncertainty here refers to the total combined uncertainty $u(y)$ in output variable y, where $u(y)$ is expressed as a standard deviation which accounts for a 68 % probability of the true value of y falling in the interval $\pm u(y)$, assuming infinite degrees of freedom.[85] Considering this, it was decided to make use of so-called Type B evaluations[85] which rely on the application of estimation methods not requiring a series of observations.

Swanepoel summarised the GUM framework for uncertainty estimation in seven steps[122]:

1. Find a mathematical expression for the output variable y in terms of a series of input variables x_i where $y = f(x_1, x_2, .. x_n)$.
2. Find estimates of all input variables x_i.
3. Determine the standard uncertainties $u(x_i)$ in the input variables.
4. Determine the covariances $u(x_i, x_j)$ between all correlated input variables.
5. Calculate y from the functional relationship and the estimates of the input variables x_i.
6. Propagate the input uncertainties $u(x_i)$ to calculate the standard uncertainty in the output variable y.
7. Report results.

C. Uncertainty Analysis

A brief description of what each step entails is given:

Step 1. Find a mathematical expression for the output

Either a model or a fundamental equation should be used to express the output variable y in terms of all relevant input variables x_i that contribute to the uncertainty, where possible. If it is not possible to explicitly calculate y from a series of x_i (for example, if the output variable is calculated by means of a neural network), then the uncertainty in y can be estimated by other statistical measures, such as the model test error computed with resampling methods.[96]

Step 2. Find estimates for all inputs x_i

The estimated value of all input variables needs to be determined. This is done either via direct measurement, or through calculation with a functional relationship.

Step 3. Determine the standard uncertainty $u(x_i)$ in all inputs x_i

If the standard uncertainty in x_i cannot be found via a Type A evaluation (i.e. the standard deviation of the mean of a series of observations of x_i), the uncertainty $u(x_i)$ must calculated by following steps $1 - 7$ where the input variable x_i is now considered the output variable, with its own functional relationship relating it to a series of input variables.

Step 4. Determine the covariances between correlated input quantities

The covariance $u(x_i, x_j)$ can be set to zero if the variables x_i and x_j are determined independently, if one or both are constant, or if there is not enough information to evaluate their covariance.[85] If the variables x_i and x_j are calculated form a set of L common inputs q_l, then the covariance can be estimated by Equation C.1[85]:

$$u(x_i, x_j) = \sum_{l=1}^{L} \left(\frac{\partial f_i}{\partial q_l}\right)\left(\frac{\partial f_j}{\partial q_l}\right) u^2(q_l) \qquad \text{C.1}$$

where f_i is the functional relationship between x_i and inputs q_l, f_j is the functional relationship between x_j and inputs q_l. This approach can be substituted by Equation C.2 if f_i and f_j are too complex or non-explicit[85]:

$$u(x_i, x_j) = u(x_i)u(x_j)r(x_i, x_j) \qquad \text{C.2}$$

where $r(x_i, x_j)$ is the correlation coefficient between variables x_i and x_j.

Step 5. Calculate the output variable y

The output variable y needs to be calculated from $y = f(x_1, x_2, \ldots, x_n)$ if it has not been done already.

Step 6. Calculate the standard uncertainty $u(y)$

The standard uncertainty in the output quantity y must now be calculated by means of the law of propagation of uncertainty, as given in Equation C.3[85]:

$$u^2(y) = \sum_{i=1}^{n} \left(\frac{\partial f}{\partial x_i}\right)^2 u^2(x_i) + 2\sum_{i=1}^{n-1}\sum_{j=1}^{n}\left(\frac{\partial f}{\partial x_i}\right)\left(\frac{\partial f}{\partial x_j}\right)u(x_i, x_j) \qquad \text{C.3}$$

where all $u(x_i)$ have been calculated in step 3 and all $u(x_i, x_j)$ have been calculated in step 4.

Multivariate linear regression can be performed with matrix algebra, which greatly simplifies the calculation of variances and covariances between input quantities. The uncertainty in sensor-indicator measurements can be estimated by means of Equation C.4[85]:

$$u(x) = \sqrt{\frac{p^2}{3} + \frac{r^2}{12} + \frac{h^2}{12}} \qquad \text{C.4}$$

where p is the sensor precision, often defined as an absolute interval $\pm p$ or as a percentage of full-scale output (FSO), r is the sensor resolution, which defines the smallest detectable increment in an indicated measurement, and h is the sensor hysteresis, which defines the difference between sensor readings at the same conditions, where a load has been applied and then removed from the sensor.

Sometimes it might be necessary to account for a random error that does not contribute to the value of the measurand. In that case a quantity δ is added to the measurand, where δ is equal to zero, but has a nonzero variance, meaning that in the calculation of the uncertainty in the measurand, a contribution of $u^2(\delta)$ must be added.[85,122]

C. Uncertainty Analysis

C.2. Uncertainty Reports

C.2.1. Measured quantities

Concise uncertainty reports are provided to explain the calculation and contributing sources of uncertainty for relevant measured quantities.

Table C.1: Uncertainty report for the measured temperature in the binary CO_2 + FAME HPBDP experiments.

Measurand model	$T_{exp} = T_{ind} + \varepsilon_T + \delta_{fluct}$	$u(T_{exp})$	0.2 °C
Systematic corrections	$\varepsilon_T = \alpha + \beta T_{ind}$		
$u(x_i)$	Evaluation of $u(x_i)$	Value	Units
$u(T_{ind})$ & $u(\varepsilon_T)$ [a]	The temperature probe was calibrated by WIKA Laboratories (Pty) Ltd (certificate number 14-00000098, see Appendix B.4), who provided a combined measurement uncertainty accounting for both the sensor-indicated value, as well as the correction uncertainty.	0.21	°C
$u(\delta_{fluct})$	During measurements, temperature fluctuated by ± 0.1 °C, giving $u(\delta_{fluct}) = 0.1/\sqrt{3}$.[85]	0.06	°C

[a] WIKA is SANAS accredited, and it is assumed that all covariances were accounted for.

Table C.2: Uncertainty report for the measured temperature in the ternary CO_2 + M18:0 + M18:1 HPBDP experiments.

Measurand model	$T_{exp} = T_{ind} + \varepsilon_T + \delta_{fluct}$	$u(T_{exp})$	0.3 °C
Systematic corrections	$\varepsilon_T = \alpha + \beta T_{ind}$		
$u(x_i)$	Evaluation of $u(x_i)$	Value	Units
$u(T_{ind})$ & $u(\varepsilon_T)$ [a]	The temperature probe was calibrated by WIKA Laboratories (Pty) Ltd (certificate number 14-00000553, see Appendix B.4), who provided a combined measurement uncertainty accounting for both the sensor-indicated value, as well as the correction uncertainty.	0.31	°C
$u(\delta_{fluct})$	During measurements, temperature fluctuated by ± 0.1 °C, giving $u(\delta_{fluct}) = 0.1/\sqrt{3}$.[85]	0.06	°C

[a] WIKA is SANAS accredited, and it is assumed that all covariances were accounted for.

Table C.3: Uncertainty report for the measured temperature in the ternary CO_2 + M18:0 + M18:1 VLE experiments.

Measurand model	$T_{exp} = T_{ind} + \varepsilon_T + \delta_{fluct}$	$u(T_{exp})$	0.3 °C
Systematic corrections	$\varepsilon_T = \alpha + \beta T_{ind}$		
$u(x_i)$	*Evaluation of $u(x_i)$*	*Value*	*Units*
$u(T_{ind})$ & $u(\varepsilon_T)$ [a]	The temperature probe was calibrated by WIKA Laboratories (Pty) Ltd (certificate number 14-00000555, see Appendix B.4), who provided a combined measurement uncertainty accounting for both the sensor-indicated value, as well as the correction uncertainty.	0.30	°C
$u(\delta_{fluct})$	During measurements, temperature fluctuated by ± 0.03 °C, giving $u(\delta_{fluct}) = 0.03/\sqrt{3}$.[85]	0.02	°C

[a] *WIKA is SANAS accredited, and it is assumed that all covariances were accounted for.*

C. Uncertainty Analysis

Table C.4: Uncertainty report for the measured pressure in the binary CO_2 + FAME HPBDP experiments performed with the small synthetic-visual cell – generally for bubble points.

Measurand model	$P_{meas} = P_{ind} + \varepsilon_P + \delta_{hyst} + \delta_{fluct} + \delta_{method}$	$u(P_{meas})$	1.2 bar
Systematic corrections	$\varepsilon_P = \beta_4 P_{ind}^3 + \beta_3 P_{ind}^2 + \beta_2 P_{ind} + \beta_1 T_{ind} + \beta_0$		

$u(x_i)$	Evaluation of $u(x_i)$	Value	Units
$u(P_{ind})^a$	Calculated from the sensor-indicator specifications according to $\sqrt{p^2/3 + r^2/12 + h^2/12}$, where p is the precision, r is the resolution, and h is the hysteresis.[85]	0.30	bar
$u(\varepsilon_P)^b$	The uncertainty introduced through the calibration of the OneHalf20 pressure transducer-indicator with a dead weight tester. Determined from the multivariate linear regression of a set of experimentally calculated pressure corrections ε_P^{EXP} at five temperatures (see Appendix B.1). Calibration experiments were performed with monotonically increasing pressure and monotonically decreasing pressure to account for sensor hysteresis.	0.30	bar
$u(\delta_{hyst})$	Calculated by recasting the maximum sensor hysteresis of 3.5 bar observed during the pressure calibration to a standard uncertainty, giving $u(\delta_{hyst}) = 3.5/\sqrt{12}$.[85]	1.01	bar
$u(\delta_{fluct})$	During measurements, pressure fluctuated by ± 0.1 bar, giving $u(\delta_{fluct}) = 0.1/\sqrt{3}$.[85]	0.06	bar
$u(\delta_{method})^c$	The uncertainty associated with the visual determination of phase transitions, calculated as the standard error of the verification system data compared to literature data.	0.47	bar
$u(x_i, x_j)$	*Covariances*	*Value*	*Units*
$u(P_{ind}, \varepsilon_P)$	Both P_{ind} and ε_P depend on P_{ind}, and so their covariance was determined from the results of pressure calibration experiments with $u(P_{ind}, \varepsilon_P) = r(P_{ind}, \varepsilon_P)u(P_{ind})u(\varepsilon_P)$, where the covariance was taken as the average of the covariances of the increasing pressure and decreasing pressure experiments.	0.02	bar²

[a] In this calculation, p was 0.525 bar, and r was 0.1 bar. h was set to zero, since the hysteresis was accounted for explicitly in the measurand model. The precision here differs from the other pressure reports due to the use of a different indicator connected to the pressure transmitter.

[b] In order to account for the uncertainty introduced by the measured ε_P^{EXP} during the calibration experiment, the squared uncertainty $u^2(\varepsilon_P^{EXP})$ was added to the variance of parameter β_0 determined from multivariate linear regression. $u(\varepsilon_P^{EXP}) = \sqrt{u^2(P_{ind}) + u^2(P_{ref})}$, where $u(P_{ref}) = 0.06$ bar, and is the uncertainty to which the dead weight tester was independently calibrated by Unique Metrology. See calibration certificate 1602P6223-1 in Appendix B.1.

[c] HPBDP data measured for the CO_2 + 1-octanol verification system at four temperatures and six solute fractions were compared to the literature data measured by Fourie[80] in order to calculate the standard deviation $S_{\Delta P}$ of the pressure deviations from literature. The standard error of the average pressure deviation was determined from $u(\delta_{method}) = S_{\Delta P}/\sqrt{n}$ where the number of data points n was equal to 21.[85]

Table C.5: Uncertainty report for the measured pressure in the binary CO_2 + FAME HPBDP experiments performed with the large synthetic-visual cell – generally for dew points.

Measurand model	$P_{meas} = P_{ind} + \varepsilon_P + \delta_{hyst} + \delta_{fluct} + \delta_{method}$	$u(P_{meas})$	0.5 bar
Systematic corrections	$\varepsilon_P = \beta_4 P_{ind}^3 + \beta_3 P_{ind}^2 + \beta_2 P_{ind} + \beta_1 T_{ind} + \beta_0$		
$u(x_i)$	Evaluation of $u(x_i)$	*Value*	*Units*
$u(P_{ind})^a$	Calculated from the sensor-indicator specifications according to $\sqrt{p^2/3 + r^2/12 + h^2/12}$, where p is the precision, r is the resolution, and h is the hysteresis.[85]	0.16	bar
$u(\varepsilon_P)^b$	The uncertainty introduced through the calibration of the OneHalf20 pressure transducer-indicator with a dead weight tester. Determined from the multivariate linear regression of a set of experimentally calculated pressure corrections ε_P^{EXP} at five temperatures (see Appendix B.1). Calibration experiments were performed with monotonically increasing pressure and monotonically decreasing pressure to account for sensor hysteresis.	0.18	bar
$u(\delta_{hyst})$	Calculated by recasting the maximum sensor hysteresis of 0.5 bar observed during the pressure calibration to a standard uncertainty, giving $u(\delta_{hyst}) = 0.5/\sqrt{12}$.[85]	0.14	bar
$u(\delta_{fluct})$	During measurements, pressure fluctuated by ± 0.1 bar, giving $u(\delta_{fluct}) = 0.1/\sqrt{3}$.[85]	0.06	bar
$u(\delta_{method})^c$	The uncertainty associated with the visual determination of phase transitions, calculated as the standard error of the verification system data compared to literature data.	0.47	bar
$u(x_i, x_j)$	Covariances	*Value*	*Units*
$u(P_{ind}, \varepsilon_P)$	Both P_{ind} and ε_P depend on P_{ind}, and so their covariance was determined from the results of pressure calibration experiments with $u(P_{ind}, \varepsilon_P) = r(P_{ind}, \varepsilon_P)u(P_{ind})u(\varepsilon_P)$, where the covariance was taken as the average of the covariances of the increasing pressure and decreasing pressure experiments.	-8.7e-03	bar²

[a] *In this calculation, p was 0.28 bar, and r was 0.1 bar. h was set to zero, since the hysteresis was accounted for explicitly in the measurand model.*

[b] *In order to account for the uncertainty introduced by the measured ε_P^{EXP} during the calibration experiment, the squared uncertainty $u^2(\varepsilon_P^{EXP})$ was added to the variance of parameter β_0 determined from multivariate linear regression. $u(\varepsilon_P^{EXP}) = \sqrt{u^2(P_{ind}) + u^2(P_{ref})}$, where $u(P_{ref})$ = 0.06 bar, and is the uncertainty to which the dead weight tester was independently calibrated by Unique Metrology. See calibration certificate 1602P6223-1 in Appendix B.1.*

[c] *HPBDP data measured for the CO_2 + 1-octanol verification system at four temperatures and six solute fractions were compared to the literature data measured by Fourie[80] in order to calculate the standard deviation $S_{\Delta P}$ of the pressure deviations from literature. The standard error of the average pressure deviation was determined from $u(\delta_{method}) = S_{\Delta P}/\sqrt{n}$ where the number of data points n was equal to 21.[85]*

C. Uncertainty Analysis

Table C.6: Uncertainty report for the measured pressure in the ternary CO_2 + M18:0 + M18:1 HPBDP experiments performed with the small synthetic-visual cell – generally for bubble points.

Measurand model	$P_{meas} = P_{ind} + \varepsilon_P + \delta_{hyst} + \delta_{fluct} + \delta_{method}$			
Systematic corrections	$\varepsilon_P = \beta_4 P_{ind}^3 + \beta_3 P_{ind}^2 + \beta_2 P_{ind} + \beta_1 T_{ind} + \beta_0$		$u(P_{meas})$	**0.6 bar**
$u(x_i)$	Evaluation of $u(x_i)$		*Value*	*Units*
$u(P_{ind})^a$	Calculated from the sensor-indicator specifications according to $\sqrt{p^2/3 + r^2/12 + h^2/12}$, where p is the precision, r is the resolution, and h is the hysteresis.[85]		0.16	bar
$u(\varepsilon_P)^b$	The uncertainty introduced through the calibration of the OneHalf20 pressure transducer-indicator with a dead weight tester. Determined from the multivariate linear regression of a set of experimentally calculated pressure corrections ε_P^{EXP} at five temperatures (see Appendix B.1). Calibration experiments were performed with monotonically increasing pressure and monotonically decreasing pressure to account for sensor hysteresis.		0.19	bar
$u(\delta_{hyst})$	Calculated by recasting the maximum sensor hysteresis of 0.6 bar observed during the pressure calibration to a standard uncertainty, giving $u(\delta_{hyst}) = 0.6/\sqrt{12}$.[85]		0.17	bar
$u(\delta_{fluct})$	During measurements, pressure fluctuated by ± 0.1 bar, giving $u(\delta_{fluct}) = 0.1/\sqrt{3}$.[85]		0.06	bar
$u(\delta_{method})^c$	The uncertainty associated with the visual determination of phase transitions, calculated as the standard error of the verification system data compared to literature data.		0.47	bar
$u(x_i, x_j)$	Covariances		*Value*	*Units*
$u(P_{ind}, \varepsilon_P)$	Both P_{ind} and ε_P depend on P_{ind}, and so their covariance was determined from the results of pressure calibration experiments with $u(P_{ind}, \varepsilon_P) = r(P_{ind}, \varepsilon_P)u(P_{ind})u(\varepsilon_P)$, where the covariance was taken as the average of the covariances of the increasing pressure and decreasing pressure experiments.		8.6e-03	bar²

[a] In this calculation, p was 0.28 bar, and r was 0.1 bar. h was set to zero, since the hysteresis was accounted for explicitly in the measurand model.

[b] In order to account for the uncertainty introduced by the measured ε_P^{EXP} during the calibration experiment, the squared uncertainty $u^2(\varepsilon_P^{EXP})$ was added to the variance of parameter β_0 determined from multivariate linear regression. $u(\varepsilon_P^{EXP}) = \sqrt{u^2(P_{ind}) + u^2(P_{ref})}$, where $u(P_{ref})$ = 0.06 bar, and is the uncertainty to which the dead weight tester was independently calibrated by Unique Metrology. See calibration certificate 1602P6223-1 in Appendix B.1.

[c] HPBDP data measured for the CO_2 + 1-octanol verification system at four temperatures and six solute fractions were compared to the literature data measured by Fourie[80] in order to calculate the standard deviation $S_{\Delta P}$ of the pressure deviations from literature. The standard error of the average pressure deviation was determined from $u(\delta_{method}) = S_{\Delta P}/\sqrt{n}$ where the number of data points n was equal to 21.[85]

Table C.7: Uncertainty report for the measured pressure in the ternary CO_2 + M18:0 + M18:1 HPBDP experiments performed with the large synthetic-visual cell – generally for dew points.

Measurand model	$P_{meas} = P_{ind} + \varepsilon_P + \delta_{hyst} + \delta_{fluct} + \delta_{method}$	$u(P_{meas})$	0.6 bar
Systematic corrections	$\varepsilon_P = \beta_4 P_{ind}^3 + \beta_3 P_{ind}^2 + \beta_2 P_{ind} + \beta_1 T_{ind} + \beta_0$		

$u(x_i)$	Evaluation of $u(x_i)$	Value	Units
$u(P_{ind})^a$	Calculated from the sensor-indicator specifications according to $\sqrt{p^2/3 + r^2/12 + h^2/12}$, where p is the precision, r is the resolution, and h is the hysteresis.[85]	0.16	bar
$u(\varepsilon_P)^b$	The uncertainty introduced through the calibration of the OneHalf20 pressure transducer-indicator with a dead weight tester. Determined from the multivariate linear regression of a set of experimentally calculated pressure corrections ε_P^{EXP} at five temperatures (see Appendix B.1). Calibration experiments were performed with monotonically increasing pressure and monotonically decreasing pressure to account for sensor hysteresis.	0.18	bar
$u(\delta_{hyst})$	Calculated by recasting the maximum sensor hysteresis of 0.5 bar observed during the pressure calibration to a standard uncertainty, giving $u(\delta_{hyst}) = 0.5/\sqrt{12}$.[85]	0.14	bar
$u(\delta_{fluct})$	During measurements, pressure fluctuated by ± 0.1 bar, giving $u(\delta_{fluct}) = 0.1/\sqrt{3}$.[85]	0.06	bar
$u(\delta_{method})^c$	The uncertainty associated with the visual determination of phase transitions, calculated as the standard error of the verification system data compared to literature data.	0.47	bar
$u(x_i, x_j)$	Covariances	Value	Units
$u(P_{ind}, \varepsilon_P)$	Both P_{ind} and ε_P depend on P_{ind}, and so their covariance was determined from the results of pressure calibration experiments with $u(P_{ind}, \varepsilon_P) = r(P_{ind}, \varepsilon_P)u(P_{ind})u(\varepsilon_P)$, where the covariance was taken as the average of the covariances of the increasing pressure and decreasing pressure experiments.	8.7e-03	bar²

[a] *In this calculation, p was 0.28 bar, and r was 0.1 bar. h was set to zero, since the hysteresis was accounted for explicitly in the measurand model.*

[b] *In order to account for the uncertainty introduced by the measured ε_P^{EXP} during the calibration experiment, the squared uncertainty $u^2(\varepsilon_P^{EXP})$ was added to the variance of parameter β_0 determined from multivariate linear regression. $u(\varepsilon_P^{EXP}) = \sqrt{u^2(P_{ind}) + u^2(P_{ref})}$, where $u(P_{ref}) = 0.06$ bar, and is the uncertainty to which the dead weight tester was independently calibrated by Unique Metrology. See calibration certificate 1602P6223-1 in Appendix B.1.*

[c] *HPBDP data measured for the CO_2 + 1-octanol verification system at four temperatures and six solute fractions were compared to the literature data measured by Fourie[80] in order to calculate the standard deviation $S_{\Delta P}$ of the pressure deviations from literature. The standard error of the average pressure deviation was determined from $u(\delta_{method}) = S_{\Delta P}/\sqrt{n}$ where the number of data points n was equal to 21.[85]*

C. Uncertainty Analysis

Table C.8: Uncertainty report for the measured and reported pressure in the ternary CO_2 + M18:0 + M18:1 high-pressure VLE experiments performed with the synthetic-analytic cell.

Measurand model	$P_{meas} = P_{ind} + \varepsilon_P + \delta_{hyst} + \delta_{fluct}$	$u(P_{meas})$	0.3 bar
Systematic corrections	$\varepsilon_P = \beta_4 P_{ind}^3 + \beta_3 P_{ind}^2 + \beta_2 P_{ind} + \beta_1 T_{ind} + \beta_0$		

$u(x_i)$	Evaluation of $u(x_i)$	Value	Units
$u(P_{ind})^a$	Calculated from the sensor-indicator specifications according to $\sqrt{p^2/3 + r^2/12 + h^2/12}$, where p is the precision, r is the resolution, and h is the hysteresis.[85]	0.16	bar
$u(\varepsilon_P)^b$	The uncertainty introduced through the calibration of the OneHalf20 pressure transducer-indicator with a dead weight tester. Determined from the multivariate linear regression of a set of experimentally calculated pressure corrections ε_P^{EXP} at three temperatures (see Appendix B.1). Calibration experiments were performed with monotonically increasing pressure and monotonically decreasing pressure to account for sensor hysteresis.	0.18	bar
$u(\delta_{hyst})$	Calculated by recasting the maximum sensor hysteresis of 0.9 bar observed during the pressure calibration to a standard uncertainty, giving $u(\delta_{hyst}) = 0.9/\sqrt{12}$.[85]	0.26	bar
$u(\delta_{fluct})$	During measurements, pressure fluctuated by ± 0.2 bar, giving $u(\delta_{fluct}) = 0.2/\sqrt{3}$.[85]	0.12	bar

$u(x_i, x_j)$	Covariances	Value	Units
$u(P_{ind}, \varepsilon_P)$	Both P_{ind} and ε_P depend on P_{ind}, and so their covariance was determined from the results of pressure calibration experiments with $u(P_{ind}, \varepsilon_P) = r(P_{ind}, \varepsilon_P) u(P_{ind}) u(\varepsilon_P)$, where the covariance was taken as the average of the covariances of the increasing pressure and decreasing pressure experiments.	-9.5e-03	bar²

[a] *In this calculation, p was 0.28 bar, and r was 0.1 bar. h was set to zero, since the hysteresis was accounted for explicitly in the measurand model.*

[b] *In order to account for the uncertainty introduced by the measured ε_P^{EXP} during the calibration experiment, the squared uncertainty $u^2(\varepsilon_P^{EXP})$ was added to the variance of parameter β_0 determined from multivariate linear regression. $u(\varepsilon_P^{EXP}) = \sqrt{u^2(P_{ind}) + u^2(P_{ref})}$, where $u(P_{ref})$ = 0.06 bar, and is the uncertainty to which the dead weight tester was independently calibrated by Unique Metrology. See calibration certificate 1602P6223-1 in Appendix B.1.*

Table C.9: Uncertainty report for the measured mass of total FAME solute loaded for HPBDP experiments.

Measurand model	$m_{FAME} = m_i - m_f$	$u(m_{FAME})$	0.001 - 0.026 g
$u(x_i)$	Evaluation of $u(x_i)$	Value	Units
$u(m_i)$	The uncertainty in the initial mass for the glassware containing the FAME solute on the 3-decimal Ohaus scale, as determined from an independent calibration certificate. See certificate number M2779/1 in Appendix B.5.	0.0009	g
$u(m_f)^a$	The uncertainty in the indicated mass for the glassware after loading the FAME solute to the cell. This uncertainty contribution accounts for the uncertainty of the indicated mass, as well as the uncertainty associated with the purity of the stock FAME: $u^2(m_f) = u^2(m_{ind}) + u^2(\delta_{purity})$. Where the uncertainty contributed by the impurities are determined from $u^2(\delta_{purity}) = p^2 m_{FAME}^2/12$ as derived by Swanepoel.[122]	0.0011 - 0.0257	g

^{a} The impurity mass fraction p was taken as 0.01 g·g^{-1} for all three FAMEs investigated (see Table 4.1). $u(m_f)$ is a linear function of m_{FAME}: $u(m_f) = 0.0029 m_{FAME} + 0.0002$, with $R_{adj}^2 = 0.9999$ determined from 34 data points.

Table C.10: Uncertainty report for the measured mass of CO_2 solvent loaded for HPBDP experiments.

Measurand model	$m_{CO_2} = m_i - m_f$	$u(m_{CO_2})$	0.006 g
$u(x_i)$	Evaluation of $u(x_i)$	Value	Units
$u(m_i)$	The uncertainty in the initial mass for the gas bomb loaded with CO_2 on the 3-decimal Precisa scale, as determined from an independent calibration certificate. See certificate number M2779/3 in Appendix B.5.	0.0045	g
$u(m_f)^a$	The uncertainty in the indicated mass for the gas bomb after loading the CO_2 solvent to the cell. This uncertainty contribution accounts for the uncertainty of the indicated mass, as well as the uncertainty associated with the purity of the CO_2: $u^2(m_f) = u^2(m_{ind}) + u^2(\delta_{purity})$. Where the uncertainty contributed by the impurities are determined from $u^2(\delta_{purity}) = p^2 m_{CO_2}^2/12$ as derived by Swanepoel.[122]	0.0045	g

^{a} The impurity mass fraction p was taken as 0.00005 g·g^{-1} for CO_2 (see Table 4.1).

C. Uncertainty Analysis

Table C.11: Uncertainty report for the measured mass fraction M18:0 in a recovered solute mixture of M18:0 (1) + M18:1 (2) determined from gas chromatography.

Measurand model	$\phi = \dfrac{m_1}{m_1 + m_2}$	$u(\phi)^c$	0.0244 g·g^{-1}
$u(x_i)$	*Evaluation of* $u(x_i)$	*Value*	*Units*
$u(m_1)^a$	The uncertainty in the measured M18:0 mass as determined from GC analysis. The uncertainty is determined from statistical analysis of the calibration curve data.	4.56e-06	g
$u(m_2)^b$	The uncertainty in the measured M18:1 mass as determined from GC analysis. The uncertainty is determined from statistical analysis of the calibration curve data.	7.13e-06	g

^{a} $u(m_1)$ *was determined from the propagation uncertainty through the GC calibration equation* $m_1 = \beta_1 A_1 + \alpha_1$, *accounting for the uncertainty in the calibration curve parameters. The uncertainty contributed from the measured masses and solute impurities during the calibration experiment was added to the uncertainty of* α_1.

^{b} $u(m_2)$ *was determined from the propagation uncertainty through the GC calibration equation* $m_2 = \beta_2 A_2 + \alpha_2$, *accounting for the uncertainty in the calibration curve parameters. The uncertainty contributed from the measured masses and solute impurities during the calibration experiment was added to the uncertainty of* α_2.

$^c \left(\dfrac{\partial \phi}{\partial m_1}\right)^2 = 7777218 \ g^{-2}$ *and* $\left(\dfrac{\partial \phi}{\partial m_2}\right)^2 = 8509686 \ g^{-2}$.

Table C.12: Uncertainty report for the reduced mass fraction M18:0 in the solute mixture M18:0 (1) + M18:1 (2) loaded during ternary HPBDP experiments. Nominal fraction of 0.501 g·g^{-1}.

Measurand model	$w_1^{red} = \dfrac{m_1}{m_1 + m_2}$	$u(w_1^{red})^a$	0.001 g·g^{-1}
$u(x_i)$	*Evaluation of* $u(x_i)$	*Value*	*Units*
$u(m_1)$	The uncertainty in the measured M18:0 mass determined from the 3-decimal scale specifications and the impurity contribution. See Table C.9.	0.0002	g
$u(m_2)$	The uncertainty in the measured M18:1 mass determined from the 3-decimal scale specifications and the impurity contribution. See Table C.9.	0.0002	g

$^a \left(\dfrac{\partial w_1^{red}}{\partial m_1}\right)^2 = 0.0026 \ g^{-2}$ *and* $\left(\dfrac{\partial w_1^{red}}{\partial m_2}\right)^2 = 0.0026 \ g^{-2}$.

Table C.13:Uncertainty report for the reduced mass fraction M18:0 in the solute mixture M18:0 (1) + M18:1 (2) loaded during ternary HPBDP experiments. Nominal fraction of 0.237 g·g^{-1}. Mixture was prepared by adding fresh M18:1 solute to a recovered residue of M18:0 + M18:1 mixture from previous experiments.

Measurand model	$w_1^{red} = \dfrac{\phi m_{res}}{m_{res} + m_2}$	$u(w_1^{red})^a$	0.011 g·g^{-1}
$u(x_i)$	*Evaluation of $u(x_i)$*	*Value*	*Units*
$u(\phi)$	Determined from GC analysis. See Table C.11.	0.0244	g·g^{-1}
$u(m_{res})$	The uncertainty in the mass of mixture residue added, determined from the 3-decimal scale specifications. See calibration certificate M2779/1 in Appendix B.5.	0.0013	g
$u(m_2)$	The uncertainty in the measured M18:1 mass added, determined from the 3-decimal scale specifications and the impurity contribution. See Table C.9.	0.0233	g

$^a \left(\dfrac{\partial w_1^{red}}{\partial \phi}\right)^2 = \mathbf{0.2157}\ g^2 \cdot g^{-2}$, $\left(\dfrac{\partial w_1^{red}}{\partial m_{res}}\right)^2 = \mathbf{0.0013}\ g^{-2}$, and $\left(\dfrac{\partial w_1^{red}}{\partial m_2}\right)^2 = \mathbf{0.0002}\ g^{-2}$.

Table C.14: Uncertainty report for the reduced mass fraction M18:0 in the solute mixture M18:0 (1) + M18:1 (2) loaded during ternary HPBDP experiments. Nominal fraction of 0.772 g·g^{-1}. Mixture was prepared by adding fresh M18:0 solute to a recovered residue of M18:0 + M18:1 mixture from previous experiments.

Measurand model	$w_1^{red} = \dfrac{\phi m_{res} + m_1}{m_{res} + m_1}$	$u(w_1^{red})^a$	0.011 g·g^{-1}
$u(x_i)$	*Evaluation of $u(x_i)$*	*Value*	*Units*
$u(\phi)$	Determined from GC analysis. See Table C.11.	0.0244	g·g^{-1}
$u(m_{res})$	The uncertainty in the mass of mixture residue added, determined from 3-decimal scale specifications. See calibration certificate M2779/1 in Appendix B.5.	0.0013	g
$u(m_1)$	The uncertainty in the measured M18:0 mass added, determined from the 3-decimal scale specifications and the impurity contribution. See Table C.9.	0.0051	g

$^a \left(\dfrac{\partial w_1^{red}}{\partial \phi}\right)^2 = \mathbf{0.2169}\ g^2 \cdot g^{-2}$, $\left(\dfrac{\partial w_1^{red}}{\partial m_{res}}\right)^2 = \mathbf{0.0066}\ g^{-2}$, and $\left(\dfrac{\partial w_1^{red}}{\partial m_1}\right)^2 = \mathbf{0.0050}\ g^{-2}$.

C. Uncertainty Analysis

C.2.2. Calculated quantities

Summaries of the approach and equations used to calculate the uncertainty in certain calculated quantities, or quantities that presented a large amount of variation in the uncertainty over the range of measurements are provided.

C.2.2.1. Binary HPBDP experiments

The solute fraction z, the mass fraction of FAME in the mixture, was calculated from Equation C.5:

$$z = \frac{m_{FAME}}{m_{FAME} + m_{CO_2} - m_{lost}}$$

C.5

where m_{lost} is the mass of CO_2 solvent lost during the loading procedure. In order to determine the uncertainty in z, the uncertainties $u(m_{FAME})$, $u(m_{CO_2})$, and $u(m_{lost})$ need to be calculated. $u(m_{FAME})$ was determined previously in Table C.9, and $u(m_{CO_2})$ was determined previously in Table C.1. The mass of solvent lost during loading was calculated from Equation C.6:

$$m_{lost} = \rho_{CO_2} V$$

C.6

where ρ_{CO_2} is the density of CO_2 in the manifold and connecting lines, and V is the volume of the manifold and connecting lines. The density was determined by measuring the pressure ($u(P_{man})$ = 0.34 bar) and temperature ($u(T_{man})$ = 0.9 °C) in the manifold after loading, and using these measurements to find the density from the NIST Chemistry WebBook.[54] In order to quantify the uncertainty in the density, the uncertainty in pressure and temperature was propagated through the Redlich-Kwong EOS.[8] The uncertainty in the manifold volume was determined from the volume calibration data as described in Appendix B.2. $u(\rho_{CO_2})$ and $u(V)$ were then used to determine $u(m_{lost})$ for each loading, with the calculation of $u(z)$ a simple application of the law of propagation of uncertainty. None of the masses were correlated, as all of the variables were measured with separate with instruments and were completely independent of each other. The contribution of the purity of the CO_2 was negligible in the calculation of $u(m_{lost})$; $u^2(\delta_{purity})$ was in the order of 10^{-10} g[2]. The results of the calculated uncertainties in solute fraction z are given in Table C.15.

Table C.15: Calculated uncertainties in the mass fraction FAME for the binary CO_2 + FAME HPBDP experiments.

M18:0		M18:1		M18:2	
z [g·g⁻¹]	$u(z)$ [g·g⁻¹]	z [g·g⁻¹]	$u(z)$ [g·g⁻¹]	z [g·g⁻¹]	$u(z)$ [g·g⁻¹]
0.0104	0.0001	0.0110	0.0001	0.0375	0.0003
0.0510	0.0004	0.0545	0.0006	0.0862	0.0007
0.0799	0.0006	0.0874	0.0009	0.1599	0.0013
0.1225	0.0008	0.1222	0.0007	0.2638	0.0017
0.1609	0.0017	0.1582	0.0009	0.3104	0.0021
0.2463	0.0022	0.2186	0.0013	0.3861	0.0030
0.3105	0.0018	0.2569	0.0017	0.4675	0.0041
0.3675	0.0025	0.2884	0.0018	0.5414	0.0044
0.4611	0.0034	0.3690	0.0031	0.5865	0.0048
0.5449	0.0046	0.4696	0.0043		
0.6234	0.0056	0.4947	0.0045		
		0.5736	0.0051		

The uncertainty in the measured pressure calculated in Table C.4 and Table C.5 only accounts for the effect of the measurement, but there are other factors that influence the phase transition pressure of a solute-solvent system, namely the temperature and the composition. This means that, in order to calculate the uncertainty in the reported phase transition pressure, one needs to account also for the effect of the uncertainty in these variables on the pressure. This was done through Equation C.7:

$$u^2(P) = u^2(P_{meas}) + \left(\frac{\partial P}{\partial T}\right)^2 u^2(T) + \left(\frac{\partial P}{\partial z}\right)^2 u^2(z) \qquad \text{C.7}$$

With $u(P_{meas})$, $u(T)$, and $u(z)$ known, only $\left(\frac{\partial P}{\partial T}\right)$ and $\left(\frac{\partial P}{\partial z}\right)$ need to be evaluated. The sensitivity of pressure with regards to temperature was determined by inspecting the PT-correlations for the HPBDP data presented in Chapter 5. The slopes of the PT-correlations were found to be component specific, but did not vary much with temperature or composition. The average was taken for each component across all the correlations, giving $\left(\frac{\partial P}{\partial T}\right)_{M18:0}$ = 2.4 bar·°C⁻¹, $\left(\frac{\partial P}{\partial T}\right)_{M18:1}$ = 2.5 bar·°C⁻¹, and $\left(\frac{\partial P}{\partial T}\right)_{M18:2}$ = 2.5 bar·°C⁻¹. The sensitivity of pressure with regards to composition was determined by fitting polynomials to the HPBDP data and determining the analytical derivative. This allowed the sensitivity to be evaluated at each data point individually. The results of this uncertainty analysis are presented in Table C.16.

C. Uncertainty Analysis

Table C.16:Final uncertainties in the reported phase transition pressures for the binary CO_2 + FAME systems.

M18:0			M18:1			M18:2		
z	$u(P_{meas})$	$u(P)$	z	$u(P_{meas})$	$u(P)$	z	$u(P_{meas})$	$u(P)$
[g·g⁻¹]	[bar]	[bar]	[g·g⁻¹]	[bar]	[bar]	[g·g⁻¹]	[bar]	[bar]
0.0104	0.5	0.7	0.0110	0.5	0.7	0.0375	0.5	0.7
0.0510	0.5	0.7	0.0545	0.5	0.7	0.0862	0.5	0.7
0.0799	0.5	0.7	0.0874	0.5	0.7	0.1599	0.5	0.7
0.1225	0.5	0.7	0.1222	0.5	0.7	0.2638	1.2	1.3
0.1609	1.2	1.3	0.1582	0.5	0.7	0.3104	1.2	1.3
0.2463	1.2	1.3	0.2186	0.5	0.7	0.3861	1.2	1.4
0.3105	1.2	1.3	0.2569	1.2	1.3	0.4675	1.2	1.6
0.3675	1.2	1.4	0.2884	1.2	1.3	0.5414	1.2	1.7
0.4611	1.2	1.5	0.3690	1.2	1.4	0.5865	1.2	1.8
0.5449	1.2	1.7	0.4696	1.2	1.6			
0.6234	1.2	1.8	0.4947	1.2	1.6			
			0.5736	1.2	1.8			

C.2.2.2. Ternary HPBDP experiments

The uncertainty in z, the total FAME fraction in the M18:0 (1) + M18:1 (2) + CO_2 (3) system, was determined in an identical manner to the binary CO_2 + FAME systems. The individual component fractions were calculated with Equations C.8 to C.10:

$$w_1 = w_1^{red}z \tag{C.8}$$

$$w_2 = \left(1 - w_1^{red}\right)z \tag{C.9}$$

$$w_3 = 1 - w_1 - w_2 \tag{C.10}$$

where w_1 is the mass fraction M18:0, w_2 is the mass fraction M18:1, and w_3 is the mass fraction CO_2. The uncertainty in the M18:0 fraction in the loading mixture, $u\left(w_1^{red}\right)$ was previously determined in Tables C.1 to C.1. The calculated uncertainty in the individual component mass fractions are given in Table C.17.

Table C.17: Calculated uncertainties in the component mass fractions for the M18:0 (1) + M18:1 (2) + CO_2 (3) system at three different solvent-free mass fractions of M18:0.

w_1 [g·g⁻¹]	$u(w_1)$ [g·g⁻¹]	w_2 [g·g⁻¹]	$u(w_2)$ [g·g⁻¹]	w_3 [g·g⁻¹]	$u(w_3)$ [g·g⁻¹]
		w_1^{red} = 0.501 g·g⁻¹			
0.0058	0.0001	0.0058	0.0001	0.9883	0.0001
0.0253	0.0003	0.0252	0.0003	0.9494	0.0004

w_1 [g·g⁻¹]	$u(w_1)$ [g·g⁻¹]	w_2 [g·g⁻¹]	$u(w_2)$ [g·g⁻¹]	w_3 [g·g⁻¹]	$u(w_3)$ [g·g⁻¹]
0.0416	0.0004	0.0414	0.0004	0.9170	0.0007
0.0598	0.0005	0.0596	0.0005	0.8806	0.0009
0.0821	0.0007	0.0817	0.0007	0.8362	0.0012
0.1278	0.0017	0.1273	0.0017	0.7448	0.0030
0.1405	0.0019	0.1400	0.0019	0.7195	0.0032
0.1853	0.0039	0.1846	0.0039	0.6301	0.0067
0.2118	0.0028	0.2109	0.0028	0.5773	0.0049
0.2678	0.0029	0.2668	0.0029	0.4654	0.0050
0.2888	0.0026	0.2877	0.0025	0.4235	0.0044
w_1^{red} = 0.237 g·g⁻¹					
0.0023	0.0001	0.0074	0.0001	0.9903	0.0002
0.0128	0.0006	0.0411	0.0008	0.9461	0.0012
0.0189	0.0009	0.0609	0.0011	0.9202	0.0017
0.0283	0.0014	0.0912	0.0016	0.8805	0.0026
0.0378	0.0018	0.1217	0.0021	0.8406	0.0034
0.0478	0.0023	0.1540	0.0026	0.7982	0.0042
0.0633	0.0032	0.2037	0.0045	0.7331	0.0065
0.0709	0.0038	0.2282	0.0064	0.7009	0.0087
0.0838	0.0043	0.2698	0.0062	0.6464	0.0089
0.0972	0.0048	0.3130	0.0060	0.5897	0.0092
0.1128	0.0056	0.3632	0.0074	0.5240	0.0111
0.1346	0.0066	0.4332	0.0079	0.4323	0.0124
w_1^{red} = 0.772 g·g⁻¹					
0.0081	0.0002	0.0024	0.0001	0.9895	0.0002
0.0403	0.0007	0.0119	0.0006	0.9478	0.0011
0.0592	0.0011	0.0175	0.0009	0.9233	0.0017
0.0935	0.0019	0.0276	0.0014	0.8789	0.0029
0.1244	0.0022	0.0367	0.0019	0.8389	0.0035
0.1623	0.0029	0.0479	0.0024	0.7897	0.0046
0.2034	0.0047	0.0601	0.0032	0.7365	0.0067
0.2341	0.0052	0.0691	0.0036	0.6967	0.0075
0.2784	0.0057	0.0822	0.0043	0.6394	0.0085
0.3242	0.0059	0.0957	0.0049	0.5801	0.0093
0.4179	0.0075	0.1234	0.0063	0.4587	0.0118
0.4453	0.0078	0.1315	0.0067	0.4232	0.0124

C. Uncertainty Analysis

The uncertainty in the reported phase transition pressures were determined from Equation C.11:

$$u^2(P) = u^2(P_{meas}) + \left(\frac{\partial P}{\partial T}\right)^2 u^2(T) + \left(\frac{\partial P}{\partial z}\right)^2 u^2(z) + \left(\frac{\partial P}{\partial w_1^{red}}\right)^2 u^2\left(w_1^{red}\right) \qquad \text{C.11}$$

The $\left(\frac{\partial P}{\partial T}\right)$ and $\left(\frac{\partial P}{\partial z}\right)$ sensitivities were evaluated in the same way as for the binary HPBDP data. There is an additional contribution to the pressure uncertainty due to the influence of w_1^{red}, the solvent-free weight fraction of M18:0. The effect of the w_1^{red}-contribution to the uncertainty was found to be negligible, as even at the lowest temperature of 35 °C, and at a total solute fraction of 0.2 − 0.3 g·g⁻¹, where $\left(\frac{\partial P}{\partial w_1^{red}}\right)$ is at a maximum, there was no change in $u(P)$ at the reported resolution. The results are presented in Table C.18.

Table C.18:Calculated uncertainties in the reported phase transition pressure for the ternary M18:0 + M18:1 + CO₂ system at three different solvent-free mass fractions M18:0.

w_1^{red} = 0.237 g·g⁻¹			w_1^{red} = 0.501 g·g⁻¹			w_1^{red} = 0.772 g·g⁻¹		
z	$u(P_{meas})$	$u(P)$	z	$u(P_{meas})$	$u(P)$	z	$u(P_{meas})$	$u(P)$
[g·g⁻¹]	[bar]	[bar]	[g·g⁻¹]	[bar]	[bar]	[g·g⁻¹]	[bar]	[bar]
0.0097	0.6	1.0	0.0117	0.6	1.0	0.0105	0.6	1.0
0.0539	0.6	1.0	0.0506	0.6	1.0	0.0522	0.6	1.0
0.0798	0.6	1.0	0.0830	0.6	1.0	0.0767	0.6	1.0
0.1195	0.6	1.0	0.1194	0.6	1.0	0.1211	0.6	1.0
0.1595	0.6	1.0	0.1638	0.6	1.0	0.1611	0.6	1.0
0.2018	0.6	1.0	0.2552	0.6	1.0	0.2102	0.6	1.0
0.2670	0.6	1.0	0.2805	0.6	1.0	0.2635	0.6	1.0
0.2991	0.6	1.1	0.3699	0.6	1.4	0.3032	0.6	1.0
0.3536	0.6	1.2	0.4227	0.6	1.4	0.3606	0.6	1.2
0.4102	0.6	1.3	0.5346	0.6	1.6	0.4199	0.6	1.3
0.4760	0.6	1.6	0.5765	0.6	1.5	0.5413	0.6	1.6
0.5678	0.6	1.6				0.5768	0.6	1.5

C.2.2.3. Ternary VLE Experiments

The main measurements provided from the VLE experiments were chromatographic signal data. These data was converted to component masses through various methods, where both the measurement and the calculation contributed to the uncertainty. Considering the vapour phase first, there were two methods for determining the sample masses, one for the heavy FAME components, and one for CO₂.

The masses of M18:0 and M18:1 were determined from the integration bounding peak deconvolution technique. The uncertainty in the resultant masses were quantified from the test error based on a cross-validation analysis, as described in Section 4.3.3. In the analysis, however, the calculated deconvoluted masses were compared to the actual masses as known from the prepared samples to calculate the test error. This means that additional uncertainty was contributed due to the uncertainty associated with known masses from the error associated with the scale and the syringe used to inject the samples. The total uncertainty in the total FAME masses in the analysed vapour samples were determined from Equation C.12:

$$u^2(m_i) = u^2(m_{i,CV}) + u^2(m_{i,calib}) \qquad \text{C.12}$$

where $u^2(m_{1,CV})$ was found to be 1.52E-13 g^2 M18:0, and $u^2(m_{2,CV})$ was found to be 1.29e-13 g^2 M18:1.

The actual calibration masses were calculated with Equation C.13:

$$m_{i,calib} = z_i \rho_{sample} V_{sample} \qquad \text{C.13}$$

where z_i is the mass fraction of component i in the prepared 2 mL sample, ρ_{sample} is the density of the sample as calculated from the Riedel correlation for liquid density,[123] and V_{sample} is the volume of the sample injected during the calibration analysis run. The uncertainty in z_i was determined by propagating the uncertainty in the measured masses, accounting for the measurement error associated with the 4-decimal scale, as well as the uncertainty contributed by impurities in the stock FAME. The uncertainty in V_{sample} was calculated from the specifications of the 0.5 µL syringe used to inject samples, where the resolution r was 0.02 µL, and the precision p was 2 % of the injected volume. The uncertainty in ρ_{sample} was taken to be negligible when compared to the other factors influencing the uncertainty in the mass, since the prepared samples consisted of about 98 mol % hexane solvent, the density of which the Riedel correlation predicts with a high degree of accuracy. Subsequently, the uncertainty contributions of the calibration could be calculated as $u^2(m_{1,calib})$ = 3.27e-14 g^2 M18:0, and $u^2(m_{2,calib})$ = 2.64e-14 g^2 M18:1, yielding $u^2(m_1)$ = 1.85e-13 g^2 M18:0 and $u^2(m_2)$ = 1.55e-13 g^2 M18:1 when combined with the test error.

The mass of CO$_2$ was determined from a standard GC calibration curve, given in Equation C.14:

$$m_3 = \alpha_3 + \beta_3 A_3' \qquad \text{C.14}$$

where α_3 and β_3 are the intercept and slope of the calibration curve, and A_3' is the adjusted chromatogram area for CO$_2$. The uncertainty in the calibration curve parameters was determined from a statistical analysis of the calibration data used to regress the calibration curve. Additionally, $u^2(\alpha_3)$ was increased by adding to it a term $u^2(m_{calib})$ to account for the uncertainty associated with the

C. Uncertainty Analysis

known calibration masses. The known calibration mass injected on the GC was calculated with the ideal gas law, according to Equation C.15:

$$m_{calib} = \frac{MPV}{RT}$$

C.15

CO_2 was loaded into a gas bomb to a pressure slightly above atmospheric ($\pm$ 1.5 bar). A gastight microsyringe was used to extract and inject the sample onto the GC. Knowing the pressure in the bomb (measured with a digital 0-4 bar gauge), the temperature in the bomb (measured with a direct-contact Pt100 probe), and the volume injected, as well as their respective uncertainties, the uncertainty in the calibration mass could be determined, incorporating a term for the error associated with impurities in the CO_2. Given $u(P)$ = 0.006 bar, $u(T)$ = 0.3 °C, and $u(V) \approx$ 3 µL, the uncertainty $u^2(m_{calib})$ was found to be 7.68e-11 g^2.

The adjusted peak area A_3' was calculated with Equation C.16:

$$A_3' = A_3 \frac{PFSV}{t_{avg}}$$

C.16

where A_3 is the unadjusted peak area, $PFSV$ is the baseline split vent flow time, and t_{avg} is the average split vent flow time for a given analysis experiment. It was assumed that the uncertainty in the GC peak area was negligible. The value of $PFSV$ was determined from repeating 30 bubble-flow tests, with the uncertainty being the standard error of the data sample. The uncertainty in t_{avg} was taken as the standard error of the average of four or five repeat bubble-flow tests. The area was adjusted in this way to account for potential drift in the split vent flowrate over the course of the experimental work that might cause deviation from the calibration experiment. With all the necessary analyses done, the uncertainty in the mass of CO_2 in a vapour-phase sample could be determined.

The masses determined from the GC analysis were used to calculate the mass fractions of components in the vapour phase. The uncertainty in the mass fraction y_i was calculated by propagating the uncertainty forward from the component masses, and adding a term to account for the effect of pressure on the composition of the vapour phase, as shown in Equation C.17:

$$u^2(y_i) = u^2(y_{i,mass}) + \left(\frac{\partial y_i}{\partial P}\right)^2 u^2(P)$$

C.17

The sensitivity $\left(\frac{\partial y_i}{\partial P}\right)$ was determined by fitting a polynomial to the experimental y-P data, and taking the slope as the sensitivity. The VLE measurements were not conducted isobarically for different temperatures, so the effect of the uncertainty in temperature on y_i could not be determined. The vapour phase compositions and their uncertainties are provided in Table C.19.

Table C.19: Calculated uncertainties in the vapour phase compositions for the M18:0 (1) + M18:1 (2) + CO₂ (3) system at three different temperatures.

P [bar]	y_1 [g·g⁻¹]	$u(y_1)$ [g·g⁻¹]	y_2 [g·g⁻¹]	$u(y_2)$ [g·g⁻¹]	y_3 [g·g⁻¹]	$u(y_3)$ [g·g⁻¹]
			T = 35 °C			
90.0	0.0360	0.0061	0.0160	0.0037	0.9481	0.0087
103.4	0.0536	0.0093	0.0382	0.0069	0.9081	0.0155
110.4	0.0689	0.0102	0.0580	0.0086	0.8731	0.0183
113.1	0.0906	0.0111	0.0812	0.0101	0.8282	0.0208
			T = 55 °C			
146.1	0.0217	0.0024	0.0136	0.0020	0.9646	0.0035
157.4	0.0377	0.0033	0.0321	0.0029	0.9301	0.0056
165.9	0.0677	0.0060	0.0644	0.0055	0.8679	0.0112
168.5	0.0787	0.0100	0.0802	0.0049	0.8411	0.0142
			T = 75 °C			
196.2	0.0320	0.0023	0.0254	0.0020	0.9425	0.0037
206.6	0.0476	0.0024	0.0433	0.0023	0.9091	0.0042
214.3	0.0700	0.0043	0.0749	0.0046	0.8551	0.0086

Now, consider the liquid phase samples. The main measurement output was chromatographic data that was converted into an ester ratio r_{21}, the mass ratio of M18:1 to M18:0. This conversion was done with an artificial neural network as described in Section 4.3.3. The uncertainty $u(r_{21})$ was calculated with two components, a component relating to the uncertainty introduced by the neural network, and a component relating to the uncertainty in the calibration data used to train the neural network, as shown in Equation C.18:

$$u^2(r_{21}) = u^2(r_{21,CV}) + u^2(r_{21,calib})$$
C.18

The uncertainty imparted by the neural network was taken as the test error and was calculated with a cross-validation approach. The uncertainty associated with the error in the calculated mass ratio in the prepared sample was determined by propagating the error from the known sample masses, as was determined during the analysis of the vapour phase samples. This gave $u^2(r_{21})$ = 0.090 g²·g⁻².

Knowledge of the ester mass ratio was used together with previously measured ternary HPBDP data to determine the liquid component mass fractions. Fitting a curve $x_2 = \alpha + \beta x_1$ to the ternary HPBDP data, the intersection with the line of constant ester mass ratio $x_2 = r_{21}x_1$ was determined to find the fraction of M18:0 x_1, according to Equation C.19:

$$x_1 = \frac{\alpha}{r_{21} - \beta}$$
C.19

C. Uncertainty Analysis

where α and β are the intercept and slope of the HPBDP data fit. The uncertainty in the fit parameters was determined through statistical analysis of the data, including an added term to increase $u(\alpha)$ in order to account for the uncertainty in the measured HPBDP data according to Equation C.20:

$$u^2(\alpha) = var(\alpha) + u^2(x_{HPBDP}) \qquad \text{C.20}$$

where $u(x_{HPBDP})$ was taken as the maximum uncertainty in the M18:1 mass fraction for the measured HPBDP data as previously calculated, and was found to be 0.0079 g·g^{-1}. Having determined the uncertainty in x_1 (including the covariance between parameters α and β), this uncertainty was propagated to the mass fraction of M18:1 in the liquid phase through Equation C.21:

$$x_2 = r_{21}x_1 \qquad \text{C.21}$$

The uncertainty in x_2 also accounted for the covariance between α and β, and was then further propagated to the CO_2 mass fraction in the liquid through Equation C.22, where the covariance between x_1 and x_2 was also taken into account:

$$x_3 = 1 - x_1 - x_2 \qquad \text{C.22}$$

The composition of the liquid phase is influenced by the pressure, and so the uncertainty in the pressure contributes to the uncertainty in the composition. This was accounted for by applying Equation C.23:

$$u^2(x_i) = u^2(x_{i,mass}) + \left(\frac{\partial x_i}{\partial P}\right)^2 u^2(P) \qquad \text{C.23}$$

$\left(\frac{\partial x_i}{\partial P}\right)$ was calculated in an identical manner to $\left(\frac{\partial y_i}{\partial P}\right)$. The VLE measurements were not conducted isobarically for different temperatures, so the effect of the uncertainty in temperature on y_i could not be determined. The calculated liquid phase composition uncertainty is summarised in Table C.20.

Table C.20: Calculated uncertainties in the liquid phase compositions for the M18:0 (1) + M18:1 (2) + CO$_2$ (3) system at three different temperatures.

P [bar]	x_1 [g·g^{-1}]	$u(x_1)$ [g·g^{-1}]	x_2 [g·g^{-1}]	$u(x_2)$ [g·g^{-1}]	x_3 [g·g^{-1}]	$u(x_3)$ [g·g^{-1}]
			T = 35 °C			
90.0	0.2097	0.0289	0.2675	0.0730	0.5228	0.0685
103.4	0.1859	0.0275	0.2247	0.0649	0.5894	0.0616
110.4	0.1639	0.0241	0.2058	0.0578	0.6303	0.0552
113.1	0.1401	0.0179	0.1906	0.0494	0.6693	0.0511
			T = 55 °C			
146.1	0.2149	0.0301	0.2614	0.0742	0.5237	0.0691
157.4	0.1877	0.0262	0.2371	0.0654	0.5752	0.0615
165.9	0.1756	0.0259	0.2059	0.0608	0.6185	0.0571
168.5	0.1713	0.0267	0.1883	0.0593	0.6403	0.0555
			T = 75 °C			
196.2	0.2024	0.0276	0.2584	0.0702	0.5392	0.0659
206.6	0.1879	0.0266	0.2289	0.0650	0.5832	0.0610
214.3	0.1670	0.0245	0.2075	0.0587	0.6255	0.0557

With the compositions of the coexisting phases and their uncertainties known, the separation quantifiers could be evaluated. Distribution coefficients K_i were calculated for M18:0 and M18:1 with Equation C.24:

$$K_i = \frac{y_i}{x_i} \hspace{4cm} \text{C.24}$$

The uncertainty in the liquid and vapour mass fractions was propagated to the distribution coefficients. This information was then used to calculate the relative solubility α_{12} at each pressure with Equation C.25:

$$\alpha_{12} = \frac{K_1}{K_2} = \frac{y_1 x_2}{x_1 y_2} \hspace{4cm} \text{C.25}$$

Since both K_1 and K_2 have variables in common (the same masses were used to calculate y_1 and y_2, and the same parameters were used to calculate x_1 and x_2), the covariance $u(K_1, K_2)$ had to be determined and accounted for in the calculation of the uncertainty in α_{12}. The calculated uncertainty in the relative solubility is presented in Table C.21.

C. Uncertainty Analysis

Table C.21: Calculated uncertainties for the relative solubility between M18:0 and M18:1 in supercritical CO$_2$.

P [bar]	α_{12} [-]	$u(\alpha_{12})$ [-]
T = 35 °C		
90.0	2.88	0.88
103.4	1.70	0.48
110.4	1.49	0.39
113.1	1.52	0.51[a]
T = 55 °C		
146.1	1.94	0.57
157.4	1.48	0.39
165.9	1.23	0.35
168.5	1.08	0.35
T = 75 °C		
196.2	1.61	0.41
206.6	1.34	0.35
214.3	1.16	0.32

[a] *The covariance $u(K_1, K_2)$ was not added for this point, as it resulted in a negative squared standard uncertainty.*

APPENDIX D:
Experimental Data

D.1. Reported Experimental Data

D.1.1. Binary HPBDP data

Tables D.1 to D.3 provide summaries of the reported phase transition pressures and P-T correlations determined for the three binary FAME + CO_2 systems measured in this work.

Table D.1: Summary of the measured phase transition data and P-T correlations for the M18:0 (1) + CO_2 (2) system over a range of temperatures.$u(z_1)$ = (0.0001 to 0.0056) g·g^{-1} ^{a}, $u(P)$ = (0.7 to 1.8) bar^b.

z_1 [g·g^{-1}]	P [bar]					$P = AT^2 + BT + C$ with P in bar and T in °C		
	35 °C	45 °C	55 °C	65 °C	75 °C	A	B	C
0.6234	72.7	92.2	111.6	131.0	150.4	0.0000	1.9427	4.74
0.5449	80.2	106.9	131.5	154.1	174.7	-1.0212e-2	3.4843	-29.21
0.4611	99.7	128.4	154.8	178.9	200.7	-1.1447e-2	3.7856	-18.79
0.3675	117.8	145.7	171.7	195.5	217.3	-1.0244e-2	3.6155	3.79
0.3105	122.2	150.4	176.3	200.0	221.4	-1.1448e-2	3.7386	5.35
0.2463	123.8	151.4	177.0	200.6	222.2	-9.9923e-3	3.5579	11.54
0.1609	120.6	148.8	174.6	198.0	219.1	-1.1832e-2	3.7656	3.27
0.1225	117.4	145.3	170.8	194.0	214.8	-1.1838e-2	3.7368	1.12
0.0799	107.9	135.6	160.9	183.7	204.1	-1.2374e-2	3.7665	-8.81
0.0510	97.2	124.5	149.3	171.6	191.4	-1.2389e-2	3.7166	-17.67
0.0104	79.7	101.2	120.5	137.8	152.9	-1.0563e-2	2.9904	-11.98

^{a}$u(z_1)$ = (u_{min} to u_{max}) where u_{min} and u_{max} are respectively the minimum and maximum standard uncertainties in the solute fraction.

^{b} $u(P)$ = (u_{min} to u_{max}) where u_{min} and u_{max} are respectively the minimum and maximum standard uncertainties in the phase transition pressure.

D. Experimental Data

Table D.2: Summary of the measured phase transition data and P-T correlations for the M18:1 (1) + CO_2 (2) system over a range of temperatures. $u(z_1)$ = (0.0001 to 0.0051) $g \cdot g^{-1}$ [a], $u(P)$ = (0.7 to 1.8) bar[b].

z_1 [g·g^{-1}]	P [bar]					$P = AT^2 + BT + C$ with P in bar and T in °C		
	35 °C	45 °C	55 °C	65 °C	75 °C	A	B	C
0.5736	74.5	95.8	117.2	138.5	159.9	0	2.1345	-0.23
0.4947	81.8	111.0	138.0	162.7	185.3	-1.1186e-2	3.8178	-38.15
0.4696	87.7	117.6	144.9	169.6	191.7	-1.3096e-2	4.0403	-37.68
0.3690	103.5	134.1	161.8	186.9	209.1	-1.3824e-2	4.1601	-25.14
0.2884	109.1	139.8	167.8	192.9	215.2	-1.4084e-2	4.2009	-20.68
0.2569	110.3	140.8	168.4	193.2	215.3	-1.3906e-2	4.1539	-18.01
0.2186	109.8	139.6	166.8	191.5	213.6	-1.2815e-2	4.0038	-14.64
0.1582	108.1	138.4	165.9	190.4	212.1	-1.4477e-2	4.1918	-20.89
0.1222	104.3	134.0	161.1	185.8	207.9	-1.2565e-2	3.9739	-19.42
0.0874	99.2	129.1	155.9	179.8	200.6	-1.5065e-2	4.1905	-28.98
0.0545	91.7	120.9	146.8	169.6	189.2	-1.5906e-2	4.1874	-35.35
0.0110	79.8	101.5	121.4	139.5	155.7	-8.9930e-3	2.8886	-10.31

[a] $u(z_1)$ = (u_{min} to u_{max}) where u_{min} and u_{max} are respectively the minimum and maximum standard uncertainties in the solute fraction.
[b] $u(P)$ = (u_{min} to u_{max}) where u_{min} and u_{max} are respectively the minimum and maximum standard uncertainties in the phase transition pressure.

Table D.3: Summary of the measured phase transition data and P-T correlations for the M18:2 (1) + CO_2 (2) system over a range of temperatures. $u(z_1)$ = (0.0003 to 0.0048) $g \cdot g^{-1}$ [a], $u(P)$ = (0.7 to 1.8) bar[b].

z_1 [g·g^{-1}]	P [bar]					$P = AT^2 + BT + C$ with P in bar and T in °C		
	35 °C	45 °C	55 °C	65 °C	75 °C	A	B	C
0.5865	72.9	93.4	113.9	134.4	154.9	0.0000	2.0502	1.17
0.5414	76.4	99.9	123.5	147.1	170.6	0.0000	2.3567	-6.11
0.4675	85.2	114.7	142.1	167.2	190.1	-1.0987e-2	3.8306	-35.39
0.3861	98.6	130.1	158.9	184.9	208.1	-1.3967e-2	4.2737	-33.90
0.3104	107.5	138.5	166.8	192.4	215.3	-1.3323e-2	4.1606	-21.77
0.2638	108.7	139.6	167.8	193.4	216.3	-1.3269e-2	4.1504	-20.32
0.1599	105.7	136.8	165.0	190.4	212.9	-1.4286e-2	4.2511	-25.57
0.0862	98.6	129.3	156.9	181.6	203.2	-1.5045e-2	4.2691	-32.35
0.0375	87.3	116.2	141.7	163.9	182.9	-1.6471e-2	4.1996	-39.47

[a] $u(z_1)$ = (u_{min} to u_{max}) where u_{min} and u_{max} are respectively the minimum and maximum standard uncertainties in the solute fraction.
[b] $u(P)$ = (u_{min} to u_{max}) where u_{min} and u_{max} are respectively the minimum and maximum standard uncertainties in the phase transition pressure.

D.1.2. Ternary HPBDP data

Tables D.4 to D.6 provide summaries of the reported phase transition pressures and P-T correlations determined for the three ternary M18:0 (1) + M18:1 (2) + CO_2 (3) systems measured in this work.

Table D.4: Summary of the measured phase transition data and P-T correlations for the w_1^{red} = 0.237 g·g^{-1} system over a range of temperatures. $u(w_1)$ = (0.0001 to 0.0066) g·g^{-1}, $u(w_2)$ = (0.0001 to 0.0079) g·g^{-1}, $u(w_3)$ = (0.0002 to 0.0124) g·g^{-1}. $u(P)$ = (1.0 to 1.6) bar^a.

w_1 [g·g^{-1}]	w_2 [g·g^{-1}]	w_3 [g·g^{-1}]	P [bar]					$P = AT^2 + BT + C$ with P in bar and T in °C		
			35 °C	45 °C	55 °C	65 °C	75 °C	A	B	C
0.0023	0.0074	0.9903	80.1	102.3	122.4	140.4	156.2	-1.0588e-2	3.0693	-14.40
0.0128	0.0411	0.9461	91.3	120.9	147.4	170.9	191.2	-1.5398e-2	4.1915	-36.51
0.0189	0.0609	0.9202	99.5	129.3	156.3	180.7	202.3	-1.3664e-2	4.0724	-26.32
0.0283	0.0912	0.8805	106.9	136.9	164.3	189.0	211.1	-1.3287e-2	4.0648	-19.06
0.0378	0.1217	0.8406	111.3	140.8	167.9	192.8	215.4	-1.1409e-2	3.8572	-9.70
0.0478	0.1540	0.7982	112.0	141.2	168.4	193.3	216.2	-1.0711e-2	3.7831	-7.31
0.0633	0.2037	0.7331	113.8	143.6	171.0	196.0	218.6	-1.2014e-2	3.9425	-9.48
0.0709	0.2282	0.7009	112.5	142.4	170.0	195.3	218.4	-1.1360e-2	3.8971	-9.97
0.0838	0.2698	0.6464	110.2	140.4	168.0	193.2	215.9	-1.2381e-2	4.0041	-14.74
0.1128	0.3632	0.5240	90.1	119.0	145.9	170.6	193.2	-1.0515e-2	3.7362	-27.82
0.0972	0.3130	0.5897	103.0	132.8	160.3	185.4	208.1	-1.1850e-2	3.9322	-20.11

^{a} $u(x)$ = (u_{min} to u_{max}) with u_{min} the minimum standard uncertainty in the quantity x, and u_{max} the maximum standard uncertainty in the quantity x.

Table D.5: Summary of the measured phase transition data and P-T correlations for the w_1^{red} = 0.501 g·g^{-1} system over a range of temperatures. $u(w_1)$ = (0.0001 to 0.0039) g·g^{-1}, $u(w_2)$ = (0.0001 to 0.0039) g·g^{-1}, $u(w_3)$ = (0.0001 to 0.0067) g·g^{-1}. $u(P)$ = (1.0 to 1.6) bar^a.

w_1 [g·g^{-1}]	w_2 [g·g^{-1}]	w_3 [g·g^{-1}]	P [bar]					$P = AT^2 + BT + C$ with P in bar and T in °C		
			35 °C	45 °C	55 °C	65 °C	75 °C	A	B	C
0.2678	0.2668	0.4654	79.0	105.8	130.7	153.6	174.6	-9.6647e-3	3.4520	-29.96
0.2888	0.2877	0.4235	75.5	96.2	117.0	137.7	158.5	0.0000	2.0748	2.87
0.2118	0.2109	0.5773	102.7	131.0	157.1	180.9	202.4	-1.1325e-2	3.7391	-14.34
0.1853	0.1846	0.6301	111.4	140.3	167.2	191.9	214.6	-1.0492e-2	3.7354	-6.53
0.1405	0.1400	0.7195	115.6	144.8	171.7	196.5	219.1	-1.0968e-2	3.7932	-3.73
0.1278	0.1273	0.7448	116.1	144.8	171.5	196.4	219.3	-9.5300e-3	3.6285	0.80
0.0598	0.0596	0.8806	111.3	141.0	168.2	192.8	214.8	-1.2781e-2	3.9920	-12.72
0.0821	0.0817	0.8362	115.6	144.6	171.5	196.1	218.6	-1.1105e-2	3.7961	-3.69
0.0416	0.0414	0.9170	104.0	133.5	160.3	184.4	205.9	-1.3251e-2	4.0050	-19.92
0.0253	0.0252	0.9494	93.6	123.1	149.5	172.6	192.4	-1.6177e-2	4.2509	-35.39
0.0058	0.0058	0.9883	81.1	105.4	127.3	147.0	164.4	-1.1458e-2	3.3435	-21.89

^{a} $u(x)$ = (u_{min} to u_{max}) with u_{min} the minimum standard uncertainty in the quantity x, and u_{max} the maximum standard uncertainty in the quantity x.

D. Experimental Data

Table D.6: Summary of the measured phase transition data and P-T correlations for the w_1^{red} = 0.772 g·g⁻¹ system over a range of temperatures. $u(w_1)$ = (0.0002 to 0.0078) g·g⁻¹, $u(w_2)$ = (0.0001 to 0.0067) g·g⁻¹, $u(w_3)$ = (0.0002 to 0.0124) g·g⁻¹. $u(P)$ = (1.0 to 1.6) barᵃ.

w_1 [g·g⁻¹]	w_2 [g·g⁻¹]	w_3 [g·g⁻¹]	P [bar]					$P = AT^2 + BT + C$ with P in bar and T in °C		
			35 °C	45 °C	55 °C	65 °C	75 °C	A	B	C
0.0081	0.0024	0.9895	80.4	103.9	125.1	143.8	160.1	-1.2044e-2	3.3164	-20.90
0.0403	0.0119	0.9478	93.7	122.5	148.5	171.5	191.5	-1.4731e-2	4.0660	-30.59
0.0592	0.0175	0.9233	102.3	131.6	158.0	181.4	201.8	-1.4770e-2	4.1116	-23.47
0.0935	0.0276	0.8789	112.2	141.3	167.8	191.7	213.1	-1.2803e-2	3.9314	-9.71
0.1244	0.0367	0.8389	117.1	145.8	172.1	196.0	217.4	-1.2164e-2	3.8457	-2.60
0.1623	0.0479	0.7897	117.9	146.6	172.9	196.9	218.5	-1.1717e-2	3.8041	-0.85
0.2034	0.0601	0.7365	120.3	148.9	175.5	200.0	222.5	-1.0217e-2	3.6776	4.12
0.2341	0.0691	0.6967	119.8	148.7	175.5	200.0	222.3	-1.1054e-2	3.7793	1.03
0.2784	0.0822	0.6394	115.9	144.4	170.9	195.5	218.1	-9.7869e-3	3.6324	0.74
0.3242	0.0957	0.5801	105.5	133.7	160.0	184.5	207.1	-9.3071e-3	3.5623	-7.77
0.4179	0.1234	0.4587	79.5	104.6	128.7	151.8	173.9	-5.0647e-3	2.9165	-16.37
0.4453	0.1315	0.4232	76.6	98.0	119.5	141.0	162.5	0.0000	2.1490	1.34

ᵃ $u(x)$ = $(u_{min}$ to $u_{max})$ with u_{min} the minimum standard uncertainty in the quantity x, and u_{max} the maximum standard uncertainty in the quantity x.

D.1.3. Ternary HPVLE Data

Table D.7: Coexisting phase compositions of the liquid (x_i) and vapour (y_i) phases for the ternary M18:0 (1) + M18:1 (2) + CO₂ (3) system at different temperatures (T) and pressures (P).

P [bar]	x_1 [g·g⁻¹]	x_2 [g·g⁻¹]	x_3 [g·g⁻¹]	y_1 [g·g⁻¹]	y_2 [g·g⁻¹]	y_3 [g·g⁻¹]
			T = 35 °C			
90	0.2097	0.2675	0.5228	0.0360	0.0160	0.9481
103.4	0.1859	0.2247	0.5894	0.0536	0.0382	0.9081
110.4	0.1639	0.2058	0.6303	0.0689	0.0580	0.8731
113.1	0.1401	0.1906	0.6693	0.0906	0.0812	0.8282
			T = 55 °C			
146.1	0.2149	0.2614	0.5237	0.0217	0.0136	0.9646
157.4	0.1877	0.2371	0.5752	0.0377	0.0321	0.9301
165.9	0.1756	0.2059	0.6185	0.0677	0.0644	0.8679
168.5	0.1713	0.1883	0.6403	0.0787	0.0802	0.8411
			T = 75 °C			
196.2	0.2024	0.2584	0.5392	0.0320	0.0254	0.9425
206.6	0.1879	0.2289	0.5832	0.0476	0.0433	0.9091
214.3	0.1670	0.2075	0.6255	0.0700	0.0749	0.8551

D.2. Verification Data

D.2.1. HPBDP verification data

Table D.8: Measured verification data for the 1-octanol (1) + CO_2 (2) system as a series of phase transition pressures (P) at various solute fractions (z_1) and temperatures (T).

z_1 [g·g⁻¹]	T_1 [°C]	P_1 [bar]	T_2 [°C]	P_2 [bar]	T_3 [°C]	P_3 [bar]	T_4 [°C]	P_4 [bar]
0.746	35	68.4	45	78.0	55	87.6	75	106.8
0.569	35	110.4	45	116.9	55	126.3	75	154.1
0.359	35	165.3	45	153.8	55	158.3	75	177.4
0.289	35	167.5	45	154.2	55	158.3	75	175.9
0.112	35	126.1	45	134.0	55	144.0	75	170.4
0.030	35	78.1	45	98.2	55	115.3	75	140.3

D.2.2. VLE verification data

Table D.9: Measured verification data for the CO_2 (1) + nC_{12} (2) + 1-$C_{10}OH$(3) system as two VLE tie-lines at pressure (P) and temperature (T) having vapour phase compositions (y_i) and liquid phase compositions (x_i).

T [°C]	P [bar]	y_1 [g·g⁻¹]	y_2 [g·g⁻¹]	y_3 [g·g⁻¹]	x_1 [g·g⁻¹]	x_2 [g·g⁻¹]	x_3 [g·g⁻¹]
55	123	0.902	0.038	0.060	0.460	0.124	0.416
75	157	0.917	0.030	0.052	0.469	0.118	0.413

D.3. Unprocessed Data

D.3.1. Binary HPBDP data

Tables D.10 to D.12 provide the unprocessed data measured during the binary HPBDP experiments. This data was used to set up the pressure-temperature correlations which were used to predict the phase transition pressure at nominal temperature values.

Table D.10: Unprocessed data measured for the binary M18:0 + CO_2 system.

z [g·g⁻¹]	T_1 [°C]	P_1 [bar]	T_2 [°C]	P_2 [bar]	T_3 [°C]	P_3 [bar]	T_4 [°C]	P_4 [bar]	T_5 [°C]	P_5 [bar]
0.0104	34.1	78.6	44.1	101.7	54.1	123.6	64.0	142.6	74.1	159.8
0.0510	34.1	95.7	44.2	125.1	54.1	151.9	64.0	176.5	74.4	198.8
0.0799	34.0	106.0	44.0	135.9	54.2	163.9	63.8	188.1	74.1	211.0
0.1225	34.0	115.6	44.2	146.3	54.1	173.7	63.9	198.5	74.1	221.8
0.1609	34.7	116.1	44.6	145.5	54.4	172.2	64.2	196.5	74.4	220.0
0.2463	34.7	119.6	44.5	147.4	54.4	174.9	64.0	198.8	74.3	222.7
0.3105	34.8	118.1	44.7	147.3	54.5	174.1	64.2	198.8	74.4	222.1
0.3675	34.9	114.0	44.8	142.9	54.7	169.9	64.4	194.6	74.8	218.9
0.4611	35.3	97.2	44.9	125.7	54.8	153.2	64.5	177.6	74.9	202.3
0.5449	34.9	77.2	44.9	103.8	54.8	129.6	64.6	153.3	74.9	175.4
0.6234	35.0	70.6	44.8	88.8	54.8	109.2	64.5	130.2	74.9	150.8

D. Experimental Data

Table D.11: Unprocessed data measured for the binary M18:1 + CO₂ system.

z [g·g⁻¹]	T₁ [°C]	P₁ [bar]	T₂ [°C]	P₂ [bar]	T₃ [°C]	P₃ [bar]	T₄ [°C]	P₄ [bar]	T₅ [°C]	P₅ [bar]
0.0110	33.9	78.3	43.8	100.9	53.8	123.8	63.5	143.5	73.9	162.1
0.0545	33.9	89.1	44.0	121.0	53.8	148.8	63.5	172.8	73.9	195.9
0.0874	34.1	97.3	44.1	129.5	54.1	158.7	64.0	184.1	74.1	207.6
0.1222	33.8	101.4	43.9	134.0	53.8	162.7	63.5	189.1	74.1	214.8
0.1582	33.8	105.0	44.6	141.0	54.2	168.5	63.6	193.8	73.9	218.7
0.2186	33.9	107.4	43.8	139.1	53.8	168.6	63.4	194.6	73.7	219.5
0.2569	34.4	104.8	43.7	134.7	52.6	160.7	61.5	184.5	71.1	208.6
0.2884	34.5	103.9	44.0	134.6	53.5	162.6	62.1	185.6	71.2	208.6
0.3690	34.9	99.9	44.7	130.5	54.5	159.5	64.2	185.2	74.5	209.8
0.4696	34.7	83.3	44.5	114.4	54.4	141.6	64.0	166.8	74.3	191.8
0.4947	34.8	78.3	44.7	107.4	54.6	135.5	64.3	161.1	74.7	185.8
0.5736	34.8	71.4	44.7	91.7	54.5	115.3	64.2	137.7	73.9	157.0

Table D.12: Unprocessed data measured for the binary M18:2 + CO₂ system.

z [g·g⁻¹]	T₁ [°C]	P₁ [bar]	T₂ [°C]	P₂ [bar]	T₃ [°C]	P₃ [bar]	T₄ [°C]	P₄ [bar]	T₅ [°C]	P₅ [bar]
0.0375	33.9	84.8	43.9	115.8	53.9	143.8	63.8	168.1	74.0	189.6
0.0862	33.8	95.6	44.0	129.3	53.8	158.8	63.5	184.6	73.8	209.5
0.1599	33.8	102.6	43.9	136.8	53.9	167.0	63.6	193.6	73.8	219.2
0.2638	34.5	103.7	44.4	135.1	54.3	165.0	64.0	191.3	74.4	216.9
0.3104	34.4	102.1	44.3	134.0	54.2	163.4	63.9	190	74.3	215.7
0.3861	34.6	93.8	44.3	125.7	54.1	155.1	63.7	181.6	73.9	207.4
0.4675	34.6	80.8	44.1	110.0	53.7	136.6	63.1	162.5	73.0	186.8
0.5414	34.6	72.9	44.4	95.1	54.3	120.8	63.7	144.3	73.1	166.3
0.5865	34.6	70.2	44.4	88.7	54.3	110.8	64.0	132.2	74.3	154.2

D.3.2. Ternary HPBDP Data

Tables D.13 to D.15 provide the unprocessed data measured during the ternary HPBDP experiments. This data was used to set up the pressure-temperature correlations which were used to predict the phase transition pressure at nominal temperature values.

Table D.13: Unprocessed data measured for the ternary M18:0 + M18:1 + CO₂ system at w = 0.237 g·g⁻¹.

z [g·g⁻¹]	T₁ [°C]	P₁ [bar]	T₂ [°C]	P₂ [bar]	T₃ [°C]	P₃ [bar]	T₄ [°C]	P₄ [bar]	T₅ [°C]	P₅ [bar]
0.0097	34.4	80.8	44.6	104.8	54.7	127.5	64.9	147.7	74.0	163.5
0.0539	34.3	91.2	44.4	123.4	54.3	151.6	64.2	176.3	73.6	197.9
0.0798	34.3	99.5	44.4	131.7	54.5	160.9	64.3	186.7	73.4	208.2
0.1195	34.3	107.0	44.3	139.2	54.3	168.4	64.2	194.8	73.3	216.8
0.1595	34.3	111.6	44.5	143.4	54.7	173.3	64.5	199.5	73.4	221.2
0.2018	34.4	112.6	44.1	142.7	54.8	173.9	64.8	200.9	74.0	223.3
0.2670	34.8	114.8	45.3	148.0	55.4	177.4	66.0	205.1	74.6	226.2
0.2991	34.7	113.3	45.3	146.7	55.2	175.9	65.2	202.6	74.8	226.4
0.3536	34.7	111.0	45.3	144.5	55.4	174.4	65.5	201.3	75.5	225.4
0.4102	34.8	104.2	45.4	136.8	55.4	166.7	65.5	193.7	75.7	217.9
0.4760	34.7	90.5	45.2	123.0	55.2	151.3	65.2	177.5	75.4	202.5
0.5678	34.4	78.4	44.8	103.0	54.7	129.5	64.5	153.3	74.4	176.4

Table D.14: Unprocessed data measured for the ternary M18:0 + M18:1 + CO$_2$ system at w = 0.501 g·g^{-1}.

z [g·g^{-1}]	T$_1$ [°C]	P$_1$ [bar]	T$_2$ [°C]	P$_2$ [bar]	T$_3$ [°C]	P$_3$ [bar]	T$_4$ [°C]	P$_4$ [bar]	T$_5$ [°C]	P$_5$ [bar]
0.0117	34.8	83.0	45.1	108.6	55.3	134.4	65.3	155.0	74.3	172.2
0.0506	34.5	94.1	44.6	126.5	54.5	153.6	64.5	179.3	73.8	199.4
0.0830	34.7	105.4	44.6	136.6	54.8	165.8	64.8	191.6	74.0	213.3
0.1194	34.6	112.8	44.4	142.8	54.8	174.3	64.9	200.4	74.0	222.0
0.1638	34.6	116.9	44.6	147.6	54.8	177.2	64.9	203.9	74.1	226.0
0.2552	34.7	102.0	44.8	131.3	55.6	161.2	66.1	188.3	75.7	210.8
0.2805	34.8	101.8	44.8	131.2	55.5	161.2	66.0	188.1	75.7	210.5
0.3699	35.0	98.1	44.8	127.0	55.3	155.9	65.5	182.2	75.1	204.7
0.4227	34.8	88.7	44.8	117.9	55.5	146.6	65.9	170.8	75.4	193.3
0.5346	34.8	66.0	44.7	92.0	55.4	119.5	65.8	143.7	75.3	164.3
0.5765	34.9	63.1	44.8	82.6	55.6	105.9	65.9	128.0	75.4	148.2

Table D.15: Unprocessed data measured for the ternary M18:0 + M18:1 + CO$_2$ system at w = 0.772 g·g^{-1}.

z [g·g^{-1}]	T$_1$ [°C]	P$_1$ [bar]	T$_2$ [°C]	P$_2$ [bar]	T$_3$ [°C]	P$_3$ [bar]	T$_4$ [°C]	P$_4$ [bar]	T$_5$ [°C]	P$_5$ [bar]
0.0105	34.2	80.5	44.3	105.9	54.4	129.4	64.2	149.8	73.2	166
0.0522	34.3	93.6	44.5	125.5	54.7	153.4	64.7	178.4	73.7	198.3
0.0767	33.3	99.1	43.2	130.6	56.4	167.6	65.6	190.6	74.8	210.9
0.1211	35.2	115.4	44.3	143.4	54.4	172.2	64.1	197.6	74	220.4
0.1611	35	119.6	44.9	149.9	55	178.4	65	203.7	75.3	227.7
0.2102	35.2	122.9	45.1	152.8	55.7	182.8	66	209	75.5	230.9
0.2635	34.2	119.5	44.2	150.2	54.2	178.4	64.5	205.5	73.4	227.2
0.3032	34.4	119.6	44.6	151	54.8	180.2	64.3	204.9	73.8	228
0.3606	31.9	107.8	44.2	145.5	54.3	174.3	64	199.5	73.8	223.8
0.4199	34.5	105.6	44.8	136.4	55	165	65.3	192	74.9	215.1
0.5413	33.4	76.8	44.8	106.3	55.1	133.9	65.3	159.5	74.7	180.9
0.5768	34.6	77.4	45	99.8	55.4	125.6	65.8	149.6	75.1	170.4